UNIVERSITY OF CANTERBURY

Department of Physics and Astronomy

CHRISTCHURCH NEW ZEALAND

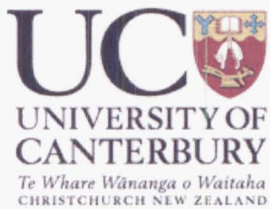

The design and performance of high resolution échelle spectrographs in astronomy

---

A thesis submitted in
partial fulfilment of the
requirements for the degree of
Doctor of Philosophy in Astronomy

by

Stuart Barnes

University of Canterbury
2004

The design and performance of high resolution échelle spectrographs in astronomy

Stuart Barnes

Abstract

The design and performance of several high resolution spectrographs for use in astronomy will be described. After a basic outline of the required theory, the design and performance of HERCULES will be presented. HERCULES is an R2 spectrograph fibre-fed from the MJUO 1-m telescope. The échelle grating has 31.6 grooves/mm and it uses a BK7 prism with a 50° apex angle in double-pass for cross-dispersion. A folded Schmidt camera is used for imaging. With a detector having an area 50 × 50 mm, and pixels less than 25 μm, HERCULES is capable of resolving powers of 40 000 to 80 000 and wavelength coverage from 380 to 880 nm. The total throughput (from the fibre entrance to the CCD) is expected to be nearly 20% (in 1″ seeing). Measured efficiencies are only slightly less than this. HERCULES is also shown to be capable of excellent radial velocity precision with no apparent difference between long-term and short-term stability. Several significant upgrade options are also described.

As part of the evolution of the design of a high resolution spectrograph for SALT, several instruments were developed for 10-metre class telescopes. Early designs, based in part on the successful HERCULES design, did not meet the requirements of a number of potential users, due in particular to the limited ability to inter-leave object and sky orders. This resulted in the design of SALT HRS R2 which uses a mosaic of two 308 × 413 mm R2 échelle gratings with 87 grooves/mm. Cross-dispersion is achieved with a pair of large 40° apex angle BK7 prisms used in double-pass. The échelle grating accepts a 365-mm collimated beam. The camera is a catadioptric system having a 1.2-m primary mirror and three lenses made of BK7 each around 850 mm in diameter. Complete unvignetted (except by the CCD obstruction) wavelength coverage from 370 nm to 890 nm is possible on a mosaic of three 2k by 4k CCDs with 15 μm pixels. A maximum resolving power of $R \approx 80\,000$ is possible. For immunity to atmospheric pressure and temperature changes the entire spectrograph is designed to be housed inside either a helium atmosphere or a light vacuum. The spectrograph chamber is nearly seven metres long.

An alternative to the R2 SALT HRS is also described. This instrument is an R4 dual beam spectrograph based on a white pupil layout. The design is based on suggestions by B. Delabre and follows closely this authors SOAR HRS instrument. SALT HRS R4 uses volume-phased holographic gratings for cross-dispersion and a 836×204 mm échelle grating with 41.6 grooves/mm. The grating will be replicated from two smaller gratings onto a single Zerodur blank. The spectrograph is split into blue and red arms by a dichroic located near the white pupil relay intermediate focus. Wavelengths from 370 nm to 890 nm are covered by two fixed format blue and red dedicated dioptric cameras. The detectors will be a single 2k by 4k CCD with 15 μm pixels for the blue camera and a 4k by 4k CCD with 15 μm pixels for the red. The size of the cameras is reduced significantly by white pupil demagnification from an initial 200-mm diameter collimated beam incident on the échelle grating to around 100 mm (in undispersed light) on the VPH gratings. The final SALT HRS R4 instrument is also designed to be immersed in a vacuum vessel which is considerably smaller than that proposed for the R2 spectrograph. SALT HRS R4 is currently being developed in detail and will be presented for a critical design review in 2005 April.

Contents

Figures

Tables

Acknowledgments

The design and construction of HERCULES would not have been possible without the support of many people. I thank my supervisor, John Hearnshaw, for leading this project in which I have taken great pleasure being involved. I would like to thank all the members of the HERCULES design and construction team. In particular, the support of Graeme Kershaw, Nigel Frost, Ross Ritchie, and Geoff Graham from the Department of Physics and Astronomy, and optical fabricators Gary Nankivell and Dave Cochran has been of great value. The excellent performance of HERCULES would never have been demonstrated without the considerable efforts of Jovan Skuljan and David Ramm. Thanks also to Jovan (and Ljiljana), and to David for many interesting conversations and for tolerating my sometimes wild ideas.

The design of SALT HRS has involved a large number of people. The principle investigator Peter Cottrell, and project scientist Michael Albrow have both given considerable support to my design work. Without their continued enthusiasm, this project would not have continued to progress Peters encouragement in particular has allowed us all to persevere through the sometimes difficult times we have faced. Thanks to Andrew Rakich and Damien Jones for casting their expert eyes over my optical design work. I would also like to acknowledge the support of SALT project scientist David Buckley. Along with the combined SALT science working group, David has ensured that the SALT HRS design has matured into what will become a very capable instrument. The especially thorough examination by the SALT HRS external reviewers has been greatly appreciated. Reviewers have included Richard Bingham, Bernard Delabre, Hans Dekker, Steve Shectman and David Walker.

I would like to acknowledge being in receipt of the Michael Kidger Memorial Scholarship and the William Price Scholarship for Optical Design. I also received a University of Canterbury Doctoral Scholarship for which I am grateful. I acknowledge support from the Moore Fund, the Royal Society of New Zealand (Canterbury Branch), SPIE, for funds to attend overseas conferences. The financial and logistical support of the Department of Physics and Astronomy has been considerable for both the HERCULES and SALT HRS projects.

Of course, I thank all of my family, without whom none of this would have been possible. Special thanks to my good friends Mike and Teina, and to J. Bedford and the rest of the derelicts on Tilford Street for providing many welcome distractions. Thanks also to Katja for her love and support during recent months. Finally, thanks also to all the beautiful freaks I have come to know who make life so interesting.

This research has made use of NASA's Astrophysics Data System.

Chapter 1

Echelle spectrograph theory

1.1 Introduction

Even at the time the French philosopher August Comte (1835) wrote despairingly of the hope of how to "study by any means" anything other than the "geometrical or mechanical phenomena" of stars, Fraunhofer, using both prism and grating spectroscopes, had already observed absorption lines in the spectra of the sun (see Hearnshaw, 1986 pp. 24–29 and references therein). Later, when Kirchhoff and Bunsen (1860) made the connection between these lines and the chemical composition of the Sun, it became possible to extend the reach of spectrographic analysis to what were then the most distant known objects in the universe: the stars. This ability was described by Sir William Huggins as being "like the coming upon a spring of water in a dry and thirsty land" (Huggins, 1897). The science of spectroscopy has since become one of the most fundamental tools used in astronomy.

1.1.1 The development of astronomical spectroscopy

The early experiments by Issac Newton with prismatic dispersion of sunlight in 1666 mark the beginnings of astronomical spectroscopy. Newton is acknowledged to have made an observation of the spectrum of Venus although the resolving power of his prismatic instruments was insufficient to recognize anything other than a continuous spectrum. It took another 135 years before Thomas Young, using the results of interference experiments, demonstrated that colour and wavelength are the same thing and interest in astronomical objects did not develop until the 1820s when Joseph Fraunhofer made numerous observations of the spectra of stars and planets as part of his examination of optical glasses. Later, laboratory flame spectra were used in an attempt to explain the "Fraunhofer lines", and progress was made after the observational and theoretical work of Gustav Kirchhoff and others. This ultimately led to the formulation of Kirchhoff's laws of emission and absorption.[1]

[1]Kirchhoff's law states that the ratio between the degree of emission and the degree of absorption for rays of the same wavelength is constant for all bodies at the same temperature. This can be written as:

$$\frac{\epsilon_\lambda(T)}{\kappa_\lambda(T)} = \text{constant}$$

where ϵ and κ are the coefficients of emission and absorption at a wavelength λ and temperature T. (After Kitchin, 1995.) To this law should be added the three corollaries:

1. The wavelengths emitted by a substance depend upon that substance and the temperature
2. The absorption of a substance is a maximum at those wavelengths which it also emits.
3. A luminous solid, liquid, or compressed gas emits a continuous spectrum whereas a rarefied gas produces a discontinuous spectrum of bright lines.

By the late 19th and early 20th centuries prismatic spectrographs were commonplace on telescopes as large as 15–30 inches and some objective prisms as large as 4–8 inches were also being used. In 1862 Huggins built his first (prismatic) stellar spectroscope and began spectroscopic observations. He gave life to modern astrophysics by making the fundamental observation that laboratory flames, our Sun, the planets and the stars share a common chemistry. Huggins was also the first person to attempt to measure the radial velocity of a star. Over the next three or four decades prism spectrographs became commonplace at numerous astronomical observatories.

The development of grating spectrographs

It was Lord Rayleigh who showed that the ideal diffraction grating would be better suited than prisms for achieving high resolution. However, it was extremely difficult to produce gratings of the required quality. The efficiency of diffraction gratings was also quite low as the light is dispersed into several orders. Gratings which consisted of many finely ruled apertures on glass were used by Fraunhofer, and in the 1870's Lewis Rutherfurd ruled a small number of gratings in speculum metal (see Palmer, 2000, pp. 9–10). In 1882 Henry A. Rowland of Johns Hopkins University perfected his "ruling engine" and was subsequently able to produce gratings which approached the necessary tolerances (see Palmer and Verrill, 1968) and in 1912, J.A. Anderson, who succeeded Rowland in the manufacture of gratings at John Hopkins University, was able to produce "blazed" gratings (see Hearnshaw, 1986, p. 11). It was claimed that these blazed gratings were able to diffract up to 50% of the light into the first order. Large gratings with near theoretical resolving power became possible after the development by G. Harrison and G.W. Stoke in the 1950's of interferometrically controlled ruling engines (see Palmer and Verrill, 1968).

The earliest grating instrument to be used for stellar spectroscopy was likely to have been used by H. C. Vogel in 1881 and J. Keller from 1890 to 1891 used the Lick refractor with a spectrograph which had interchangeable prisms and gratings (see Hearnshaw, 1986, p.10). The 1929 Cassegrain spectrograph constructed by P. W. Merrill (1931) was a significant advancement and incorporated several techniques for the control of flexure. The development of the coudé telescope allowed flexure to be eliminated. Coudé spectrographs were first used with prisms, but quickly took advantage of first blazed gratings and later the revolutionary Schmidt camera. In the coudé configuration large gratings (needed for the highest resolving powers) could readily be used without the limitations of space at the Cassegrain focus and long focal length cameras could be used in conjunction with large photographic plates in order to achieve high dispersion. These advantages were first demonstrated on the Mt Wilson spectrographs in the mid 1930s, and were thereafter copied by many observatories around the world (see Hearnshaw, 1986, pp. 14–17).

From blazed to échelle grating spectrographs

The resolving power of a grating is proportional to the product of N, the total number of grating rulings, and m, the order of diffraction. Given this, the quest for higher resolving power can be achieved in one of two ways: (i) by increasing the number of rulings on a grating, or (ii) by increasing the order of diffraction. During the first half of the twentieth century much work had been done on achieving the former, with the result that larger more finely ruled gratings were being used; particularly in coudé spectrographs. Some

progress toward the latter was made by the ability precisely to shape the tools of ruling instruments so that gratings blazed in the second or third order could be used efficiently. However, as noted by Michelson, little progress was being made to produce gratings which efficiently disperse light into orders as high as one hundred (Michelson, 1898). Clearly, if such a feat were possible, gratings having a fraction of the number of rulings as before would achieve comparable resolving powers.

Michelson (1898) experimented with producing high order "échelon" gratings which were comprised of a small number of parallel plates of glass and were used in transmission. This method was later used by Williams in 1933 (see Harrison, 1949b) to produce a grating having a resolving power of the order of one million, but the difficulties of producing the glass plates limited the size of such gratings. R. W. Wood, in 1910, proposed and then constructed a reflecting échelon grating for use in the infra-red (Wood, 1910). This grating, which was ruled on metal, he termed the "échelette" and it threw light into only a few orders. The advantages of the reflecting "échelle "[2] grating, which, like the échelon grating, works in high order numbers, but is more coarsely ruled than an échelette, were described in detail by Harrison in 1949 (op. cit.). However, the échelle grating demands groove profiles where the reflecting facets are accurate to $\lambda/10$ and where the relative position of all grooves is maintained to a similar accuracy. By the early 1950s échelle gratings of up to 126×254-mm in area had been constructed which had resolutions close to the theoretical (see Harrison et al., 1976 and references therein) and by 1970 even better gratings which were up to 300×400-mm in area were possible (op. cit.).

The theoretical properties of the échelle grating will be discussed in the following section (Section 1.2). In Section 1.3 the requirements for efficient use of échelle gratings on astronomy will be outlined.

[2]The term appears to have been coined by Harrison (op. cit) and derives from the French for a "ladder, scale, or pair of steps"

1.2 Properties of échelle gratings

1.2.1 Grating equation

A schematic of a diffraction grating is shown in Figure 1.1. A reflective surface (having a normal N) has been ruled with grooves which have spacing σ. These grooves cause the light incident at an angle α to be diffracted through an angle β. According to Huygen's principle each groove facet, which has a width σ_s, acts as a source for (plane) diffracted wavefronts. A given wavelength λ will interfere constructively only if the following condition applies:

$$m\lambda = \sigma(\sin\alpha \pm \sin\beta) \quad . \tag{1.1}$$

This is the classical form of the diffraction grating equation which assumes that the incident and diffracted rays are all perpendicular to the grooves. It is also possible to illuminate the grating at angle γ with respect to the facet normal (in the x-z plane, see Figure 1.2) in which case the grating equation becomes

$$m\lambda = \sigma(\sin\alpha \pm \sin\beta)\cos\gamma \quad . \tag{1.2}$$

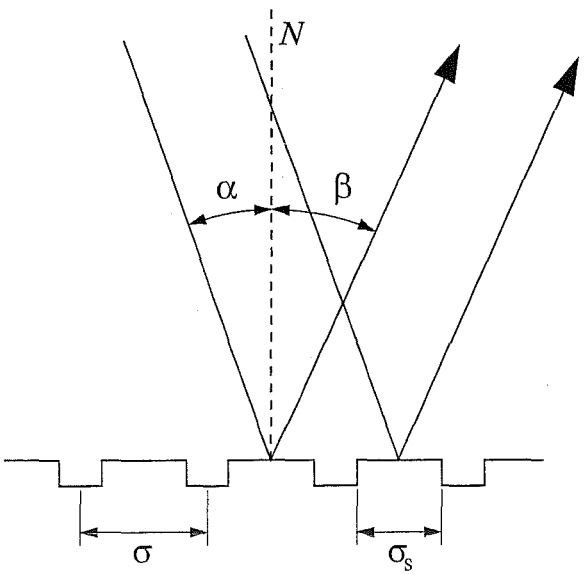

Figure 1.1: Schematic diagram of a (reflection) diffraction grating.

1.2.2 Blazed gratings

The grating can be made to diffract a high proportion of the energy into a single diffraction direction by orientating the grating facets such that a chosen wavelength (in a given diffraction order) is incident and diffracted at very nearly the same angle. This effect is termed blazing, and is achieved by orientating the grating facets so that the diffraction angle is very nearly same as the angle of specular reflection. As shown in Figure 1.3a, the grating facet angle with respect to the grating normal is called the blaze angle θ_B. An échelle grating is simply a standard blazed grating which has a large blaze angle. Such gratings are often referred to in terms of an "R-number" which is the tangent of the blaze angle. For instance an R2 grating has a blaze angle $\theta_B = 63.4°$ while an R4 grating has a

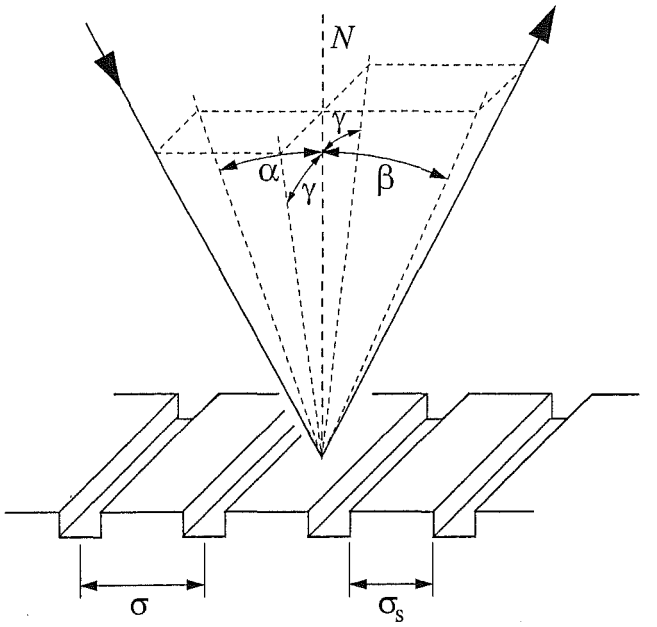

Figure 1.2: Schematic diagram of a grating where $\gamma \neq 0$.

blaze angle $\theta_B = 76.0°$. From Figure 1.3a it can be seen that the angles of incidence and dispersion α and $\bar{\beta}$ are related to the blaze angle θ_B of the grating by:

$$\begin{aligned} \alpha &= \theta_B + \theta \quad \text{and} \\ \bar{\beta} &= \theta_B - \theta \quad , \end{aligned} \tag{1.3}$$

where θ is the facet illumination angle with respect to the facet normal. That is $\bar{\beta}$ is the angle of diffraction for a wavelength λ_B (the blaze wavelength) in the centre of order m. Echelle gratings can also be illuminated out of the normal plane (see Figure 1.3b) and it follows that the blaze wavelength λ_B is defined in terms of the grating equation (equation 1.2) as

$$\begin{aligned} m\lambda_B &= \sigma(\sin\alpha + \sin\bar{\beta})\cos\gamma \\ &= 2\sigma \sin\theta_B \cos\theta \cos\gamma \quad . \end{aligned} \tag{1.4}$$

For reasons of efficiency the only viable modes in which an échelle grating can be operated are where $\alpha > \bar{\beta}$ or that $\alpha \approx \bar{\beta}$ (see Schroeder and Hilliard, 1980 and Section 1.2.11). The situation where $\theta = 0$ (i.e., $\alpha = \bar{\beta}$) is termed the Littrow condition and if $\gamma \neq 0$ the condition becomes quasi-Littrow. Under Littrow illumination, the optical depth of a grating σ_t is given by

$$\sigma_t = \sigma \sin\theta_B \quad , \tag{1.5}$$

and the facet width is

$$\sigma_s = \sigma \cos\theta_B \quad . \tag{1.6}$$

This determines the order of interference for diffracted light. That is,

$$m = \frac{2\sigma_t}{\lambda} \quad . \tag{1.7}$$

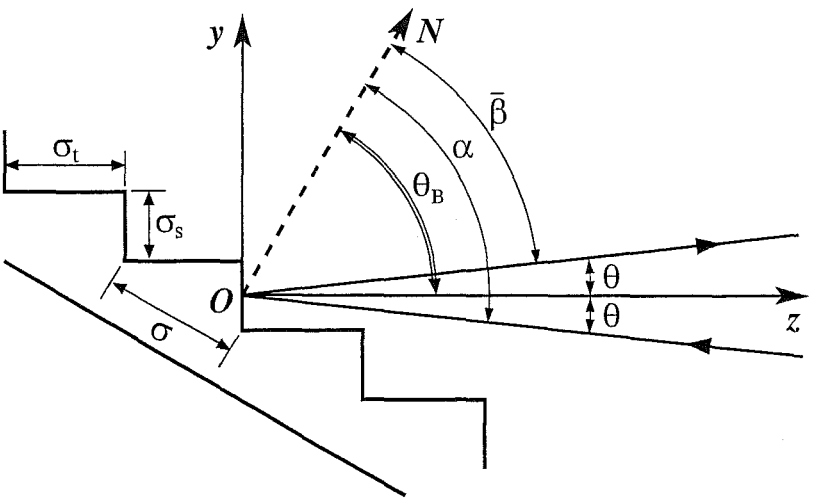

(a) Profile of échelle grating.

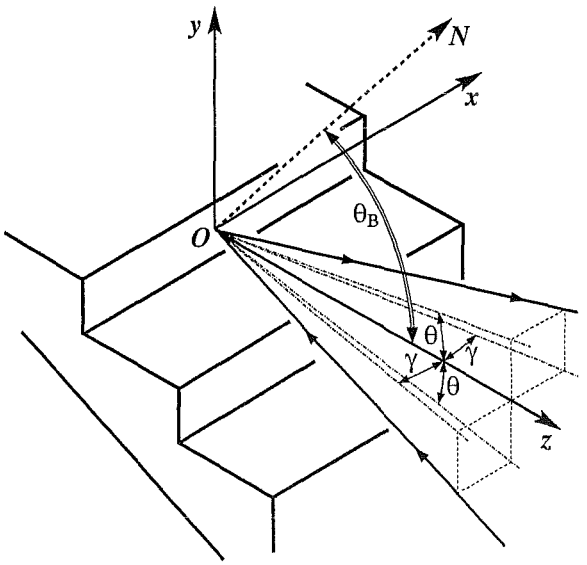

(b) Isometric view of échelle grating.

Figure 1.3: Schematic diagram of an échelle grating. The definitions of the blaze angle θ_B, angle of incidence α and the angle of diffraction β are shown in (a). The angle $\bar{\beta}$ is the angle of diffraction in the centre of each order m. The facet illumination angle θ is defined with respect to the facet normal O-z. All these angles are defined in the y-z plane. The definition of γ is shown in (b). It is the angle of incidence with respect to the facet normal as measured in the x-z plane.

1.2.3 Angular and linear dispersion

The angular dispersion of a grating is found by differentiating equation 1.2 with respect to λ for a given α. This gives

$$\frac{\mathrm{d}\beta}{\mathrm{d}\lambda} = \frac{m}{\sigma \cos\beta \cos\gamma} \quad , \tag{1.8}$$

or

$$\frac{\mathrm{d}\beta}{\mathrm{d}\lambda} = \frac{\sin\alpha + \sin\beta}{\lambda \cos\beta} \quad , \tag{1.9}$$

which in the centre of an order, at the blaze wavelength, becomes

$$\frac{\mathrm{d}\beta}{\mathrm{d}\lambda} = \frac{2 \sin\theta_\mathrm{B} \cos\theta}{\lambda_\mathrm{B} \cos\bar{\beta}} \quad . \tag{1.10}$$

From these equations it can be seen that for a given wavelength high angular dispersion can be obtained either by making α (and β) large or by increasing the grating groove density (i.e., small σ). Echelle gratings make use of this fact by having large blaze angles. Typical échelle gratings have from 30 to 300 grooves mm^{-1}) and they therefore operate with large values of m (i.e., $m = 10$ to > 100).

The angular dispersion is independent of the optical system of which the grating is part. The linear dispersion determines the extent δl of a spectral region $\delta\lambda$ on a given detector and is given by

$$\delta l = f_\mathrm{cam} \frac{\mathrm{d}\beta}{\mathrm{d}\lambda} \delta\lambda \quad , \tag{1.11}$$

where f_cam is the focal length of the camera used to image the spectrum. The plate factor P is the reciprocal linear dispersion and is therefore

$$P = \left(f_\mathrm{cam} \frac{\mathrm{d}\beta}{\mathrm{d}\lambda} \right)^{-1} \quad . \tag{1.12}$$

1.2.4 Free spectral range

The free spectral range $\Delta\lambda_\mathrm{FSR}$ is defined as the change in wavelength from an order m to the next $(m \pm 1)$. Any wavelength that appears in an order m will also appear in orders $m-1$ and $m+1$; however the angle of diffraction will be quite different as will the diffracted intensity. The free spectral range is given by

$$\Delta\lambda_\mathrm{FSR} = \frac{\lambda}{m}, \tag{1.13}$$

which in terms of the blaze wavelength, λ_B, becomes

$$\begin{aligned} \Delta\lambda_\mathrm{FSR} &= \frac{\lambda_\mathrm{B}^2}{2\sigma \sin\theta_\mathrm{B} \cos\theta \cos\gamma} \\ &\approx \frac{\lambda_\mathrm{B}^2}{2t} \quad . \end{aligned} \tag{1.14}$$

The angular extent of one free spectral range is determined by multiplying the free spectral range (equation 1.13) with the angular dispersion (equation 1.8). That is,

$$\begin{aligned} \Delta\beta_{\mathrm{FSR}} &= \frac{\mathrm{d}\beta}{\mathrm{d}\lambda}\Delta\lambda_{\mathrm{FSR}} \\ &= \frac{\lambda_{\mathrm{B}}}{\sigma\cos\bar{\beta}\cos\gamma} \quad , \end{aligned} \tag{1.15}$$

which, if $\theta = 0$, becomes $\Delta\beta_{\mathrm{FSR}} = \lambda_{\mathrm{B}}/(\sigma_{\mathrm{s}}\cos\gamma)$. This is simply diffraction from a rectangular slit of width σ_{s}. The diffraction pattern has an angular width $\lambda/\sigma_{\mathrm{s}}$. From the above equations it can be seen that for a given diffraction angle β and order number m the angular extent of an échelle spectrum depends largely on the density of the échelle rulings. A coarsely ruled grating (large σ) will produce a spectrum with a smaller angular extent (per free spectral range) than a more finely ruled grating.

1.2.5 Anamorphic magnification

If a source is of angular distance $\delta\alpha$ as viewed from the grating then after dispersion it will have an angular separation $\delta\beta$, where

$$\delta\beta = \delta\alpha\frac{\mathrm{d}\beta}{\mathrm{d}\alpha} \quad . \tag{1.16}$$

Now, from equation 1.1, it is straight-forward to show that

$$r = \left|\frac{\mathrm{d}\beta}{\mathrm{d}\alpha}\right| = \frac{\cos\alpha}{\cos\beta} \quad . \tag{1.17}$$

The quantity $r = \cos\alpha/\cos\beta$ is called the anamorphic magnification. The effect of anamorphic magnification on the dispersed light from an échelle grating is illustrated in Figure 1.4. It can be shown that a beam with a diameter B which is incident on a grating at angle α will after diffraction through an angle β have a diameter B' given by

$$B' = \frac{B}{r} \quad . \tag{1.18}$$

It should be noted that the anamorphic magnification can vary considerably across a single free spectra range. This is particularly significant for high R-number gratings, which generally have a larger angular free spectral range.

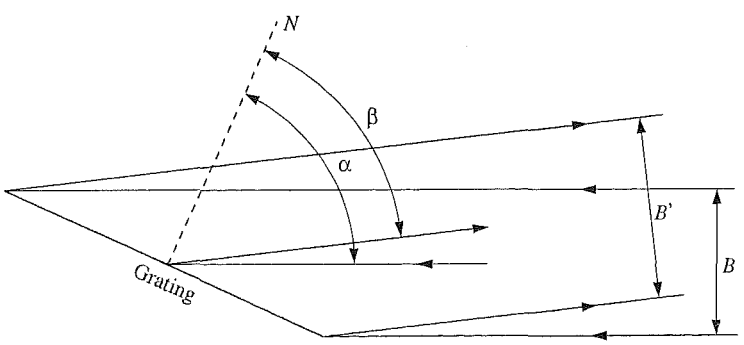

Figure 1.4: The effect of anamorphic magnification on beam size.

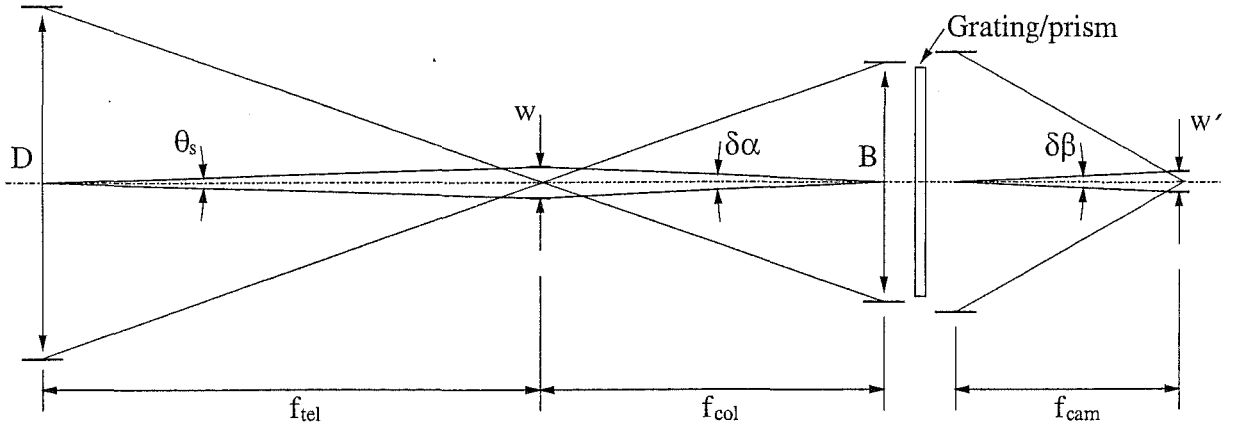

Figure 1.5: Schematic diagram of a slit limited spectrograph (after Schroeder, 2000).

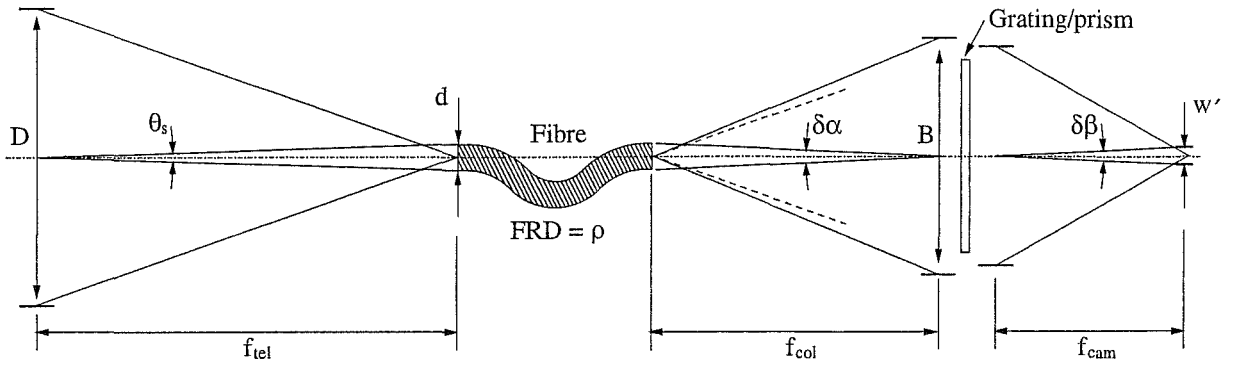

Figure 1.6: Schematic diagram of a fibre-fed spectrograph. The cone of light which exits the fibre is slightly larger than would be expected in the absence of a fibre (dashed line).

1.2.6 Direct and fibre spectrographs

A schematic slit-limited spectrograph is shown in Figure 1.5. A telescope of diameter D and focal length $f_{\rm tel}$ feeds a spectrograph which has an entrance slit width w. The fibre-fed spectrograph (Figure 1.6) is identical to the directly fed spectrograph except that a fibre of diameter d replaces the slit. In both cases the angle subtended by the slit or fibre on the sky is

$$\begin{aligned} \theta_{\rm s} &= \frac{w}{f_{\rm tel}} \quad \text{or} \\ \theta_{\rm s} &= \frac{d}{f_{\rm tel}} \quad . \end{aligned} \tag{1.19}$$

If the spectrograph is directly coupled to the telescope (for instance, in coudé, Cassegrain or Nasmyth configurations) then the following equality will apply:

$$\frac{f_{\rm tel}}{D} = \frac{f_{\rm col}}{B} \quad , \tag{1.20}$$

where $f_{\rm col}$ is the focal length of the collimator. If instead the spectrograph is coupled to a telescope via an optical fibre then after the light has passed through the fibre it will

emerge with an output focal ratio $F_{\rm out}$ which is faster than the input focal ratio $F_{\rm in}$, where

$$F_{\rm in} = \frac{f_{\rm tel}}{D} \quad \text{and} \quad F_{\rm out} = \frac{f_{\rm col}}{B} \quad . \tag{1.21}$$

This effect is known as focal ratio degradation (FRD, see for example Angel, 1977 or Ramsey, 1988) and can be described in terms of a FRD parameter ρ:

$$\rho = \frac{F_{\rm in}}{F_{\rm out}} \quad . \tag{1.22}$$

Although FRD always has the effect of decreasing the focal ratio, the amount by which it is decreased depends upon the focal ratio at which the fibre is fed. A typical fibre fed at an optimal focal ratio will decrease the focal ratio by about 10% to 20% (i.e., $\rho = 1.1$ to 1.2). Now, because of FRD, the equality given in equation 1.20 becomes for fibre-fed instruments

$$\frac{f_{\rm tel}}{D} = \rho\frac{f_{\rm col}}{B} \quad . \tag{1.23}$$

That is, in order for the beam size to remain constant on the same spectrograph which is first directly fed and then later fibre-fed, the focal length of the collimator must be reduced. In order to preserve throughput, the effective resolving power will thereby be reduced (see Section 1.2.10) which justifies this effect being termed a degradation. The use of fibres for spectroscopy will also be briefly discussed in Section 1.3.4.

1.2.7 Slit width and height

As viewed from the grating, the angular size of the slit is $\delta\alpha = w/f_{\rm col}$ or $\delta\alpha = d/f_{\rm col}$. It was shown above that this slit will undergo anamorphic magnification and therefore the image of this slit will have a width w' given by

$$\begin{aligned} w' &= w\frac{f_{\rm cam}}{f_{\rm col}}r \quad \text{or} \\ &= d\frac{f_{\rm cam}}{f_{\rm col}}r \quad . \end{aligned} \tag{1.24}$$

The slit height h' will be

$$\begin{aligned} h' &= h\frac{f_{\rm cam}}{f_{\rm col}}r' \quad \text{or} \\ &= d\frac{f_{\rm cam}}{f_{\rm col}}r' \quad , \end{aligned} \tag{1.25}$$

where r' is the anamorphic magnification introduced by the cross-disperser. This is generally (but not always) negligible.

1.2.8 Line tilt

Although the quasi-Littrow mode of grating illumination offers advantages in terms of efficiency, a non-zero γ has the effect of tilting the slit image with respect to the direction of dispersion. Due to the finite height of the slit, there is a small change in the angle of incidence with respect to the facet normal (in the x-z plane) from the bottom of the slit to the top. As shown in Figure 1.7, if the change in γ is $\delta\gamma$, then there will be a corresponding change in the angle of diffraction, $\delta\beta$, which will result in a line tilt ϕ given by

$$\tan\phi = \frac{\delta\beta}{\delta\gamma} = \frac{\mathrm{d}\beta}{\mathrm{d}\gamma} \quad , \tag{1.26}$$

where it should be noted that $\delta\beta/\delta\gamma$ is not necessarily a constant, and hence the tilt angle ϕ will vary across the slit image height. This line curvature will only be noticeable for very long slit heights. It follows that

$$\frac{\mathrm{d}\beta}{\mathrm{d}\gamma} = \frac{\mathrm{d}\beta}{\mathrm{d}\lambda}\,\frac{\mathrm{d}\lambda}{\mathrm{d}\gamma} \quad , \tag{1.27}$$

where $\mathrm{d}\beta/\mathrm{d}\lambda$ is the échelle angular dispersion (equation 1.8 or 1.9) and from the grating equation

$$\frac{\mathrm{d}\lambda}{\mathrm{d}\gamma} = -\frac{\sigma}{m}(\sin\alpha + \sin\beta)\sin\gamma \quad . \tag{1.28}$$

Therefore

$$\begin{aligned} \tan\phi &= \frac{\sin\alpha + \sin\beta}{\cos\beta}\,\frac{\sin\gamma}{\cos\gamma} \\ &= \lambda\frac{\mathrm{d}\beta}{\mathrm{d}\lambda}\tan\gamma \quad , \end{aligned} \tag{1.29}$$

which at the blaze wavelength λ_{B} the line tilt becomes

$$\tan\phi = 2\tan\theta_{\mathrm{B}}\tan\gamma \quad . \tag{1.30}$$

Note that from equation 1.30 it can be seen that high R-number gratings are more susceptible to line tilt. It is also significant to note that if some of the cross-dispersive power occurs before the échelle grating then the line tilt will have a wavelength dependence.

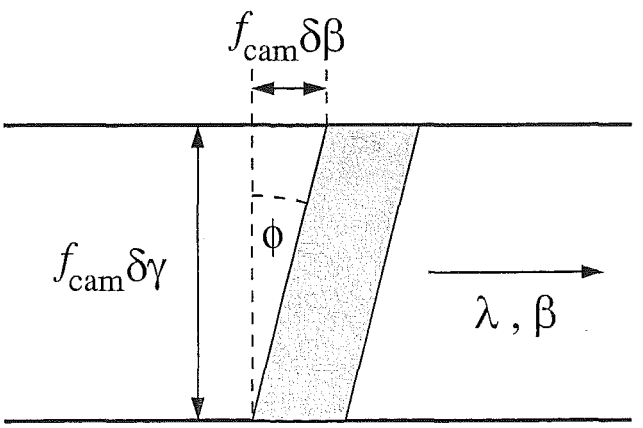

Figure 1.7: Schematic of a tilted slit image. This is due to the finite height of the slit which slightly changes γ.

Fibre tilt

The effect of line tilt on a fibre requires more detailed consideration. As before, a non-zero γ will tilt the dispersed fibre image by an amount ϕ given by equation 1.29. This tilt will however simply shear the fibre in the direction of échelle dispersion (see Figure 1.8). A detailed schematic of this sheared fibre is shown in Figure 1.9. The unsheared image of the fibre is an ellipse (due to anamorphic magnification of the circular fibre) which has a height h and width w. This ellipse has an equation

$$\frac{4x^2}{w^2} + \frac{4y^2}{h^2} = 1 \quad , \quad \text{or} \quad h'^2x^2 + w^2y^2 - \frac{w^2h^2}{4} = 0 \quad . \tag{1.31}$$

The ellipse is then sheared through an angle ϕ giving

$$\begin{aligned} x' &= x + y\tan\phi \quad \text{and} \\ y' &= y \quad , \end{aligned} \tag{1.32}$$

which if substituted into equation 1.31 gives

$$x'^2 - 2\tan\phi\, x'y' + \left(\tan^2\phi + \frac{w^2}{h^2}\right)y'^2 - \frac{w^2}{4} = 0 \quad . \tag{1.33}$$

Equation 1.33 can be recognized as a quadratic equation of the form

$$A'x'^2 + B'x'y' + C'y'^2 + F' = 0 \quad , \tag{1.34}$$

where the coefficients are

$$\begin{aligned} A' &= 1 \quad , \\ B' &= -2\tan\phi \quad , \\ C' &= \tan^2\phi + \frac{w^2}{h^2} \quad \text{and} \\ F' &= -\frac{w^2}{4} \quad . \end{aligned} \tag{1.35}$$

Because the discriminant $B'^2 - 4A'C' = -4\frac{w^2}{h^2} < 0$ this sheared ellipse is also an ellipse. However, the major axis of this ellipse does not form an angle ϕ to the major axis of the unsheared ellipse. In fact, it can be shown that the sheared ellipse is equivalent to an ellipse of the form

$$A''x''^2 + C''y''^2 + F'' = 0 \quad , \tag{1.36}$$

which has been rotated through an angle ϕ_e given by

$$\begin{aligned} \cot 2\phi_e &= \frac{A' - C'}{B'} \\ &= \frac{1}{2\tan\phi}\left(\tan^2\phi + \frac{w^2}{h^2} - 1\right) \\ &= \frac{1}{2}\frac{w^2}{h^2}\cot\phi - \cot 2\phi \quad . \end{aligned} \tag{1.37}$$

The coefficients of the unrotated ellipse are

$$\begin{aligned} A'' &= A' \cos^2 \phi_e + B' \cos \phi_e \sin \phi_e + C' \sin^2 \phi_e \quad , \\ C'' &= A' \sin^2 \phi_e - B' \sin \phi_e \cos \phi_e + C' \cos^2 \phi_e \quad \text{and} \\ F'' &= F' \quad . \end{aligned} \tag{1.38}$$

Now, if equation 1.36 is rewritten in the form

$$\frac{x''^2}{a^2} + \frac{y''^2}{b^2} = 1 \quad , \tag{1.39}$$

we find that the major and minor axis lengths a and b are given by

$$a^2 = \frac{-F''}{A''} \quad \text{and} \quad b^2 = \frac{-F''}{C''} \quad . \tag{1.40}$$

The full width w_e of the sheared ellipse is given by

$$\frac{w_e}{2} = x_e + y_e \tan \phi \quad , \tag{1.41}$$

and can be derived by noting that at $(x, y) = (x_e, y_e)$

$$\frac{dy}{dx} = -\cot \phi \quad . \tag{1.42}$$

Given that in polar coordinates

$$x = \frac{w}{2} \cos \theta \quad \text{and} \quad y = \frac{h}{2} \sin \theta \tag{1.43}$$

it is straightforward to show that

$$w_e = w \sec \phi_e \quad , \tag{1.44}$$

where

$$\tan \phi_e = \tan \left(\frac{h}{w} \tan \phi \right) \quad . \tag{1.45}$$

The relevance of the above derivation will become apparent when the resolving power of fibre-fed échelle spectrographs is considered below (Section 1.2.10).

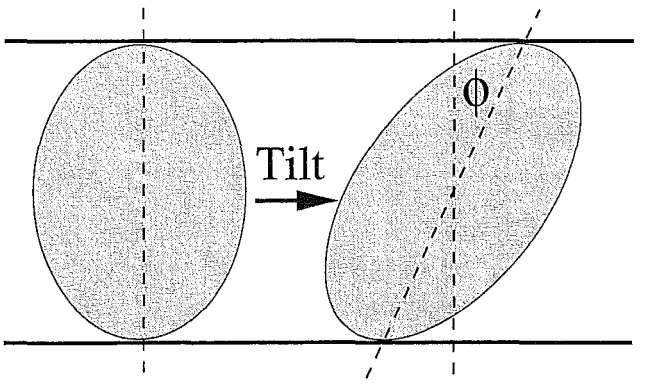

Figure 1.8: A fibre image sheared by line tilt.

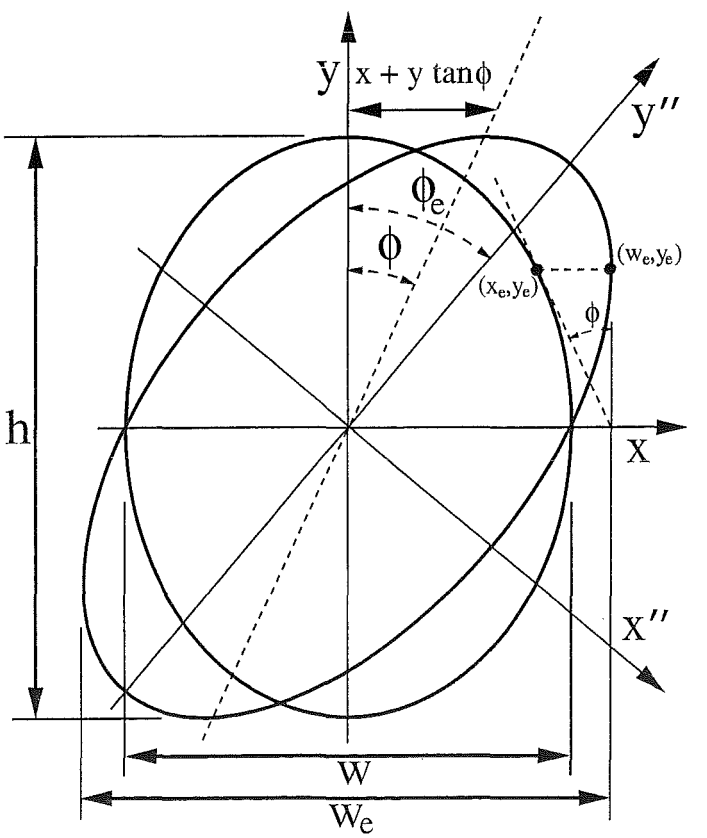

Figure 1.9: Schematic of a tilted fibre. The fibre image has been sheared by line tilt through an angle ϕ. The sheared image is an ellipse with axes which have been rotated through an angle ϕ_e. See text for details.

1.2.9 Cross dispersion

Because échelle gratings generally work at relatively high order numbers (i.e, $m \gg 1$) there are many combinations of m and λ that satisfy the grating equation. Therefore, an échelle grating will usually be used in conjunction with a second dispersive element which will disperse the spectra in a direction that is orthogonal to the main échelle dispersion. This element could be either a grating or a prism (or a combination of the two; for instance, a grism). This is shown schematically in Figure 1.10. It would also be possible to separate the orders by using a filter which is tuned to allow transmittance of only one free spectral range centred on the wavelength of interest. However, this would negate one of the most attractive features of an échelle spectrograph. That is, if the order separation is done by an element with low dispersive power it is possible to arrange many orders into a 2-dimensional format which can be simultaneously imaged by a single camera. The choice of cross-dispersers will be discussed further in Section 1.3.2.

Order separation

If the spectrograph camera has a focal length $f_{\rm cam}$, then the separation between orders will be

$$\Delta y = f_{\rm cam} \frac{{\rm d}\beta}{{\rm d}\lambda_{\rm XD}} \Delta\lambda_{\rm FSR} \quad , \tag{1.46}$$

where ${\rm d}\beta/{\rm d}\lambda_{\rm XD}$ is the angular dispersion of the cross-disperser. If we express the free spectral range in terms of the blaze wavelength $\lambda_{\rm B}$ then equation 1.46 becomes

$$\Delta y = f_{\rm cam} \frac{{\rm d}\beta}{{\rm d}\lambda_{\rm XD}} \frac{\lambda_{\rm B}^2}{2\sigma \sin\theta_{\rm B} \cos\theta \cos\gamma} \quad . \tag{1.47}$$

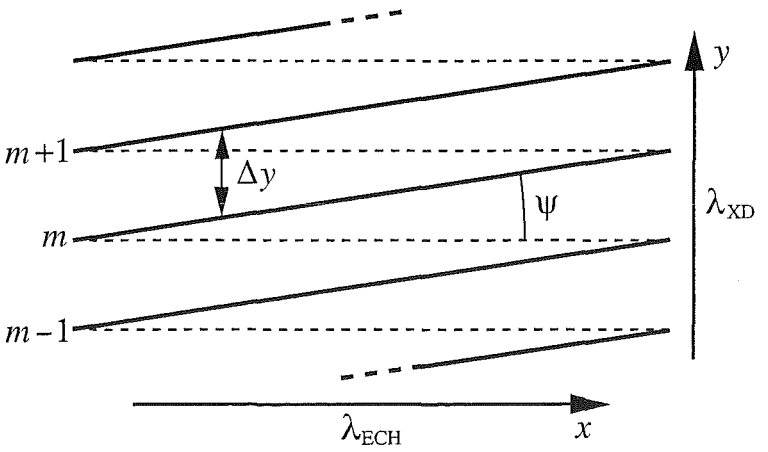

Figure 1.10: Schematic of échelle cross-dispersion.

Order tilt and curvature

As shown in Figure 1.10 the orders will be tilted by an amount ψ. The angle ψ is given by

$$\tan\psi = \frac{{\rm d}\beta/{\rm d}\lambda_{\rm XD}}{{\rm d}\beta/{\rm d}\lambda_{\rm ECH}} \quad , \tag{1.48}$$

where $\mathrm{d}\beta/\mathrm{d}\lambda_{\mathrm{ECH}}$ is the angular dispersion of the échelle grating and $\mathrm{d}\beta/\mathrm{d}\lambda_{\mathrm{XD}}$ is the angular cross dispersion. In the order centre the tilt is

$$\tan\psi_{\mathrm{B}} = \frac{\mathrm{d}\beta}{\mathrm{d}\lambda_{\mathrm{XD}}} \frac{\lambda\cos\bar{\beta}}{2\sin\theta_{\mathrm{B}}\cos\theta} \quad . \tag{1.49}$$

However, because the échelle angular dispersion is not completely uniform throughout an individual order (i.e, equations 1.8 and 1.9) the orders will be slightly curved.

1.2.10 Resolving power

If a spectrograph has marginally sufficient resolution to distinguish between two wavelengths λ_1 and $\lambda_2 = \lambda_1 + \delta\lambda$ then the resolving power is defined as

$$R = \frac{\lambda}{\delta\lambda}, \tag{1.50}$$

where $\lambda \approx \lambda_1 \approx \lambda_2$. The angular width between the two wavelengths λ_1 and λ_2 in the dispersed beam will be $\delta\beta$, so in terms of the angular dispersion $(\mathrm{d}\beta/\mathrm{d}\lambda)$, equation 1.50 may be written as

$$R = \frac{\lambda}{\delta\beta}\frac{\mathrm{d}\beta}{\mathrm{d}\lambda} \quad . \tag{1.51}$$

Now, from equation 1.16 the above becomes

$$R = \frac{\lambda}{\delta\alpha}\frac{\mathrm{d}\alpha}{\mathrm{d}\lambda} \quad . \tag{1.52}$$

The resolving power may now be written in a more useful form by noting that

$$\frac{\mathrm{d}\alpha}{\mathrm{d}\lambda} = \frac{\sin\alpha + \sin\beta}{\lambda\cos\alpha} \quad , \tag{1.53}$$

which gives

$$\begin{aligned} R &= \frac{1}{\delta\alpha}\frac{\sin\alpha + \sin\beta}{\cos\alpha} \\ &= \frac{1}{\delta\alpha}\frac{2\tan\theta_\mathrm{B}}{(1 - \tan\theta_\mathrm{B}\tan\theta)} \quad . \end{aligned} \tag{1.54}$$

The term $\cos\gamma$ is ignored here as γ is always small and therefore $\cos\gamma \approx 1$.

Diffraction limit

The diffraction limited resolving power can be derived from equation 1.54 by noting that,

$$m\lambda = \frac{L}{N}(\sin\alpha + \sin\beta) \quad , \tag{1.55}$$

where N is the number of grooves across a grating which has a length L. If the collimated beam size is B, then it follows that $B = L\cos\alpha$ and that the diffraction limited angular slit size $\delta\alpha$ is approximately λ/B (or, equivalently $\theta_\mathrm{s} \approx \lambda/D$). Therefore, in the diffraction limit,

$$R = mN \quad . \tag{1.56}$$

Directly fed spectrographs

In the case of a directly fed spectrograph equation 1.54 becomes

$$R = \frac{f_\mathrm{col}}{w}\frac{2\tan\theta_\mathrm{B}}{(1 - \tan\theta_\mathrm{B}\tan\theta)} \quad . \tag{1.57}$$

Combining equations 1.57, 1.19 and 1.20 gives

$$R = \frac{2B \tan \theta_B}{\theta_s D(1 - \tan \theta_B \tan \theta)} \quad . \tag{1.58}$$

This provides a very useful way of determining the resolving power of a spectrograph in terms of the diameter and focal length of the telescope, the slit width (expressed in terms of the angle the slit subtends on the sky), and the size of the collimated beam which is incident on the spectrograph's grating. If the collimated beam can be matched to the projected length of the échelle grating (i.e., $B = L \cos \alpha$) then equation 1.58 can be rewritten as

$$R = \frac{2L \sin \theta_B \cos \theta}{\theta_s D} \quad . \tag{1.59}$$

This equation was first given by Bingham (1979).

What these equations (1.58 and 1.59) show is that in order to obtain a large resolving power with a given slit size it is necessary either to have a large grating size or a large collimated beam (i.e., large L or B). This was the solution for the large coudé spectrographs used from 1910 to 1980. Equation 1.58 shows the merit of the échelle solution; that is, to use large θ_B. However, as shown by equation 1.59, the usefulness of increasing the blaze angle is not without limits; that is, for R2 gratings, $\sin \theta_B = 0.89$ while for R4 $\sin \theta_B = 0.97$. Also, if the dimensions of the collimated beam are such that $B > L \cos \alpha$ then equation 1.58 is more appropriate. As will be shown (Section 1.2.12) although the overfilled grating will result in the loss of light, it is still possible to improve the overall throughput of the spectrograph for a given product of R and θ_s.

Fibre-fed spectrographs

The effect of FRD has been described in Section 1.2.6. The FRD term ρ modifies the resolving power of a fibre-fed spectrograph to

$$R = \frac{2B \tan \theta_B}{\rho \theta_s D(1 - \tan \theta_B \tan \theta)} \quad \text{and} \tag{1.60}$$

$$R = \frac{2L \sin \theta_B \cos \theta}{\rho \theta_s D} \quad . \tag{1.61}$$

It is relevant to note that because the FRD of a given fibre depends only on the input focal ratio, this is the only means by which the focal ratio of the telescope can effect the resolving power of a fibre-fed spectrograph.

Effective fibre resolving power

The resolving power of a slit limited spectrograph will be given by equations 1.58 and 1.59 only if the seeing disk is considerably larger than the slit width, thereby providing a uniformly illuminated rectangle. If the seeing disk only partially fills the spectrograph's entrance slit, or if the entrance slit is entirely absent, then the resolving power equations must be somewhat modified. This will not be discussed here. However, for a discussion see Schroeder (2000, pp 318–320).

The entrance slit of a fibre is always circular and essentially uniform in surface brightness. The effective resolving power R' of a circular fibre of diameter d can be calculated

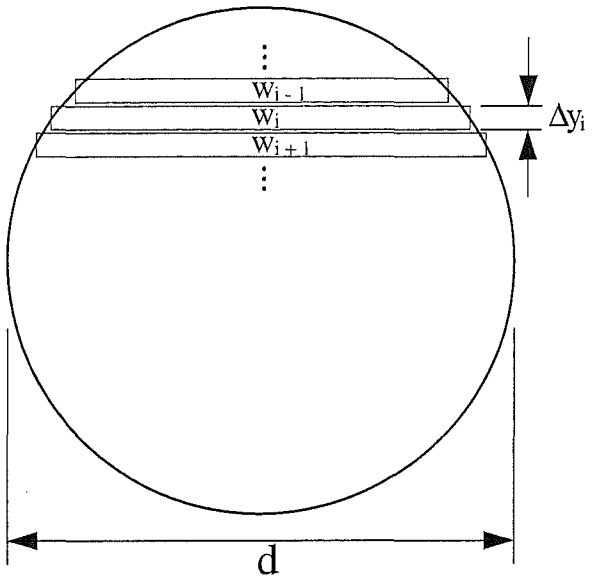

Figure 1.11: The flux weighted fibre width is calculated by weighting each chord by the area it encompasses.

by subdividing the fibre into many narrow slits which have widths w_i equal to the chord which is parallel to the direction of dispersion. This is shown in Figure 1.11. Each slit will then have a weighting which equals the fraction of the total flux which the slit encloses. This fraction is proportional to the area of each slit, where the normalized area A_i of each slit is

$$A_\mathrm{i} = \frac{w_\mathrm{i}\Delta y_\mathrm{i}}{\pi\frac{d^2}{4}} \quad . \tag{1.62}$$

Therefore, the flux weighted fibre width is given by

$$\bar{w} = \sum_{\mathrm{i}=1}^{\mathrm{n}} w_\mathrm{i} A_\mathrm{i} \quad , \tag{1.63}$$

In the limit where $n \to \infty$ $\Delta y_\mathrm{i} \to \mathrm{d}y$ and $A_\mathrm{i} \to w\mathrm{d}y$ equation 1.63 can be solved to give

$$\bar{w} = \frac{8}{3\pi} d \quad . \tag{1.64}$$

This factor was first derived by Vaughnn (1994), although he gave an expression for the flux-weighted slit width of a fibre which has been reimaged onto a slit which is smaller than the fibre diameter (or alternatively, the slit could be imprinted directly on the fibre exit face). If the slit width is w_s the flux-weighted slit width becomes

$$\bar{w} = \frac{8}{3\pi} d \left(1 - \left(1 - \left(\frac{w_\mathrm{s}}{d}\right)^2\right)^{3/2}\right) \frac{1}{T} \quad , \tag{1.65}$$

where the relative transmission T of the clipped fibre is given by

$$T = 1 + \frac{2}{\pi}\left(\frac{w_\mathrm{s}}{d}\left(1 - \left(\frac{w_\mathrm{s}}{d}\right)^2\right)^{1/2} - \cos\left(\frac{w_\mathrm{s}}{d}\right)\right) \quad . \tag{1.66}$$

Obviously, if $w_s = d$, $T = 1$, and $\bar{w} = 8 / 3\pi d$. Hence, the effective resolving power of a (fully illuminated) fibre is

$$\begin{aligned} R' &= \frac{d}{\bar{w}} R \\ &= \frac{3\pi}{8} R \\ &\approx \frac{R}{0.849} \quad . \end{aligned} \tag{1.67}$$

While the above shows that a fibre will deliver a resolving power that is considerably better than the resolving power that can be achieved with a uniformly illuminated slit with a width equal to the diameter of the fibre, the convention is to measure the full-width at half-maximum (FWHM) of a monochromatic light source which can be either a single laser line or the emission lines formed by an appropriate calibration light source. This method makes the assumption that the profile of a single line, after extraction to one-dimension (hereinafter called the line-spread function, or LSF) can be approximated by a gaussian. In fact, as will be shown below, this will not be the case, and the resolving power measured by this method will be quite different from that derived above.

The extracted profile (or LSF) of a fibre image can be determined by noting that the extraction in one dimension of an elliptical fibre image produces another ellipse which will have a normalized height of one and a minor-axis equal to the fibre image width w. That is, the equation of an extracted fibre will be:

$$I_{\text{fib}} = \sqrt{1 - \frac{4x^2}{w^2}} \quad , \qquad \frac{-w}{2} < x < \frac{w}{2} \quad . \tag{1.68}$$

In order to approximate the observed fibre profile I_{obs} the extracted profile is then convolved with a one-dimensional point-spread function (PSF); i.e.,

$$I_{\text{obs}} = I_{\text{fib}} \otimes I_{\text{psf}} \quad . \tag{1.69}$$

The effect of the PSF will depend on the image quality that the spectrograph produces. To show how image quality affects the final line profile, gaussians with FWHMs, which varied in proportion to the fibre image width, were used. The FWHM of the PSF varied from $w_{\text{psf}} = 0.1w$ to $w_{\text{psf}} = 0.5w$. The changing ratio can be used to represent either a change in image quality or a change in the size of the fibre image.

The FWHM of the fibre profiles can now be determined by fitting a gaussian to the extracted and convolved fibre profile. It appears reasonable to insist that the fitted gaussian is normalized to have the same equivalent width as the fibre profile, although in practice this makes little difference to the parameters of the fitted gaussian (assuming both width and height are variables). The results are shown in Figure 1.12. The fibre profiles determined using this method are shown in Figure 1.13. It is noted that the fit to a gaussian is very poor when the effect of the PSF is small, although as the relative effect of the PSF increases the approximation by a gaussian becomes more appropriate. The limit of the FWHM as $w_{\text{psf}} \to 0$ is $w_{\text{fwhm}} = 0.682w$. Hence, if the spectrograph has perfect optics, the resolving power would be measured as

$$R(w_{\text{psf}} = 0) \approx \frac{R}{0.682} \quad , \tag{1.70}$$

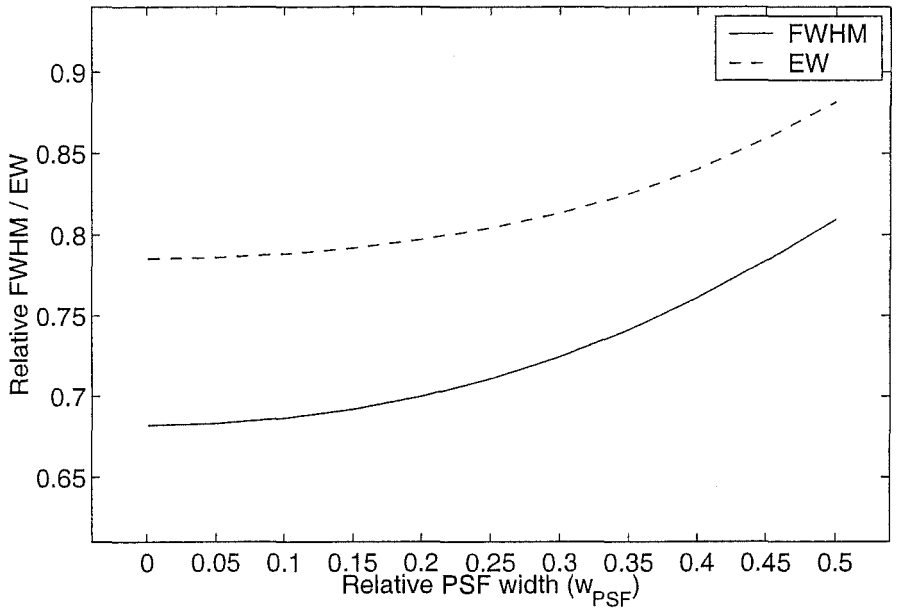

Figure 1.12: The FWHM of synthetic fibre profiles. Normalized gaussians were fitted to the profiles shown in Figure 1.13 in order to obtain the FWHM. Equivalent widths of the fibre profiles are shown for comparison.

and to a good approximation, the resolving power as a function of $w_{\rm psf}$ is given by

$$R(w_{\rm psf}) \approx \frac{R(w_{\rm psf}=0)}{\sqrt{1+1.6\,w_{\rm psf}^2}} \quad . \tag{1.71}$$

In practice, the optics of the spectrograph (as well as the properties of the CCD) will tend to degrade the resolving power. If a degradation in resolving power (which is measured using the above method) due to optical performance of 10% is acceptable, then the FWHM of the PSF should be no more than $0.35 \rightarrow 0.40 \times w$.

Effect of line tilt

As described in Section 1.2.8 the effect of a non-zero γ will be to tilt the dispersed slit image by an amount ϕ given by equation 1.27. This will have the effect of decreasing the resolving power. In the case of a slit spectrograph it may be possible to counter-rotate the slit in order to minimize this tilt, although as pointed out by Schroeder and Hilliard (Schroeder and Hilliard, 1980) the throughput-resolution product remains constant.

The entrance slit of a fibre-fed spectrograph cannot however be rotated. It will be stated without proof that the extracted profile of a tilted fibre is simply equation 1.68 where the fibre image width w is replaced by the full-width $w_{\rm e}$ of the tilted fibre (equation 1.44). Hence, the extracted profile of a tilted fibre will be given by

$$I' = \sqrt{1-\frac{4x^2}{{w_{\rm e}}^2}} \quad , \qquad \frac{-w_{\rm e}}{2} < x < \frac{w_{\rm e}}{2} \quad . \tag{1.72}$$

The observed fibre profile can now be obtained by convolving equation 1.72 with a one-dimensional PSF. As above, the FWHM of this profile can be measured. This is shown in Figure 1.14 and the measured equivalent widths are shown in Figure 1.15.

The relative change in FWHM is shown in Figure 1.16. It can be seen that as image

quality becomes worse the relative effect of line tilt decreases. If, for a given image quality the resolving power at zero line tilt is $R'(\phi = 0)$ (see equation 1.71) then the resolving power as a function of line tilt is given by

$$R'(\phi) = R'(\phi = 0)\frac{w}{w_e} \quad . \tag{1.73}$$

In the small angle approximation this reduces to

$$R'(\phi) = \frac{R'(\phi = 0)}{\sqrt{1 + \frac{h^2}{w^2}\phi^2}} \quad , \tag{1.74}$$

where it should be noted that the fibre image height h must also be considered. Hence, in order for line tilt to degrade the resolving power by less than 10% it can be seen that a line tilt of up to $\phi \approx 20°$ can be tolerated.

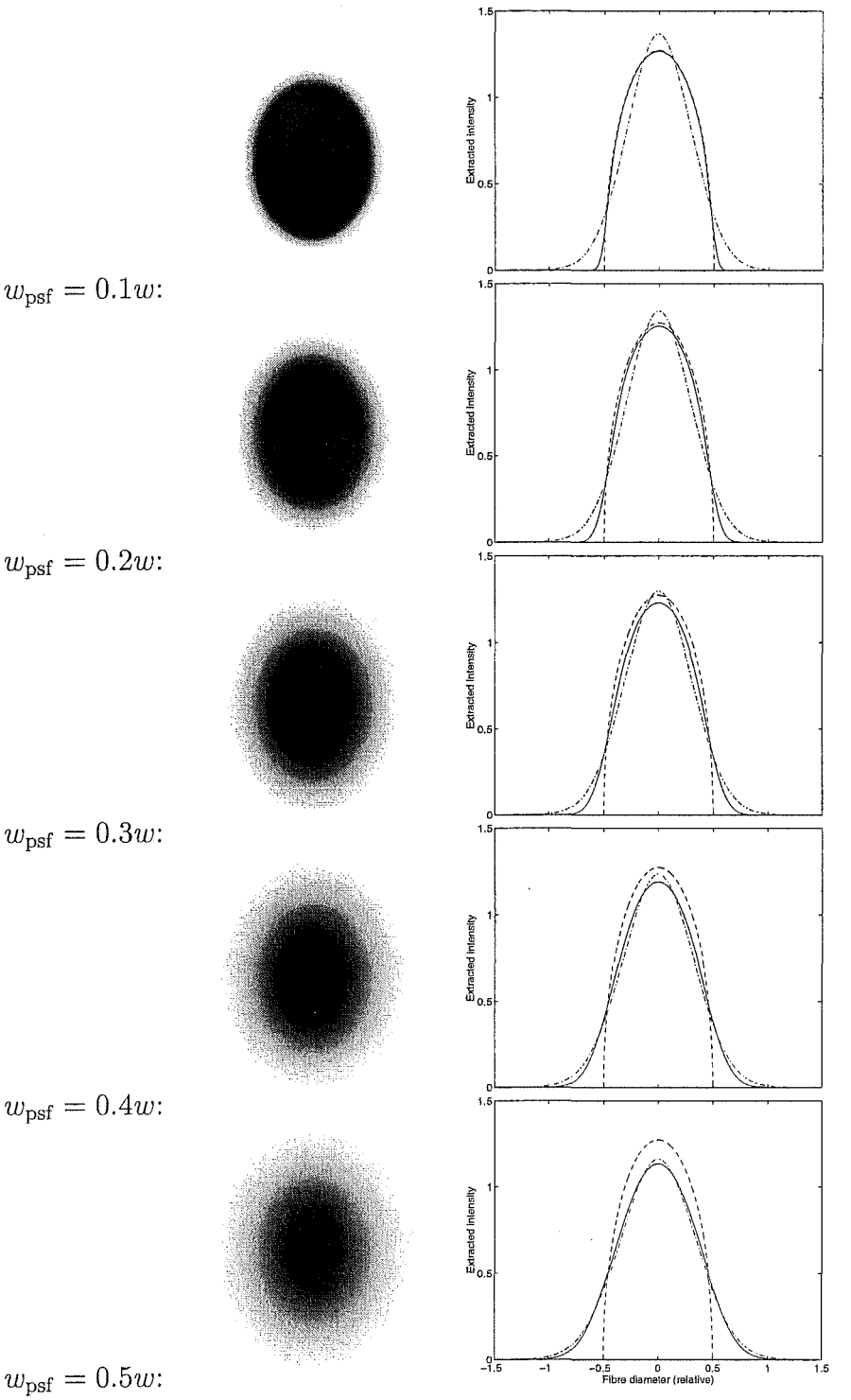

Figure 1.13: Synthetic fibre images and profiles. The output from a circular fibre has been convolved with a gaussian PSF (left). The PSF's have a FWHM ranging from 0.1 to 0.5 times the fibre image width w. The extracted profile (bold) is then normalized and fitted by a gaussian (dot-dashed). Note that the extracted fibre profile is well approximated by a gaussian only when the influence of the PSF is large. The dashed line shows the extracted profile of an unconvolved fibre

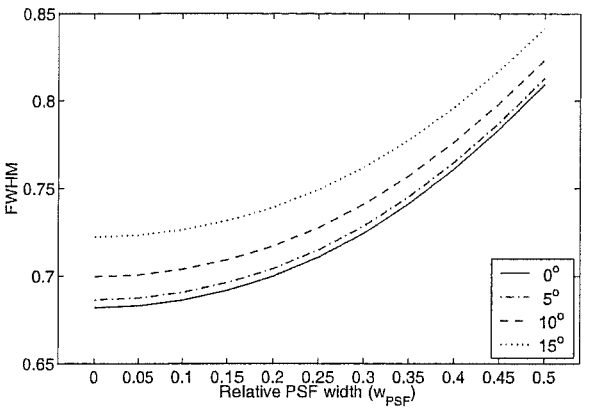

Figure 1.14: The FWHM of extracted and tilted fibre profiles.

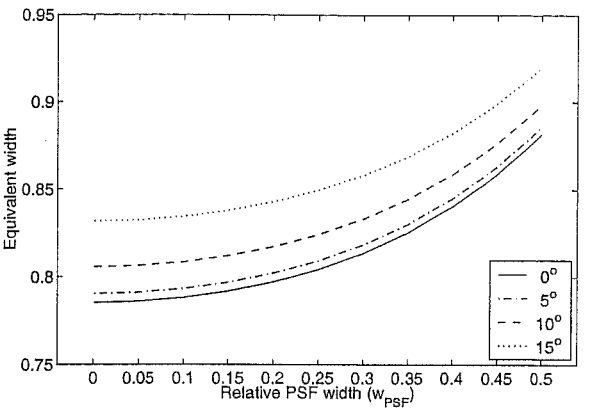

Figure 1.15: The equivalent width of extracted and tilted fibre profiles.

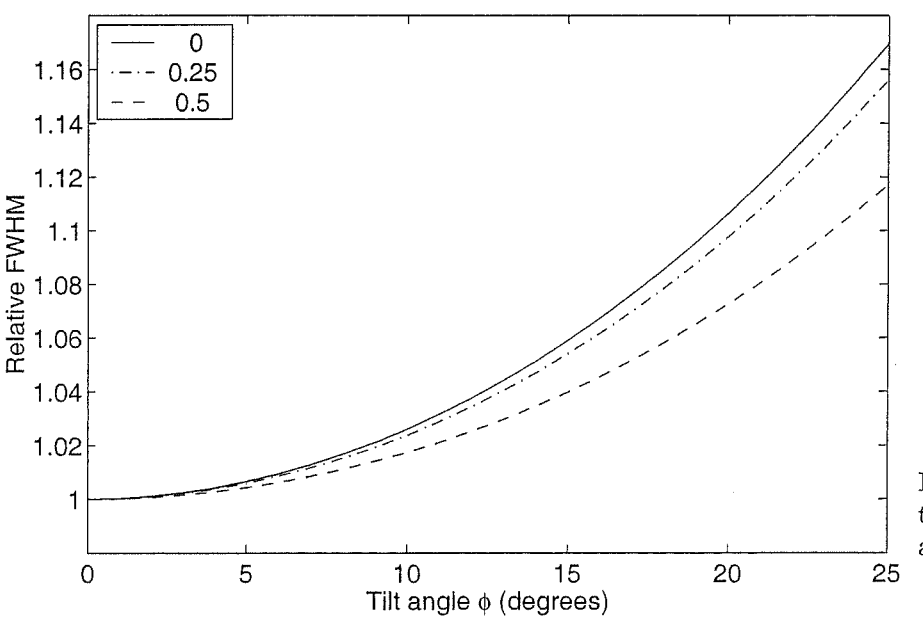

Figure 1.16: The relative FWHM of extracted and tilted fibre profiles.

Total resolving power

The above equations (equations 1.58, 1.59, 1.60 and 1.61) give only the slit or fibre limited resolving power of a given spectrograph. The total effective resolving power will however be degraded by several additional factors; for example by imperfect optics and detectors. If these degrading factors can each be assigned to resolving power influences $R_{\rm i}$, then the total resolving power of the spectrograph $R_{\rm tot}$ will be given by,

$$\frac{1}{R_{\rm tot}^2} = \sum_{\rm i=1}^{\rm n} \frac{1}{R_{\rm i}^2} \quad , \tag{1.75}$$

where it is assumed that each factor can be modeled by a gaussian function with a FWHM given by $R_{\rm i}$. Some of the contributors to the total resolving power include the following:

- the diffraction limited resolving power given by $R_{\rm dif} = mN$, where N is the total number of grooves being illuminated. The diffraction limit will invariably be somewhat degraded by imperfections in the grating surface; for instance, surface irregularities and groove ruling errors.
- optical aberrations. The use of imperfect optics is unavoidable.
- detector properties. These include the effects of the depletion layer and charge migration in silicon detectors. The effects of finite pixel sampling must also be considered.

The optical quality and detector properties must therefore be chosen in order to ensure that the degradation is acceptable. While all of the above influences are unavoidable, there may be other transient effects such as focus errors or image motion which will further degrade the image quality of the spectrograph. The design of the spectrograph should attempt to mitigate all such effects.

1.2.11 Efficiency

Upon striking a grating at an angle α a collimated beam will be diffracted through an angle β, which depends on the wavelength λ and the grating groove spacing σ according to the grating equation (equation 1.2.1). The intensity I of this diffracted beam results from the combination of an interference function (IF) and a blaze function (BF); that is,

$$I = IF \times BF \quad . \tag{1.76}$$

The interference function that results from a grating which has a total of N equally spaced grooves is given by

$$IF = \left(\frac{\sin N\nu'}{N \sin \nu'} \right)^2 \quad , \tag{1.77}$$

where $2\nu'$ is the phase difference between rays diffracted off the centres of adjacent grooves. The blaze function is given by

$$BF = \left(\frac{\sin \nu}{\nu} \right)^2 \quad , \tag{1.78}$$

where ν is the phase difference between the centre and edge of an individual groove. These phase differences are given by

$$2\nu' = \frac{2\pi\sigma}{\lambda}(\sin\alpha + \sin\beta) \quad , \quad \text{and} \tag{1.79}$$

$$\nu = \frac{\pi\sigma_s}{\lambda}(\sin\alpha + \sin\beta) \quad . \tag{1.80}$$

Each individual grating facet has a width σ_s which may be smaller than the groove spacing σ in which case the blaze function will be broadened.

The diffracted intensity pattern for a single wavelength is shown in Figure 1.17. It

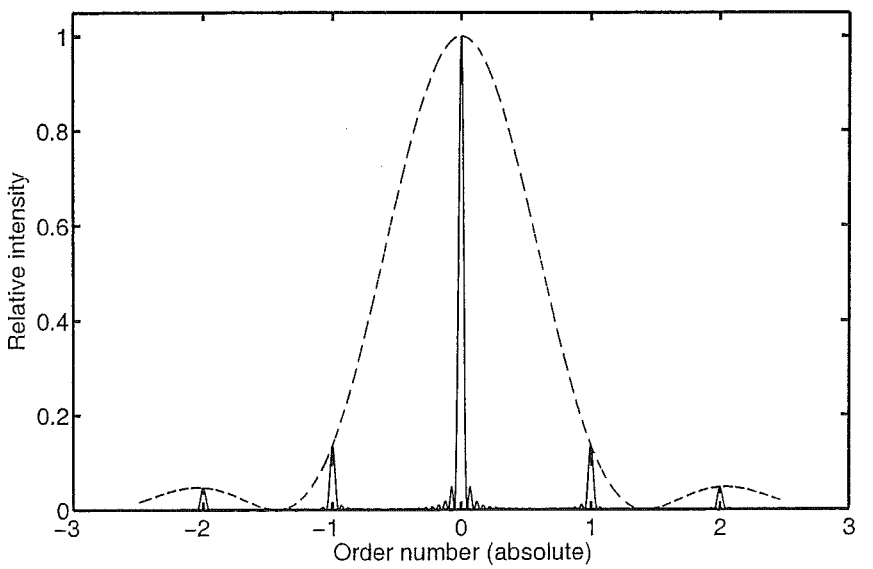

Figure 1.17: The diffracted intensity of a single wavelength (solid line). The blaze function (dashed line) modulates the interference function, which is maximum when the order number m is an integer. The intensity in diffracted orders ($m \neq 0$) is low.

can be seen that the majority of the energy incident on the grating is returned in the zeroth order ($m = 0$) where it is simply reflected. Only a small portion of the energy is diffracted into other orders.

Blaze function

The purpose of blazing a grating is to shift the blaze function so that the maximum diffracted intensity of a given wavelength coincides with the chosen diffraction order. The phase difference between successive grooves (equation 1.80) is now given by

$$\nu = \frac{\pi\sigma_s'}{\lambda}\big(\sin(\alpha - \theta_B) + \sin(\beta - \theta_B)\big) \quad , \tag{1.81}$$

where σ_s' is the effective size of each facet (see Figure 1.18). The effective facet size (when $\alpha > \beta$ is

$$\begin{aligned} \sigma_s' &= \sigma(\cos\theta_B - \sin\theta_B \tan\theta) \\ &= \frac{\sigma\cos\alpha}{\cos\theta} \quad , \end{aligned} \tag{1.82}$$

which should be compared to the size of a clear facet σ_s, which is $\sigma_s = \sigma\cos\theta_B$.

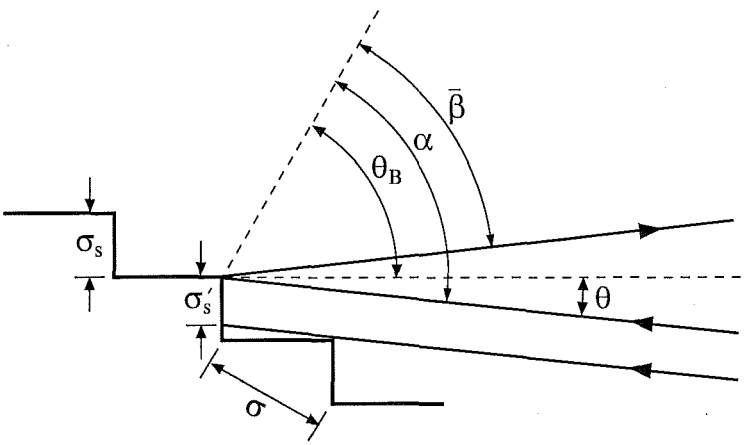

Figure 1.18: The effective facet size of a blazed grating is reduced because of shadowing (after Schroeder, 2000).

The normalized intensity of a wavelength diffracted by a grating blazed at $\theta_B = 63.5°$ is shown in Figure 1.19. The wavelength has been chosen so that it coincides with the maximum of the blaze function which occurs in order $m = 40$.

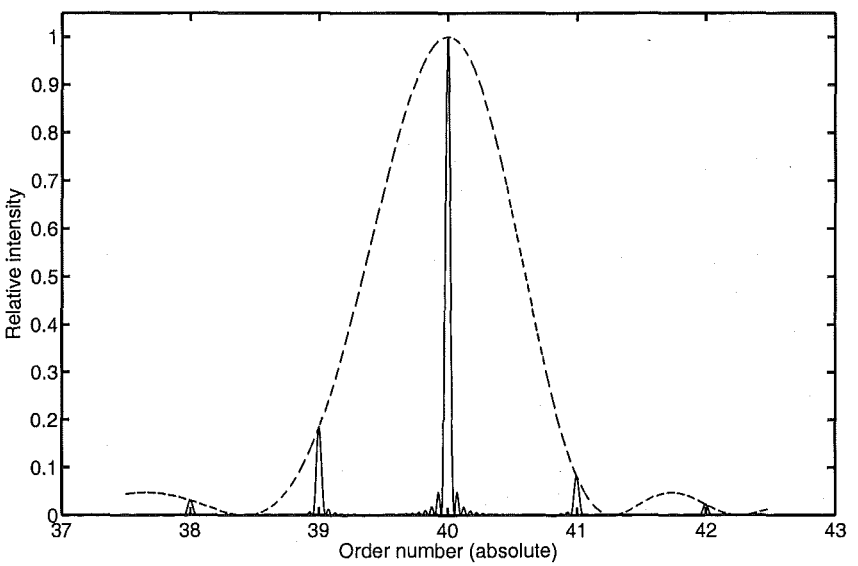

Figure 1.19: The diffracted intensity of a single wavelength using blazed grating. The blaze function is now centred on an order $m \neq 0$. Compare with Figure 1.17.

Absolute efficiency

In order to calculate the efficiency of an échelle grating it is necessary to determine the distribution of light of a given wavelength across all possible orders. A wavelength that is not at the centre of the blaze function will have a significant fraction of its energy diffracted into other orders. This is shown in Figure 1.20. The method prescribed by

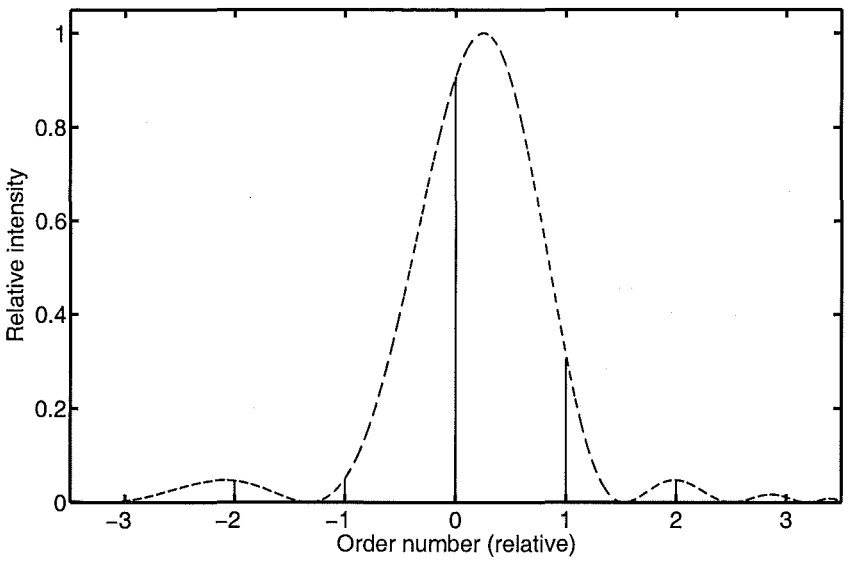

Figure 1.20: A method for computing the efficiency of an échelle grating. See text for details.

Schroeder and Hilliard (1980) is simply to sum the intensities across all possible orders and then derive the fraction that remains in the order of interest. However, as commented by Bottema (1981), this definition of efficiency is not quite correct, although it is conceded that in most cases of interest the results will be correct (Schroeder, 1981). Therefore, the absolute diffractive efficiency of an échelle grating for a wavelength in order m is

$$T_{\text{ech}} = \frac{I_{\Delta m=0}}{I_{\Delta m=0} + \sum_{\Delta m \neq 0} I_{\Delta m}} \quad , \tag{1.83}$$

where Δm and I are the relative order number and intensity respectively.

The relative efficiency of an échelle grating which is blazed at $\theta_{\text{B}} = 63°$ is shown in Figure 1.21. This grating is illuminated at $\theta = 0°$, which means that the wavelength free spectral range is equal to the FWHM of the blaze function. If the grating is illuminated in a non-Littrow mode ($\theta \neq 0$) then the fraction of the blaze function that is covered by one free spectral range is increased by a factor $\cos\beta / \cos\alpha$; that is

$$\Delta\lambda_{\text{FWHM}} = \frac{\Delta\lambda_{\text{FSR}}}{r} \quad , \tag{1.84}$$

where r is the anamorphic magnification. The blaze function for a range of Littrow angles (θ), such that $1.0 < 1/r < 1.5$ is shown in Figure 1.22. Note that the values of r refer to the order centre only.

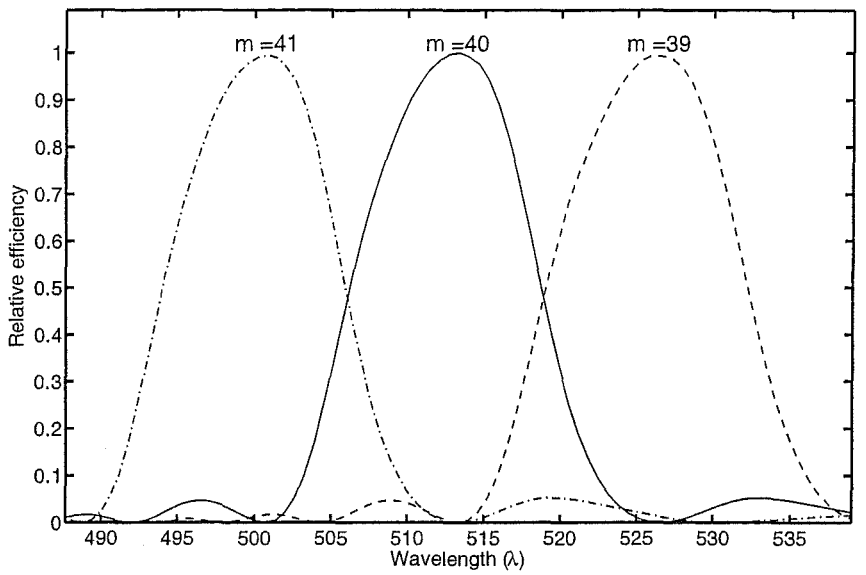

Figure 1.21: Relative efficiency of an échelle grating which is blazed at $\theta_B = 63°$.

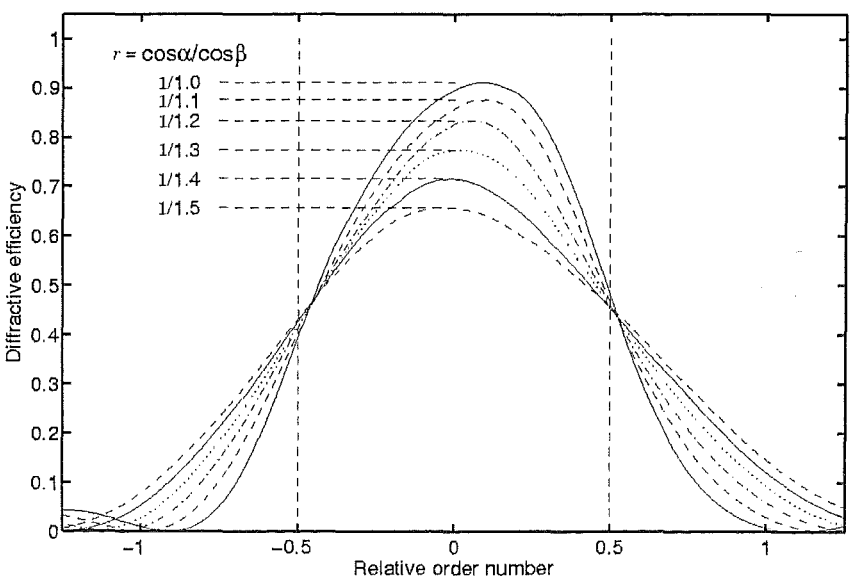

Figure 1.22: Blaze function for a range of Littrow angles (θ).

1.2.12 Overfilling

Although it has been assumed thus far that the collimated beam is matched to the projected size of the échelle grating, it is not always possible to do this. As shown in Figure 1.23, the amount by which a grating is overfilled is a function of the size of the grating (W and L) and the angle of illumination (α). Depending on the size of the grating, the

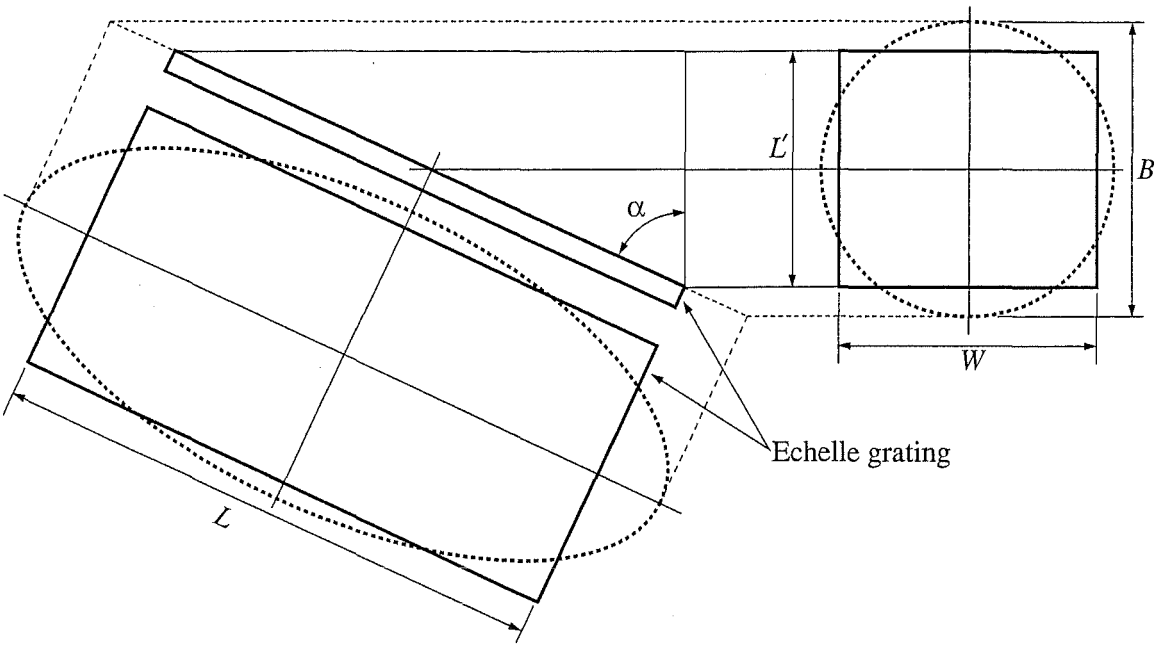

Figure 1.23: The overfilling of an échelle grating. The collimated beam, which has a diameter B, projects to an ellipse on the échelle grating (width W, length L). This projects to a height $L' = L\cos\alpha$ in the collimated beam.

elliptical footprint of the collimated beam may overfill the grating either perpendicular or parallel to the direction of the rulings (or both, as shown in Figure 1.23). If, as is shown in Figures 1.24a and 1.24b, we consider the overfilling in each of the directions separately then the fraction F of a collimated beam that is incident on a grating is given by

$$F = F_{\mathrm{W}} + F_{\mathrm{L}} - 1 \quad , \tag{1.85}$$

where F_{W} and F_{L} are the fractions of the beam captured when the overfilling in the parallel and perpendicular directions respectively. Once the grating has been projected into the collimated beam these fractions may be calculated by integrating the equation of a circle, with appropriate limits. That is,

$$F_{\mathrm{W}} = \frac{16}{\pi B^2}\int_0^{W/2}\sqrt{\frac{B^2}{4} - x}\,\mathrm{d}x \quad , \tag{1.86}$$

$$F_{\mathrm{L}} = \frac{16}{\pi B^2}\int_0^{L'/2}\sqrt{\frac{B^2}{4} - x}\,\mathrm{d}x \quad . \tag{1.87}$$

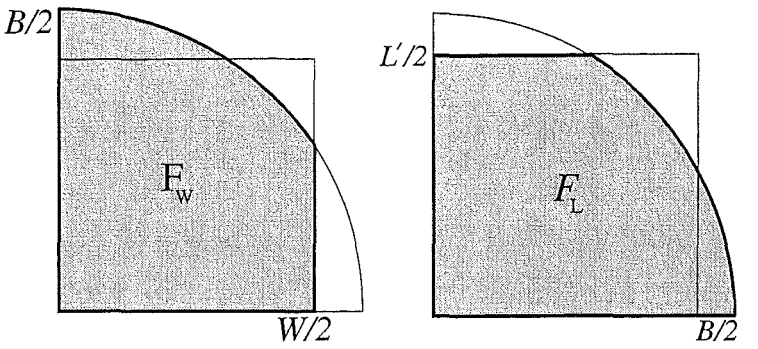

(a) W (b) L

Figure 1.24: The grating may be overfilled parallel and perpendicular to the rulings. The fraction F of the collimated beam that is incident on the échelle grating may be computed by considering the amount the grating is overfilled parallel (F_{W}) and perpendicular (F_{L}) to the ruling separately. See text for details.

In polar coordinates, these equations become

$$F_{\mathrm{W}} = \frac{4}{\pi}\int_{\theta_{\mathrm{W}}}^{\pi/2} \sin^2\theta \, \mathrm{d}\theta \quad , \tag{1.88}$$

$$F_{\mathrm{L}} = \frac{4}{\pi}\int_{\theta_{\mathrm{L}}}^{\pi/2} \sin^2\theta \, \mathrm{d}\theta \quad , \tag{1.89}$$

where the polar angle limits θ_{W} and θ_{L} are given by

$$\cos\theta_{\mathrm{W}} = \frac{W}{B} \quad \text{and} \quad \cos\theta_{\mathrm{L}} = \frac{L'}{B} \quad . \tag{1.90}$$

Evaluating equations 1.88 and 1.89 gives

$$F_{\mathrm{W}} = \frac{4}{\pi}\left[\frac{\pi}{4} - \frac{1}{2}\theta_{\mathrm{W}} + \frac{1}{4}\sin 2\theta_{\mathrm{W}}\right] \quad , \tag{1.91}$$

$$F_{\mathrm{L}} = \frac{4}{\pi}\left[\frac{\pi}{4} - \frac{1}{2}\theta_{\mathrm{L}} + \frac{1}{4}\sin 2\theta_{\mathrm{L}}\right] \quad . \tag{1.92}$$

If $W > B$, and/or $L' > B$, then the grating is not overfilled (or overfilled in one direction only) and consequently either $\theta_{\mathrm{W}} = 0$ or $\theta_{\mathrm{L}} = 0$. Hence, either $F_{\mathrm{W}} = 1$ or $F_{\mathrm{L}} = 1$ depending on the direction of overfilling.

1.3 Design of échelle spectrographs

1.3.1 Choice of échelle

The choice of grating is one of the most fundamental choices in the design of an échelle spectrograph. In the following sections some factors which influence this choice will be discussed.

Beam size

For a given échelle grating with a blaze angle θ_B which is used to obtain a given resolving power R it is not necessarily the case that the ideal beam width will be the width of the échelle grating W. It has been pointed out by Diego and Walker (1985) (see also Walker and Diego, 1985) that the échelle grating may be considerably overfilled without compromising throughput. This is because while the grating becomes less efficient as the beam size increases (due to overfilled light being lost) the angular size of the slit on the sky can be increased in order to maintain a constant resolving power.

The effect is illustrated in Figures 1.25a and 1.25b. Here an R2 échelle with $W \times L = 300 \times 840$ mm is illuminated (in Littrow configuration) by a beam which can vary in diameter. This is done in practice by varying the telescope focal ratio. The angular slit width is varied so that a constant resolving power of $R = 25\,000$ is maintained at all beam sizes. The efficiency of the grating is therefore a function of both beam size and seeing. Figure 1.25b shows the throughput relative to a beam size of 300 mm. For small seeing values it can be seen that increasing the beam size leads to rapidly decreasing throughput as the slit throughput always remains high. However, at larger values of seeing, the throughput of the spectrograph actually increases as the beam size is increased. This is because the overfilling of the échelle becomes increasingly mitigated by the larger angular slit width.

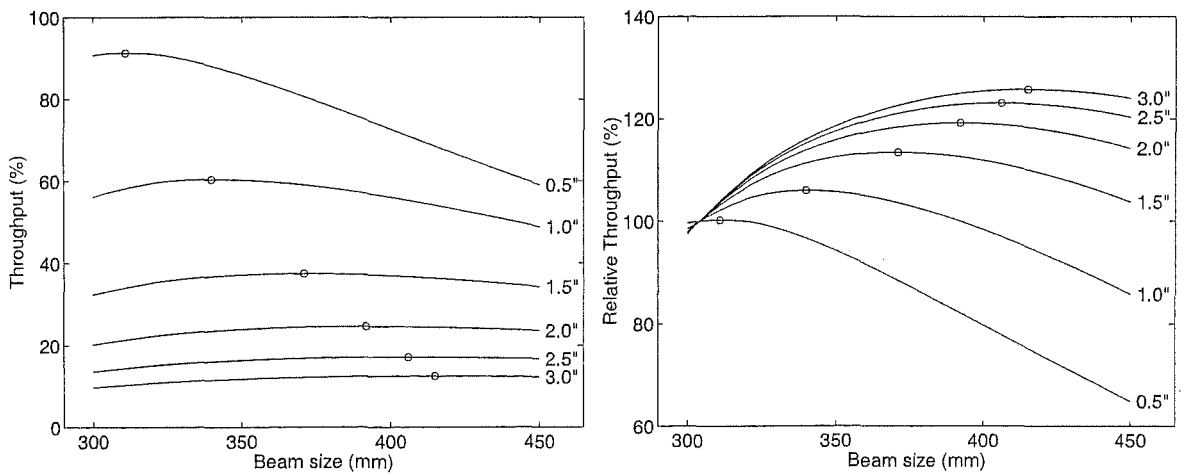

(a) Absolute efficiency (b) Relative efficiency

Figure 1.25: The absolute (a) and relative (b) efficiency for an R2 échelle grating with $W \times L = 300 \times 840$ for a resolving power of $R = 25\,000$ as a function of beam size and atmospheric seeing. Open circles indicate the most efficient beam size as a function of seeing.

Using such an analysis, for a given telescope and échelle grating combination, it is possible to choose an optimum beam size, where the weighting function would depend on the expected seeing conditions. A more detailed analysis would require that the effects of the secondary obstruction be considered (for directly fed spectrographs) and/or the effects of non-uniform illumination of the échelle grating (due, for instance, to the incomplete radial scrambling of the fibre far-field).

Blaze angle

As is shown in the following section, the choice of blaze angle will have little direct impact on the cross-dispersion. However, the blaze angle has a significant effect on the collimator and camera properties. These will be discussed in Section 1.3.3. For a further discussion of the choice of échelle grating blaze angle, and its implications on the spectrograph design, the reader is referred to Section 2.1.2 and to Hearnshaw et al. (1999).

Effect on cross-dispersion

The amount of inter-order space can be tuned by altering the properties of the échelle grating. As shown above (equations 1.46 and 1.47) the inter-order spacing depends on the free spectral range of the échelle grating. That is, if the wavelength extent from one order to the next is increased, while the cross-dispersion remains constant, then the inter-order spacing will increase accordingly. Given that the free spectral range depends most sensitively on the grating groove spacing (equation 1.14), simply changing σ will change the inter-order spacing. If the échelle grating is more densely ruled (σ decreased) then the free spectral range will increase, and therefore the total number of orders over a given wavelength range will decrease. The effect this will have on the spectral format is shown in Figure 1.26. One consequence of changing the échelle ruling density simply to increase the inter-order spacing is that the angular width of the orders also increases. This might be a problem if the angular field of view of the camera and detector is limited.

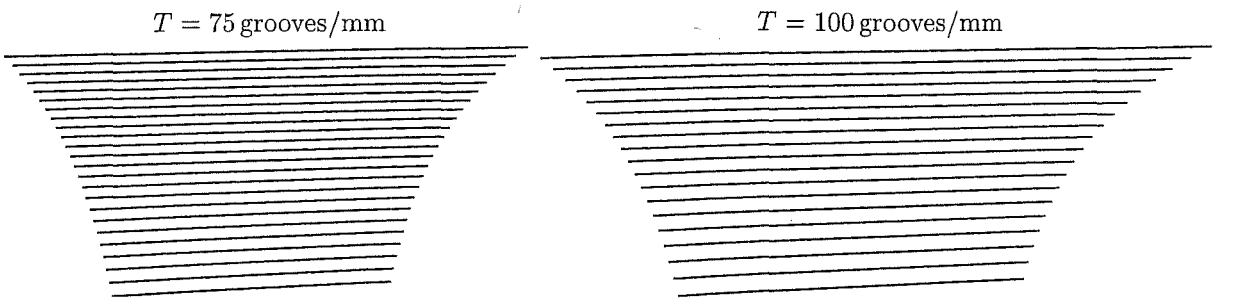

Figure 1.26: The effect of changing the échelle groove ruling density on order separation. The same (prism) cross-disperser and camera is used for the two examples however the échelle groove spacing has changed as indicated.

Changing the blaze angle of the échelle grating has relatively little effect on the spectral format. That is, as discussed above in Section 1.2.9, the order separation Δy, for a given échelle and cross-disperser combination, is given by

$$\Delta y = \text{Const.} \times \frac{1}{\sin \theta_{\mathrm{B}}} \quad , \tag{1.93}$$

(i.e., equations 1.47). Therefore, changing from an R2 grating to an R4 grating will decrease the order spacing by less than 10%. A description of the methods of cross-dispersion follows.

1.3.2 Cross dispersion

As has already being discussed, any combination of order number m and wavelength λ that satisfies the grating equation (equation 1.1) will have equal diffraction angles. If the wavelength coverage of interest spans more than a single free spectral range it will therefore be necessary to introduce dispersion in a direction that is orthogonal to the main échelle dispersion. Some possibilities for such cross-dispersion are discussed below.

Grating cross dispersion

The angular dispersion of a grating cross-disperser is

$$\frac{\mathrm{d}\beta}{\mathrm{d}\lambda_{\mathrm{XD}}} = \frac{m_{\mathrm{g}}}{\sigma_{\mathrm{g}} \cos\beta_{\mathrm{g}}} \quad , \tag{1.94}$$

where the grating order number m_{g} is generally low and the grating ruling density σ_{g} is high. Because the overall angular dispersion is quite low, the cross-disperser will be blazed at quite a shallow angle (i.e, β_{g} is small). The physical separation between orders is given by combining equation 1.94 with equation 1.47. That is,

$$\begin{aligned} \Delta y &= f_{\mathrm{cam}} \frac{m_{\mathrm{g}}}{\sigma_{\mathrm{g}} \cos\beta_{\mathrm{g}}} \frac{\lambda_{\mathrm{B}}^2}{2 \sin\theta_{\mathrm{B}} \cos\theta} \\ &= \text{Const.} \times \lambda_{\mathrm{B}}^2 \quad . \end{aligned} \tag{1.95}$$

Prism cross dispersion

When using a prism for cross-dispersion the angle of incidence is usually such that the dispersed rays are very nearly parallel to the base of the prism (see Figure 1.27). While

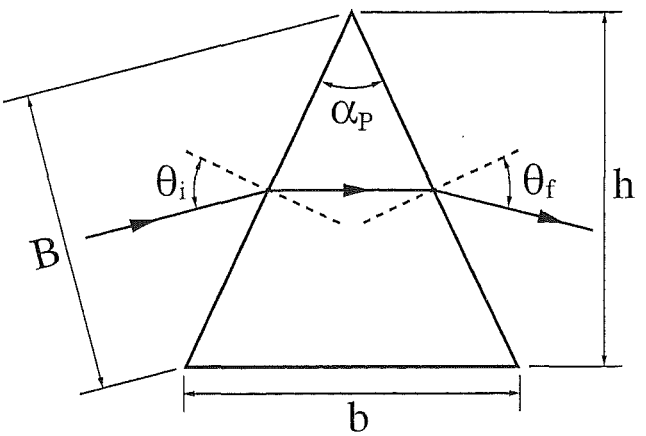

Figure 1.27: A prism used at minimum deviation.

this is close to the situation where a prism with a given apex angle has the least overall dispersion, this arrangement minimizes the total path length (of a wavelength which travels parallel to the base) and lessens the effects of polarization and reflection losses at

each face. The size of the prism is also minimized. The angular dispersion of a prism used near minimum deviation is given by

$$\frac{\mathrm{d}\beta}{\mathrm{d}\lambda_{\mathrm{XD}}} = \frac{b}{B}\frac{\mathrm{d}n}{\mathrm{d}\lambda} \quad , \tag{1.96}$$

where b is the length of the prism's base and B is the diameter of the incident beam. The ratio b/B effectively determines the prism apex angle α_{P}. That is,

$$\frac{b}{B} = \frac{\tan\theta_{\mathrm{i}}}{n_\lambda}\cot\frac{\alpha_{\mathrm{P}}}{2} \quad , \tag{1.97}$$

where θ_{i} is the angle of incidence of a wavelength (for which the prism refractive index is n_λ) such that

$$\sin\theta_{\mathrm{i}} = n_\lambda \sin\frac{\alpha_{\mathrm{P}}}{2} \quad . \tag{1.98}$$

This is the angle of incidence of a wavelength which has a minimum path length through the prism. Now, the refractive index of a prism can be approximated using the Conrady formula by

$$n(\lambda) = k_1 + \frac{k_2}{\lambda^2} \quad , \tag{1.99}$$

where k_1 and k_2 are constants, and hence the angular dispersion of a prism is

$$\frac{\mathrm{d}\beta}{\mathrm{d}\lambda_{\mathrm{XD}}} = -2\frac{b}{B}\frac{k_2}{\lambda^3} \quad . \tag{1.100}$$

The separation between orders produced by a prism can be found by substituting Equation 1.100 into Equation 1.47 which gives

$$\begin{aligned} \Delta y &= -2f_{\mathrm{cam}}\frac{b}{B}\frac{k_2}{\lambda_{\mathrm{B}}^3}\frac{\lambda_{\mathrm{B}}^2}{2\sin\theta_{\mathrm{B}}\cos\theta} \\ &= \text{Const.} \times \frac{1}{\lambda_{\mathrm{B}}} \quad . \end{aligned} \tag{1.101}$$

Gratings or prisms?

The order separation for both prisms and gratings was derived above (equations 1.95 and 1.101). It was shown that the order separation was

$$\begin{aligned} \text{Gratings}: \quad \Delta y &= \text{Const.} \times \lambda_{\mathrm{B}}^2 \quad \text{and} \\ \text{Prisms}: \quad \Delta y &= \text{Const.} \times \frac{1}{\lambda_{\mathrm{B}}} \quad . \end{aligned}$$

This shows that the order separation given by a grating increases rapidly as the wavelength increases (i.e, as the square of the wavelength), while the order separation decreases (at a lesser rate) for a prism. This fact makes prisms particularly attractive in situations where it is desirable to capture a large wavelength range on a single detector. That is, if a prism and grating is chosen such that the total cross dispersion is the same (see Figure 1.28), the range of inter-order spacing of a grating will vary considerably. Generally this forces the design of an échelle spectrograph with grating cross-dispersion to incorporate several grating cross-dispersers so that the inter-order spacing at a chosen wavelength can

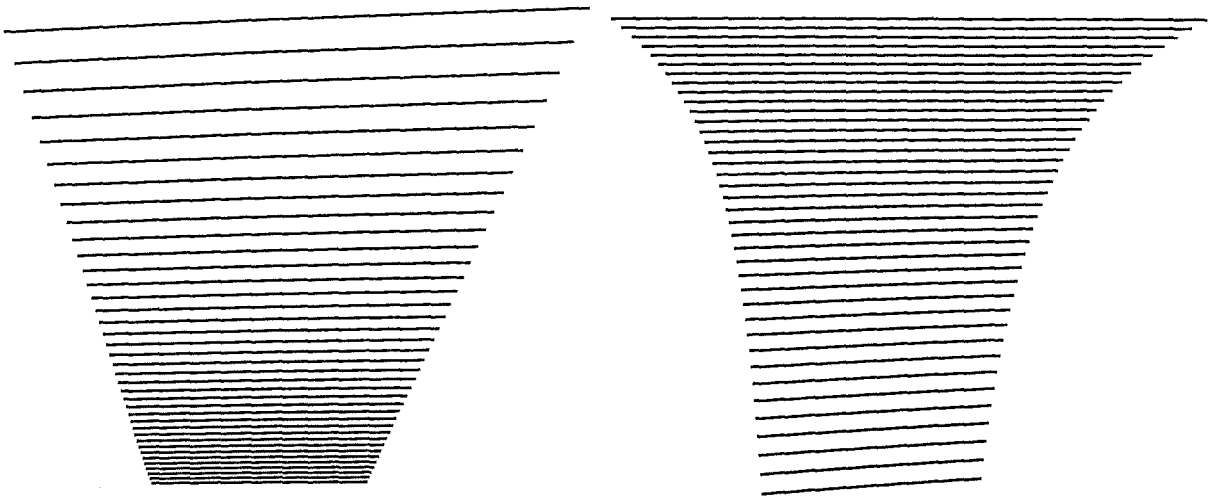

(a) Grating cross dispersion

(b) Prism cross dispersion

Figure 1.28: The relative order separation of gratings (right) and prisms (left).

be varied. However, a prism has relatively uniform inter-order spacing, and one prism (or prismatic system) is sufficient for all wavelength regions. Alternatively, a combination of gratings and prisms (or a grism) could be considered.

Another aspect to consider is the relative efficiency of grating and prism cross-dispersers. It is generally the case that a high quality prism will have significantly higher efficiency over a broader wavelength range than any grating. This is because gratings are subject to the effects of the blaze function. A typical high efficiency surface relief grating will have a FWHM which is about equal to the blaze wavelength, and hence may only be considered useful over a small wavelength range. Recently however high efficiency gratings have been developed that have a periodic grating structure which arises from modulation of the index of refraction of a thin layer of light sensitive material. Such gratings are termed volume-phase holographic (VPH) gratings and are discussed further in Chapter 3. These gratings cannot however be used over more than a single octave of spectral coverage and two or more gratings would still be required to cover a wavelength band spanning the near-UV to the near-IR (i.e., the approximate pass-band of a high efficiency CCD detector).

1.3.3 Collimator, camera and detector properties

Collimator

The required focal length of the collimator ($f_{\rm col}$) follows from the equality given by equation 1.23. That is,

$$f_{\rm col} = \frac{1}{\rho}\frac{f_{\rm tel}}{D}B \quad , \tag{1.102}$$

where the focal ration degradation factor $\rho = 1$ if the spectrograph is directly fed. The actual collimator focal length is a completely free parameter as long as the equality given by equation 1.23 is maintained.

Camera

The focal length of the camera $f_{\rm cam}$ is determined by noting that in order for the maximum resolving power $R_{\rm max}$ to be achieved the CCD must sample at least two resolution elements. It therefore follows that

$$f_{\rm cam} = \frac{n_{\rm samp}}{2} R_{\rm max} s_{\rm pix} \cot\theta_{\rm B} (1 + \tan\theta_{\rm B} \tan\theta) \quad , \tag{1.103}$$

where $n_{\rm samp}$ is the number of CCD pixels per resolution element. Typically $n_{\rm samp} = 2$ for critical Nyquist sampling with pixels each having a size $s_{\rm pix}$, giving

$$f_{\rm cam} \simeq R_{\rm max} s_{\rm pix} \cot\theta_{\rm B} \quad , \tag{1.104}$$

for small θ. This shows that large blaze angle gratings require short focal length cameras. However, because $R = \text{Const.} \times B \tan\theta_{\rm B}$, (equation 1.58) the monochromatic focal ratio of the camera will be given by

$$\frac{f_{\rm cam}}{B} = \text{Const.} \times s_{\rm pix} \quad . \tag{1.105}$$

That is, for a given maximum attainable resolving power, the focal ratio of the spectrograph's camera will depend only on the CCD pixel size. The effective focal ratio of a spectrograph camera, which determines the camera's actual size, depends rather more on the location of the entrance pupil.

Detector

That the chosen pixel size influences the camera's focal length was pointed out in the previous section. The number of pixels $n_{\rm pix}$ required by a detector to completely sample an order is given by

$$n_{\rm pix} = \frac{f_{\rm cam} \Delta\beta_{\rm FSR}}{s_{\rm pix}} \quad , \tag{1.106}$$

which, given equations 1.15 and 1.104, can be approximated to give

$$n_{\rm pix} \approx \frac{R_{\rm max} \lambda_{\rm B}}{\sigma \sin\theta_{\rm B}} \quad . \tag{1.107}$$

Given that $m\lambda_{\rm B} \approx 2\sigma \sin\theta_{\rm B}$, equation 1.107 can also be written as

$$n_{\rm pix} \approx \frac{2R_{\rm max}}{m} \quad , \tag{1.108}$$

which shows that all high resolution spectrographs require large detectors if wavelength coverage is complete. Often, for the sake of economy, compromises are made either in the maximum resolving power and/or wavelength coverage.

1.3.4 Fibres

The use of fibres in astronomy was first suggested by Angel et al. (1977). Their idea, which was made possible by the recent development of high quality fused silica fibres, was to link numerous small aperture telescopes to a single instrument. Subsequently

fibres were used in multi-fibre applications such as the simultaneous observation of many objects (for example, the Medusa spectrograph (Hill et al., 1980)), or to obtain spectra over a two-dimensional area (for example, the DensePax fibre optic array (Barden and Wade, 1988)). Both of these applications demonstrate that fibres contribute towards considerable improvements in the efficiency of spectroscopic observations.

Another practical benefit of the use of fibres is that the instrument is removed from the telescope. Hubbard et al. demonstrated the feasibility of this in 1979 (Hubbard et al., 1979). This removes the constraints of size and weight of any fibre-coupled instrument, while also allowing such an instrument to be placed in a potentially more stable environment, where the effects of flexure, temperature, and pressure changes may be absent. Hence fibres are of particular value for the high-precision measurement of radial velocities.

A further advantage of the use of fibres in precision spectroscopy is the ability of a fibre to scramble the input image structure. This means that regardless of the distribution of light on the input face of the fibre, the output face will appear more uniform. Hence, systematic errors due to slit illumination may be reduced. This type of image scrambling is referred to as "near-field" scrambling. It was also realized that the optics of a fibre-fed instrument may be illuminated more uniformly due to the scrambling properties of a fibre. That is, the angular distribution of rays exiting a fibre will not betray the distribution that entered the fibre. This type of "far-field" scrambling also has the potential to increase the stability of the spectrograph. However, as observed by Hunter and Ramsey (1992), and predicted by Heacox (1987), while the azimuthal scrambling of rays in the far field is nearly complete, the radial scrambling is not quite as good. These effects also impinge subtly on the illumination of the slit exit (or the "near-field" image) and hence may cause significant drifts in line profiles or positions. A method for increasing the scrambling via means of a "double-scrambler" has been proposed by Brown (1990). The double-scrambler is inserted in a break in the fibre and its purpose is to invert the positional and angular dependence of the rays crossing the junction between the two fibre halves.

The implications of coupling a spectrograph to a telescope via optical fibres was discussed above in Sections 1.2.6, 1.2.8, 1.2.10.

1.3.5 Merit functions

A common merit function used for comparing spectrographs is the slit-resolving power ($R\theta_s$) product which follows from equation 1.61 (or equation 1.59). That is,

$$R\theta_s = \frac{2L \sin\theta_B \cos\theta}{\rho D} \quad . \tag{1.109}$$

As stated in Section 1.2.10, this equation shows that for a given resolving power and angular slit size, a large telescope requires a large grating. A more complete merit function would also take into account the throughput of the spectrograph, T; i.e., $TR\theta_s$. This was introduced by Jacquinot (1954) in a different form. However, as pointed out by Vaughnn (1994), a more appropriate merit function would maximize the product of the signal-to-noise ratio (for each spectral element) and the total number of resolution elements. This is applicable because the performance of the spectrogragh is then intimately linked to the telescope and its environment.

1.4 Summary

A theoretical basis for the design of high resolution échelle spectrographs in astronomy has been outlined. A particular emphasis has been placed on the implication of coupling the spectrograph to a telescope via an optical fibre. In the following chapter (Chapter 2) the design and performance of a fibre-fed spectrograph designed for small to medium-sized telescopes will be described. In Chapter 3 the design evolution of a high resolution spectrograph for an 11-metre telescope will be presented.

Chapter 2

Design and performance of HERCULES

The optical design of HERCULES is described in detail in the following section (Section 2.1). The detailed design of HERCULES was not part of this thesis, however some justification for the design is given here. In Section 2.2 a summary of the predicted and measured performance is given. Finally, Section 2.3 describes a few upgrade options which could improve the performance of HERCULES. The HERCULES observing manual is included as an appendix (Appendix C).

2.1 Design

2.1.1 Introduction

Since 1977 a Cassegrain échelle spectrograph has been in operation at Mt John University Observatory (MJUO). Initially this instrument was designed to operate with the Boller and Chivens 0.60 m telescope. The spectrograph design is based on the Harvard-Smithsonian design (see Hearnshaw 1977, 1978). It uses a 79 grooves per millimeter grating, which has an area of 102 × 206 mm. The grating has a blaze angle of $\theta_B \approx 63°$ (i.e., $\tan\theta_B = 2$).

In 1987 the 1 m McLellan telescope was built, and the échelle spectrograph was used with this telescope until 2001 when it was decommissioned. The McLellan telescope is a Dall-Kirkham design which uses an ellipsoidal primary mirror and a spherical secondary (Nankivell and Rumsey, 1986). Although the telescope delivers an f/13.5 beam to the spectrograph a focal reducing lens immediately in front of the slit reduces this to f/10. A 100 μm slit therefore subtends an angle of 2.1″ on the sky and delivers a resolving power of $R \approx 35\,000$ with a collimated beam size of 54 mm. The camera, which is a spherical mirror, was designed for use with photographic plates approximately 50 mm square and the collimator, which is an off-axis paraboloid, produces astigmatism in the direction of cross-dispersion. This was deliberate in order to avoid saturating the photographic emulsion. A schematic of this instrument is shown in Figure 2.1, and Figure 2.2 shows an early photographic spectrum.

For increased sensitivity the spectrograph was used with a cryogenically cooled linear diode array (MacQueen, 1986). The Reticon RL1872F chip was capable of observing a 25 mm length of a single order. A Photometrics CCD with a Thomson TH7882 CDA detector (384 × 576 pixels each 24 μm square) was acquired in 1988 (Tobin, 1992). In April 1996 this CCD was replaced with a larger format CCD (Barnes et al., 2000); a thinned and back-illuminated SITe SI-003AB which has 1024 × 1024 24 μm square pixels. However, this CCD was still incapable of observing more than a small fraction of the available spectral format. The spectral coverage was considerably improved in 1998 when a focal reducer was installed (Tobin et al., 1998).

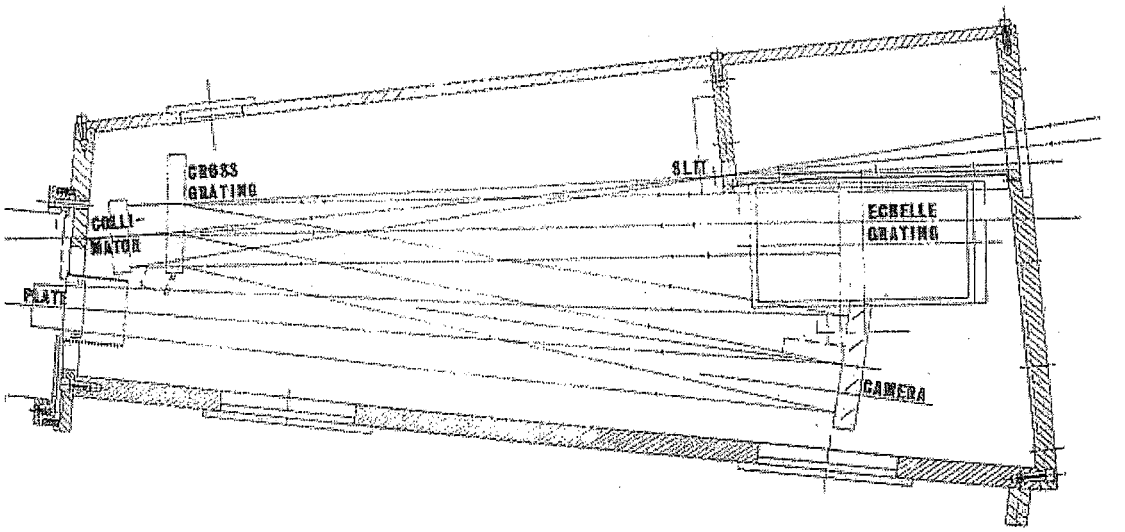

Figure 2.1: The Mt John University Observatory Cassegrain échelle spectrograph. The design uses an R2 grating, with 79 grooves per millimeter. The grating has an area of 102 × 206 mm, and three interchangeable gratings are available for cross-dispersion.

The fibre-fed adaptation

The MJUO échelle spectrograph was adapted for fibre fed work in 1989 (Kershaw and Hearnshaw, 1989). By removing the spectrograph from the Cassegrain mount, where flexure is a major problem, and enclosing the spectrograph in a thermally isolated room the spectrograph could be used for obtaining precise radial velocities. Initially the detector used was the Reticon linear diode array. Later CCD s were used, and radial velocities of bright stars ($V \leq 7$) could be obtained to a precision of about $50\,\mathrm{ms}^{-1}$ (Murdoch et al., 1993; Skuljan et al., 1999; Cummings et al., 1999).

Although this system worked well, and gave some excellent and precise radial velocity measurements, it was inherently inefficient because of the low throughput into the fibre, the need to reimage the fibre onto a slit to improve resolving power, the small beam size of the spectrograph, the use of grating rather than prism cross-dispersion, the absence of anti-reflection coatings or high-efficiency reflecting surfaces and the large cross-order profile (due to deliberate collimator astigmatism) and the consequently limited number of orders, and hence overall wavelength coverage, that were available on the CCD. The need to allow this instrument to be used in both Cassegrain and fibre-fed modes, and the variety of manual adjustments and interchangeable gratings undoubtedly contributed to its instability.

It was realized that a much more efficient and stable spectrograph was possible in principle if care were taken in matching all parameters to the image size, pixel size and CCD dimensions, if very efficient optical coatings were applied to relevant surfaces and if great care was taken to stabilize the environment in which the spectrograph operated.

This new instrument, which meets all these design criteria, is known as HERCULES (High Efficiency and Resolution Canterbury University Large Echelle Spectrograph) and came into operation at MJUO in April 2001.

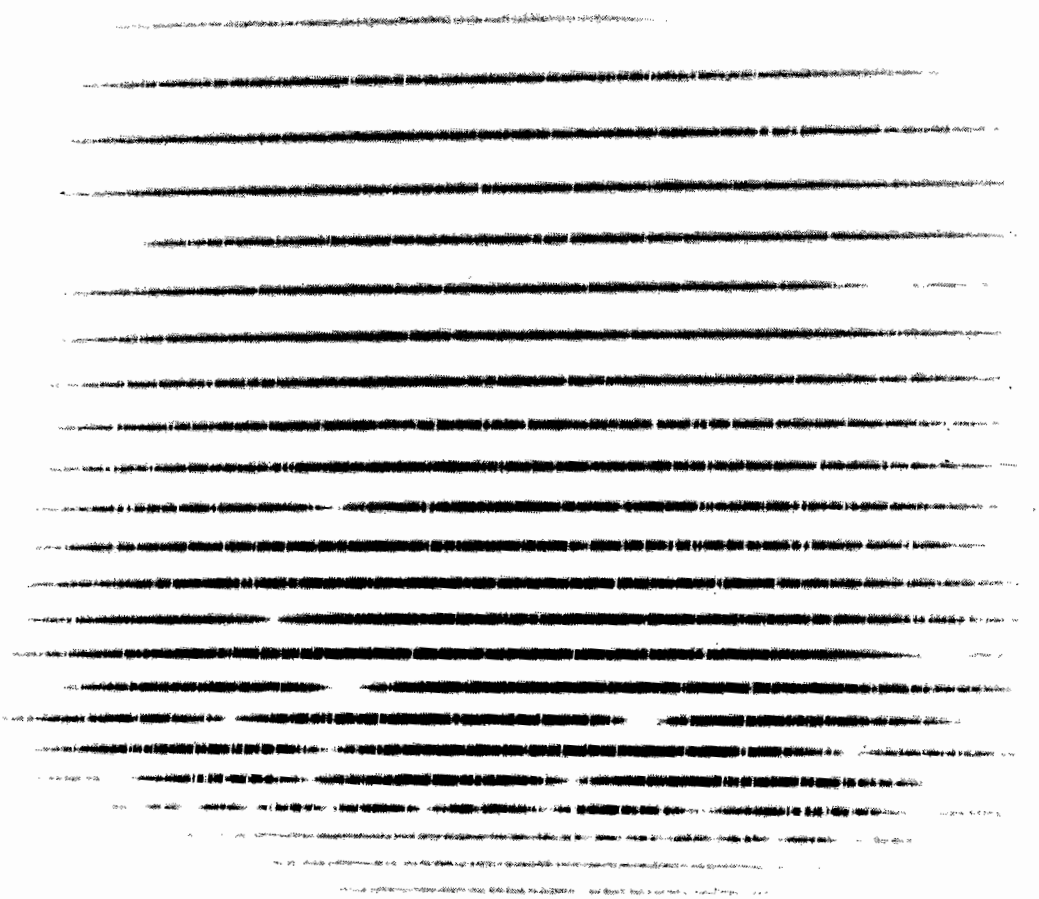

Figure 2.2: A photographic spectrum of Canopus taken with the MJUO Cassegrain échelle 1978 June 24.

2.1.2 Optical design

The optical layout of HERCULES is shown in Figure 2.3 and a schematic of the mechanical design is shown in Figure 2.4. The design of HERCULES was done by J. Hearnshaw. G. Nankivell and N. Rumsey advised on the prism glass and developed the Zemax optical model and G. Nankivell produced the Schmidt plate parameters. The present author designed the fibre feed optics, including the guide and acquisition cameras, as well as the exposure meter. A summary of the HERCULES parameters can be found in Appendix A.2.1 and the design is summarized by Hearnshaw et al. (2002).

The nominal wavelength coverage of HERCULES is from 380 nm to 880 nm and with a fibre entrance aperture of 4.5″ (on a 1-metre telescope) a resolving power of $R = 40\,000$ is possible.

Design evolution

Design work on HERCULES commenced in 1995 and from 1995-1996 two design options were explored. One was an R2 spectrograph with a folded Schmidt camera. The other was an R4 instrument with a white pupil and employing a multi-element refracting camera. The white pupil reimages the undispersed pupil incident on the échelle onto the entrance pupil of the camera, thereby ensuring smaller optical components and better control of camera aberrations. These two designs were developed further in 1997–98. The R4 instrument was considerably more compact and used a 10-cm collimator beam size falling on an area of 400×100 mm (ruled surface area) for the R4 échelle. The cost advantage of this compactness was offset by the complexity of the camera which was necessary for such a wide wavelength coverage; three different all-refracting cameras were designed, all with 10 optical elements, some of which entailed use of rather exotic (hence expensive) glasses (the best performance came from the camera using several fluorite lens components). The R2 spectrograph was relatively large, thereby adding to the cost of some components, including the échelle (about 400×200 mm), but this instrument employed a folded Schmidt camera, giving superior near achromatic performance over a wide field of view and wavelength range, together with relative simplicity of camera fabrication. The light loss inherent in the folded Schmidt design due to the hole in the fold flat is moderate ($\leq 23\%$) for the R2 design, but would be prohibitive for an R4 instrument, which is why an all-refracting camera is unavoidable for that spectrograph. The overall size of the instrument was not considered an issue given that it would be fibre-feed. In mid-1998, after carefully evaluating both R2 and R4 designs, a decision was made to proceed with the former (Hearnshaw et al., 1999).

Construction of HERCULES proceeded from July 1998. The prism was optically figured and polished by D. Cochrane at Industrial Research Limited[1]. All other optical components of HERCULES were fabricated by G. Nankivell, also in Lower Hutt, at his private optical workshop. The mechanical design and construction took place in the workshops of the Department of Physics and Astronomy under the direction of G. Kershaw. N. Frost designed and built the fibre-feed module with electronics provided by R. Ritchie. The control software was developed by G. Graham. HERCULES was commissioned on 2001 April 3.

[1]Industrial Research Ltd, Lower Hutt, New Zealand

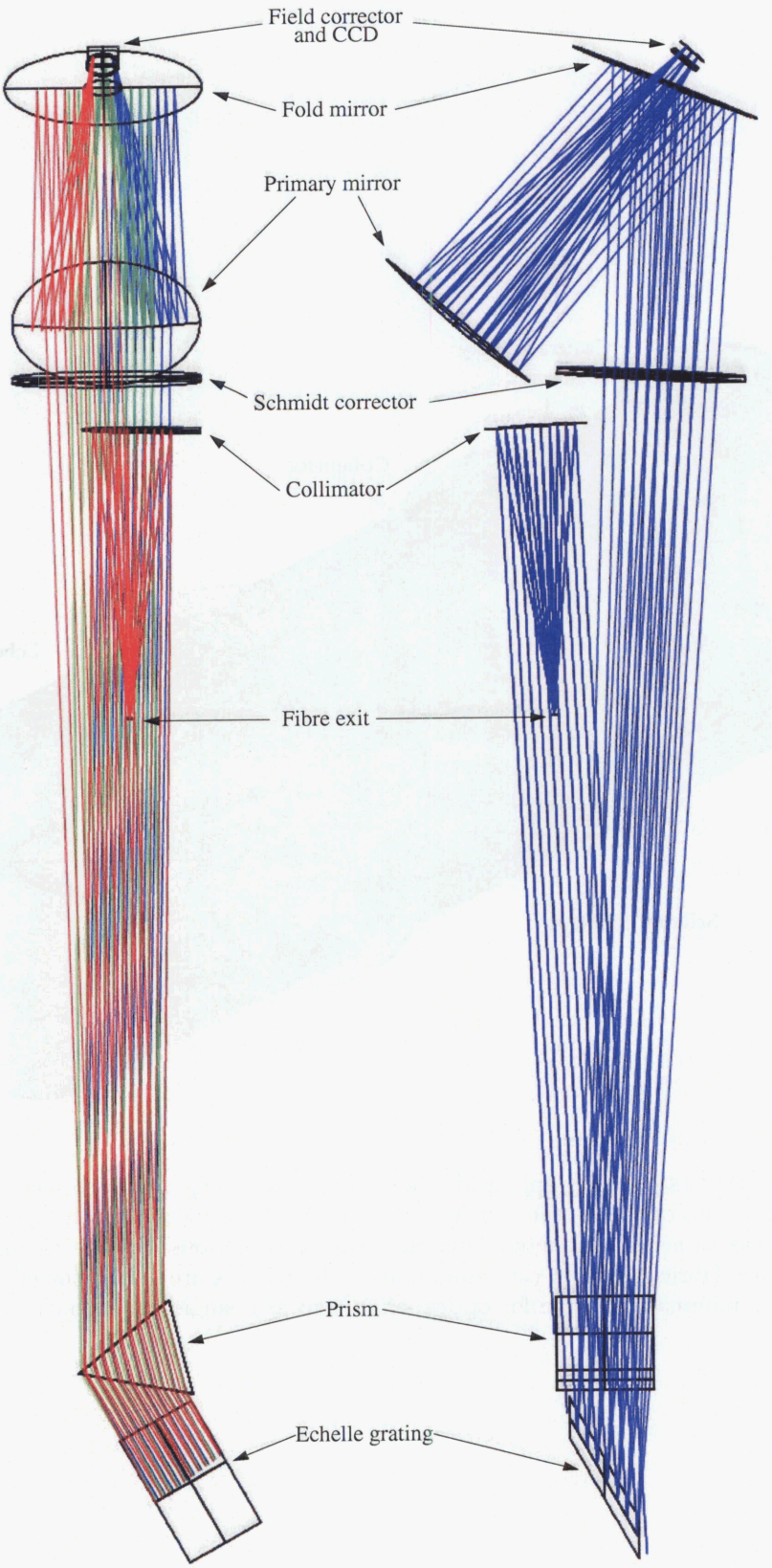

Figure 2.3: The optical design of HERCULES.

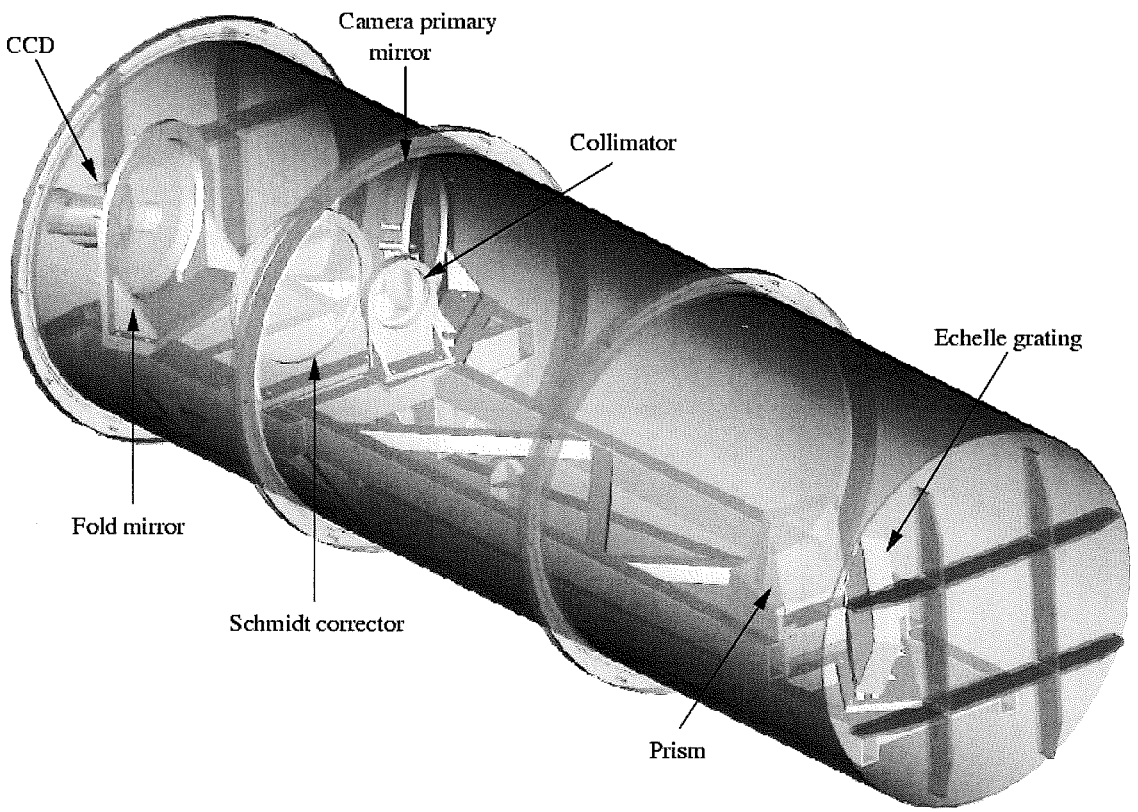

Figure 2.4: The HERCULES spectrograph inside the vacuum tank. The tank is formed in three sections. The first section, which encompasses the camera optics, is rigidly connected to the spectrograph bench. The lid (on which the camera is mounted) and the other two sections are free to roll away on rails. All optical mounts are fabricated from cast aluminium. The mirrors are all supported by thin stainless steel bands. There is minimal provision for optical alignment as a single alignment is made during final assembly.

Vacuum tank

From the outset it was intended to put HERCULES in an environment which would be immune from the effects of changes of either atmospheric pressure or the temperature of the spectrograph room. The importance of such immunity to the precision of the spectrograph is emphasized by considering that a 1 mbar (hPa) increase in air pressure (at sea level) will give rise to a spurious Doppler shift of -80 m/s, while a temperature change of 1°(at 25°) will result in a shift of 270 m/s (Murdoch et al., 1993). These effects, which are caused by the pressure and temperature dependence of the refractive index of air, can be completely eliminated if the spectrograph were enclosed inside a vacuum. A vacuum will also eliminate both convection currents and temperature stratification; both of which would impact on the spectrograph's stability. The use of helium was also considered. This monotonic gas has a refractive index very close to that of a pure vacuum with a consequently small dependence on temperature or pressure. The high thermal conductivity of the gas would aid the thermal equalization of the spectrograph structure. Concerns about the permeability of helium versus the relative ease of constructing and maintaining a light vacuum tank were behind the decision to use a vacuum. The vacuum is supplied by an aluminizing chamber located around 20 m from the HERCULES room.

Echelle grating

HERCULES uses a large R2 31.6 gr/mm échelle grating from the master ruling MR152 from the Richardson Grating Laboratory[2]. for which the $\theta_B = 64.33°$; $\tan\theta_B = 2.08$. The ruled area is 204×408 mm. The relatively coarse ruling gives a small angular width of the orders and hence an optimum match to a 50 mm square CCD detector. The Littrow angle θ is made as small as practicable (small θ requires a much longer spectrograph, in order to separate the incident and diffracted échelle beams) so as to give high peak efficiency to the orders within a free spectral range (see Section 1.2.11 and references therein). In the case of HERCULES we chose $\theta = 3.0°$, which with a 200 mm collimated beam allows the entire spectrograph to be housed inside a 4.50-m long tank.

Cross-dispersion

The choice of prism cross-dispersion gives high efficiency at all wavelengths (a maximum of 90% of the photons are preserved after two passes) while ruled grating cross-dispersion peaks at about 70% and suffers from a limited wavelength range each side of the blaze. The cross-dispersion arrangement adopted was influenced by the similar design of Libbrecht and Peri (1995) for the Hale 5-m telescope fibre-fed échelle at Palomar, but HERCULES differs from the Hale instrument in most other aspects of its design. Cross-dispersion is provided by a single BK7 prism (PH3 quality glass which has a maximum deviation of the refractive index of no more than $\pm 2 \times 10^{-6}$) in a double pass-mode. The prism apex angle is $\alpha_P = 49.50°$ and dimensions are a height of 276 mm, a base of 258 mm and a length (between triangular faces) of 255 mm. The mass of the prism is 22.7 kg. The cross-dispersion is sufficient for a minimum of 17″ separation between adjacent orders.

[2]Richardson Grating Laboratory, Rochester, New York, U.S.A.

The refractive indices at standard wavelengths were measured by Glass Fab[3] and the data are given in Table 2.1. The measured dispersion (at 587.6 nm) is

$$V_d = 64.25 \quad ,$$

and both this measurement and the refractive indices are within the standard tolerances for this glass; that is,

$$n_d = 1.51680 \pm 0.001 \quad \text{and} \quad V_d = 64.17 \pm 0.8\% \quad .$$

The refractive indices are reliably modeled by the Conrady formula

$$n(\lambda) = n_o + \frac{A}{\lambda} + \frac{B}{\lambda^{3.5}} \quad , \tag{2.1}$$

where the coefficients are:

$$\begin{aligned} n_o &= 1.500301 \quad , \\ A &= 8.24268 \times 10^{-3} \quad \text{and} \\ B &= 4.46946 \times 10^{-4} \quad . \end{aligned}$$

Line	Wavelength (nm)	Refractive index
$n_{F'}$	480.0	1.52330
n_F	486.1	1.52285
n_e	546.1	1.51909
n_d	587.6	1.51722
$n_{C'}$	643.8	1.51520
n_C	656.3	1.51480

Table 2.1: Refractive index melt data for HERCULES BK7 prism. The measurements were provided by Glass Fab.

As shown in Section 1.2.8 every spectral line will be tilted by an amount ϕ given by

$$\tan\phi \approx 2\tan\theta_B \tan\gamma \quad . \tag{2.2}$$

Because half the cross-dispersive power is located before the échelle grating and the total variation in the angle γ will be approximately equal to half the total angular cross dispersion $\Delta\beta_{XD}$.Therefore, the variation in line tilt $\tan(\Delta\phi)$ will be

$$\begin{aligned} \tan(\Delta\phi) &= 2\tan\gamma\tan\theta_B \\ &\approx 4\tan\left(\frac{1}{2}\Delta\beta_{XD}\right) \quad , \end{aligned}$$

and given that $\Delta\beta_{XD} \approx \pm 2.5°$, the variation in γ is $\Delta\gamma \approx \pm 1.25°$, and hence the variation in line tilt across the HERCULES spectrum will be $\Delta\phi \approx \pm 5°$.

[3]Glass Fab Inc, Rochester, N.Y.

Collimator

The collimator mirror of HERCULES is an on-axis paraboloid with a 783 mm focal length. The diameter of 210 mm is designed to be used at f/3.75 where the fibres are placed at the mirror's focal point. This is possible because the number of fibres used is small, and there are no pre-slit optics, and therefore the resulting obstruction is small (< 5 mm in diameter). The elliptical illumination on the échelle overfills the ruled area by 14.5% (i.e., the semi-major axis of the beam is 272 mm). However, a large collimated beam size B allows a larger angular slit size θ_s for a given resolving power, and hence a net efficiency gain (see Section 1.2.12 and references therein). The collimator mirror was made from Zerodur with a 35-mm edge thickness.

Camera

The HERCULES camera is a folded Schmidt which gives outstanding performance with respect to aberrations over a very large wavelength range (380–880 nm) and high efficiency. The arrangement with a perforated fold flat (perforation diameter 100 mm at an angle of 19.0° to the mirror's normal) gives rise to a light loss of up to about 23% at some central wavelengths. On the other hand, placing the CCD dewar in the beam would have led to even more obscuration and lack of access to the detector. The fold flat is 55 cm in diameter and tilted at 19.0° to the optical axis from the Schmidt plate. In our folded design the CCD dewar is located outside of the HERCULES vacuum tank, and the field-flattening lens immediately in front of the detector acts as a window for the tank. The BK7 Schmidt corrector plate has a 525-mm trim diameter and 15-mm thickness. The camera mirror of HERCULES is 500 mm in diameter with an edge thickness of 66 mm and a centre thickness of 50 mm. The optical surface is spherical and the concave radius of curvature is 1946 mm, giving a focal length of 973 mm. The material is Zerodur. The camera is shown in Figure 2.5.

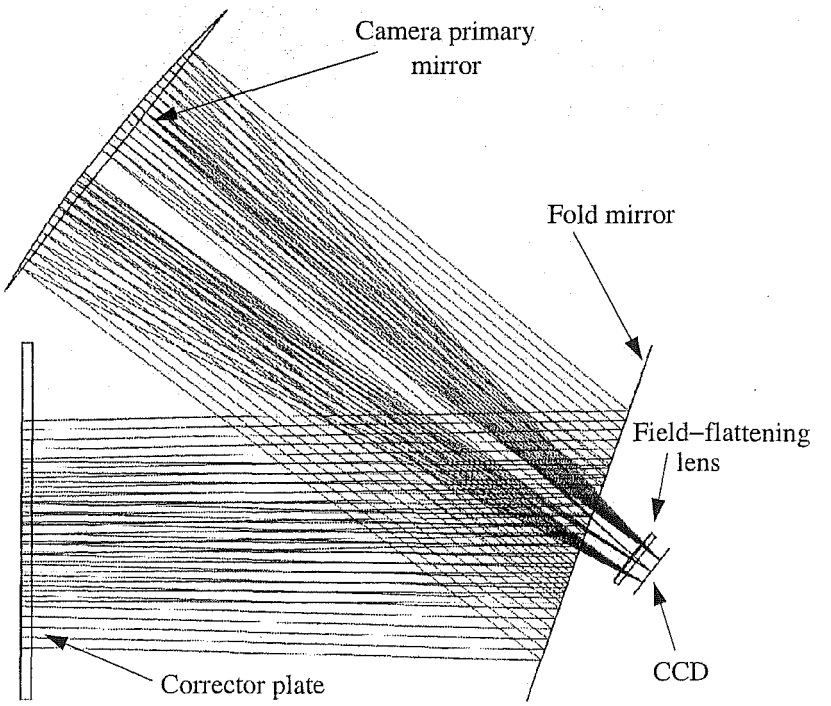

Figure 2.5: The HERCULES camera. The design is a folded Schmidt.

Spot diagrams for a variety of wavelengths and spectral orders are shown in Figure 2.6. The rms spot size ranges from 4.5 μm in the UV to below 1 μm near Hβ, 3 μm at Hα, rising to 6 μm near the ends of the red orders.

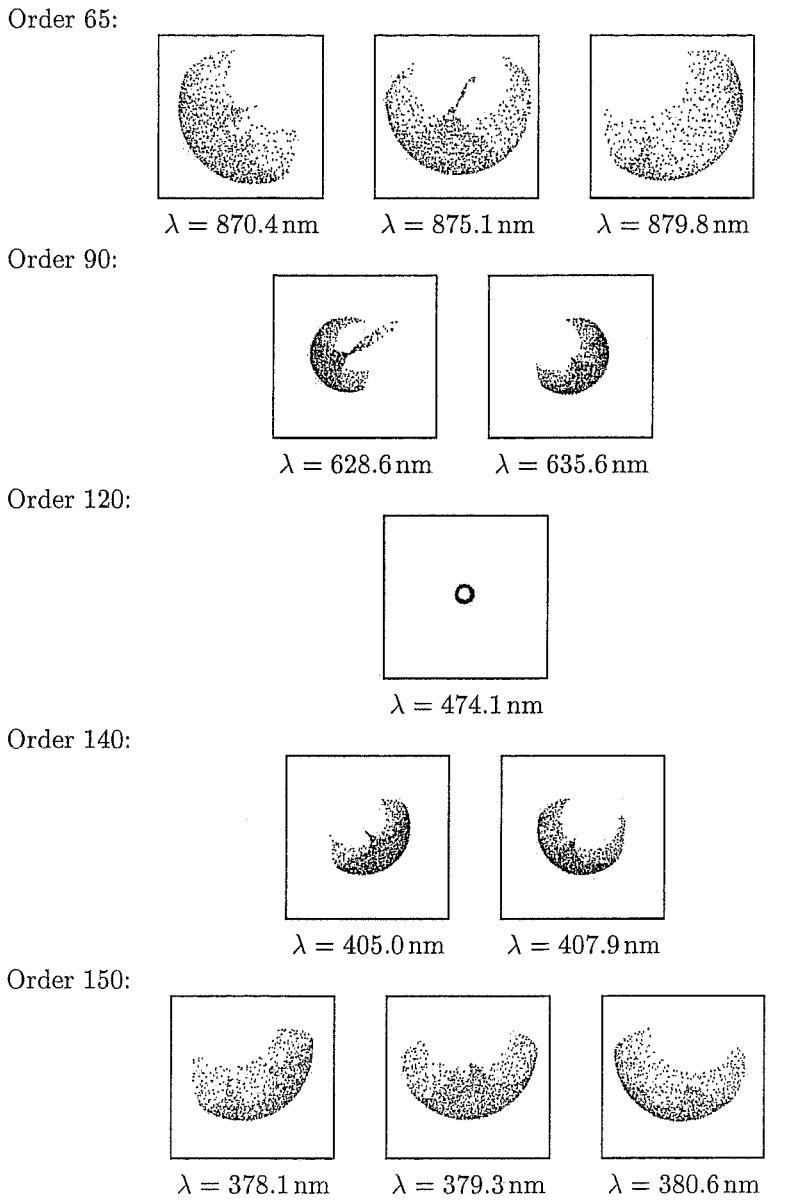

Figure 2.6: HERCULES spot diagrams as predicted by ZEMAX. All boxes are 15 μm square.

Spectral format

The spectral format of HERCULES is shown in Figures 2.8 to 2.10. Examples of small regions of spectra are shown in Figure 2.7. As was noted above, HERCULES was originally intended to be used with a 2k by 2k CCD having 25 μm pixels which would have enabled complete spectral coverage from 380 nm to 880 nm (see Figure 2.8). At the time of construction only the Series 200 CCD with 1024 $\times$ 1024 pixels each 24 μm square was available to be used with HERCULES. It is therefore not possible to observe the entire spectral range simultaneously. In order to observe all of the spectral format a detector cradle was constructed which has four discrete CCD positions. The design was intended to cover the spectral regions shown in Figure 2.9. However, during assembly the spectral format was slightly altered to give a more centrally located CCD position which is better suited to precision radial velocities. The CCD positions currently available with HERCULES are shown in Figure 2.10. Note that it is currently impossible to observe spectra above 720 nm and the lower limit of 370 nm is a result of the instrument efficiency (i.e., fibres, mirrors and CCD). It is likely that a new CCD will be acquired which will capture the entire visible region from 360 nm to 1 μm (see Section 2.3.1).

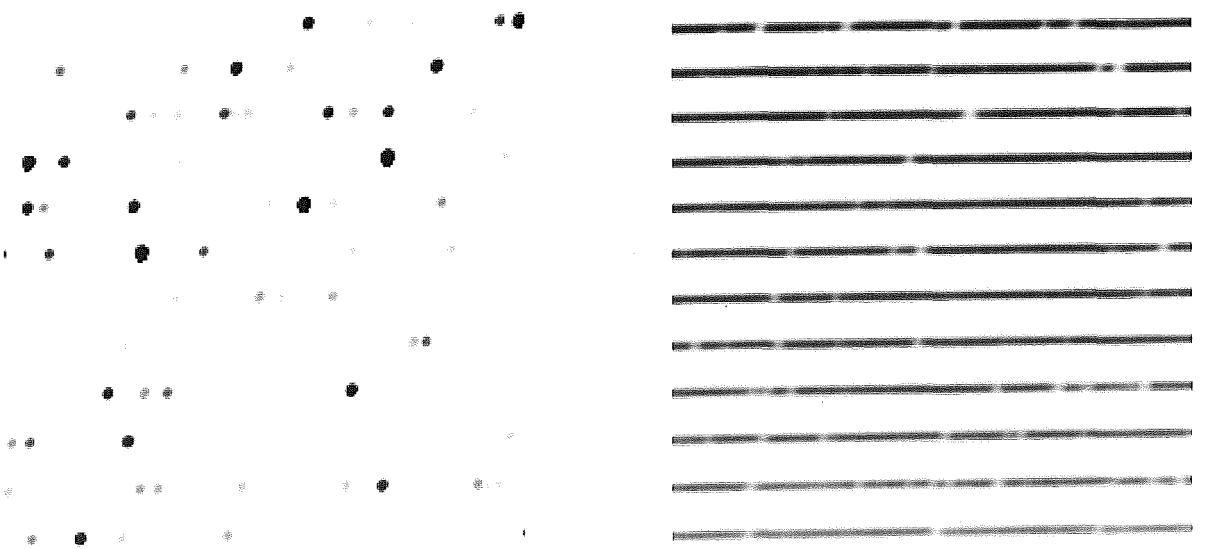

(a) A Th-Ar lamp spectrum

(b) A stellar spectrum (31 Aql, G8IV)

Figure 2.7: A small region of the HERCULES spectrum.

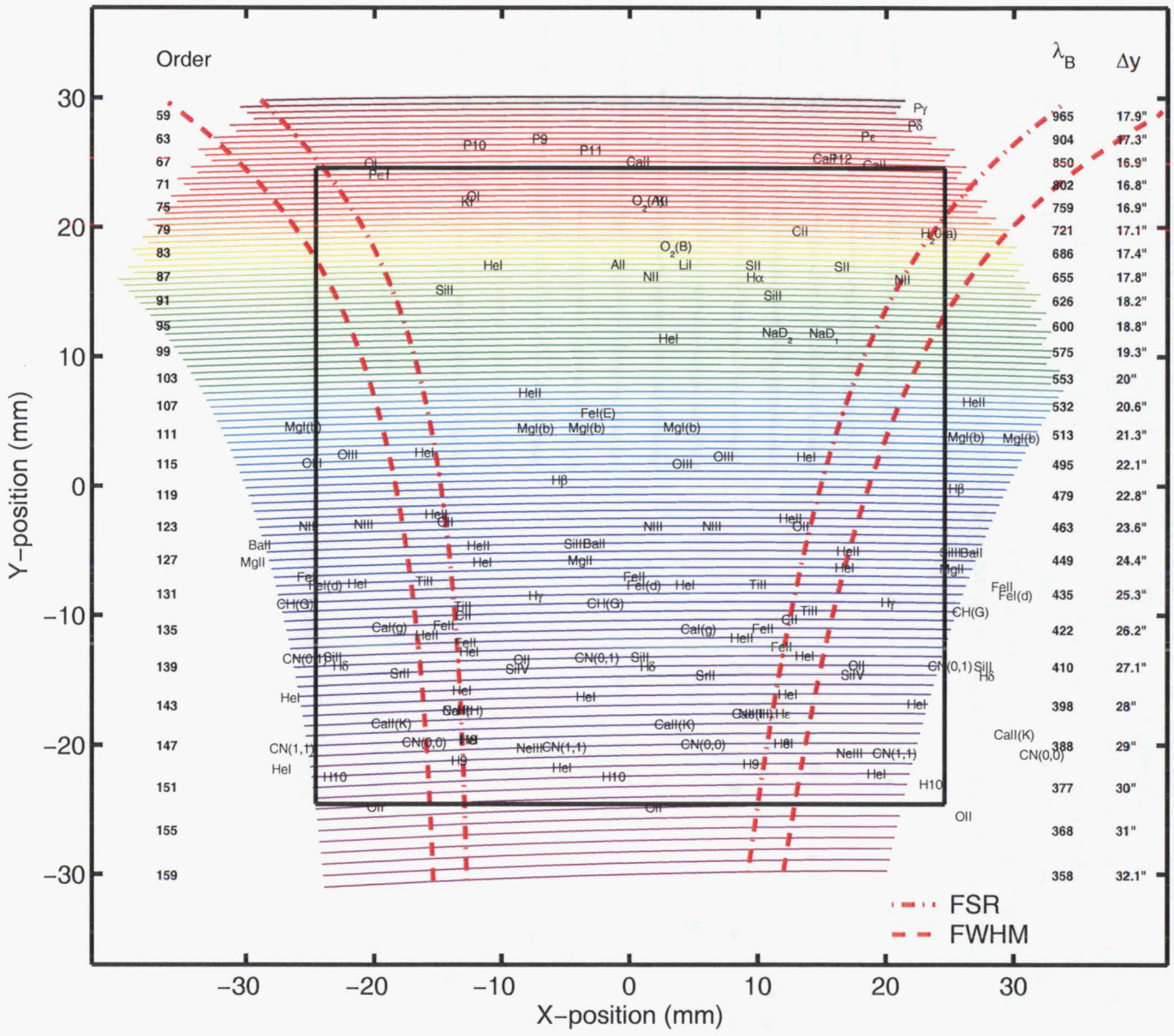

Figure 2.8: The HERCULES spectral format with a single 2k × 2k CCD with 25 μm pixels. Each order extends over two free spectral ranges (FSR) except in the far red. At these wavelengths (which are beyond the nominal design limits) the vignetting due to the hole in the fold-flat mirror and the field-flattening lens limits its spectral coverage.

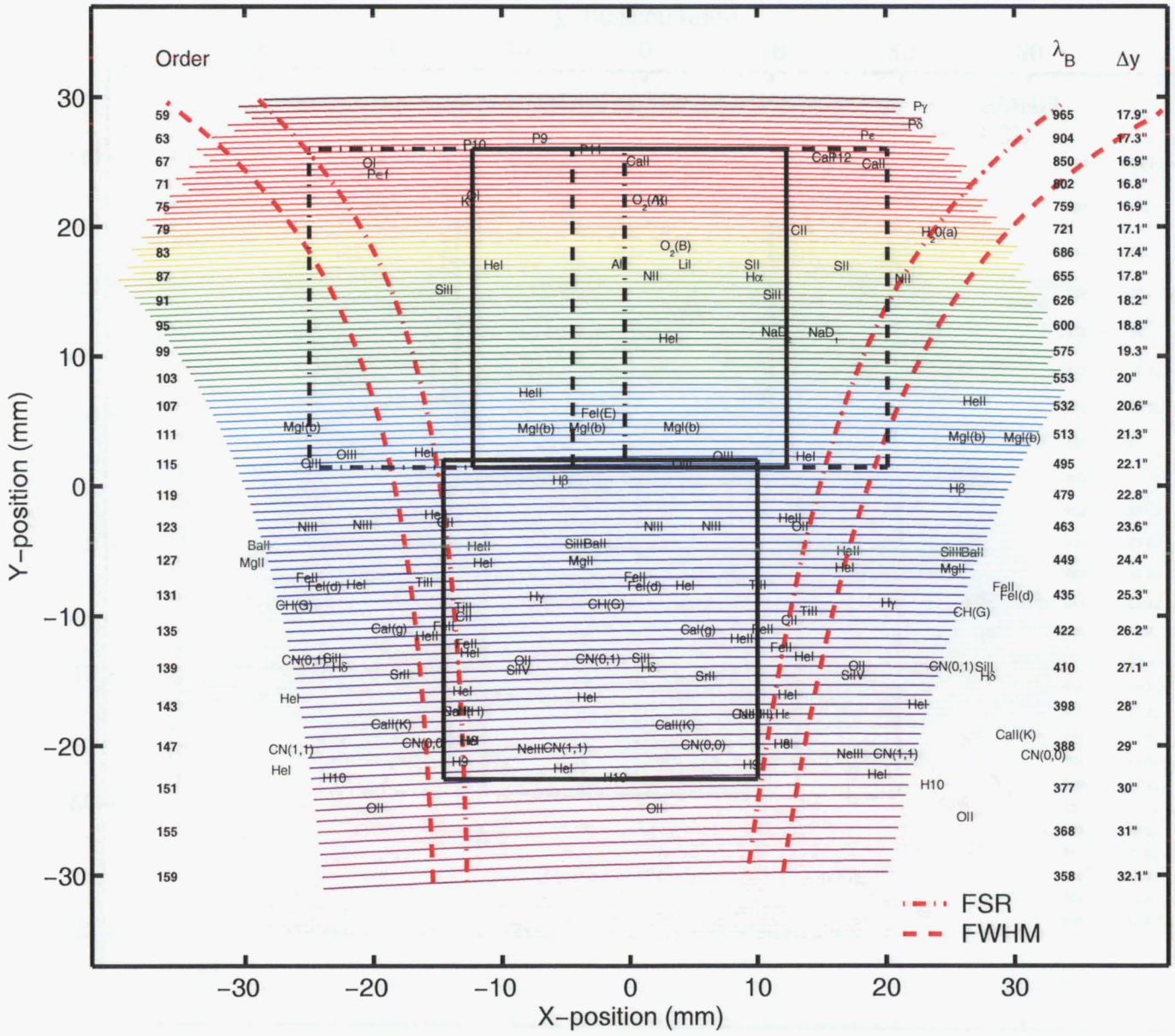

Figure 2.9: The HERCULES spectral format showing the four nominal positions of the Series 200 1k × 1k CCD with 24 μm pixels. The actual positions are shown in Figure 2.10.

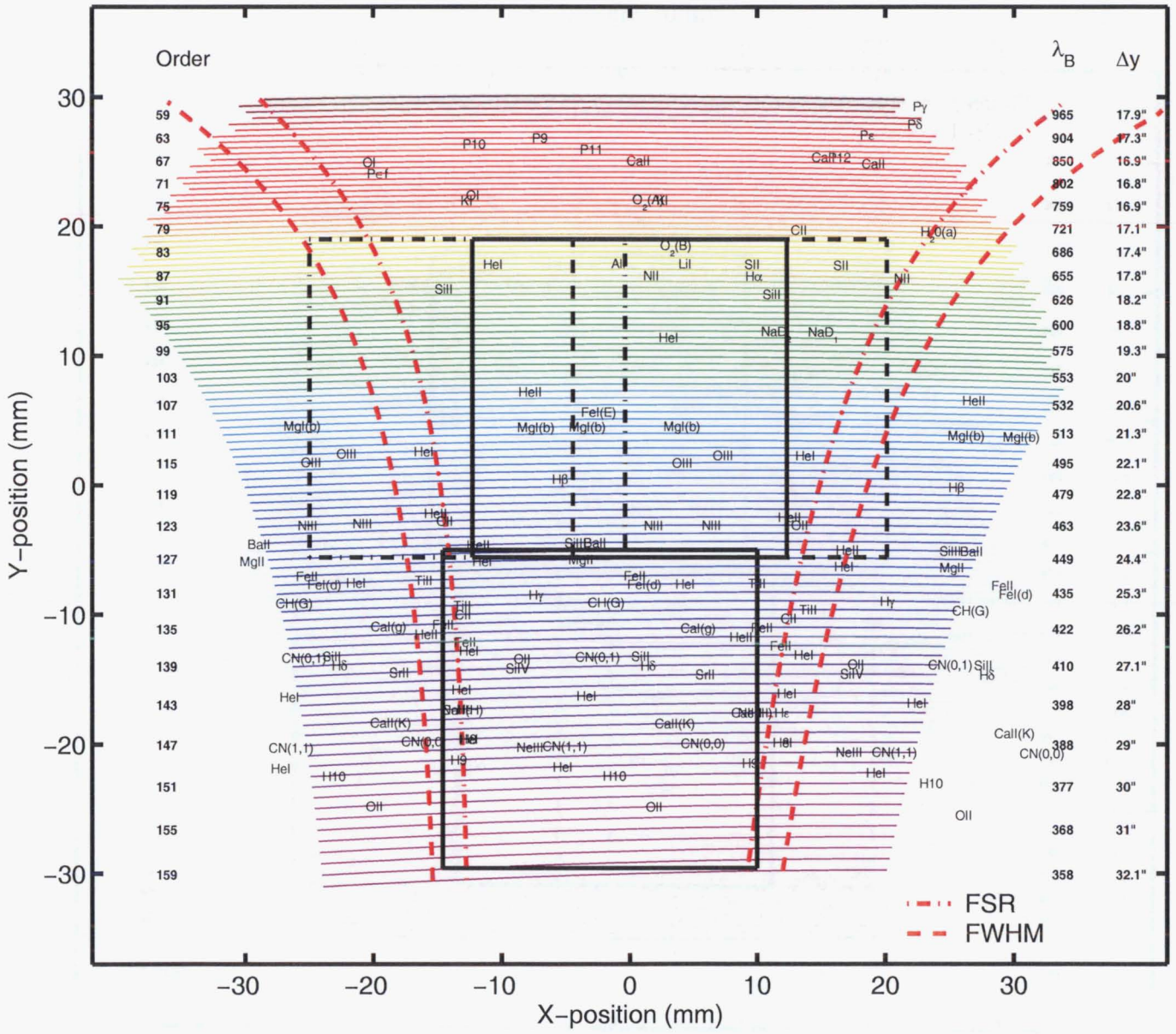

Figure 2.10: The HERCULES spectral format showing the approximate location of the four positions of the Series 200 1k × 1k CCD with 24 μm pixels.

2.1.3 Fibre feed

Fibres

The three fibres used with HERCULES are all mounted in close proximity around the focal point of the collimator. Table 2.2 gives details of the fibres available and the expected resolving powers. Fibres 1 and 2 are used as bare fibres and fibre 3 (a 100-μm core diameter fibre) has a 50-μm micro-slit on the exit face.

Fibre #	core diam. (μm)	micro-slit (μm)	R
1	100	–	41 000
2	50	–	82 000
3	100	50	70 000

Table 2.2: HERCULES fibres and resolving powers.

The fibres selected are Ceramoptec step index fibres with enhanced UV transmission (see Figure 2.11). The cladding/jacket diameters are 60/70 μm or 140/155 μm for the 50-μm fibre and 100-μm fibres respectively. Each of the three fibres was mounted inside a hypodermic needle. The 100-μm fibres were then placed inside a 150-μm needle, while the 50-μm fibre was placed inside a 200-μm needle along with several short pieces of fibre for packing. The fibres were fixed in place with an epoxy resin, and the three needles were in turn mounted inside a brass ferrule. The exit faces of these fibres were then cleaved and polished. A length of 22-m is needed to span the distance between the telescope's focal plane and the spectrograph room. All fibres were prepared by G. Kershaw.

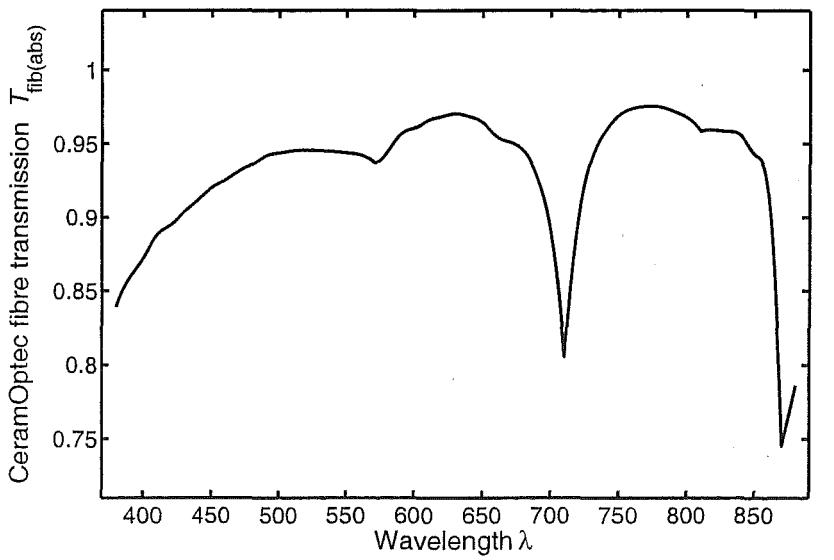

Figure 2.11: The transmission of the HERCULES fibres, $T_{\mathrm{fib(abs)}}$. The fibres are CeramOptec and have high-OH content (for enhanced UV transparency). Each fibre is 22 m long. The absorption peaks are due to OH.

Focal ratio degradation and focal reducer

The fibres listed in Table 2.3 were tested for their focal ratio degradation (FRD) properties using the apparatus which is shown schematically in Figure 2.12. All the lenses were achromatic camera lenses. The input source was a 400 μm pinhole which was illuminated with diffuse white light. The lens L_1 created a collimated beam, the diameter of which was controlled by an adjustable iris diaphragm. By this means a beam of known focal

Company	Fibre type	Core/cladding/buffer dimensions (μm)	length (m)
CeramOptec	Optran UV	050/060/070	20
CeramOptec	Optran UV	100/140/155	20
Polymicro	FH-type	055/077/220	21
Polymicro	FH-type	105/147/210	21

Table 2.3: Description of fibres tested for FRD. All the fibres are UV-enhanced high-OH fibres. The 55 and 100 μm Polymicro fibres have additional buffers which extend to 500 μm made of nylon and acrylate respectively. These fibres were kindly provided by Prof. Fred Watson of the Anglo-Australian Observatory, Siding Spring, Australia and were manufactured for the FLAIR multi-object spectrograph.

ratio can be produced at the focus of the lens L_2. That is,

$$f/D_{\rm in} = f_2/D_{\rm iris}, \tag{2.3}$$

where f_2 is the focal length of lens L_2 and $D_{\rm iris}$ is the diameter of the iris. The purpose of creating a collimated beam from the output of the fibre using the lens L_3 was to allow access to both the near-field (P_1) and far-field (P_2) positions in the emergent beam with the repositioning of a single element. In practice, this was done by mounting the lens L_4 on a micrometer translation stage, while the detector remained in a fixed location. The detector was a Lynxx CCD camera which has a 2.64 × 2.64 mm detector area with 192 × 164 pixels which are 13.75 × 16 μm in size. The relationship between the distance d from the near-field focus and the diameter of the far-field image gives the focal ratio; i.e,

$$f/D_{\rm out} = d/D_{95}, \tag{2.4}$$

where D_{95} denotes the diameter within which 95% of the flux is enclosed.

Image reduction was done using ESO-MIDAS[4]. This involved subtracting the background, centring and normalizing the image, then computing the enclosed flux as a function of image diameter. Some examples of the far-field and near-field images are shown in Figure 2.13.

The resulting focal ratio degradation curves are given in Figure 2.14. As a check on the effects of end-face preparation and on the repeatability of results, each of the fibres (except for the 55 μm Polymicro fibre) was tested using both ends as the input. No significance difference was noted. A puzzling aspect of these results is the apparently poor FRD properties of the two Polymicro fibres (especially the 55 μm fibre). These results compare badly with other published test results for similar Polymicro fibres (for example, Ramsey, 1988). However, similar results as for the 105 μm fibre were obtained by Carrasco and Parry (1994) for a Polymicro 200 μm fibre. Whether the results obtained for both Polymicro fibres are indeed consistent with the expected behaviour of these fibres is unknown – especially given the wide variation observed in the FRD behaviour of optical fibres. It is possible that the Polymicro 50 μm fibres were damaged in transit to New Zealand, although this has not been confirmed.

[4]European Southern Observatory - Munich Image Data Analysis System

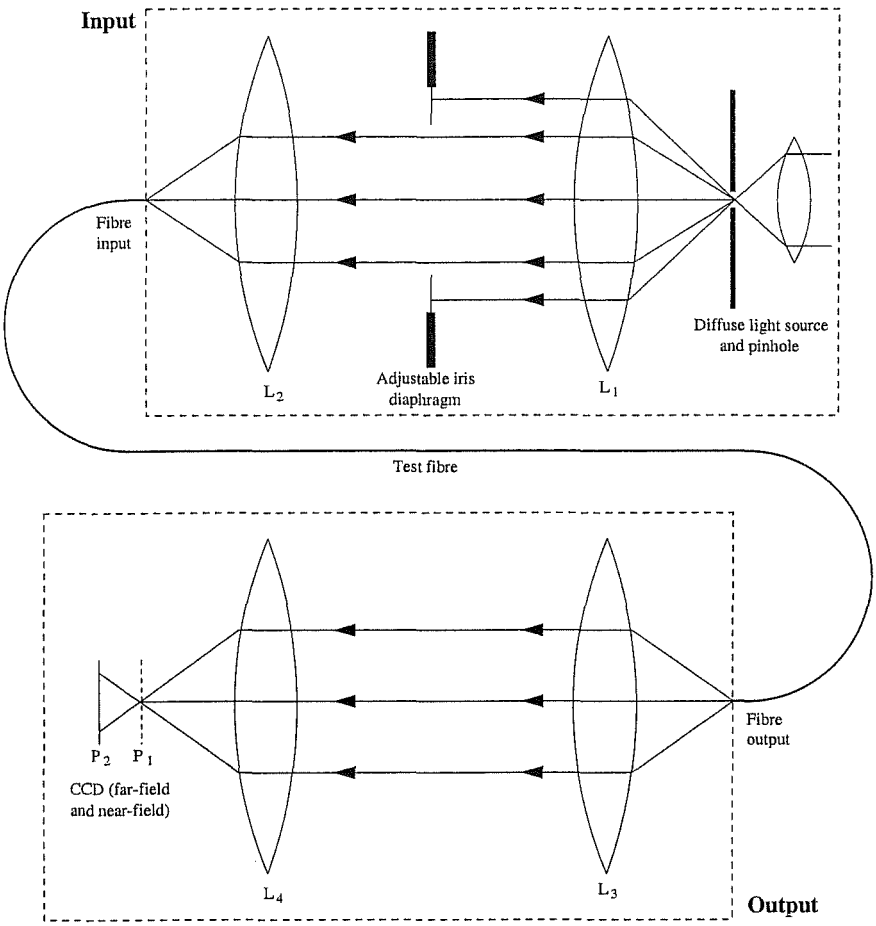

Figure 2.12: The FRD test setup.

On the basis of the above results, in order to obtain the output focal ratio of $f/3.75$ that HERCULES requires (see Section 2.1.2) the following input focal ratios are required (assuming CeramOptec or equivalent fibres are used):

$$\begin{aligned} \text{CeramOptec} \quad 100\,\mu\text{m}: \quad & f/D_{95} = f/4.6 \\ \text{CeramOptec} \quad 50\,\mu\text{m}: \quad & f/D_{95} = f/4.5, \end{aligned}$$

where in both case 95% enclosed flux is assumed. The silica micro-lens shown in Figure 2.15 is used to provide the focal conversion from the McLellan telescope $f/13.5$ beam to $f/4.5$ (or $f/6.8$ in glass). The size of the lens, which is arbitary, is a compromise between manufacturability, sensitivity to misalignment, and optical performance.

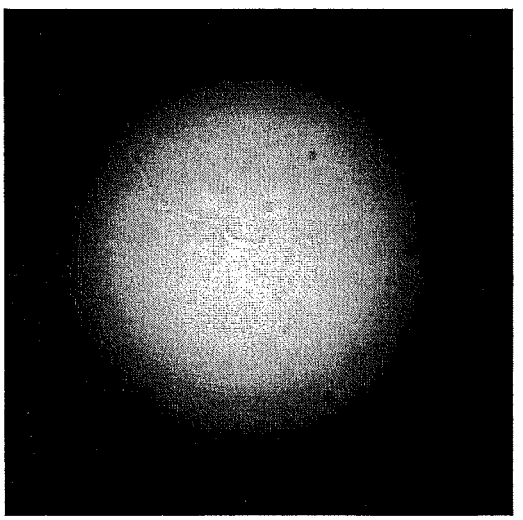

(a) Far-field image, $f/D_{\text{in}} = 2.78$

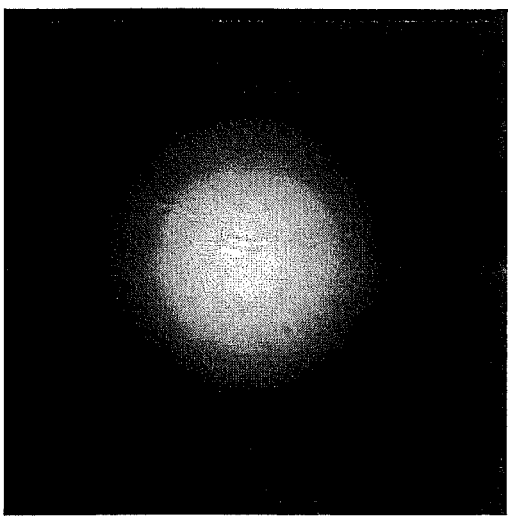

(b) Far-field image, $f/D_{\text{in}} = 4.17$

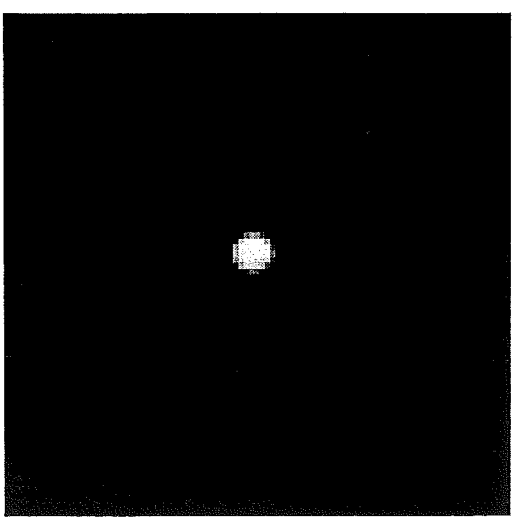

(c) Near-field image

Figure 2.13: Examples of (raw) far-field and near-field images of the fibre output (100 μm CeramOptec fibre). The far-field images (a) and (b) are taken with the CCD positioned 4.50 mm from the near-field focus and are both 2.64 mm square. Note that various blemishes and dark patches are visible in each of the images. These are due to dust on the CCD window, but have only a small effect on the measured intensities. The near-field image is of the exit face of the fibre. The size of the frame is approximately 1.3 mm square, where there is a 1.1:1 scale factor between the size of the object and its image.

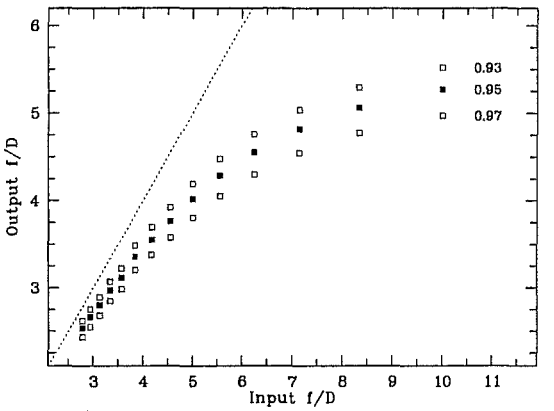

(a) CeramOptec 100 μm

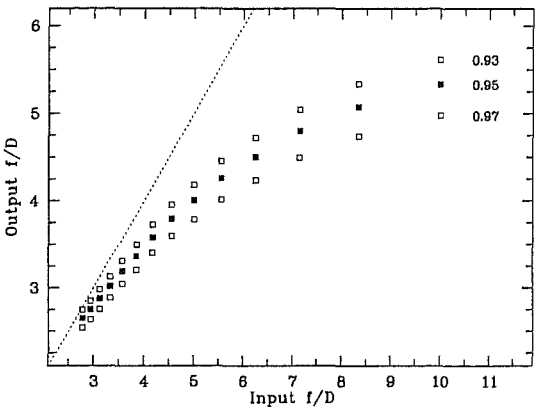

(b) CeramOptec 50 μm

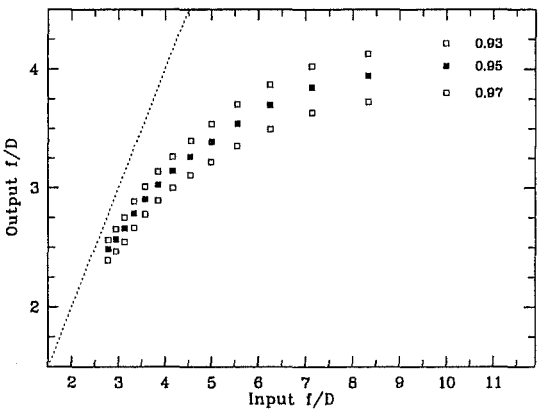

(c) Polymicro 105 μm

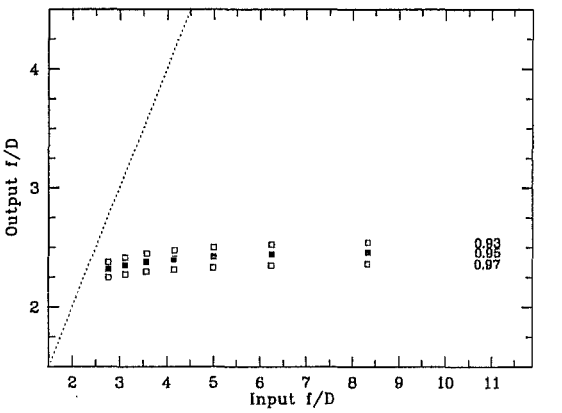

(d) Polymicro 55 μm

Figure 2.14: Measured FRD curves for four different fibres. The focal ratios have been measured at 93, 95 and 97% enclosed flux. Note the change of scale for graphs (c) and (d) and the apparently very poor performance of the 55 μm Polymicro fibre.

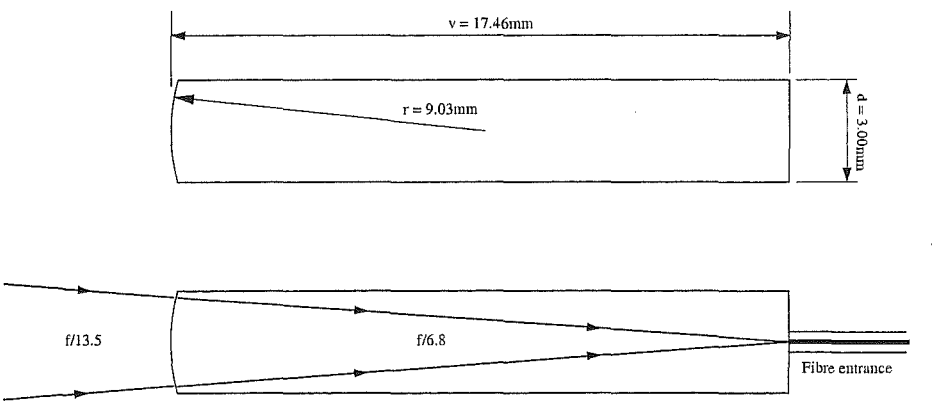

Figure 2.15: The HERCULES micro-lens.

Guide camera

An intensified CCD camera from DEP[5] is used for both acquisition and guiding. The intensifier has a useful input diameter of 18 millimeters. This is demagnified 4.5 times in order to match it with the image area (6.0 mm by 4.5 mm) of the NXA1011 CCD. Camera optics have been designed to reimage the telescope's focal plane at either $f/8.4$ or $f/21.6$ in order to provide the option of $5.3' \times 3.7'$ or $2.1' \times 1.4'$ fields of view. The optics are based on a design of G. Nankivell which was reoptimized to allow the use of off-the-shelf components. The two camera modes were intended for the "acquistion" (at $f/8.4$) or "guiding" ($f/21.6$) of an object. The object can be viewed by inserting either a fully reflective diagonal mirror or a 92/8% beam-splitter in the optical path (see Figure 2.16).

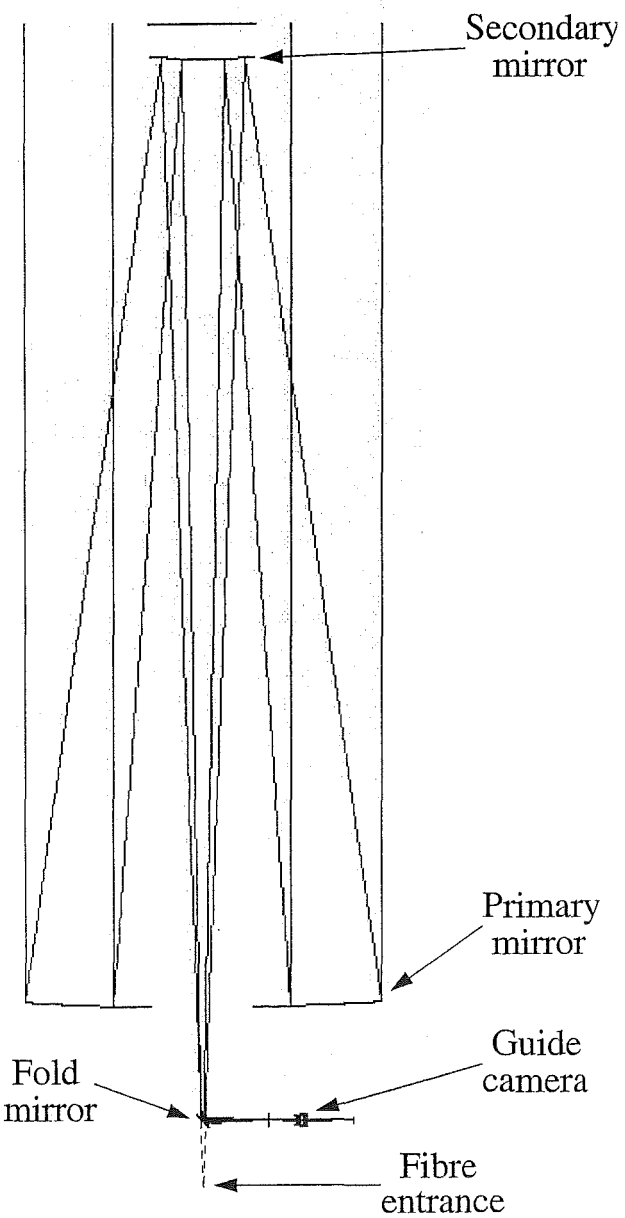

Figure 2.16: The McLellan 1 metre telescope and fibre feed guide camera.

[5]Delft Electronische Producten, Holland

The guide and acquisition modes are selected by rotating a single set of lenses about a central point (see Figure 2.17). In practice the "acquisition" mode is generally also used for guiding because the faster focal ratio mitigates to some extent the poor sensitivity of the DEP camera.

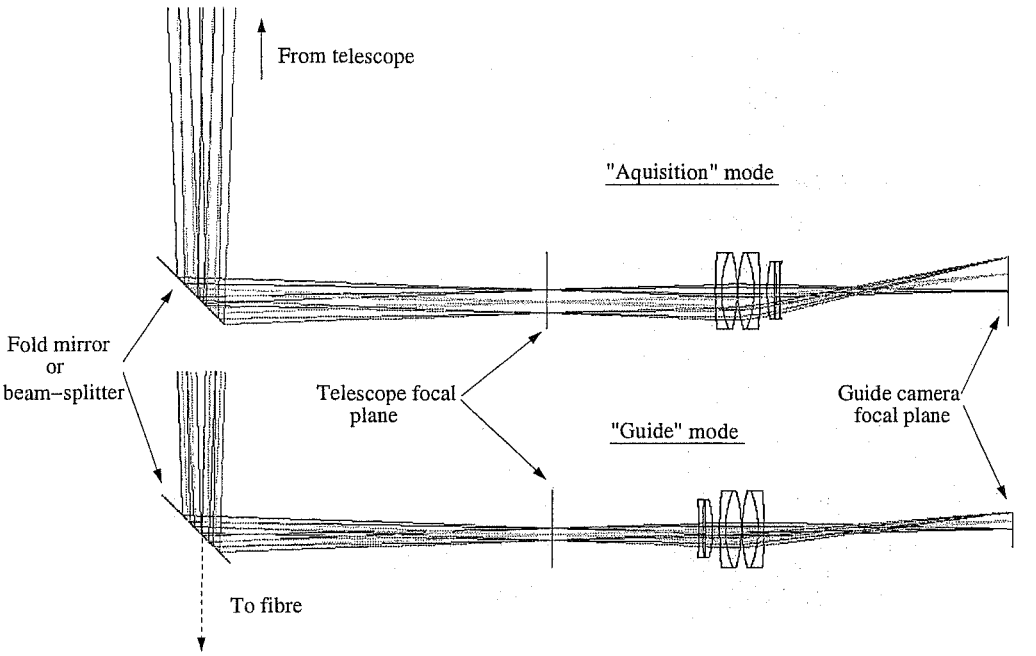

Figure 2.17: The HERCULES fibre feed guide and acquisition camera.

The calibration modes

Two calibration lamps are available; a thorium-argon hollow cathode lamp for wavelength calibration and a quartz halogen white lamp for order definition and/or flat-fielding. Simple reimaging optics have been designed for each lamp which delivers an $f/13.5$ beam to the optical axis of the fibre micro-lens. In the case of the thorium-argon lamp the cathode is used as the object whereas in the case of the white lamp a small diffuser is used instead. It is also possible to reimage the fibre entrance onto the guide camera. A set of LEDs mounted around the collimator mirror provide back illumination. This provides a means of locating the approximate position of the fibre input on the sky.

The exposure meter

Light that would otherwise be lost due to the hole in the flat mirror of the folded Schmidt camera is used by the exposure meter. A diagonal mirror and relay optics are placed immediately behind the Schmidt corrector plate which directs light to an exposure meter located outside the evacuated tank. The HERCULES exposure meter is a Thorn EMI 9924 photomultiplier tube (PMT). This type of high gain PMT has a rubidium bialkali photocathode which gives a high quantum efficiency in the blue (see Figure 2.18) although it has no response beyond 700 nm. At an operating voltage of approximately 1 kV, this photomultiplier has nominal gain of $G = 2.1 \times 10^6$.

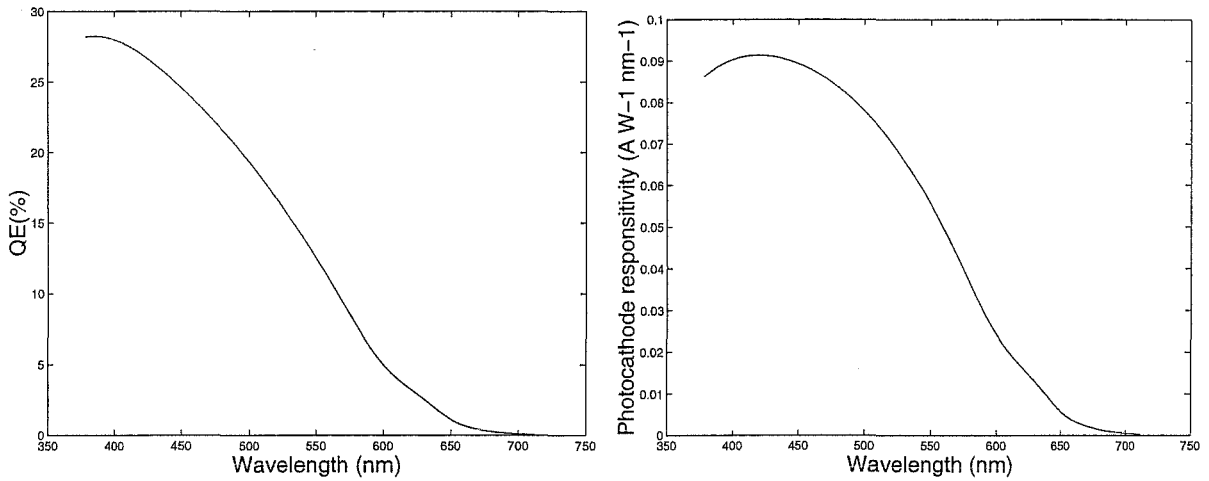

(a) Quantum efficiency

(b) Responsitivity

Figure 2.18: The spectral response of the Thorn EMI 9924 photomultiplier tube.

The exposure meter uses around 1 to 1.5% of the light exiting the fibre feed. After accounting for atmospheric transmission, telescope efficiency, telescope to spectrograph coupling efficiency and PMT responsitivity, the exposure meter photocathode current will be as shown in Figure 2.19. The integral of these curves gives the total photocathode current. The maximum and minimum photocathode currents expected are shown in Figure 2.20. This calculation shows that the photocathode current can be expected to vary anywhere from 5×10^{-11} A to 1×10^{-16} A depending on the stellar magnitude, spectral type and atmospheric seeing. Therefore, with a gain of $G = 2.1 \times 10^6$, the anode current will range from 100 mA to 0.2 nA. These values are expected to enable the exposure meter to perform adequately on stellar exposures down to $m_V = 10$ and perhaps slightly fainter in ideal conditions.

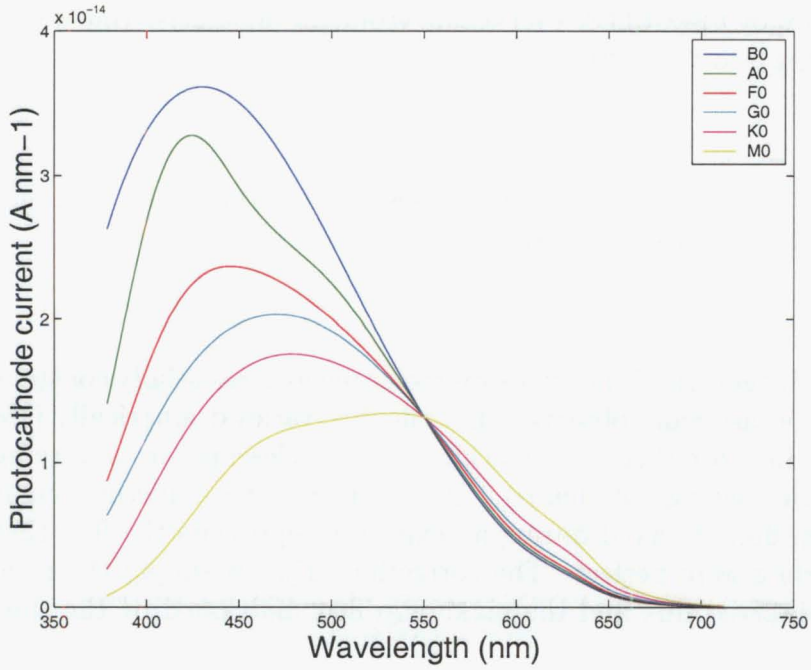

Figure 2.19: The exposure meter photocathode current as a function of wavelength for an $m_V = 0$ star.

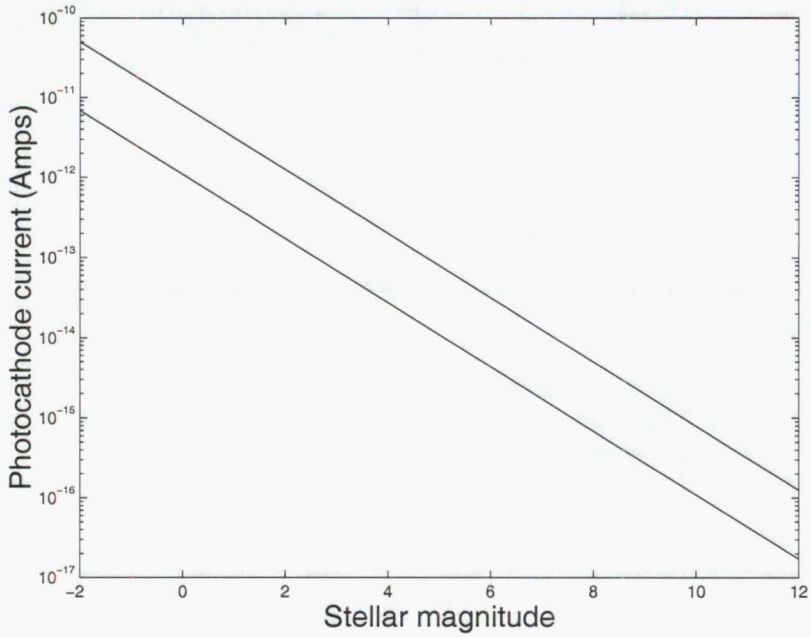

Figure 2.20: The exposure meter photocathode current as a function of stellar magnitude. The upper line is for an B0 star while the lower line is for an M0 star.

2.2 Performance

2.2.1 Efficiency predictions

When computing the efficiency of HERCULES, everything from the fibre feed (including the effects of seeing and guiding), to the CCD detector will be considered.

Fibre feed and collimator

Apart from the fibre itself, the fibre feed also includes the losses due to the finite size, and perhaps variable location, of the stellar seeing disk.

Guiding

Although the guiding is generally good and the exposure meter records essentially constant flux during an exposure, it is occasionally observed that the flux varies dramatically (see Figure 2.21). This could be due to either poor tracking of the telescope or to varying seeing conditions (including the passage of clouds). To correct for these fluctuations it is assumed that the maximum flux observed during an exposure represents the flux that would be observed if the guiding were perfect. The correction ($T_{\rm gui}$) is simply the ratio between the integral of the observed flux and the maximum flux multiplied by the time of the exposure. That is,

$$T_{\rm gui} = \frac{\int_0^{t_{\rm exp}} f(t)dt}{\max(f(t))t_{\rm exp}} \quad , \tag{2.5}$$

where $f(t)$ is the exposure meter flux and $t_{\rm exp}$ is the length of the exposure.

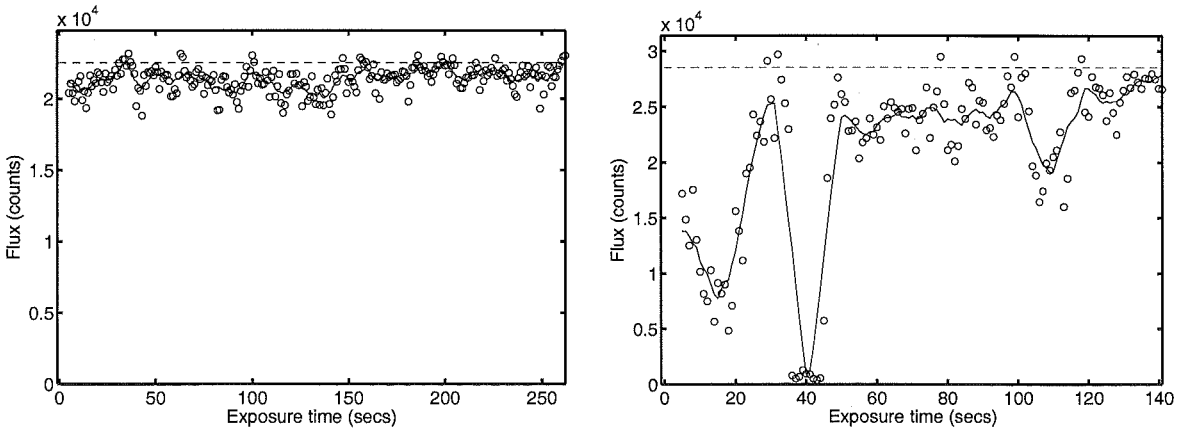

Figure 2.21: Examples of exposure meter log files. On the left is a typical log file where the star was keep well centred throughout an exposure. The example on the right might have been taken during the passage of light to heavy cloud or the variation could be due to extremely poor guiding.

Seeing

The seeing disk of a star is assumed to be of the same form as that described by Moffat (1969) to model the point spread function (PSF) of a star. Figure 2.22 shows the throughput of the three HERCULES fibres in various seeing conditions.

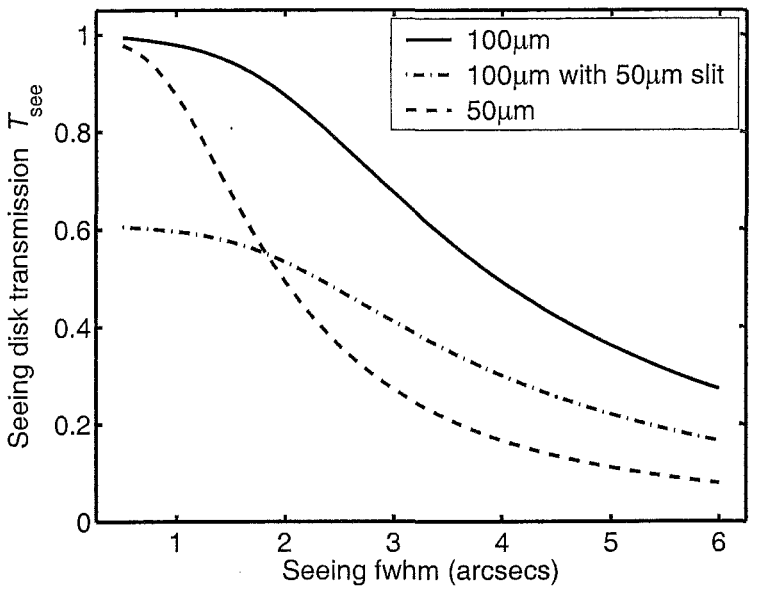

Figure 2.22: The transmission of the seeing disk through the HERCULES fibres. The entrance of the 100 μm fibres is 4.50″ and the entrance of the 50 μm fibre is 2.25″. One of the 100 μm fibres has a 50 μm slit on the exit face. It is apparent that the 100 μm fibre with micro-slit has superior throughput to that of the 50 μm fibre only when the seeing is worse than 1.8″. If the seeing is better than this then the 50 μm fibre will allow substantially more light through to the spectrograph for high-resolution observations.

Focal reducer

A (micro-)lens made from BK7 glass is used as a focal reducer. The front surface of the lens has an extremely efficient multilayer anti-reflection coating applied by Fisba Optik (see Figure 2.23), and the rear surface has been cemented directly to the fibre entrance with an index matched cement. A coupling efficiency of 99% is assumed. The average overall transmission of the focal reducer is therefore greater than 98%.

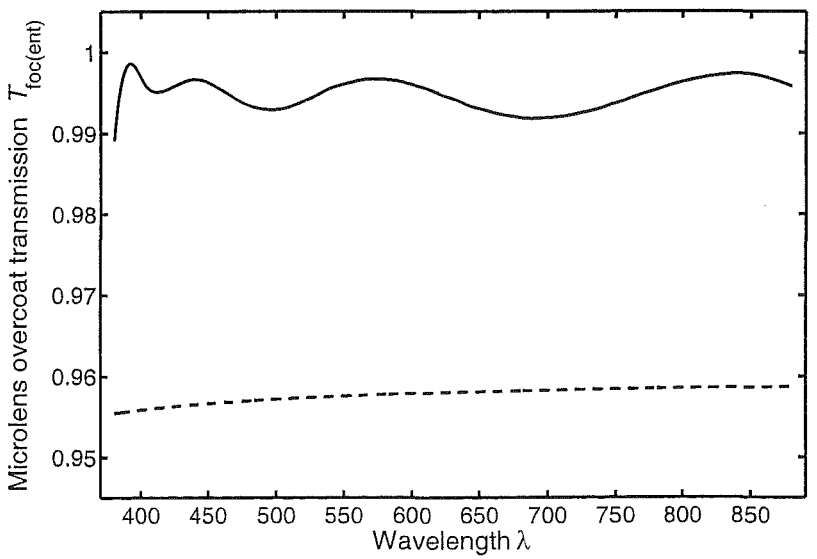

Figure 2.23: The transmission of the single layer MgF_2 coating applied by Fisba Optik on the microlens. For comparison the Fresnel reflection losses for the uncoated surface are also shown (dashed line).

Fibres

The fibres used in HERCULES are Ceramoptec step index fibres, with high OH content for enhanced ultra-violet transmission (see Section 2.1.3). Each fibre has a length of 22 m which has an absorption shown in Figure 2.11. The transmission through the fibre output glass/air interface can be calculated using the Fresnel laws of reflection. The total transmission of the HERCULES fibre is shown in Figure 2.24.

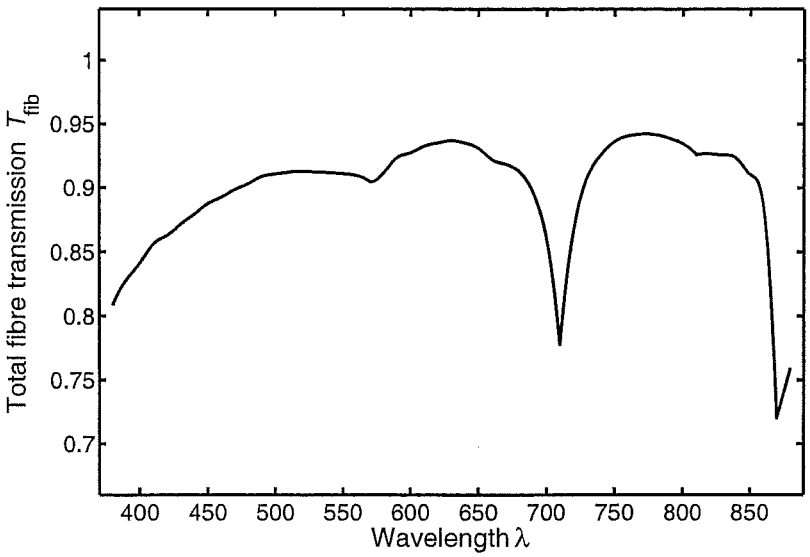

Figure 2.24: The total transmission of the HERCULES fibre. The mean transmission of the fibre is 90% and the maximum is 94% at $\lambda = 770\,\text{nm}$.

Collimator

The focal ratio of the collimator was chosen so that 95% of the beam emerging from the fibre is captured. The mirror was coated with UV-enhanced overcoated silver by Laserdyne[6] (see Figure 2.25). The obstruction of the fibre-feed assembly has been estimated at approximately 1%.

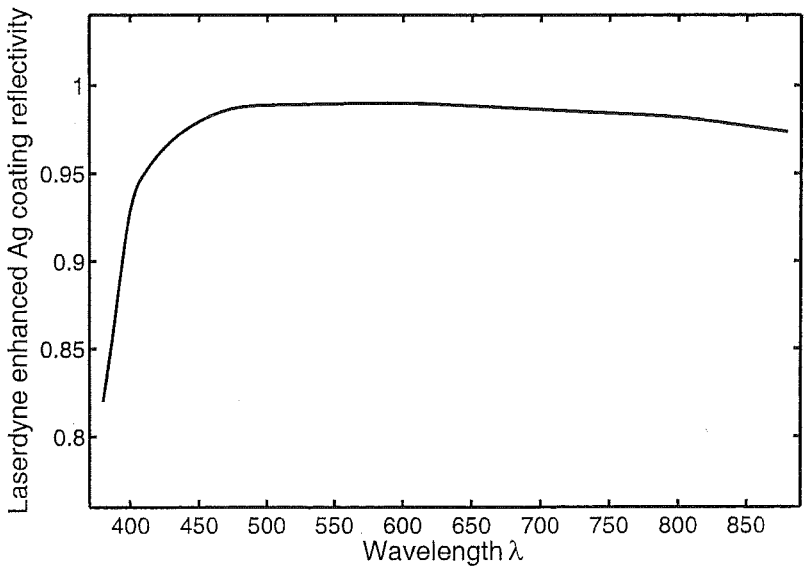

Figure 2.25: The reflectivity of Laserdyne's UV-enhanced silver mirror coating.

[6]Laserdyne Pty Ltd, Queensland, Australia.

Fibre feed and collimator summary

The total throughput of the fibre feed and collimator can now be calculated. This is shown in Figure 2.26.

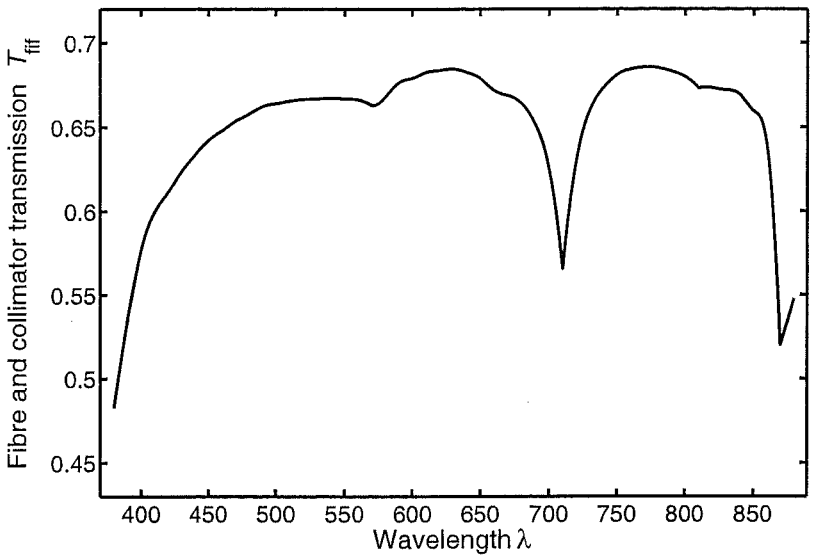

Figure 2.26: The total throughput of the HERCULES fibre feed and collimator. The calculations assume good guiding and median (2.5″) seeing.

Echelle grating and prism

Echelle grating

The $B = 210\,\text{mm}$ collimated beam forms an elliptical footprint on the échelle grating which has a major axis of $B/\cos\alpha = 545\,\text{mm}$. This extends beyond the length of the grating (408 mm) giving an overfilling in this direction of 14.5%. The grating is also overfilled across its width (204 mm) by 0.6%. Also, because of the dispersion by the first pass through the prism, the elliptical footprint is not always centred on the échelle grating. However this effect is small and can be ignored. The échelle grating and elliptical footprint are shown in Figure 2.27. The total échelle overfilling is 15.1%.

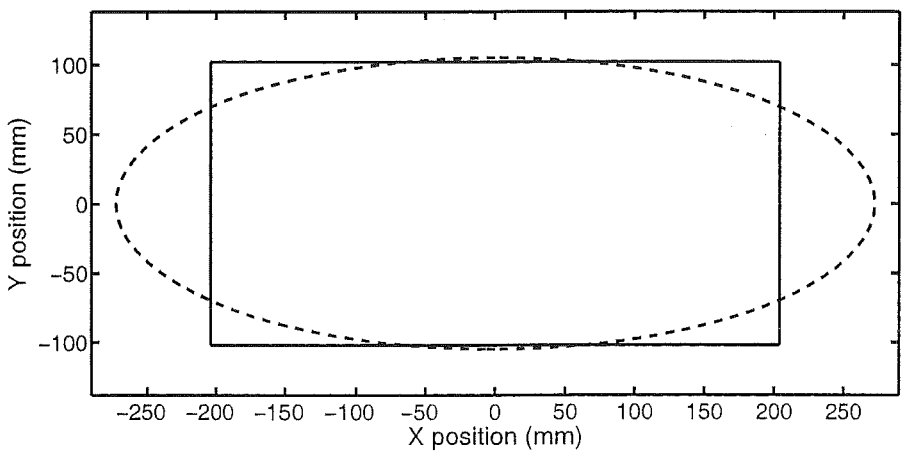

Figure 2.27: The overfilling of the HERCULES échelle grating. The collimated beam forms an elliptical footprint on the échelle grating which has a major axis of 545 mm. The overfilled portion of the beam is 15.1% of the total beam's area.

The diffractive efficency of the HERCULES échelle grating has been calculated using the method outlined in Section 1.2.11. The energy distribution across one order is shown in Figure 2.28. It can be seen that the peak theoretical efficiency at the blaze wavelength for this order is 80.8%.

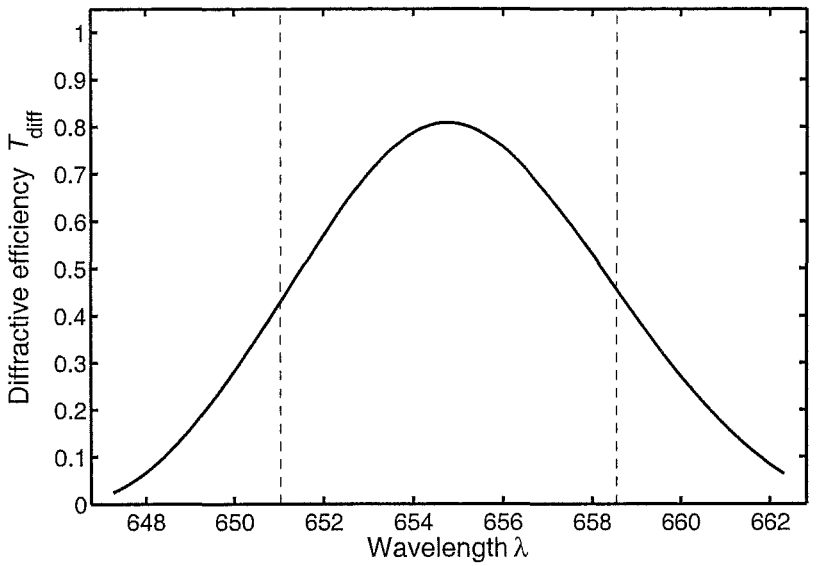

Figure 2.28: The diffractive efficiency of the HERCULES échelle grating. The blaze function is plotted for a single order $m = 87$, centred on the blaze wavelength $\lambda_B = 654.8\,\text{nm}$. The free spectral range for this order spans the wavelengths within the dashed lines. The efficiency at the blaze peak is 80.8%. Compare this figure with Figure 1.22, with $\cos\beta/\cos\alpha = 1.24$.

The reflective coating applied to the échelle grating is standard aluminium. The combination of the reflectivity of aluminium, the overfilling by the incident beam, and the diffractive efficiency gives the échelle efficiency. This is shown in Figure 2.29.

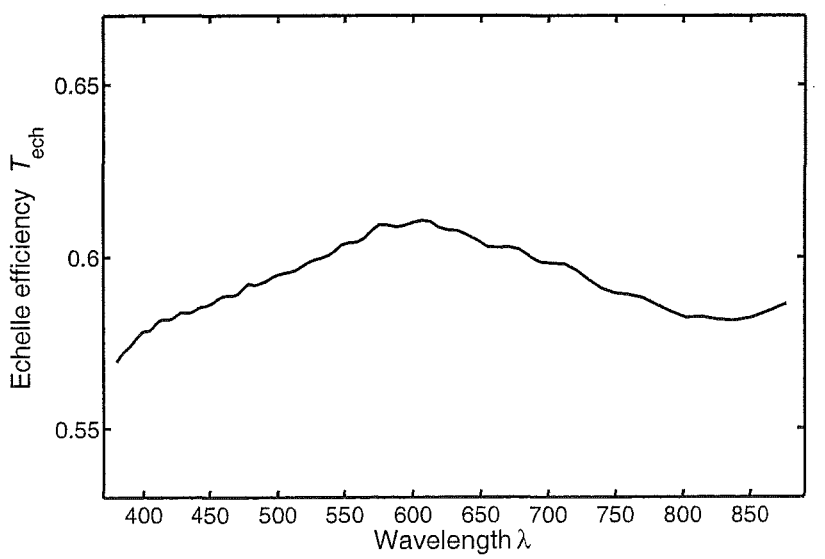

Figure 2.29: The efficiency at the blaze centre of the HERCULES échelle grating. The broad variation in efficiency as a function of wavelength is due primarily to the reflectivity of aluminium. The high frequency variation is the result of numerical errors.

Prisms

Both refractive surfaces of the prism have been anti-reflection coated with a single layer of MgF_2. The layers are optimized for an angle of incidence of $\theta_i = 40.0°$ (see Figure 2.30), although the incident angles deviate slightly from this after several refractions. The mean path length through the prism (in one direction) is 128 mm. The total throughput of the double-pass prism is shown in Figure 2.31.

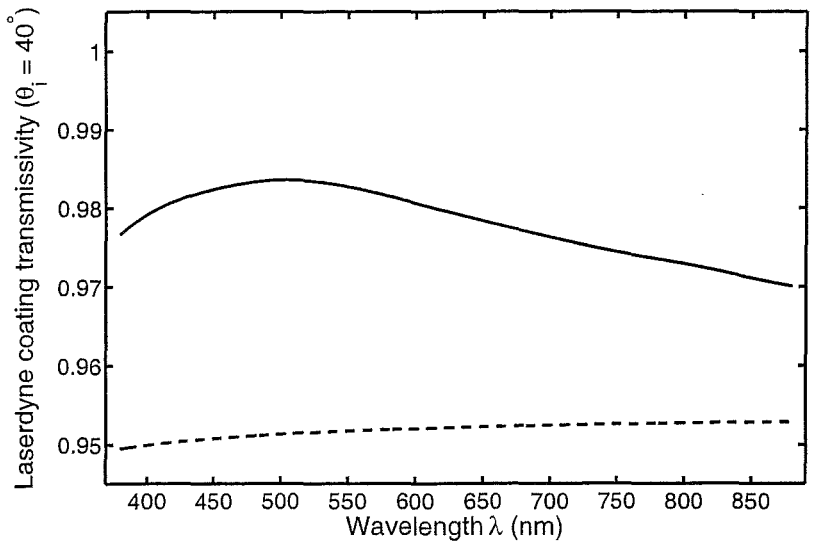

Figure 2.30: The transmission of the anti-reflection coating applied by Laserdyne to the prism. The coating has been optimized for an angle of incidence $\theta_i = 40°$.

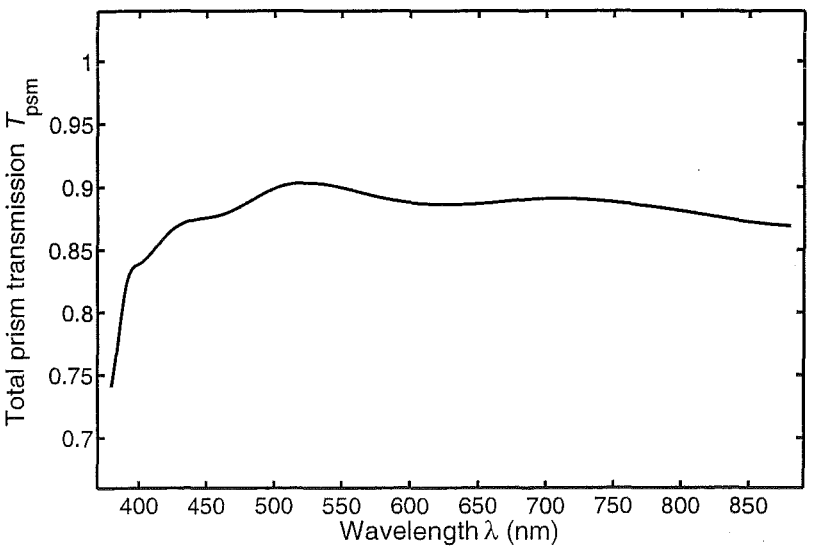

Figure 2.31: The total efficiency of the HERCULES prism. The absorption from two passes through the prism and the reflection losses from four air-glass interfaces have been included.

Echelle grating and prism summary

The combined efficiency of the HERCULES prisms and échelle grating is shown in Figure 2.32.

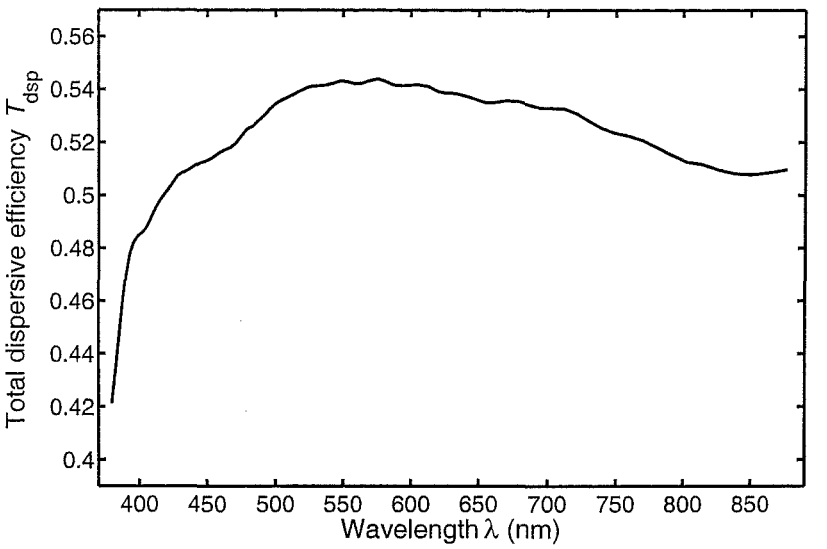

Figure 2.32: The total efficiency of the HERCULES dispersive elements.

Camera

The HERCULES camera is a folded Schmidt camera (see Section 2.1.2). Both the fold mirror and the primary mirror have been coated with Laserdyne's UV-enhanced overcoated silver (identical to that applied to the collimator; see Figure 2.25). The corrector and field-flattening lenses both have single layer MgF_2 anti-reflection coatings. The coating was applied by Laserdyne, and the transmission is shown in Figure 2.33. The thickness of the corrector plate is 15.0 mm and the mean ray path length through the field-flattening lens is 10.5 mm.

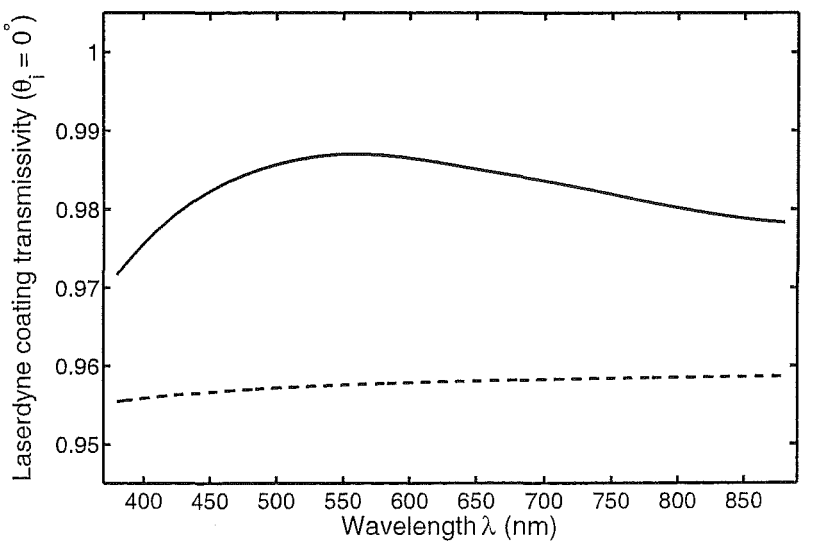

Figure 2.33: The transmission of the Laserdyne single layer MgF_2 anti-reflection overcoat. The dashed line shows the Fresnel losses of an uncoated surface.

The main source of vignetting in the HERCULES camera is the hole in the fold mirror through which the rays from the primary mirror are focused (see Figure 2.5). Due to the fact that the fold mirror is not at the entrance pupil of the camera the amount of vignetting is field-dependent, where the field angle is a function of order number and wavelength (i.e, the échelle and cross-dispersion). The effect of beam anamorphism (due to the échelle and prism dispersion) and the variable path length through the prism complicate the exact camera vignetting. Both of these effects are readily calculable and the results are shown in Figures 2.34 and 2.35.

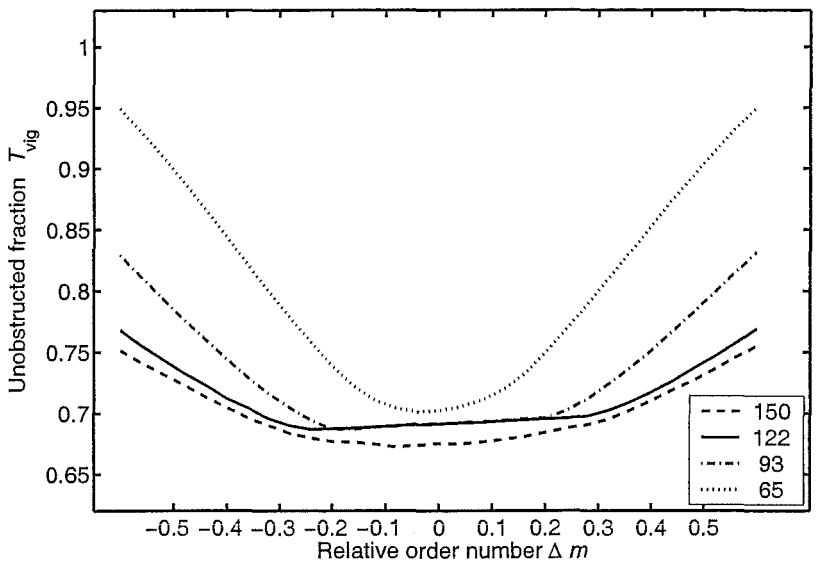

Figure 2.34: The HERCULES camera vignetting function across an order. The orders shown are centred on blaze wavelengths λ_B = 380, 490, 610, and 880 nm. These are orders m = 150, 122, 93, and 65 respectively.

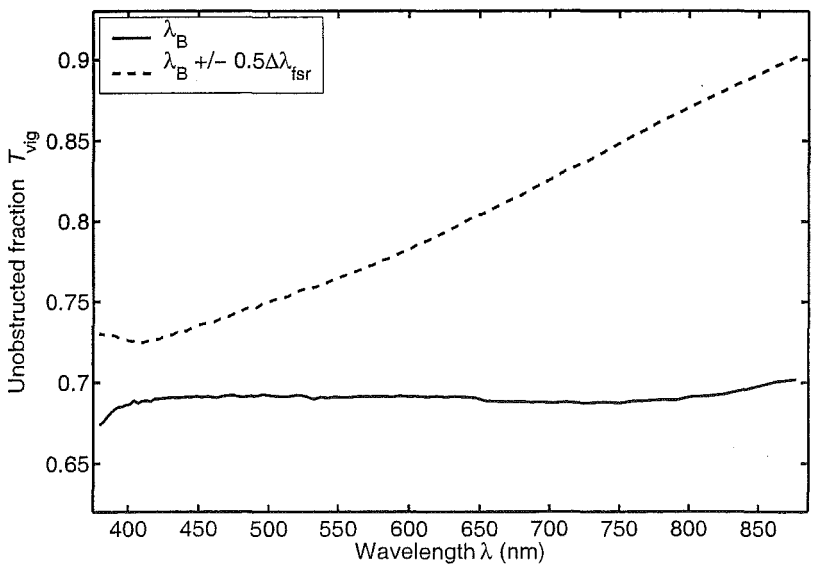

Figure 2.35: The HERCULES camera vignetting function at all wavelengths. The unvignetted fraction has been calculated for the blaze wavelength and for $\lambda = \lambda_B \pm \Delta\lambda_{fsr}/2$.

From Figure 2.34 it can be seen that for a majority of wavelengths that lie within one half of a free spectral range of the blaze wavelength, the vignetting is approximately constant. This is also shown in Figure 2.35. This is because the dispersed beam at these wavelengths invariably covers most of the obstruction. The slight decrease in obstruction across the central part of an order is due to anamorphic magnification, which changes the relative size of the obstruction. At high dispersion angles the beam becomes displaced from the obstruction and the unvignetted fraction of rays increases rapidly. This compensates to some extent the decreased blaze efficiency of these wavelengths. The total

efficiency of the HERCULES camera is shown in Figure 2.36.

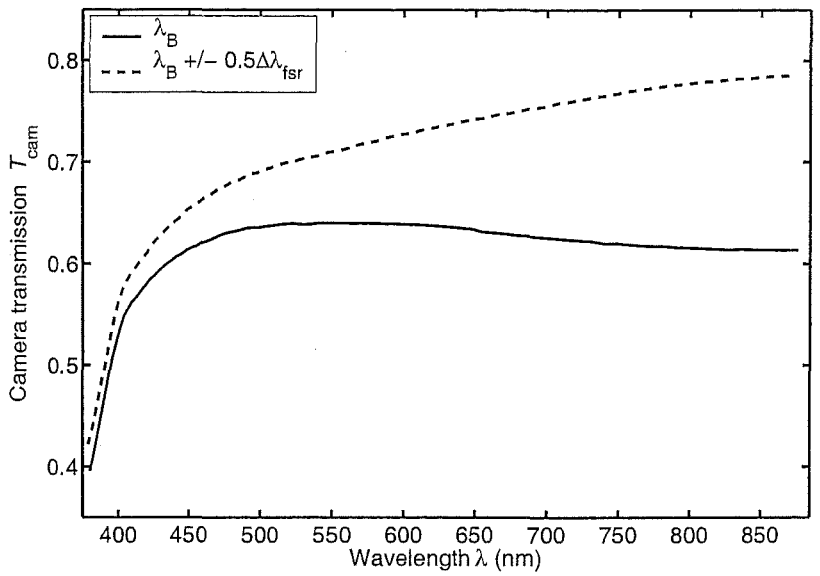

Figure 2.36: The total efficiency of the HERCULES camera. The efficiency at $\lambda = \lambda_B \pm \Delta\lambda_{fsr}/2$ is also shown.

CCD

The quantum efficiency (T_{QE}) of the SITe SI003AB CCD for the HERCULES Series 200 detector is shown in Figure 2.37. When calculating the total efficiency of the CCD the absorption by an overcoated thin silica window must also be considered.

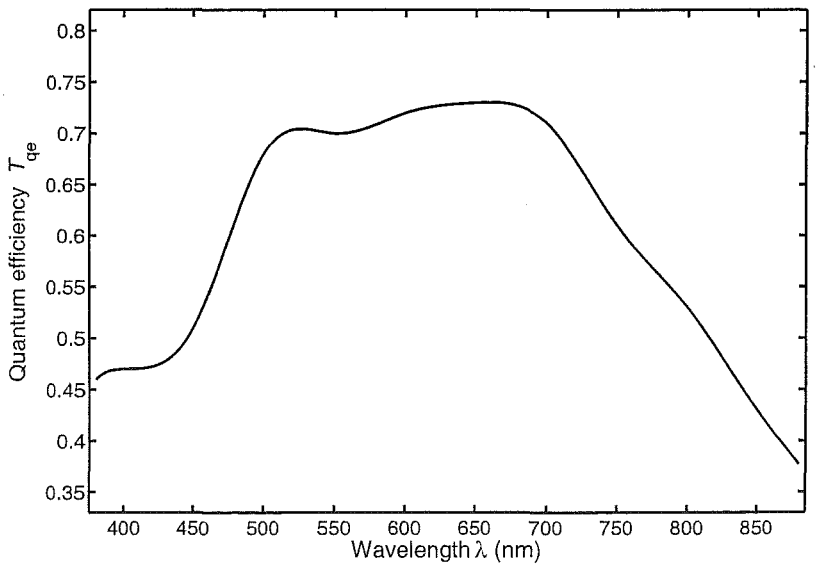

Figure 2.37: The quantum efficiency of the SITe SI003AB CCD. The detector has been overcoated for enhanced UV transparency.

Spectrograph summary

The total efficiency of HERCULES (T_{spc}), which includes everything from the transmission of the stellar seeing disk through the fibre input to the quantum efficiency of the CCD, is shown in Figure 2.38. The maximum efficiency in 1″ seeing is predicted to be just over 20% at a blaze wavelength near $\lambda = 650\,\text{nm}$. In median seeing conditions (around 2.5″)

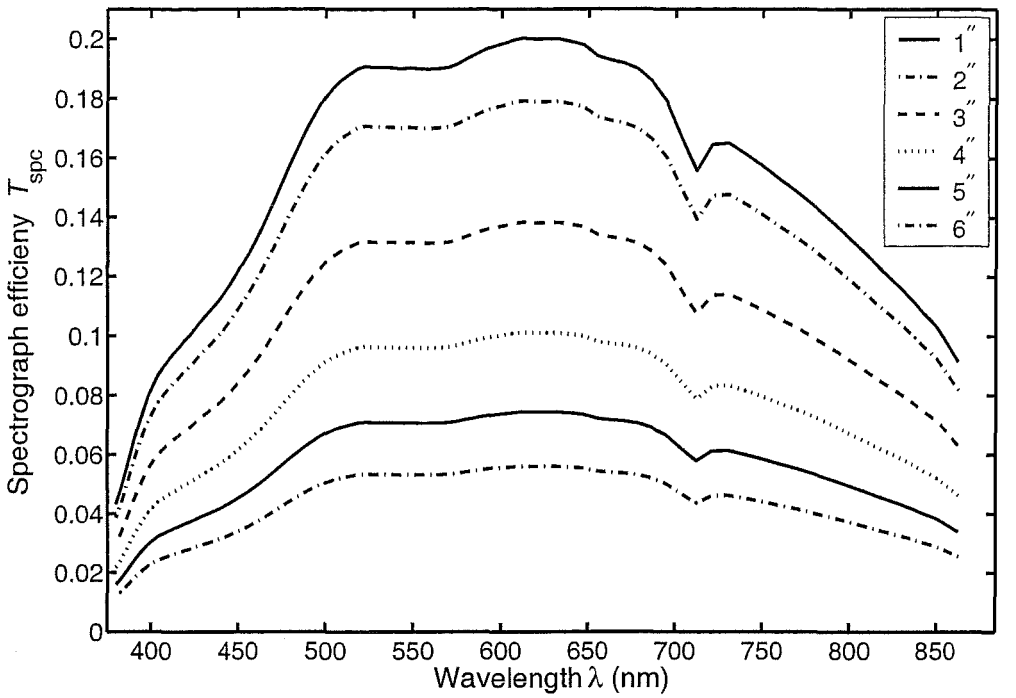

Figure 2.38: The total efficiency of the HERCULES spectrograph, including the fibre-feed and the quantum efficiency of the ccd. A 100 μm fibre is assumed and the throughput has been calculated for a range of seeing conditions.

the spectrograph throughput is expected to be approximately 12%. These efficiencies compare well with other fibre-fed spectrographs, a few of which will be discussed below.

The predicted throughput of HERCULES is slightly lower than the FEROS fibre-fed spectrograph. The system efficiency of FEROS is predicted to be 17% (including the telescope) (Kaufer et al., 1999) at a resolving power of $R = 48\,000$. Recently, this spectrograph, had a measured efficiency of approximately 19.5% when coupled to the 2.2 m MPG/ESO telescope[7]. The HERCULES efficiency is comparable with the HARPS instrument on the La Silla 3.6 m telescope. Including slit losses, and CCD quantum efficiency, the peak instrument efficiency of HARPS is 8.5% for a resolving power of $R \approx 100,000$ (Mayor et al., 2003). HERCULES is expected to have somewhat better performance than FOCES for the 2.2 m or 3.5 m Calar Alto Observatory telescopes. At a resolving power of $R = 40\,000$ this instrument was expected to have a throughput of 13% (from the fibre input to the CCD) in the best seeing conditions (Pfeiffer et al., 1998). The efficiency of ELODIE on the Observatoire de Haute-Provence 1.93 m telescope is less than HERCULES. At a resolving power of $R = 42\,000$ the throughput of the spectrograph is 4.2% (neglecting seeing losses and CCD quantum efficiency) (Baranne et al., 1996). The Hale 5-m telescope fibre-fed échelle had a detective-quantum-efficiency of 1.5% at $R = 40\,000$ (Libbrecht and Peri, 1995). The early performance of AFOE was significantly worse. This fibre-fed spectrograph was coupled to the F. L. Whipple 1.5 m Tillinghast telescope, and had a measured efficiency of 0.2% (Brown et al., 1994) for a resolving power of $R = 51\,000$. This instrument was seriously degraded by poor fibre coupling and low CCD quantum efficiency and it is expected that the performance has since improved considerably.

[7] http://www.ls.eso.org/lasilla/sciops/2p2/E2p2M/FEROS/TechnicalReports/SN/index.html

2.2.2 Signal to noise predictions

The prediction of the signal-to-noise ratio (S/N) requires that the following quantities are known:

N = number of photons per second per resolution element from object,
$N_{\rm D}$ = number of photons per second per resolution element from dark current,
$N_{\rm B}$ = number of photons per second per resolution element from sky,
$R_{\rm e}$ = rms readout noise per pixel,
$n_{\rm slt}$ = number of pixels per resolution element
t = exposure time.

That is, the signal to noise ratio can be defined as:

$$S/N = \frac{\text{Signal}}{\text{Noise}} = \frac{Nt}{\sqrt{(N + N_{\rm D} + N_{\rm B})t + \sqrt{n_{\rm slt}}R_{\rm e}}} \quad . \tag{2.6}$$

It must be noted that this is the definition for a single resolution element. However, other definitions may be used (e.g. per *extracted* pixel) in which case $n_{\rm slt}$ must also change. The photon flux N can be calculated directly from a known spectrophotometric standard assuming that the spectrograph's detective quantum efficiency $T_{\rm dqe}$ is known. Given that

$$T_{\rm dqe} = T_{\rm atm}T_{\rm tel}T_{\rm spc} \quad , \tag{2.7}$$

where $T_{\rm atm}$, $T_{\rm tel}$ and $T_{\rm spc}$ are the atmosphere transmission, telescope and spectrograph efficiencies respectively, it remains to calculate the atmospheric extinction and telescope efficiency.

Atmospheric extinction and telescope efficiency

The transmission of the local atmosphere can be computed from the extinction coefficient k. That is,

$$T_{\rm atm} = e^{\frac{-k}{1.086}X} \quad , \tag{2.8}$$

where X is the airmass of the object being observed. The following measurements of the atmospheric extinction at MJUO were made by A. Gilmore on 2001 August 8:

$$\begin{aligned} k(\mathrm{V}) &= 0.124 \\ k(\mathrm{B}-\mathrm{V}) &= 0.099 \\ k(\mathrm{U}-\mathrm{B}) &= 0.260 \\ k(\mathrm{V}-\mathrm{R}) &= 0.033 \\ k(\mathrm{V}-\mathrm{I}) &= 0.065 \quad . \end{aligned}$$

These have been used to compute the atmospheric extinction shown in Figure 2.39.

The mirrors of the McLellan telescope are both coated with standard aluminium. The secondary mirror obstructs 8% of the on-axis rays and therefore $T_{\rm tel(vig)} = 0.91$. The total transmission of the McLellan telescope is predicted to average around 68% across the wavelengths used by HERCULES.

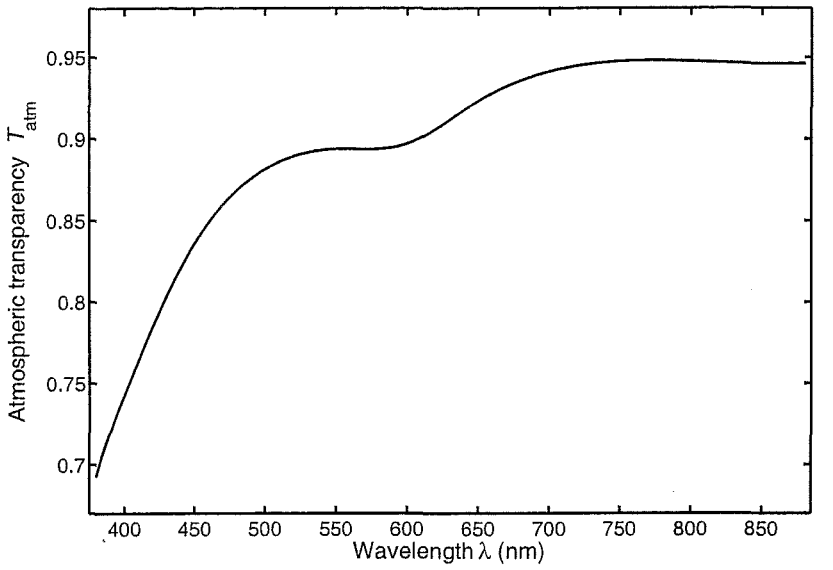

Figure 2.39: Atmospheric extinction over MJUO for an airmass of $X = 1$.

Exposure times

It is also possible to compute the exposure time required to reach a given S/N. The following is a simple Poisson based method for doing this. First we make the following definitions:

$$\begin{aligned} R_{\mathrm{S/N}} &= S/N \quad , \\ N_{\mathrm{T}} &= N + N_{\mathrm{D}} + N_{\mathrm{B}} \quad . \end{aligned}$$

Hence we have

$$R_{\mathrm{S/N}} = \frac{Nt}{\sqrt{N_{\mathrm{T}} t} + \sqrt{n} R_{\mathrm{e}}} \quad , \tag{2.9}$$

where t is the exposure time required to reach a signal-to-noise ratio $R_{\mathrm{S/N}}$. This expression may be solved to give,

$$t = \frac{R_{\mathrm{S/N}}}{2N^2} \left[P \pm \sqrt{P^2 - 4nN^2 R_{\mathrm{e}}^2} \right] \quad , \tag{2.10}$$

where

$$P = R_{\mathrm{S/N}} N_{\mathrm{T}} + 2\sqrt{n} N R_{\mathrm{e}} \quad . \tag{2.11}$$

Signal-to-noise summary

The results of the above calculations have been used to predict the signal-to-noise (S/N) expected as a function of exposure time and stellar magnitude. The predictions are shown in Figure 2.40. On this basis it is predicted that HERCULES will obtain a signal-to-noise ratio of 100/1 in 60 seconds for a G0 star with a magnitude $m_{\mathrm{V}} = 4.7$. This assumes atmospheric seeing of 2.5″, an airmass of $X = 1.3$, and a resolving power of $R = 40\,000$. By way of comparison, under operating similar conditions, FEROS is expected to reach $m_{\mathrm{V}} = 6.7$ for $S/N = 100/1$ in 60 seconds on the 2.2 m telescope, although $S/N = 100/1$ would be reached for an $m_{\mathrm{V}} = 5.1$ star in 60 seconds if this instrument were coupled to a 1 m telescope[8]. With HERCULES the limiting magnitude of a star of the same spectral

[8] `http://www.lsw.uni-heidelberg.de/cgi-bin/exp-calc.cgi`

type for a signal-to-noise of 100/1 should be $m_V = 7.1$ in 10 minutes, and $m_V = 9.1$ in one hour. On this basis it is also expected that HERCULES should achieve $S/N = 10/1$ in half an hour for an $m_V = 12.7$ solar type star, or $m_V = 13.5$ in one hour. However, due to the limitations of the guide camera, observations of such faint stars are not currently possible.

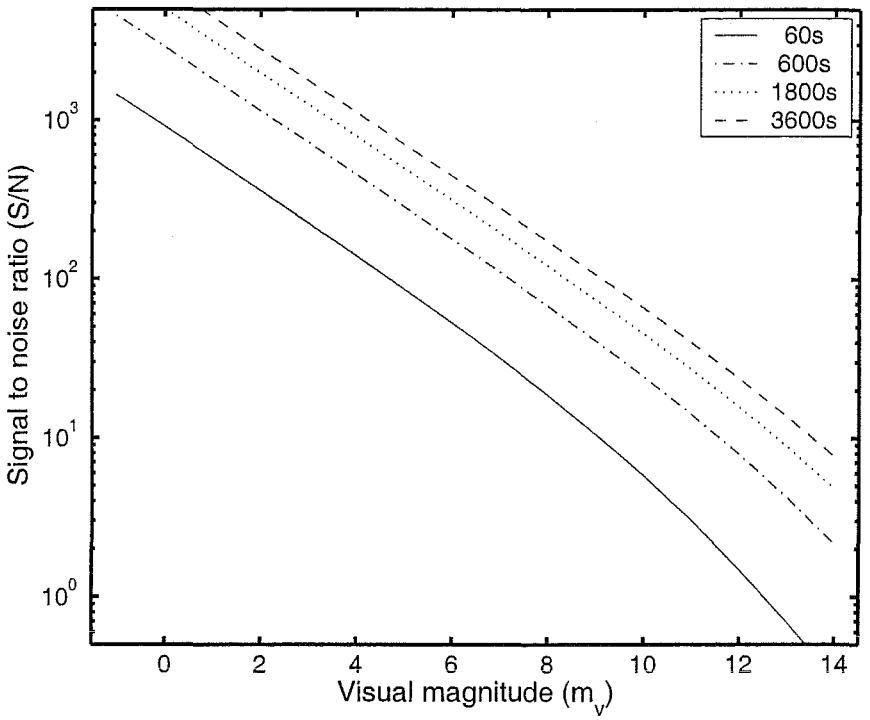

Figure 2.40: HERCULES signal-to-noise (S/N) predictions. The predictions are for a G0 star at a wavelength of 550 nm. The S/N is for each "extracted" pixel at a resolution of $R = 40\,000$. The atmospheric seeing is assumed to be 2.5″ at an airmass of $X = 1.3$.

2.2.3 Efficiency measurements

Observations were made of the spectrophotometric standards given in Table 2.4. The majority of the observations were made by the author. However, several stars were also observed by D. Ramm and J. Skuljan. Spectrophotometric data for most of the stars have been taken from either Alekseeva et al. (1997) or from Breger (1976). However, the star 31 Aql was measured using the standard spectral type calibration data of Knyazeva and Kharitonov (1996).

The spectra of the above spectrophotometric stars were extracted and wavelength-calibrated. The flux (i.e., the count rate per extracted pixel) was measured at the order centre nearest each wavelength for which spectrophotometric data exist. The absolute efficiency of HERCULES was computed by comparing this measured flux with the flux predicted for stars of the same spectral type and visual magnitude. The results are shown in Figure 2.41.

It can be seen that there is significant variation in the measured efficiency of HERCULES and that the maximum predicted efficiency is never reached. A significant portion of this variation is possibly due to widely varying atmospheric seeing conditions. Another cause of variation is likely to be due to inconsistent guiding errors. The effect of guiding can partially be removed by examining each observation's exposure meter log file (see Figure 2.21). A guide correction, which is the ratio between the integral of the observed flux and the maximum flux multiplied by the time of the exposure, is applied to each of the

HR no.	HD no.	Name	R.A.	Dec.	V mag.	Spec. Type	Rot. vel (km/s)	No. obs.	Ref.
100	2262	κ Phe	0:26:12.2	-43:40:48	3.94	A7V	219	5	P
126	2884	β^1 Tuc	0:31:32.7	-62:57:29	4.37	B9V	173	11	B
472	10144	α Eri	1:37:42.9	-57:14:12	0.46	B3Vpe	251	10	P
591	12311	α Hyi	1:58:46.2	-61:34:11	2.86	F0V	153	11	B
674	14228	ϕ Eri	2:16:30.6	-51:30:44	3.56	B8V-IV	247	10	B
705	15008	δ Hyi	2:21:44.9	-68:39:34	4.09	A3V	163	20	B
919	18978	11 τ^3 Eri	3:02:23.5	-23:37:28	4.09	A4IV	144	7	B
1084	22049	ϵ Eri	3:32:55	-09:27:30	3.73	K2V		5	P
2020	39060	β Pic	5:47:17.1	-51:03:59	3.85	A5V	139	33	P
2361	45813	λ CMa	6:28:10.1	-32:34:48	4.48	B4V	135	3	P
2451	47670	ν Pup	6:37:45.7	-43:11:46	3.17	B8III	228	9	P
3165	66811	ζ Pup	8:03:35.1	-40:00:12	2.25	O5f	211	2	P
3685	80007	β Car	9:13:12.0	-69:43:02	1.68	A2IV	133	1	P
5132	118716	ϵ Cen	13:39:53.2	-53:27:59	2.30	B1III	159	4	P
5708	136504	ϵ Lup	15:22:40.9	-44:41:22	3.37	B2IV-V	133	17	P
5812	139365	40 τ Lib	15:38:39.4	-29:46:40	3.66	B2.5V	149	8	P
5953	143275	7 δ Sco	16:00:20.0	-22:37:18	2.32	B0.3IV	181	2	B
5993	144470	9O ω^1 Sco	16:06:48.4	-20:40:09	3.96	B1V	142	1	P
7373	182572	31 Aql	19:24:58	+11:56:40	5.16	G8IV		31	K
8425	209952	α Gru	22:08:14.0	-46:57:40	1.74	B7IV	236	2	P

References: P = Alekseeva 1997, B = Breger 1976, K = Knyazeva 1996.

Table 2.4: Selected spectrophotometric standards used to measure the absolute efficiency of HERCULES.

measurements. The "guide corrected" measurements of HERCULES efficiency are shown in Figure 2.42.

Even after correcting for possible guiding errors a large variation in efficiency remains. The fact that the maximum efficiency of HERCULES is nearly obtained suggests that all the poor efficiency measurements were due to especially poor seeing and/or uncorrected guide errors. In Figure 2.43 all the measurements have been divided by the predicted efficiency and normalized about the mean. It can be seen that the same general trend is apparent for all measurements. That is, the efficiency appears to be deficient between 450 nm and 550 nm and there is a possibility that HERCULES is more efficient than predicted at wavelengths greater than 550 nm.

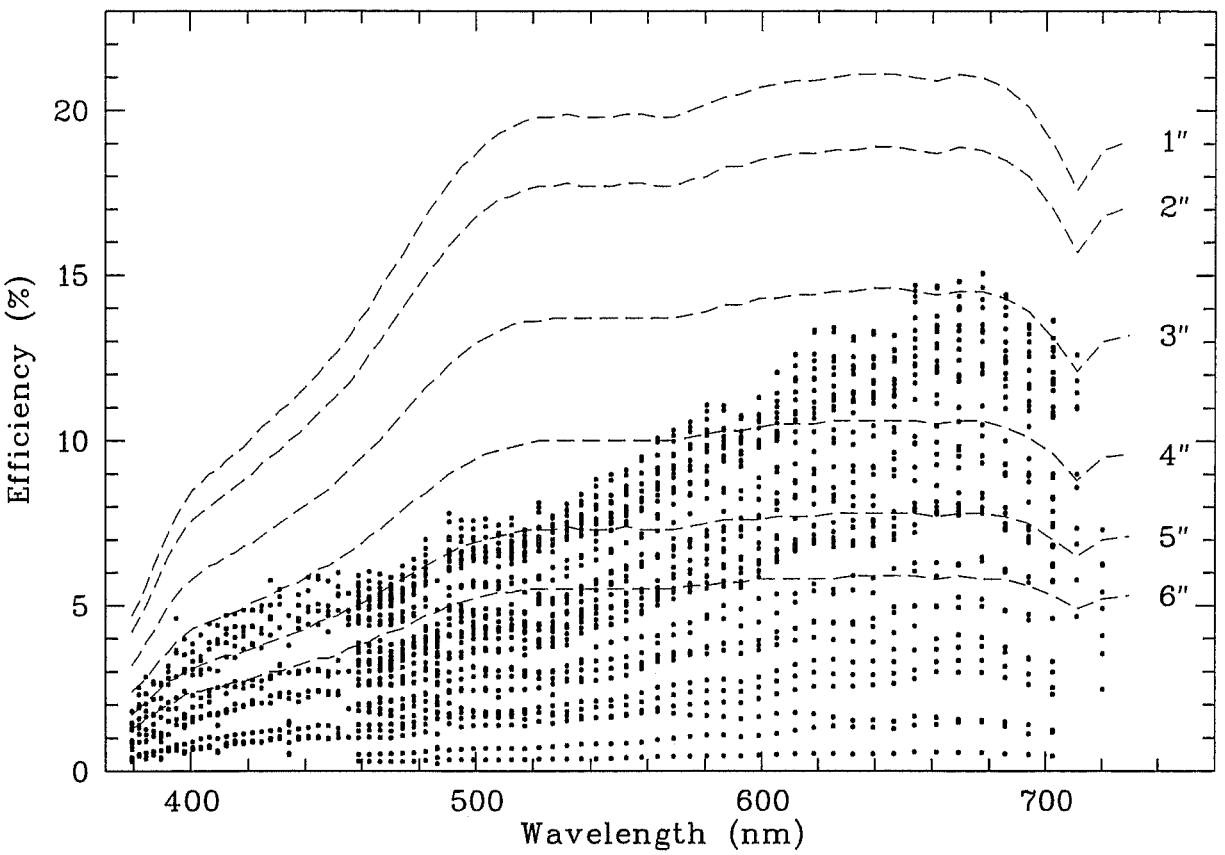

Figure 2.41: The measured efficiency of HERCULES.

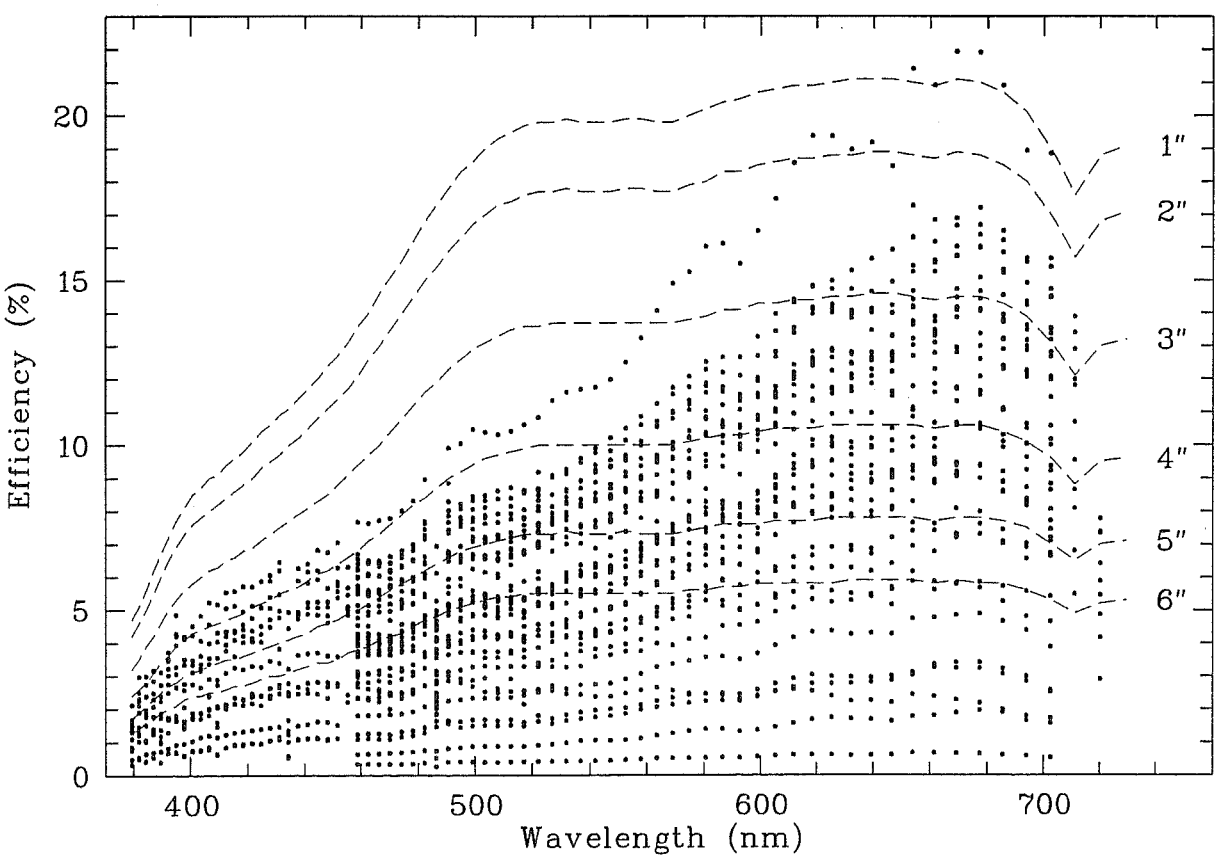

Figure 2.42: The "guide corrected" efficiency of HERCULES. See text for details.

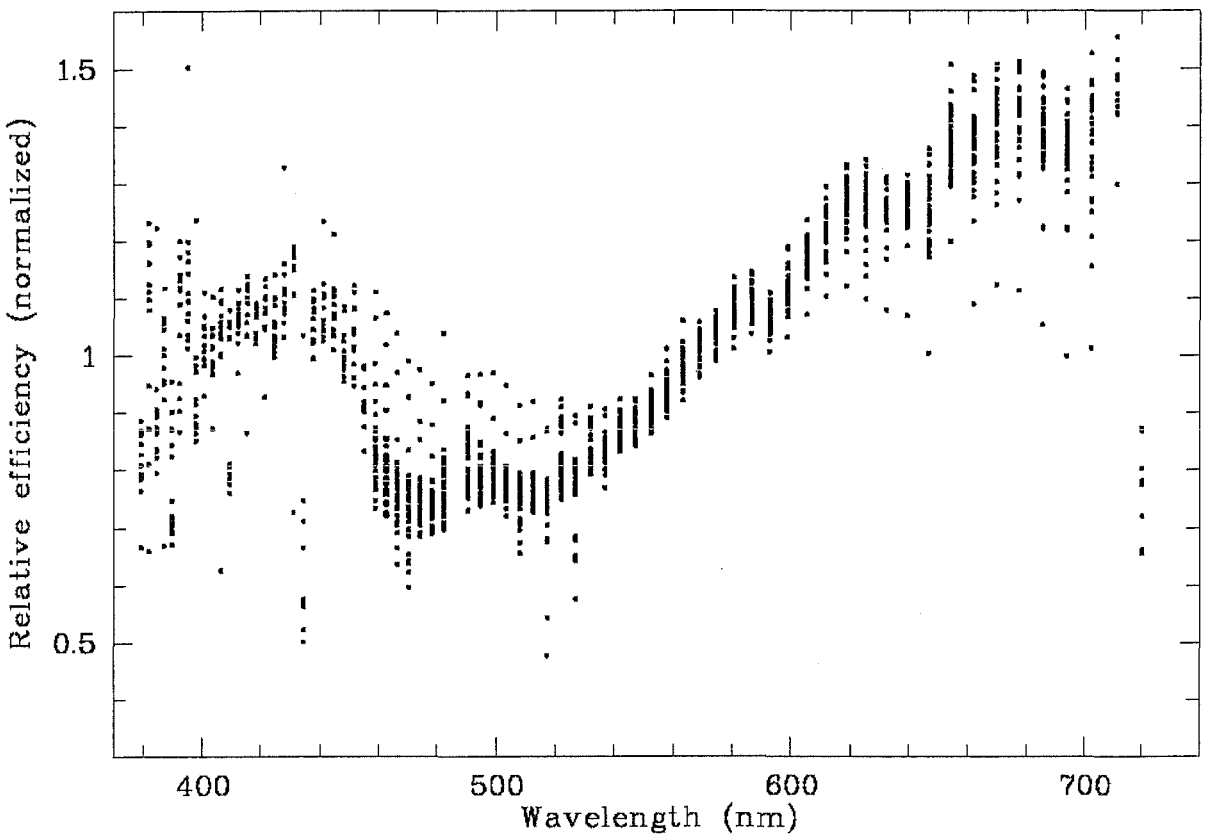

Figure 2.43: Relative efficiency of HERCULES. The efficiencies shown in Figure 2.42 have been divided by the predicted efficiency and then normalized about the mean for each observation.

2.2.4 Environmental stability

The HERCULES vacuum tank was sealed in 2001 April and later evacuated in 2001 September. Since this time the instrument has remained unaltered, except for detector replacement and repositioning.

Pressure and temperature

The pressure inside the HERCULES tank over a period of $2\frac{1}{4}$ years is shown in Figure 2.44. The vacuum is reestablished whenever the pressure rises above approximately 5 mmHg. It can be seen that the rise of pressure after each pump-down is quite steady and on average the vacuum is reestablished every 130 days. It is interesting to note that the rate of decay of the vacuum has slightly reduced over time. Initially the vacuum decayed at around 0.035 mmHg/d. However, toward the end of the 2003, the rate of decay became 0.027 mmHg/d. This is probably due to reduced out-gassing of the components inside the vacuum tank, which has not been opened since 2001 April.

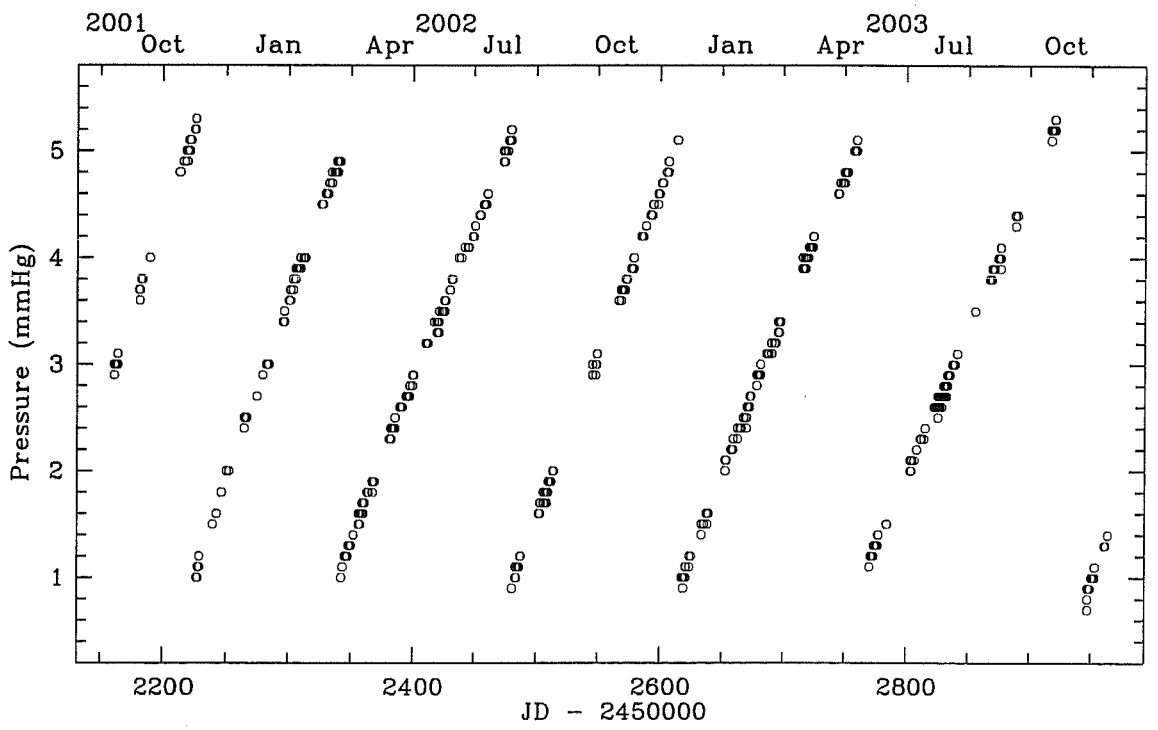

Figure 2.44: The pressure of the HERCULES vacuum tank.

The temperature of the spectrograph is monitored in several locations throughout the structure. The temperature of the mid-section for the past 2 years is shown in Figure 2.45. The room in which HERCULES is located is not temperature-controlled, and this is reflected by the clear seasonal variation of the temperature. The considerable short-term scatter of temperatures is real. This can be seen in Figure 2.46, where the temperatures over 40 days in 2002 Feb to Mar are plotted.

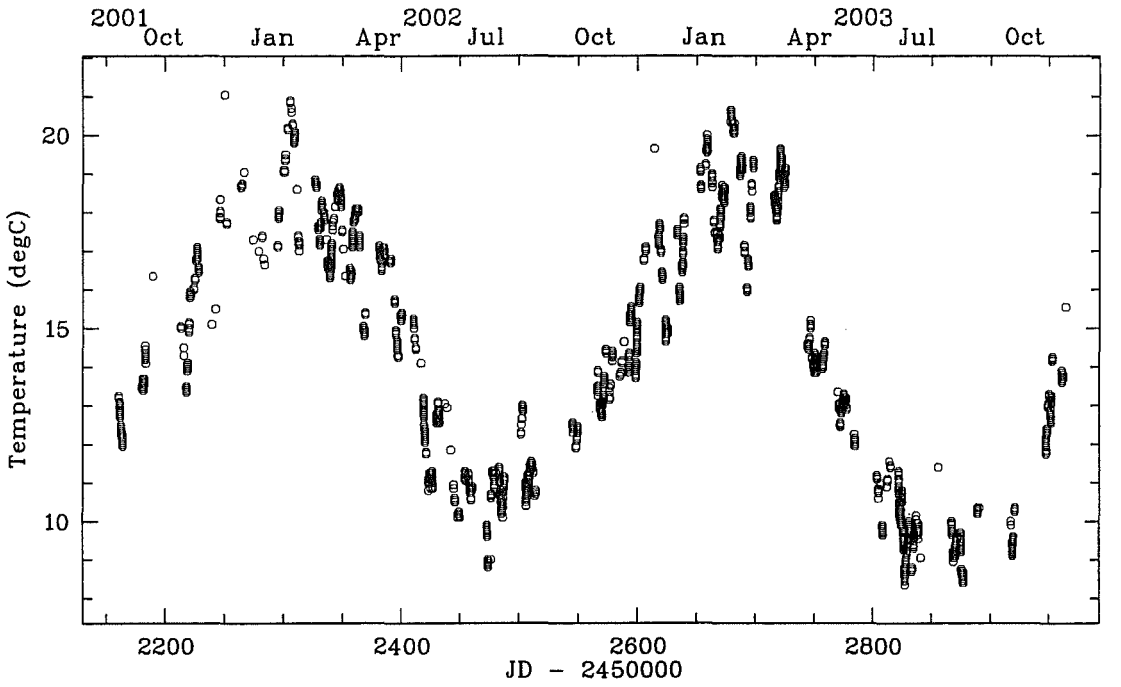

Figure 2.45: The temperatures inside HERCULES. The short-term scatter is real (see Figure 2.46).

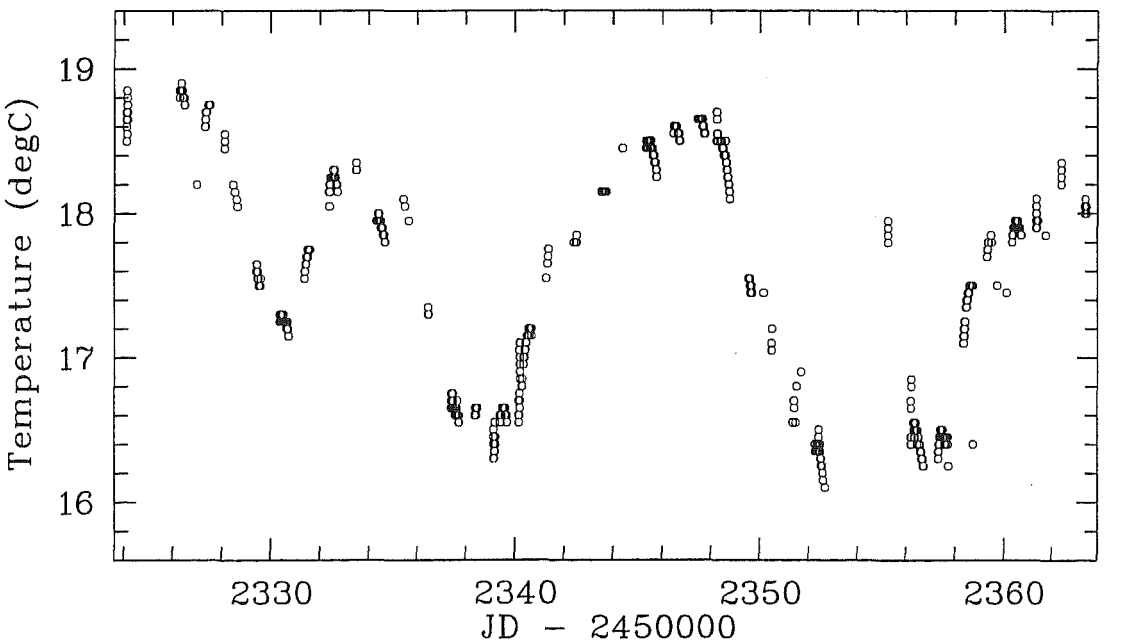

Figure 2.46: The temperatures inside HERCULES during 2002 Feb-Mar.

Mechanical stability

The mechanical stability of HERCULES is assessed by observing the positional stability of the thorium-argon spectra. The relative positions of selected lines of thorium-argon spectra have been measured by D. Ramm for the period from 2001 July to 2004 Jan and are shown in Figures 2.47 and 2.48. It is apparent that the thorium images are

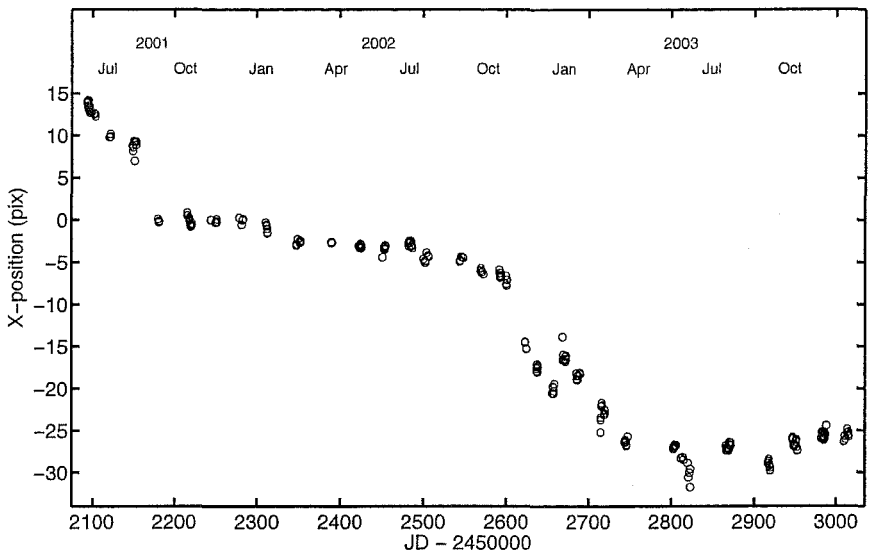

Figure 2.47: The x-shift of thorium lines (data from D Ramm).

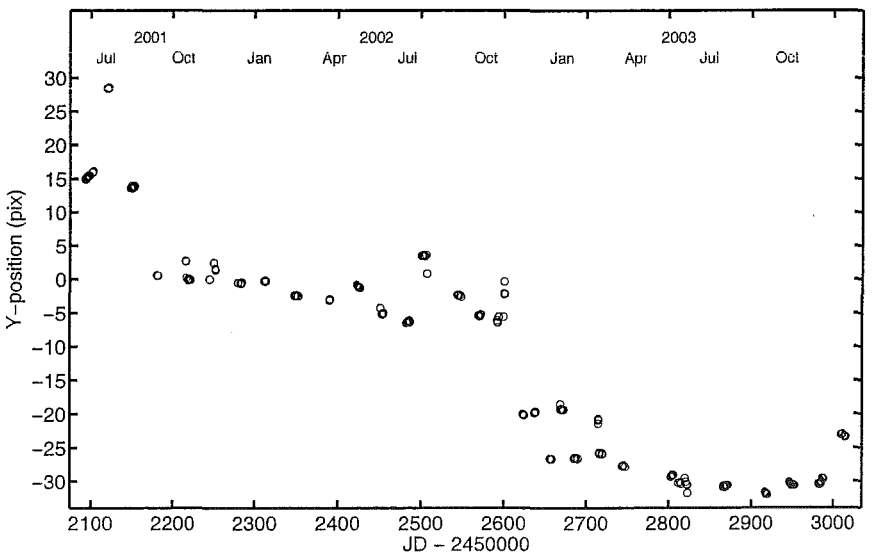

Figure 2.48: The y-shift of thorium lines (data from D Ramm).

far from stable. The abrupt shift in 2001 September occurred when the CCD cradle was repositioned in order to correct the tilt of the focal plane. The other significant change which occurs throughout 2002 December to about 2003 April is more difficult to explain; however it is noted that the cradle was dismantled during this period while adjustments to the CCD focus mechanism were being made. During the period 2001 October to 2002 November the shift (at least in x) was quite gradual at around 0.02 pixels/day (or 0.5 μm /day), although there was considerable scatter from night to night.

No attempt can be made to disentangle the relative stability of the various optical components using these data. Most significantly, it is not possible to discern whether the motions observed are due to the physical shifting of optical elements within HERCULES or simply to a gradual shift in the location of the CCD cradle. It is most likely that the latter

plays a significant role in the cumulative shift, as it must be realised that the CCD dewar is frequently removed from the cradle. The CCD dewar is quite heavy and in practice the relocation is never a smooth operation. The observer inevitably knocks the CCD cradle and a shift of half a micron (the average daily shift) is therefore quite probable. That the shift (during 2001 October to 2002 November) is generally in the same direction reinforces this speculation, as the CCD dewar is always relocated from the same direction. It should also be noted that the short-term stability is much better. There is a discernible shift throughout each night, which is likely to be due to evaporation of the CCD dewar's liquid nitrogen coolant. The shift is highly correlated for every thorium line, but it can be as much as 0.01 pixels per hour. This shift equates to around 3-5 m/s during 10 to 15 minute exposures. However, the effect on radial velocity precision will be considerably less than this if the dispersion solution is interpolated between two (or more) thoriums.

Radial velocity precision

HERCULES has proven to be capable of excellent radial-velocity precision. Ramm et al. 2004 have made observations of the 7th magnitude double-lined spectroscopic binary HD 181958 and have obtained an RMS of $50\,\mathrm{ms}^{-1}$. A radial velocity standard (HD 45067) observed as part of this program had a scatter of 20 m/s from a total of 76 measurements. Another (single-lined) spectroscopic binary ζ TrA had its very nearly circular orbit determined with high precision. An RMS scatter of $14\,\mathrm{ms}^{-1}$ was determined from 200 observations after iterative fitting to orbital parameters was performed (Skuljan et al., 2004). A dedicated reduction software package called the HERCULES Reduction Software Package (HRSP) has been written by J. Skujlan for the purpose of obtaining precise radial velocities (see op. cit. for details). Ramm and Skujlan have observed there is no significant difference between the short-term and long-term precision of HERCULES (private communication). It has also been observed by these authors that day-time sky spectra can achieve an RMS of $2\,\mathrm{ms}^{-1}$ over the short-term; however a much larger scatter is observed over longer periods of time. This scatter is assumed to be due to atmospheric winds, but could also be the result of variable atmospheric transmission across the face of the Sun as suggested by Brown et al. (1994).

2.3 HERCULES in the future

Several possibilities exist for improving the performance of HERCULES. The first, and most obvious of these, is a larger format CCD. Other improvements would include a more flexible fibre feed and collimator arrangement. The use of image slicers could improve throughput and fibre double scrambling would improve the radial velocity precision. The final upgrade possibility would be an improved guide and acquisition camera. Each of these possibilities is discussed below.

2.3.1 CCD

As described above, HERCULES was originally designed for a 2k × 2k CCD with 24 μm square pixels. At the time of construction a Series 200 CCD with 1024 × 1024 pixels each 24 μm square was the only detector available to be used with HERCULES. It is therefore not possible to observe the entire spectral range simultaneously. In order to observe all of the spectral format a detector cradle was constructed which has four discrete CCD positions (see Section 2.1.2). The design was intended to cover the spectral regions shown in Figure 2.9. However, during assembly the spectral format was slightly altered to give a more centrally located CCD position which is better suited to precise radial velocities. The CCD positions currently available with HERCULES are shown in Figure 2.10. Note that it is currently impossible to observe spectra above 720 nm and the lower limit of 370 nm is a result of the fall off in instrument efficiency (i.e., fibres, mirrors and CCD).

It appears unlikely that a 2k × 2k CCD with 24 μm pixels can be acquired for HERCULES. When HERCULES was being designed Scientific Imaging Technologies (SITe[9]) were producing 2k × 2k CCDs with 24 μm pixels. However, these have since been discontinued. Without considering mosaicking options (e.g. a mosaic of four 1k square CCDs) other possible CCD formats for HERCULES include:

- 2048 × 4096 with 15-μm pixels: These chips are available from E2V[10]. The area of such a chip (30.7 × 61.4 mm) is still not sufficient to fully cover the HERCULES spectral format, and several positions would still be required as well as a possible rotation (see Figure 2.49).
- 2048 × 4608 with 13.5-μm pixels: This chip is also available from E2V. The imaging area is 27.6 × 62.2 mm. Although the smaller pixels would improve the sampling of the smallest resolution element, the previous chip is obviously a better choice.
- 4096 × 4096 with 15 μm pixels: Fairchild Imaging[11] manufacture these chips. The imaging area (61.4 × 61.4 mm) is well matched to the available spectral format of HERCULES (see Figure 2.50). The CCD would require a single position only.

The CCDs mentioned above are available in "scientific" grades of the highest quality, and can be thinned, back-illuminated and overcoated for high quantum efficiency. The theoretical efficiency of HERCULES with an upgraded CCD is shown in Figure 2.51. Although the primary motivation for an upgraded CCD is increased spectral coverage, either of the above-mentioned detectors will double the detective quantum efficiency of HERCULES at 380 nm.

[9] http://www.site-inc.com
[10] http://e2vtechnologies.com
[11] http://www.fairchildimaaging.com

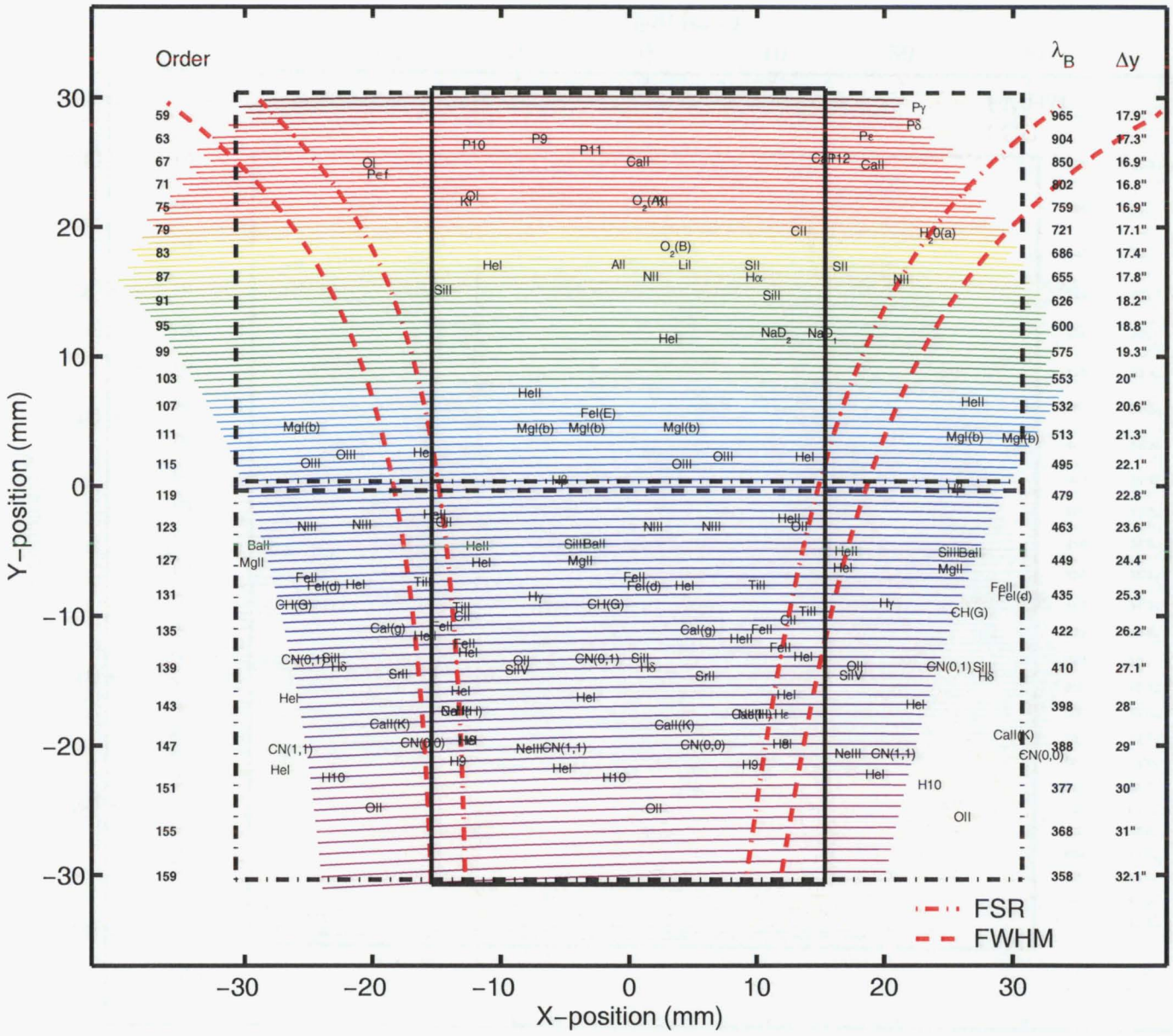

Figure 2.49: The HERCULES spectral format showing the possible locations of a single 2k × 4k CCD with 15 μm pixels. Note that a fourth horizontal centrally located position is also probably desirable.

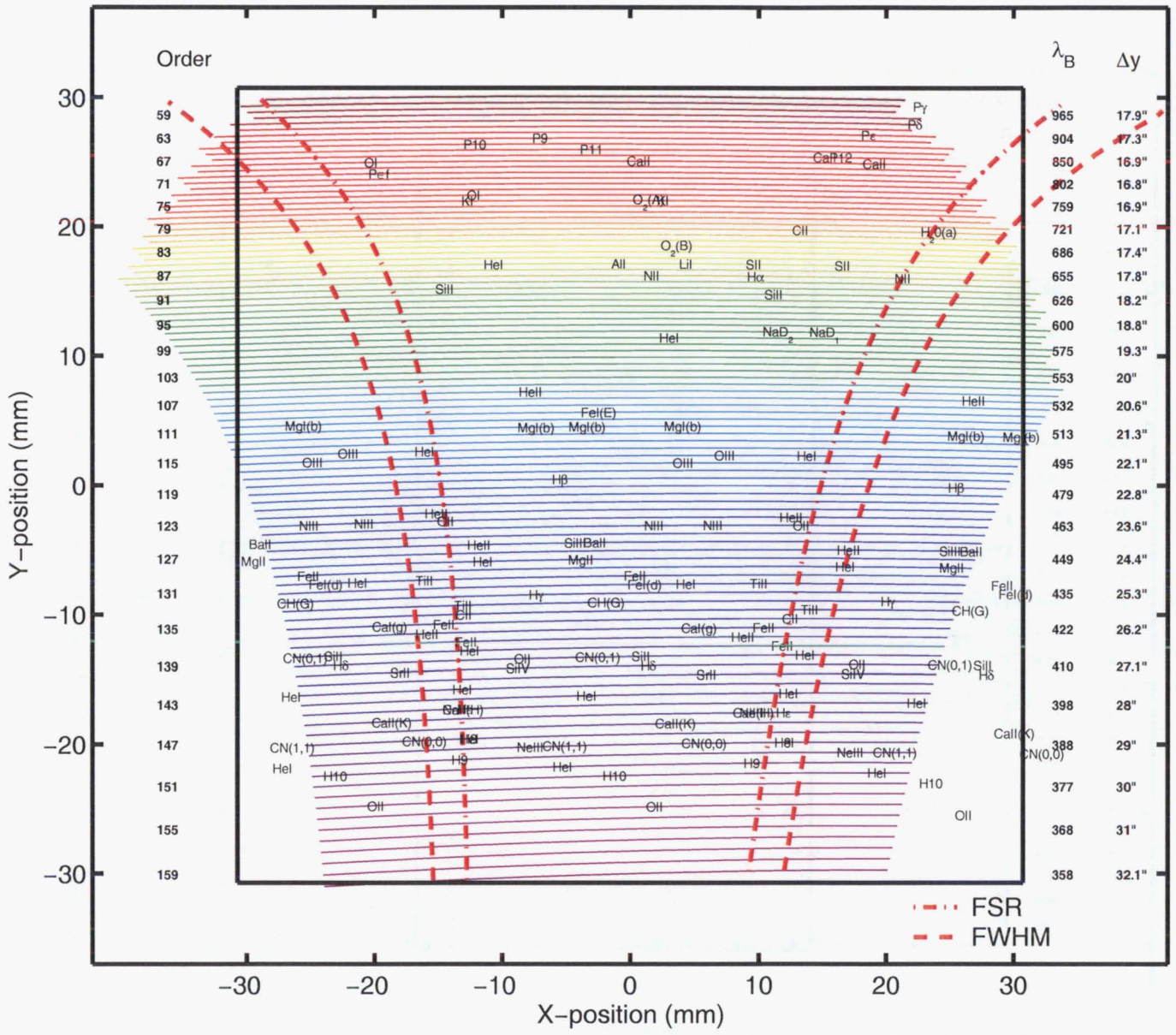

Figure 2.50: The HERCULES spectral format with a 4k × 4k CCD with 15 μm pixels. Full spectral coverage from 360 nm to 1 μm. is possible in a single exposure.

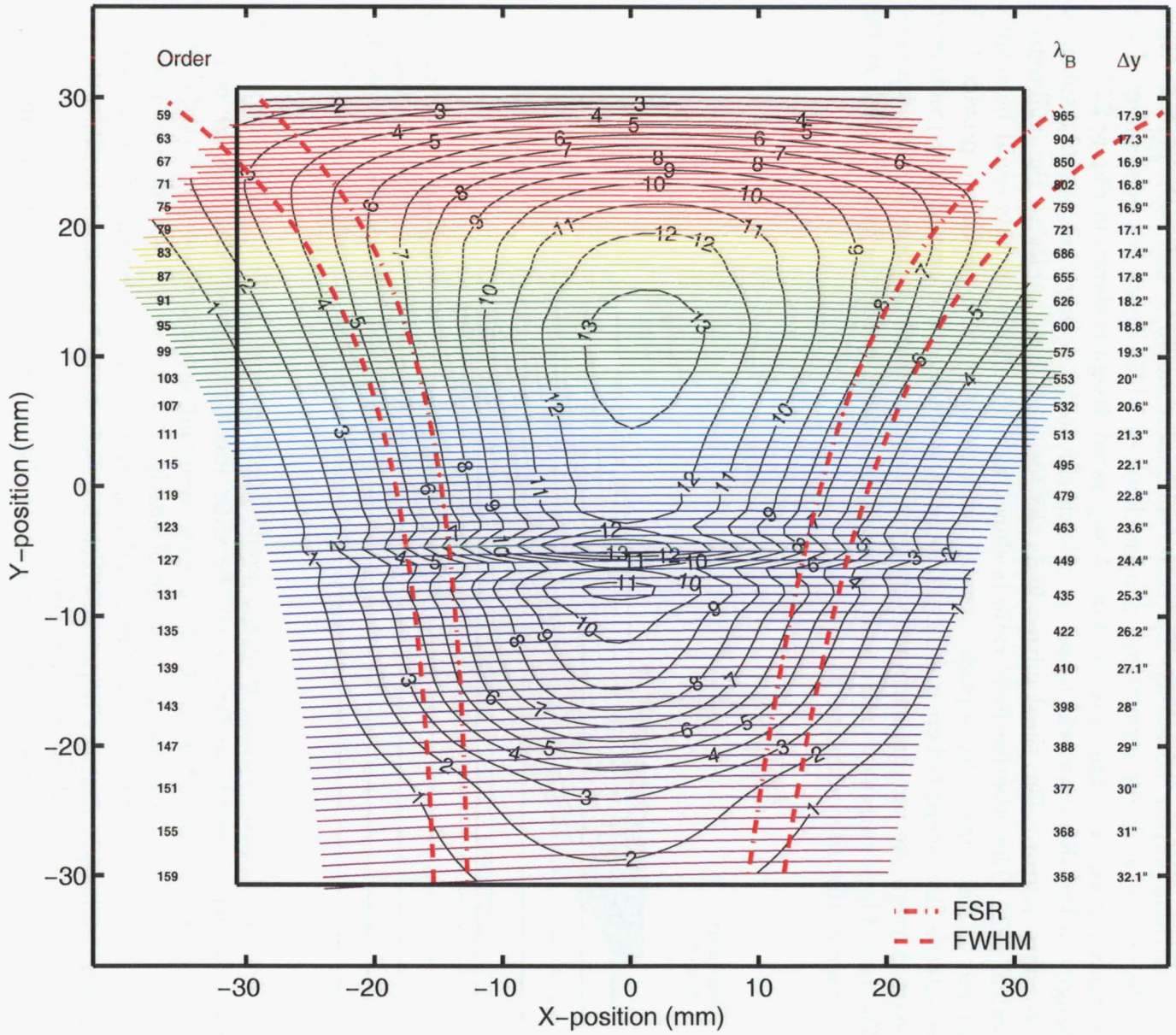

Figure 2.51: The HERCULES spectral format with a 4k × 4k CCD with 15 μm pixels. The efficiency (in %) of HERCULES (in median seeing at $R = 40\,000$) is shown by the contour lines. A Fairchild CCD with a broadband overcoat is assumed. Wavelengths that are vignetted are not plotted.

2.3.2 Collimator and fibre feed

While the current HERCULES collimator and fibre feed system allow for very stable and relatively efficient observations, it is impossible to implement any other fibre feed modes apart from the three currently in use. An alternative collimator design is proposed which will remove such limitations and hence allow for a variety of fibre feed modes to be implemented. The essential feature of this upgrade is that the spectrograph's entrance slit is placed outside the main HERCULES vacuum tank. Any number of collimator designs could achieve this. The collimator must be off-axis, thereby eliminating at least one source of light loss (the obstruction due to the fibre feed exit). It will also be folded so that the entrance slit can be conveniently placed, and hence will require at least one or possibly two additional mirror reflections. The entire collimator should be able to be placed within the fixed section of the HERCULES vacuum chamber. This limits the positioning of the entrance slit and vacuum tank window. A suggested design is shown in Figure 2.52. The design is a Dall-Kirkham which uses an off-axis ellipsoidal primary mirror and a spherical secondary mirror. The third mirror folds the focus at right angles to the collimator's optical axis. The effective focal ratio is shown as f/15. However, this could be readily altered to suit various fore-optics. It would also probably be necessary to provide both an intermediate focus (where a slit mask could be placed) and to pass a (near-)collimated beam through the vacuum entrance window in order to minimize possible flexure issues. The bare fibres currently used could therefore be placed *inside* the vacuum tank at the location of the intermediate slit.

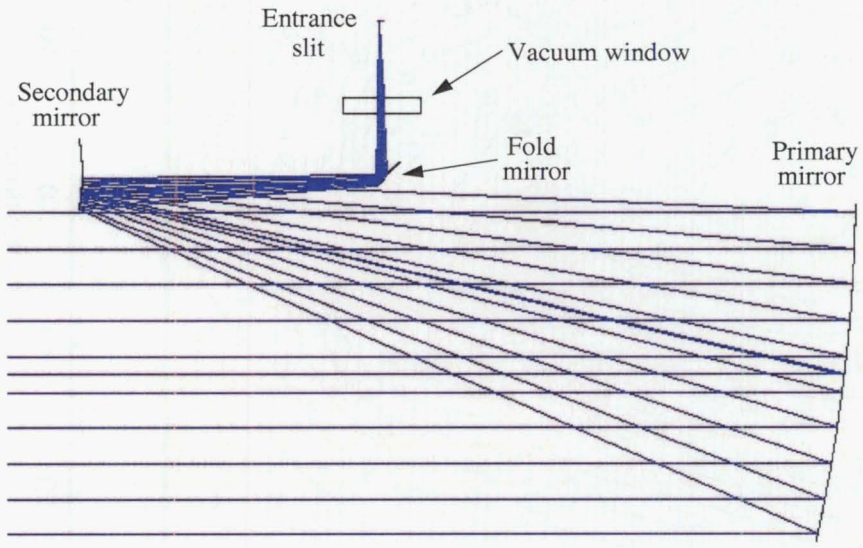

Figure 2.52: The proposed upgraded collimator is an off-axis Dall-Kirkham design. See text for details.

This alternative collimator design would allow the use of fibre image slicers similar to those being considered for use on the SALT HRS (see Section 3.2.2). These could be used to improve the efficiency at the highest resolving powers, especially during times of poorer seeing. A high resolution mode of nearly $R = 10^5$ would become available with the combination of fibre image slicing and improved detector sampling. It remains to be shown definitively that the improved efficiency and/or resolving power justifies the new collimator design and use of image slicers.

The use of an iodine cell (for improved radial velocities) would be possible in the collimated space before the vacuum window. However, the radial velocity precision would

probably be most significantly improved (without the associated losses of an iodine cell) through the use of a fibre double-scrambler (Brown, 1990). It should be noted that the use of a double-scrambler does not require an upgraded collimator design and a double-scrambled fibre feed mode could be implemented immediately alongside the currently available modes.

2.3.3 Guiding

At present it is not possible continuously to guide on the faintest stars which HERCULES is capable of observing. There is however an intermittent guide mode available which uses a fully reflective fold mirror, but this mode does not ensure the stability of the stars position on the fibre entrance and is also inefficient. A more efficient guide camera is required to improve the performance of HERCULES near the faint star limit. That is, a more sensitive detector is required to replace the image-intensified camera that is currently used. Several commercial possibilities exist which have improved quantum efficiency and are capable of on-chip binning and/or longer exposure times. The guide camera optics would probably need modification in order to accommodate a different detector. A method for more reliably centring the object onto the fibre entrance should also be investigated. Currently it is not possible to view the fibre entrance from the guide camera, and it is probable that the mis-centring of an object is one of the largest contributors to the radial velocity precision of HERCULES.

2.3.4 Mechanical stability

It was shown above that the temperature stability of HERCULES is not adequate. While it is not obvious that temperature changes significantly affect the radial-velocity precision (due to the presence of the vacuum) it would be prudent to reduce the large seasonal temperature fluctuations. A simple air-conditioning scheme could reduce the amplitude of the temperature changes by an order of magnitude; however care should be taken to avoid periodic changes in temperature.

It was also seen above that the repositioning of the CCD appears to be causing the slow shift of wavelengths. The upgraded CCD proposed, if it were dedicated to HERCULES, would entirely eliminate this effect. The CCD being considered would use a closed-cycle cryo-cooler, which would also eliminate the short-term flexure caused by the evaporation of the liquid coolant.

2.3.5 Efficiency

As discussed above, the use of fibre image slicers will enhance the throughput of HERCULES at the highest resolving powers, however the lower resolving powers will remain unchanged. The upgraded CCD would however enhance the efficiency at all wavelengths. The enhancement in the blue will be particularly noticeable. Three other options for increasing the efficiency of HERCULES at all wavelengths and resolving powers are as follows:

1. Improved fibres. The FBP fibres from Polymicro have improved UV transmission (although they are not significantly better than CeramOptec's Optran UV fibres), and they do not display the OH dip at 720 nm.

2. Telescope secondary mirror coating. The change from standard aluminium to a high efficiency (UV-enhanced) coating such as Laserdynes overcoated silver would improve the efficiency by as much as 10% at *all* wavelengths.

3. Adaptive optics. The implementation of adaptive optics would be the most significant of any improvement. Halving the median seeing at MJUO from 3″to 1.5″would improve the throughput of HERCULES by over 25% (see Figure 2.22). It is also possible that the ability to reliably maintain the centring of an object on the fibre input will improve the radial velocity precision. A program is underway at the University of Canterbury to develop an adaptive optics system for use at MJUO (Mohr et al., 2004).

It should be noted that while some of the suggested improvements (such as the use of fibre double-scramblers) would degrade the throughput of HERCULES in order to improve other functions (e.g., radial velocity precision), this degradation would be largely mitigated if all (or even some) of the above efficiency upgrade options are implemented.

2.4 Summary

The design of HERCULES has been discussed in detail. The vacuum mounted, R2 échelle grating, and prism double-pass instrument, has proved to have excellent throughput and radial velocity stability when fibre-fed by the MJUO 1-m telescope. Future upgrades, including a larger format CCD and/or improved fibre feed and guiding will significantly improve the performance of HERCULES.

While HERCULES has been designed for use on our 1-m telescope, the spectrograph would be capable of excellent performance on any 2 to 4-m telescope located at a site with reasonable seeing conditions. HERCULES would also be capable of performing competitively on even larger telescopes at sites with world-class seeing conditions. In the following chapter the design of a spectrograph for a 10-metre class telescope will be discussed.

Chapter 3

The design of SALT HRS

3.1 Introduction

The following sections detail a time series of concept and detailed optical design documents for a high resolution spectrograph (HRS) for the Southern African Large Telescope (SALT). Except where acknowledged in the text, the optical design work was done substantially by the author. However the dioptric cameras for the initial R4 design are primarily the work of D. Jones, with significant input by the author. The SALT HRS Principal Investigator (P. L. Cottrell) and Project Scientist (M. D. Albrow) provided advice and assistance on some aspects, most notably Albrow on the fibre feed arrangements. J. B. Hearnshaw, G. M. Kershaw and P. J. MacQueen also provided advice.

Details of SALT are given in Section 3.1.1 and a summary of the fibre feed options is given in Section 3.2. Section 3.3 details the development of an R2 HRS design which culminated in a design which was presented during a Preliminary Design Review (PDR) on 2003 September 4. The optical design document is included in Appendix D. Section 3.4 describes subsequent R4 designs as a response to the 2003 September PDR. This resulted in the detailed development of a design which was presented at a second PDR in 2004 July. This optical design document is also included as an appendix (Appendix E). Both of the optical design appendices form the core of a more extensive series of documents provided for the SALT consortium.

3.1.1 SALT

The Southern African Large Telescope (SALT) is located in Sutherland in the Northern Cape, South Africa. It is situated at an altitude of 1798 m above mean sea level. The telescope (Figure 3.1) has a spherical 11-metre primary mirror comprised of 91 identical hexagonal segments, which is mounted at a fixed altitude of 37° from vertical. Details of the optical design are shown in Figure 3.2. A 4-mirror reflective spherical aberration corrector (SAC) provides a science field of view of 8 arcmin over a declination range from -75° to 10°. The telescope is able to rotate in azimuth between observations and during observations objects are tracked by the moveable SAC. During an exposure the illumination of the SALT entrance pupil will vary (see Figure 3.3). The length of time an object can be tracked depends upon the object's altitude. This varies from around 2 hours to about 45 minutes. The operational wavelength range is from 320 nm to 2500 nm. Further details of the telescope can be found in Stobie et al. (2000), Swat et al. (2003) and on the web[1].

[1] http://www.salt.ac.za/

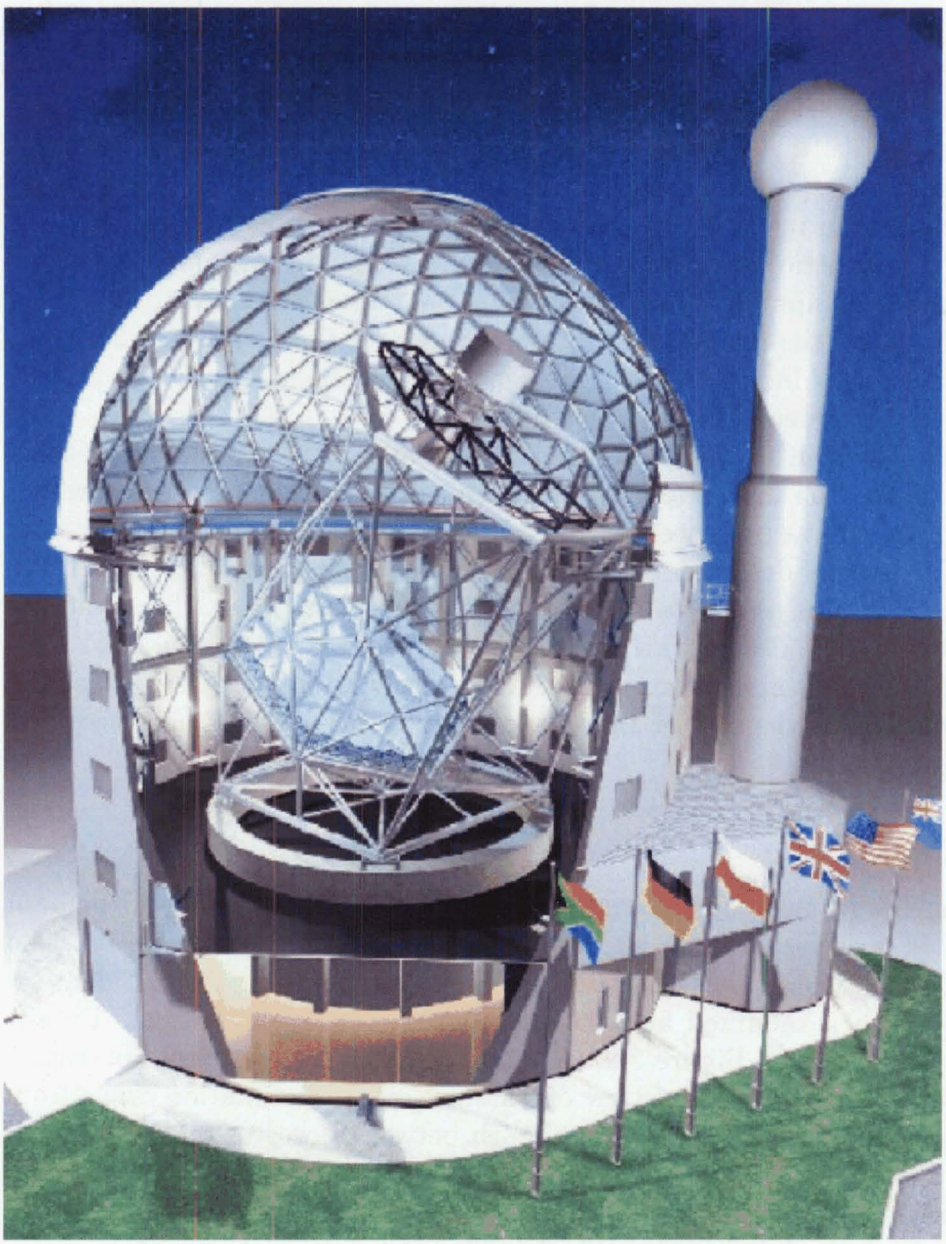

Figure 3.1: The SALT telescope.

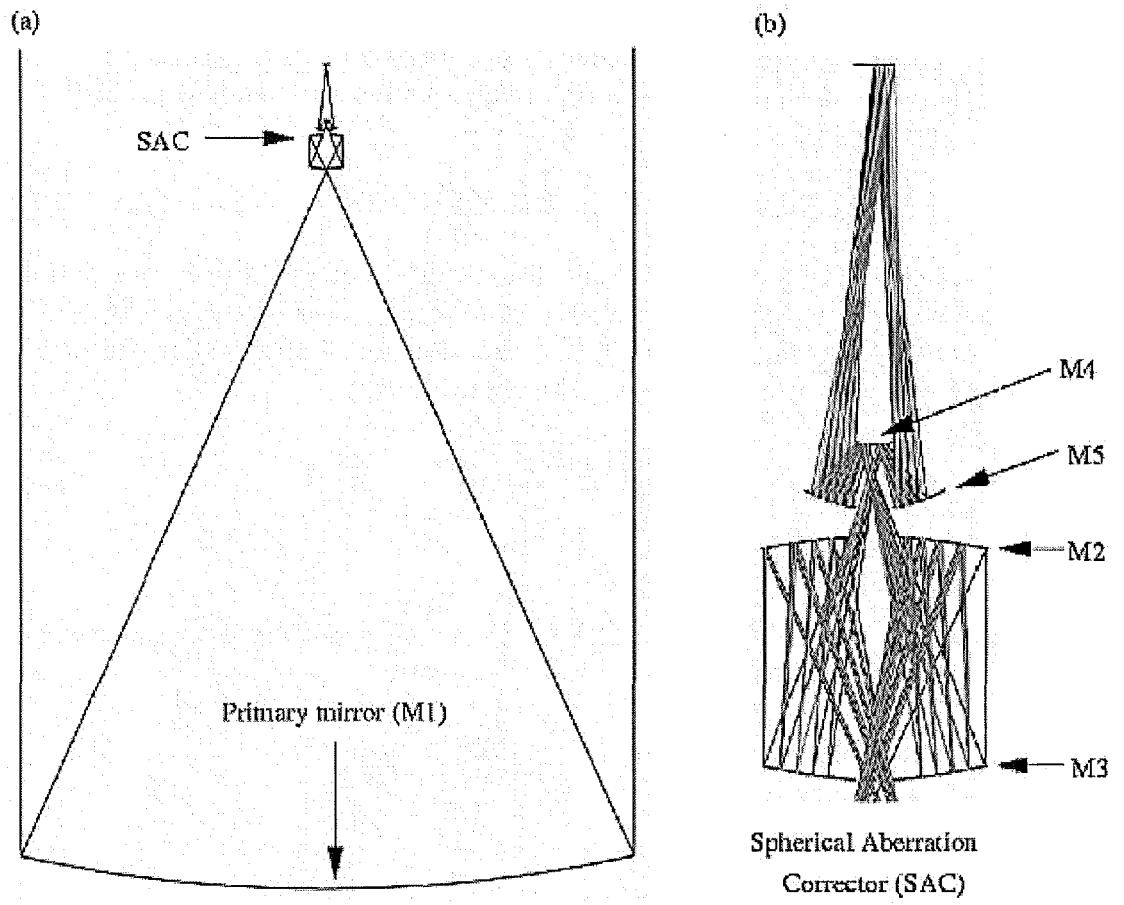

Figure 3.2: The SALT telescope (a) and detail (b) of the spherical aberration corrector (SAC).

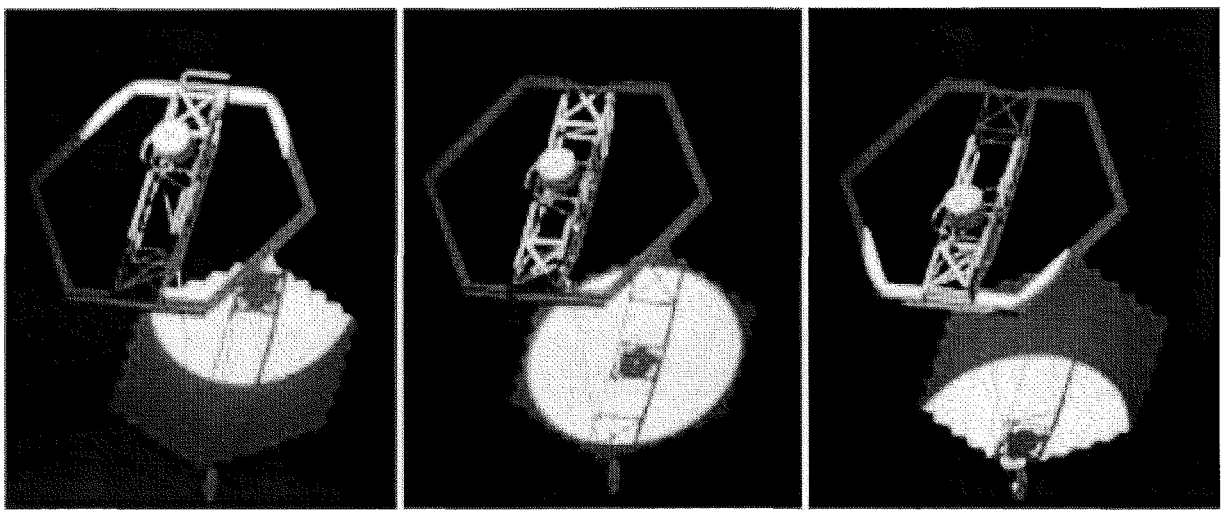

Figure 3.3: The variable illumination of the SALT entrance pupil. The figure is actually of the HET telescope.

The parameters of the SALT telescope that have been used throughout the design of the SALT HRS are given in Table 3.1. In median conditions at Sutherland the seeing is FWHM = 0.9″ (Buckley, 1995) and Erasmus (1999) gives quartile values of 0.74, 0.92 and 1.16″ respectively for the distribution. When added in quadrature with the expected image quality of the SALT optics the total SALT image quality error budget predicts that the encircled energies $EE(50)$ and $EE(80)$ will be

$$EE(50) = 1.29'' \quad \text{and} \quad EE(80) = 2.15'' \quad ,$$

during median seeing conditions at Sutherland (Swart, 2001) (see Figure 3.4 for details). The entrance aperture throughput as a function of fibre diameter and seeing conditions is shown in Figure 3.5. Throughout the rest of this document all calculations of fibre throughput will be made assuming median seeing conditions.

Parameter	Specification
Primary mirror diameter (D)	11.0 m
Focal ratio	$f/4.2$
Effective focal length	46.2 m
Image scale	224 μm /arcsec

Table 3.1: SALT parameters.

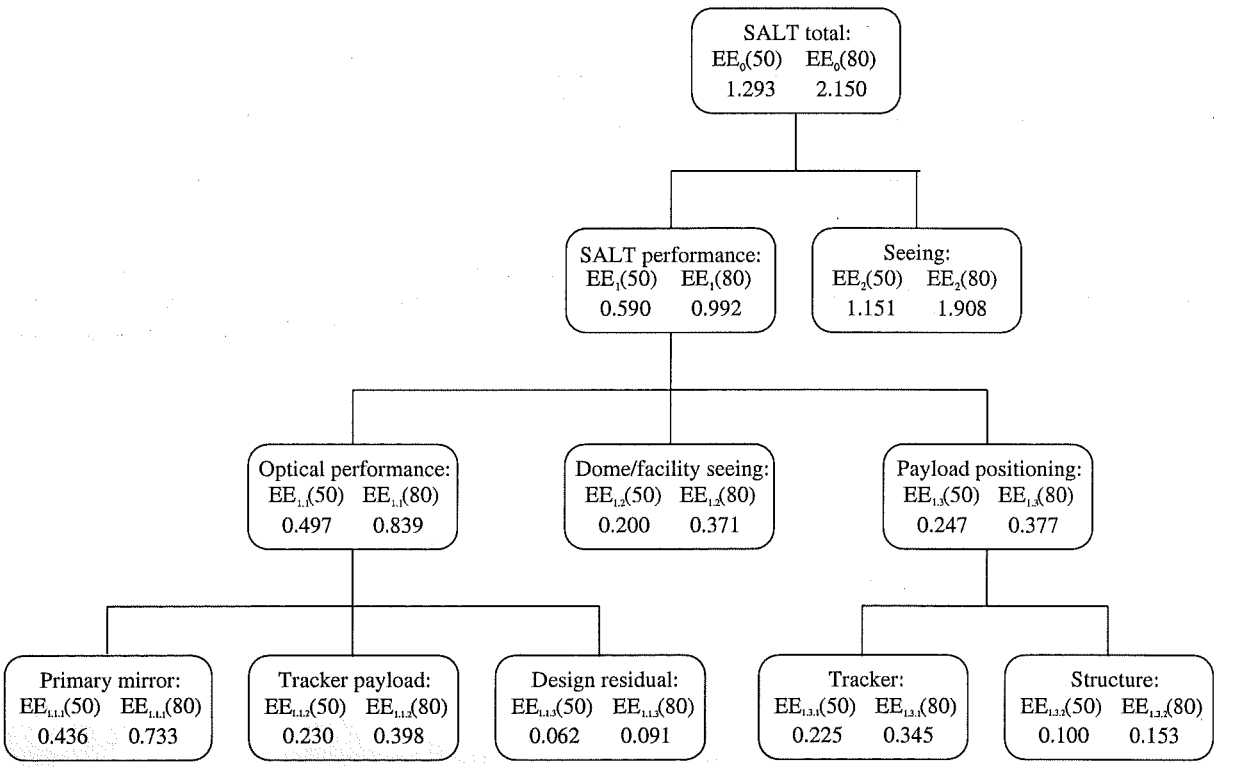

Figure 3.4: The SALT optical error budget. The site median seeing has been converted to $EE(50)$ and $EE(80)$ for a zenith angle of 37° and all calculations assume a wavelength of 633 nm. The calculations were made by G. Swart (2001).

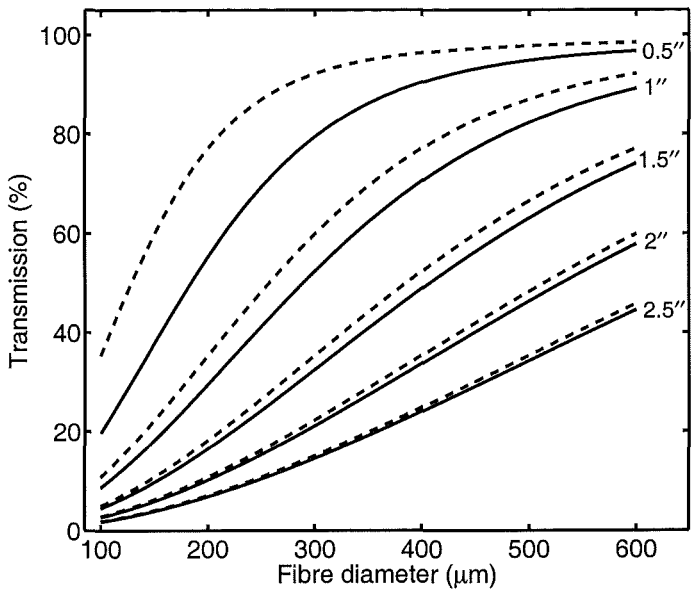

Figure 3.5: Fibre entrance aperture efficiencies for SALT. The bold line shows the throughput assuming that the stellar PSF is added in quadrature with the expected SALT image quality. The dashed line shows the throughput of the PSF alone. The stellar PSF is a Moffat function as described by Racine (1996) and references therein.

The expected throughput of SALT is as follows:

$$\begin{array}{lll} 340\,\text{nm} < \lambda < 450\,\text{nm}: & >49\% & , \\ 450\,\text{nm} < \lambda < 800\,\text{nm}: & >53\% & \text{and} \\ 800\,\text{nm} < \lambda < 2500\,\text{nm}: & >60\% & , \end{array}$$

where the total pupil obscuration due to the SAC structure vignetting and gaps between the mirrors is no more than 25% (Buckley, 2000). The throughput of the telescope has been estimated using witness measurements from the four SAC mirrors and a single aluminium surface and is shown in Figure 3.6. Included in the total efficiency is a fifth fold mirror (assumed to have the reflectivity of the average of the four SAC mirrors) and the vignetting due to to the SAC. The efficiency of the ADC is *not* included. Its efficiency is expected to be greater that 95%.

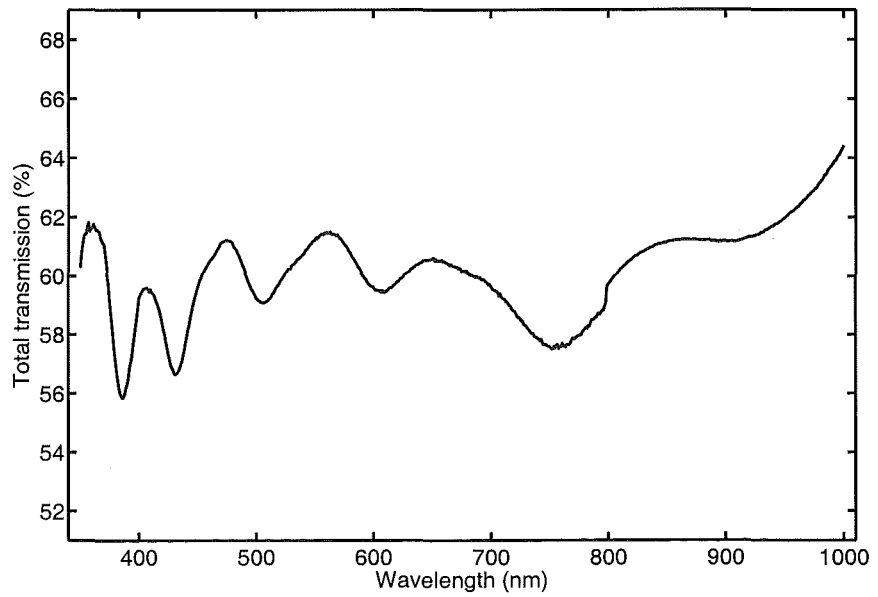

Figure 3.6: The transmission of SALT. Included are the efficiencies from the four SAC mirrors, the primary mirror, and the SAC vignetting. A fifth fold mirror is also assumed. The ADC was not included. (After Buckley et al. 2004.)

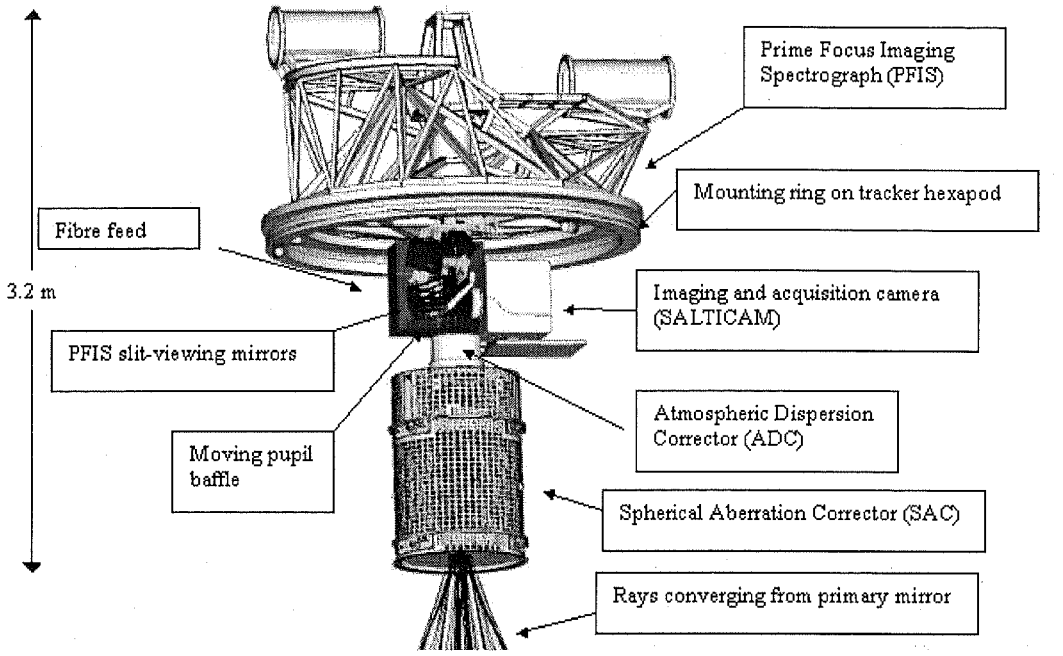

Figure 3.7: The SALT prime focus payload. The payload includes the spherical aberration corrector (SAC) and the atmospheric dispersion corrector (ADC). The location of the prime focus imaging spectrograph (PFIS) [ref] and the imaging and acquisition camera (SALTICAM) [ref] is also indicated.

3.1.2 Fibre Instrument Feed

The location of the fibre instrument feed (FIF) in the prime focus payload is shown in Figure 3.7 and a schematic diagram of the proposed instrument is shown in Figure 3.8. The FIF has been designed by Buckley and Sessions and details can be found in Buckley and Sessions, 2004. The FIF will accommodate up to 12 individual fibres which are mounted in two rows of 6 fibres each. The two rows can be moved apart along a set of rails. A second pair of rails provides motion in the orthogonal direction. This allows a pair of fibres accurately to be centred and to be separated anywhere from approximately $15''$ to $3.7'$. Five pairs of fibres are available for use by SALT HRS. The input telecentric angle varies considerably as a function of field angle (see Figure 3.9) and therefore in order to limit the effects this will have on the fibre's output focal ratio degradation the useable field for SALT HRS fibres will be limited to $\pm 1'$.

The SALT imaging camera (SALTICAM) will be used for initial acquisition of targets, where fiducials will be defined by peaking up the SALT HRS signal (using an exposure meter) on bright stars. A guidance stage is mounted directly to the FIF stage which contains a coherent fibre bundle. Again, fiducials will be predefined for each fibre input and guiding will continue on a suitable nearby field star. Given the SALT offset pointing specification of $0.1''$, and a FIF fibre repositioning specification of $27\,\mu$m (i.e., $0.12''$) RMS, this will allow targets to remain accurately centred throughout an exposure. Provision has not been made for directly viewing the fibre input.

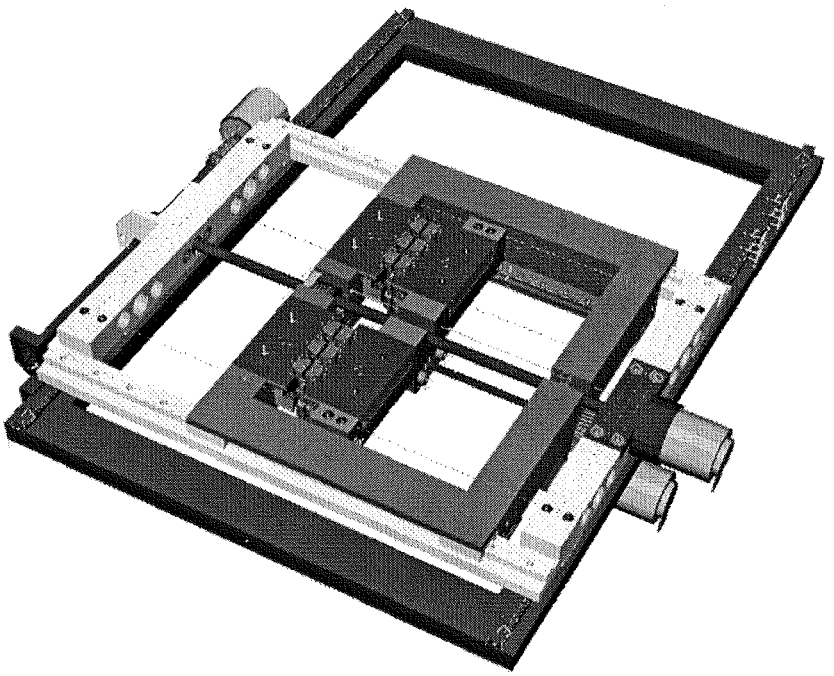

Figure 3.8: Model of the SALT fibre instrument feed (FIF). Up to 6 pairs of fibres can be accommodated. The pairs of fibres is shown at their minimum separation. (From Buckley and Sessions, 2004.)

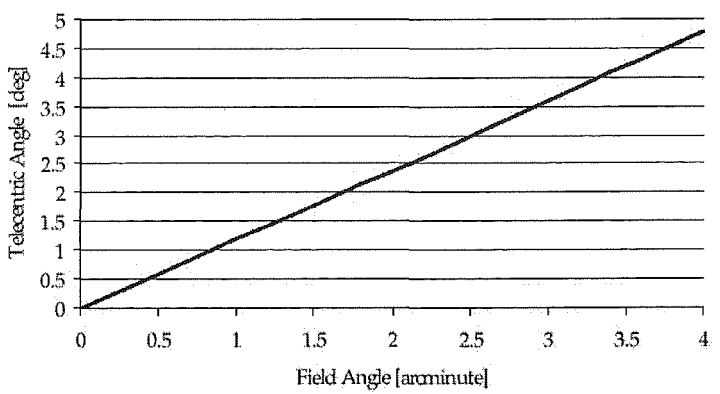

Figure 3.9: The telecentric angle at the SALT focal plane as a function of field angle. (From Buckley and Sessions, 2004.)

3.1.3 SAC calibration optics

A calibration system designed by Swat and Esterhuyse (see Buckley et. al 2004 or Meiring and Buckley, 2004) is able to mimic the illumination of the SALT pupil (i.e., Figure 3.3). This will ensure that the calibration source is injected into the spectrograph in a manner which is as nearly identical to the stellar source as is possible. The system is still under design; however a schematic of one possible concept is shown in Figure 3.10. The calibration optics can be moved into the beam either immediately prior to or after an observation, or during the daytime.

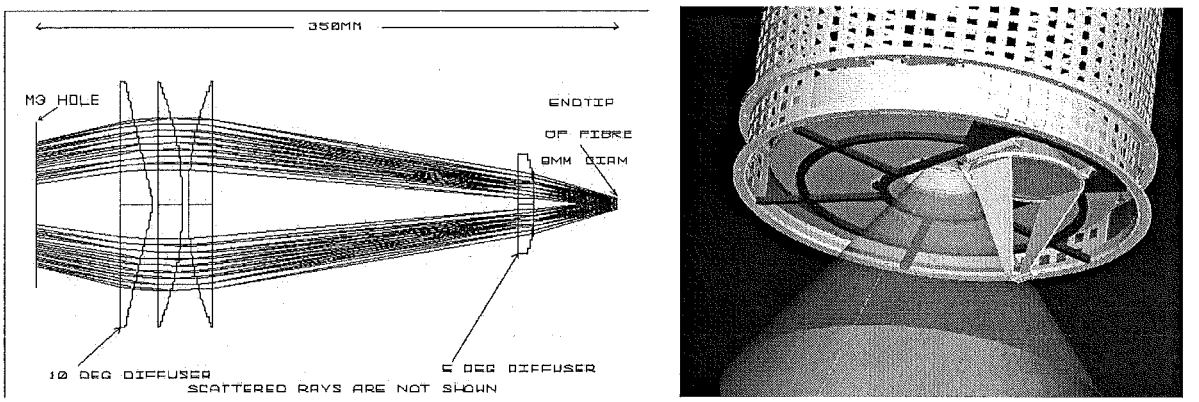

Figure 3.10: A possible SALT prime focus calibration system. The calibration light exits an 8 mm diameter fibre bundle.

3.1.4 HRS science requirements

SALT currently has two first light instruments under construction, an imaging camera (SALTICAM, see O'Donoghue et al. 2003) and a medium-resolution imaging spectrograph (PFIS, see Nordsieck et al., 2001). PFIS will cover resolving powers $500 < R < 10\,000$ with a wavelength range $320 < \lambda < 900$ nm. The proposed HRS complements PFIS by providing resolving powers $17\,000 < R < 85\,000$ and wavelength coverage $370 < \lambda < 890$ nm.

SALT HRS will address many of the fundamental questions that drove the construction of SALT. A list of more than 50 science drivers for SALT HRS arose from a potential user survey carried out by G. Mackie in late 2000 and early 2001 (Hearnshaw et al., 2001). The broad categories of science to be addressed by this instrument will be:

- element abundance studies in local group galaxies;
- extra-solar planet detection;
- stellar internal structure and dynamics;
- star cluster and galaxy dynamics;
- outflow and accretion studies;
- high- and moderate-redshift galaxy spectroscopy.

Some of the desired capabilities of SALT HRS are:

- resolving power $R = 30\,000$ to $70\,000$;
- wavelength coverage $\lambda = 380$–$880\,\mathrm{nm}$;
- high mechanical and thermal stability;
- some limited multi-object capability.

SALT HRS is designed to be competitive with other high resolution spectrographs on large telescopes (see Table 3.2).

Telescope:	VLT		Keck	Subaru	HET	Gemini S.	LBT	
Spectrograph:	UVES		HIRES	HDS	HRS	bHROS	PEPSI[d]	
D_{tel}	8.4 m		10 m	8.2 m	9.2 m	8.4 m	2×8.4 m	
Wavelength range (nm):	300–500	420–1100	320–1100	320–1100	420–1100	400–1000	390–580	580–1050
Echelle:	R4	R4	R2.8	R2.9	R4	R2	R4	
gv/mm:	41.59	31.6	52.6	31.6	31.6	87.0	31.6	
Beam size (mm):	200	200	305	305	260	200	200	
Resolution-slit product:	41 400	38 700	39 000	38 000	30 000	21 000	40 000	
Maximum Resolving power	80 000	110 000	67 000	165 000	120 000	150 000	120 000	120 000
Pupil mag.:	1	1	n/a	n/a	1	n/a	1.5	1.5
Cross-dispersion	SR grating		SR grating	SR grating	SR grating	Prism	VPH grisms	
	1000 gv/mm	600 gv/mm	?? gv/mm	400 gv/mm	600 gv/mm	2 × silica	940 l/mm	460 l/mm
	660 gv/mm	312 gv/mm	250 gv/mm	250 gv/mm	316 gv/mm	60°		
Camera:	dioptric	dioptric	catadioptric	catadioptric	dioptric	reflecting	dioptric	dioptric
	$f/1.8$	$f/2.5$	$f/1.0$	$f/0.96$	$f/2.8$	$f/0.96$	$f/2.3$	$f/2.3$
CCD:	EEV	EEV & MIT/LL	SITe	EEV	Marconi	Marconi		
Format:	2k × 4k	2k × 4k	2k × 2k	2×(2k × 4k)	2k × 4k	2k × 4k	4k × 4k	4k × 4k
Pixels:	15 μm	15 μm	24 μm	13.5 μm	15 μm	15 μm	15 μm	15 μm
Max. λ coverage:	85/126 nm	200/403 nm	~250 nm	~400 nm	380 nm	~160 nm[c]	660 nm	
DQE[a]:	12%	14%	10%	13%	~7%[b]	12.6%	–	–
λ	400 nm	600 nm	600 nm	600 nm	600 nm	600 nm		
References:	Dekker et al. 2000		Vogt et al. 1994	Noguchi et al. 2002	Tull 1998	DArrigo et al. 2000b[e]	Pallavicini et al. 2003	

a. DQE's are from top of telescope with "wide slit"
b. HET HRS predicted efficiency
c. bHROS coverage not continuous
d. PEPSI parameters based on 8″ order separation and complete wavelength coverage
e. The reference is actually for HROS

Table 3.2: High resolution spectrographs on other large telescopes.

3.2 SALT HRS fibre feed

The various fibre feed modes that were investigated during the design of SALT HRS are discussed below. It should be noted that while some options are particular to a spectrograph design, given, in particular, the inter-order separation, all of the options can readily be adapted to any design. Section 3.2.1 introduces the proposed observing modes and in Section 3.2.2 the options for improving throughput at the highest resolving powers are discussed. M. Albrow provided significant input to the latter.

3.2.1 The fibre modes

Three fibre feed modes have been considered during the design of SALT HRS. Each of these will be discussed briefly below.

"Fixed object and sky"

Because of the large SALT aperture it will be important to observe sky spectra along with every object. In the "fixed object and sky" mode a pair of fibres will be used at the telescope focal plane to observe the object along with a single patch of nearby sky. In principle this same mode could be used simultaneously to observe a calibration source. However, it may not be useful to do so, unless a third fibre is also used to capture sky.

"Nod and shuffle"

The technique of "nod and shuffle" is widely used in infra-red spectroscopy for precise subtraction of the sky background and has been proposed to increase the yield of high density multi-object surveys (see (Cuillandre et al., 2003) and (Glazebrook and Bland-Hawthorn, 2001)). It is also shown (op. cit.) that nod and shuffle spectroscopy would allow much deeper observations on large telescopes such as SALT where the sky emission is significant.

The nod and shuffle mode proposed for the SALT HRS is outlined schematically in Figure 3.11. It is assumed that the two object spectra can be shuffled so that they overlap in the focal plane, and therefore at the end of a nod and shuffle exposure the spectrum will comprise an object order and two adjacent sky orders. Each of the sky orders will have been captured by the respective fibres. It follows that the observations of the wavelength calibration and flat-fielding sources must be obtained using the same technique.

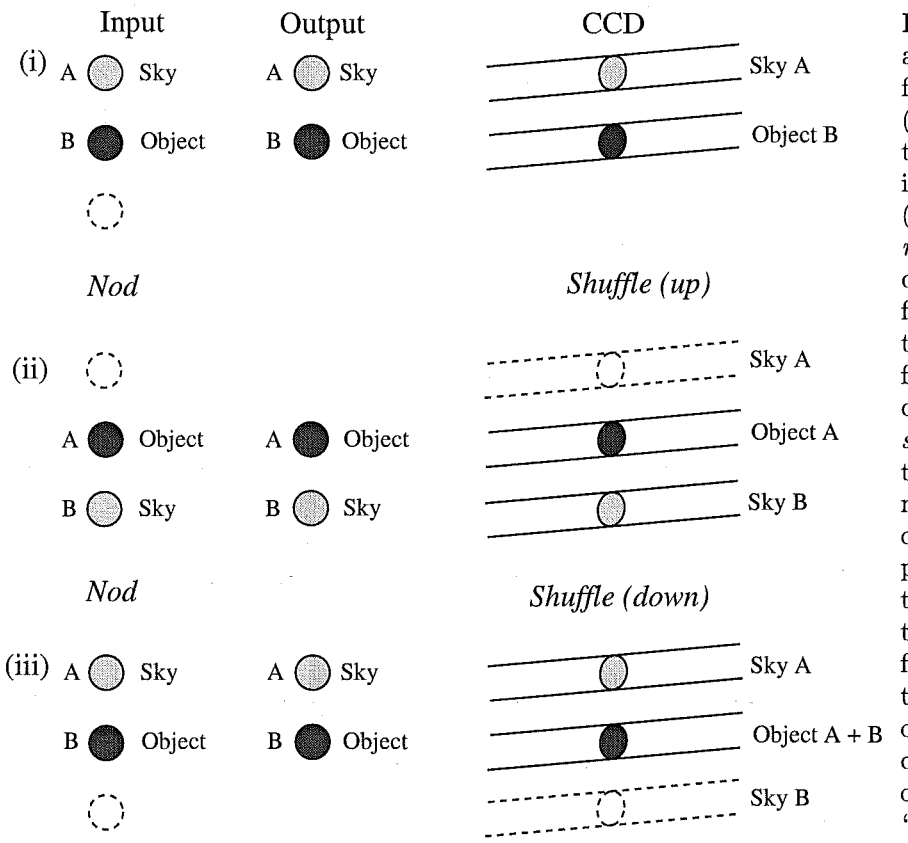

Figure 3.11: The nod and shuffle concept for fibre-fed spectrographs. (i) Fibre "A" observes the sky while fibre "B" is located on the object. (ii) The telescope is then *nodded* so that fibre "A" captures the object while fibre "B" now observes the sky. To avoid confusing these spectra, the charge on the CCD is *shuffled* upwards so that the object order "A" is now in the position of object order "B" in the previous step. (iii) Next the telescope is nodded so that the sky returns to fibre "A" and the object to fibre "B". The charge on the CCD is shuffled down so that now the object spectra from fibres "A" and "B" overlap.

Multi-object capability

In order to satisfy the requirements of the nod and shuffle mode the inter-order spacing must be sufficient to allow at least three objects to be observed at any resolving power. Assuming this is possible with bare fibres at the lowest resolving powers then the spacing between orders will be sufficient for the following multi-object possibilities:

1. $R \approx 20\,000$ (400–500 μm fibres) – a total of three 1.79–2.23″ fibres;
2. $R \approx 40\,000$ (200 μm fibres) – a total of six 0.89″ fibres;
3. $R \approx 80\,000$ (100 μm fibres) – a total of twelve 0.45″ fibres.

Unless the SALT image quality is improved and/or adaptive optics are used, the high resolution multi-object modes will be extremely inefficient. The multiplex gain is probably not sufficient mitigation against this inefficiency and a multi-object mode would also require a considerably more complicated FIF. The ability to compensate for the variation in telecentric input angle is probably vital. A SALT high resolution multi-object mode is not currently being considered.

3.2.2 Fibre slicing options

It has been shown already that if a single small diameter fibre is used to obtain the very highest resolving powers then the transmission of the stellar PSF would be very small. A number of fibre slicing options have been explored, and each of them is readily applicable to any of the concept designs.

Micro-slits

In order to obtain a higher resolving power than is possible with a simple bare fibre a smaller micro-slit can be imprinted on the fibre's output face. This option was explored for the CELESTIA design which is discussed below (see Section 3.3.1) and has already been used successfully on HERCULES (see Section 2.1.3). As was shown in Figure 3.5 the throughput of the smallest fibres is extremely poor. If it is assumed that a 100 μm fibre can be used to obtain a resolving power of $R = 100\,000$, then the optimal configuration of a range of fibres and micro-slits and their throughputs in median seeing are given in Table 3.3. While the throughput at the highest resolving power is quite poor, it is a factor of 2.2 times better than using bare fibres. It was also shown that for resolving powers less than $R \approx 30,000$ there is no advantage to using micro-slits. Otherwise, the significant advantage of micro-slits is that they require no additional inter-order spacing than is available at the lowest resolving power. Other methods of increasing the resolving power involve some form of image slicing and are therefore only possible if the inter-order separation is significantly greater. These options will be discussed below.

Fibre diam. (μm)	Micro-slit width (μm)	Resolving power ($\lambda/\delta\lambda$)	Throughput (%)
400	–	22900	67.8
350	200	37800	41.9
300	100	75500	21.9
400	70	108000	13.9

Table 3.3: The optimal configuration of fibres and micro-slits and their throughputs in median seeing. The throughput is purely geometric.

Fibre bundles

The concept of using fibre bundles is similar to integral field spectroscopy. However, for spectroscopy of a point source, only in the spectral and not the spatial resolution is of interest. A fibre bundle is used to sample a stars seeing disk and then the fibre exits are reformatted to form the spectrograph's entrance slit. Each of the nod and shuffle and fixed object plus sky modes requires different optimal fibre bundles. The order spacing in the fixed object plus sky mode must be sufficient to place the sky from the same number of fibres (which needn't be in a single input bundle) between adjacent object orders. The optimal fibre arrangements for the fixed object plus sky and their geometric efficiencies are given in Table 3.4 and the order profiles are shown in Figure 3.12. These profiles were created by convolving a uniformly illuminated fibre exit with a PSF and then collapsing in one-dimension. The PSF image quality is sufficient to just support the highest resolving power shown. The nod and shuffle mode must allow for spacing for three objects per order. The optimal fibre configurations (not shown) are therefore slightly different and

the efficiencies are somewhat lower. All calculations assume a minimum order separation of 13″.

Fibre diam. (μm)	Resolving power	No. of fibres	Efficiency (%)
100	80 000	14	58.4
200	40 000	7	71.6
500	16 000	1	87.0

Table 3.4: Fibre bundle efficiencies for fixed object mode. The bundles are arranged in the formats shown in Figure 3.12.

Fibre image slicer

The final solution to obtaining efficient high resolution spectra is to use an optical image slicer. A design similar to that used on FEROS (Kaufer et al., 1999) is considered. This is an adaptation of the classical Bowen-Walraven slicer (Bowen 1938, Walraven and Walraven 1972) that allows two fibres to be sliced with identical optical path lengths. A similar concept was used for the UVES image slicers (Dekker et al., 2003). It may also be possible to use "focusing" image slicers similar to that described by Richardson et al. (2000). Details for this type of image slicer are limited and no attempt to compare its performance with the Bowen-Walraven type of image slicers will be made. As for the fibre bundles, the throughput of the image slicer is limited by the amount of inter-order spacing available to stack sliced images. Assuming a minimum order separation of 13″, the geometric throughput of image slicers as a function of resolving power is shown in Figure 3.13. The slicer parameters are given in Tables 3.5 and the geometry for selected slicers is shown in Figure 3.14. The parameters and geometry for nod and shuffle modes are not shown.

Fibre diam. (μm)	Resolving power	No. of slices	Efficiency (%)
350	80 000	4	54.0
500	38 000	3	78.6
500	17 000	1	87.0

Table 3.5: Image slicer parameters for fixed object plus sky mode. Figures by M. Albrow.

Based on the geometrical throughput alone, the image slicer has slightly lower throughput than fibre bundles at high resolving powers. However, it is possible that the packing density of the 100 μm fibres required to give the highest resolving power has been overestimated. It may be the case that 100 μm diameter fibres require a 20% cladding rather than 10% in order to retain high throughput in the near infrared (generally a cladding 8 to 10 times greater than the longest wavelength to be carried is desirable). If this extra cladding is required, then the throughput of a 14 $\times$ 100 μm bundle reduces from 58.4% to 52.6%. It has also been suggested (R. Content, private communication) that the focal ratio degradation of fibre bundles may be significantly larger due to the stress imposed by gluing many fibres together at their input. The enhanced efficiency of the image slicers at lower resolving powers may be further decreased by the efficiency of the image slicer optics which hitherto have not been considered. The measured losses of the UVES image slicers is 21–40%, while a 10% upper limit is measured for the FEROS image slicer (Kaufer, 1998).

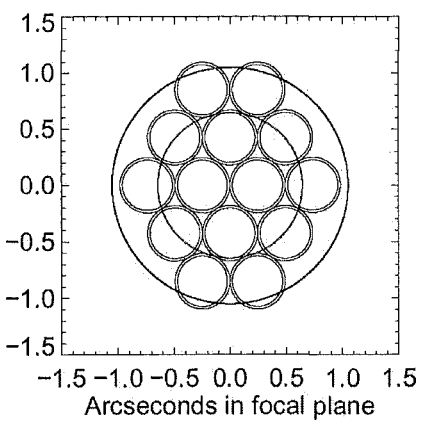

(a) Fourteen 100 μm fibres

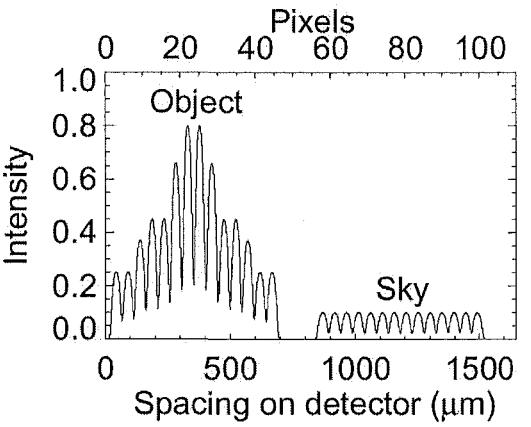

(b) Fourteen 100 μm fibres

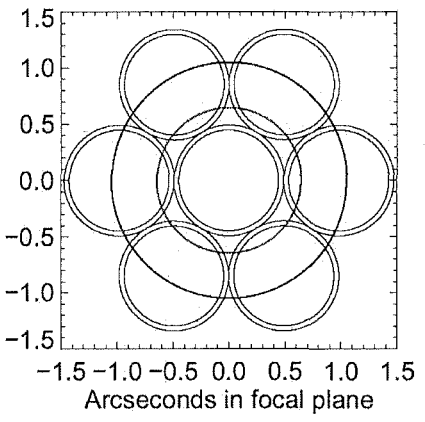

(c) Seven 200 μm fibres

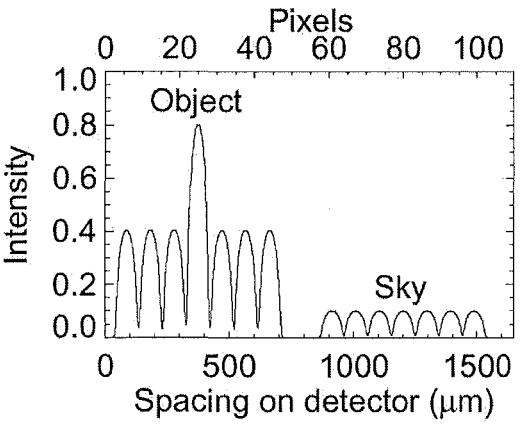

(d) Seven 200 μm fibres

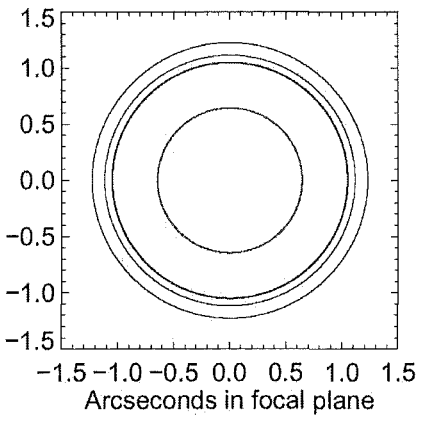

(e) One 500 μm fibre

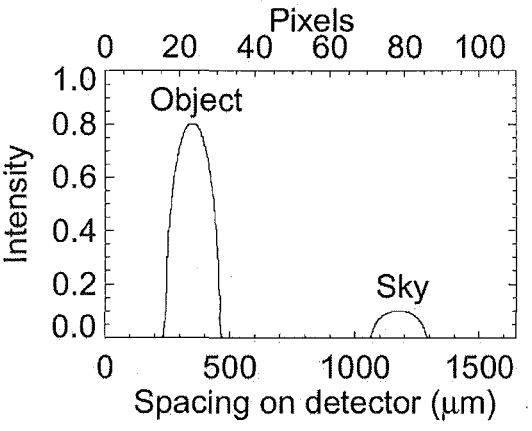

(f) One 500 μm fibre

Figure 3.12: Fixed-object observing mode inputs and outputs. Fibre bundle inputs for (a) 100 μm , (c) 200 μm and (e) 100 μm fibres. Black circles represent fibres and their claddings, red and blue circles are $EE(50)$ and $EE(80)$ expected in median seeing conditions. (b), (d) and (f) show the corresponding output intensity profiles (one set for the object, one set for the sky) on the detector across a single order.

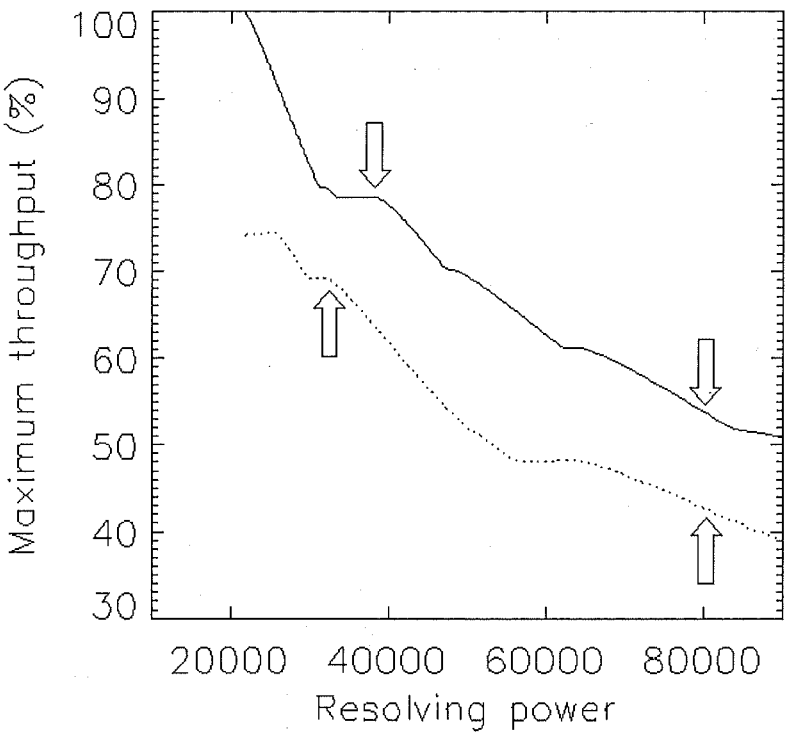

Figure 3.13: The geometrical throughput of a Bowen-Walraven type image slicer as a function of resolving power. The throughput for fixed object plus sky (solid line) differs from the nod and shuffle throughput (dashed line) owing to the reduction in available inter-order spacing for stacking image slices. The steps in this function arise from the combination of discrete fibre diameter sizes and the integral number of slices. The chosen modes are indicated. Calculations courtesy of M. Albrow.

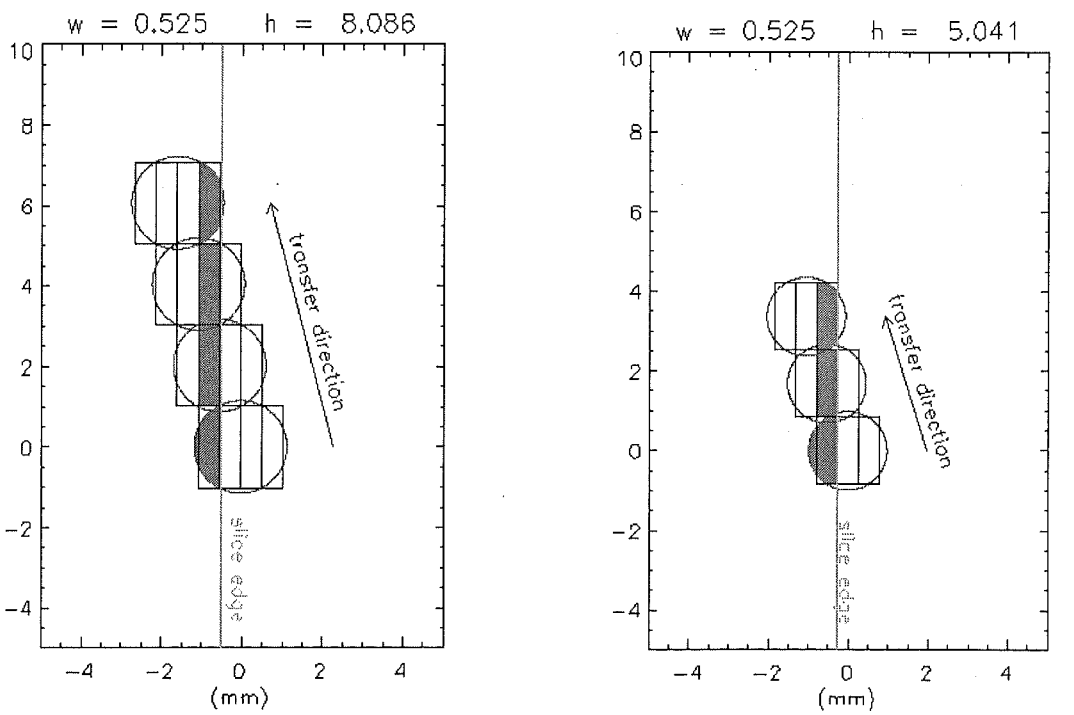

Figure 3.14: The slice geometry for fixed object plus sky mode at high (left) and medium (right) resolving powers. Figures by M. Albrow.

A schematic diagram of a proposed image slicer for SALT HRS and the output sliced image are shown in Figure 3.15. The design is based on a suggestion by R. Bingham (private communication). The slicer will require additional fore-optics in order to convert the $f/3.8$ output of the fibres to the $\sim f/20$ required by the image slicer. This slow focal ratio ensures that the defocus is kept to a minimum along the length of the sliced image while also allowing the size of the image slicer to be scaled.

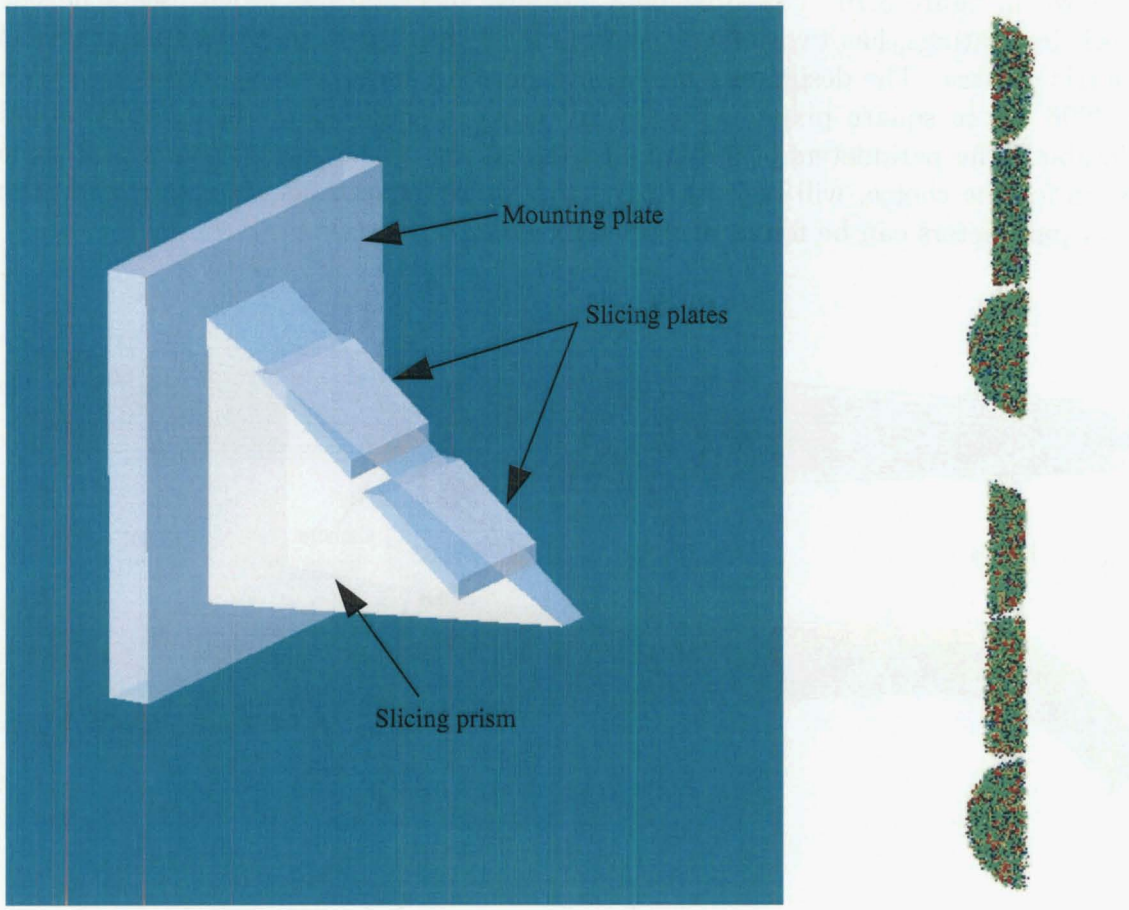

Figure 3.15: Image slicer concept for SALT HRS (left). The output from a pair of sliced fibres is shown on the right. The design is based on a suggestion by R. Bingham (private communication).

3.3 R2 and R3 designs

3.3.1 CELESTIA optical design

An initial concept design for SALT hrs was presented to the SSWG in 2001 October (Hearnshaw et al., 2001). This instrument was referred to as the Canterbury Extremely Large Echelle Spectrograph on a Telescope in Africa CELESTIA. The optical design of CELESTIA is shown in figure 3.16. CELESTIA is a fibre-fed spectrograph which uses a mosaic of two échelle gratings, has two prisms used in double-pass, and an on-axis all spherical catadioptric camera. The design assumes a CCD detector mosaic of two CCDs each with 2048×4096 $15\,\mu$m square pixels, although of course a single 4k $\times$ 4k detector would be preferable. The parameters of individual components of the spectrograph, and some motivation for the choice, will be outlined in the following sections. A summary of the CELESTIA parameters can be found in Appendix A.2.2.

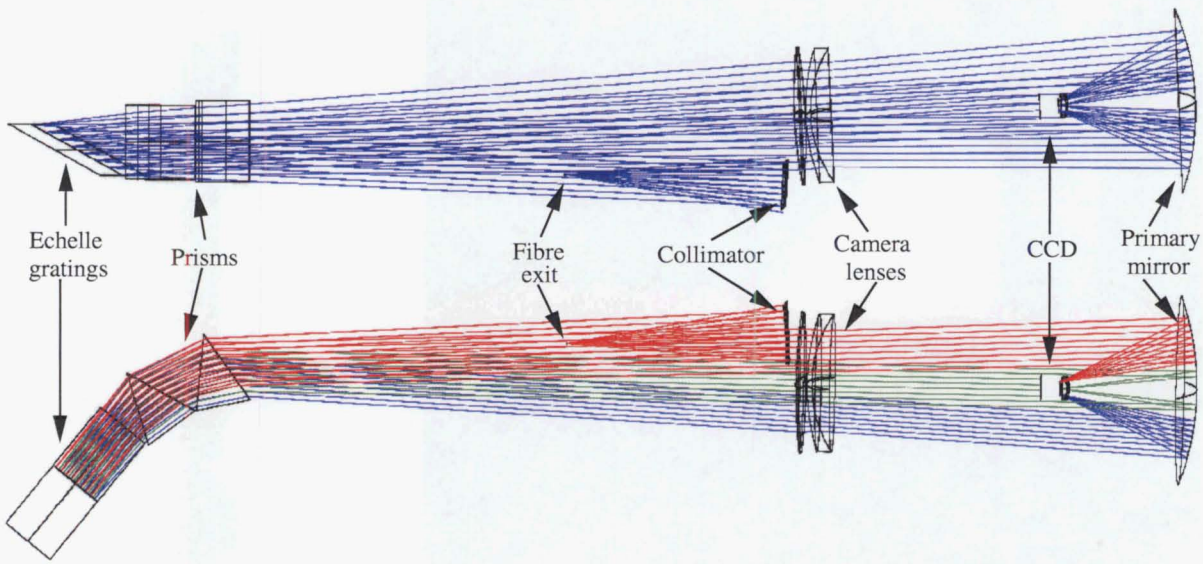

Figure 3.16: CELESTIA optical layout.

Echelle grating

In order for the HRS to be well matched to SALT image quality and to achieve the required resolving powers, a large beam size is needed, which in turn means a large (mosaic) grating. The choices of large échelle gratings ($W > 200$ mm) are quite limited and those available from Richardson Grating Laboratory are listed in Table 3.6. We have not considered custom gratings at all throughout the design of SALT HRS for reasons of financial constraint and delivery lead times.

Initially a design which used a mosaic of two R3 ($\theta_B = 71.54°$ i.e, RGL grating no. 53.453) gratings with 31.6 lines/mm was considered, but the small wavelength extent of each order meant that a large number of orders would be needed to cover the visible spectrum. This would make the inter-order spacing intolerably small, especially if interleaving sky or reference-object orders is to be considered.

Catalogue no.	Ruling Density (lines/mm)	Blaze angle θ_B	$R\#$ ($\tan\theta_B$)	Ruled size (mm) W	L
53.408	79	62°	1.9	210	411
53.401	79	63°	2.0	204	408
53.127	87	63°	2.0	308	413
53.451	316	63°	2.0	204	408
53.411	31.6	63.9°	2.0	204	408
53.121	110	64°	2.1	310	413
53.424	52.67	65°	2.1	204	408
53.417	52.67	69°	2.6	308	408
53.453	31.6	71°	2.9	308	408
53.414	31.6	76°	4.0	204	408
53.425	41.59	76°	4.0	204	410
53.113	94.13	79°	5.1	206	413

Table 3.6: Properties of the large échelle gratings available from Richardson Grating Laboratory RGL.

A grating that was felt to deliver a good compromise between (almost) complete wavelength coverage and sufficient inter-order spacing was the R2.8 ($\theta_B = 70.45°$) grating with 52.67 lines/mm[2]. A mosaic of two such gratings is required and they are to be aligned with a 25 mm spacing. The échelle grating is illuminated at an angle of incidence $\theta = 2.75°$which is a compromise between reasonable path lengths, feasible camera sizes and échelle blaze efficiency.

The use of R4 gratings was not considered at this stage in the design, for reasons similar to those given during the design of HERCULES (see Section 2.1.2). While a detailed design was not attempted, it was realized that prism cross-dispersion would have to be abandoned (because of the need for large angular dispersion); a white pupil design would probably be necessary (to limit the size of the optics); and complete wavelength coverage could only efficiently be obtained by splitting the instrument and using separate blue and red cross-dispersion gratings. Two very fast, wide field, dioptric cameras would be required.

Collimator

The collimator is an on-axis paraboloid which has a focal length of 1160 mm which gives a beam diameter of $B = 305$ mm. This assumes that the fibre input is approximately $f/4.2$ and that the focal ratio degradation factor is $\phi = 1.10$. That is, the output focal ratio is $f/3.8$. The collimator may be truncated to match the pupil on the échelle grating and to avoid conflict with the camera lenses. The collimated beam overfills the échelle grating by 14%. It should be noted that this collimator design could have easily been adapted to a slower off-axis design which would place the fibre exits out of the beam. This would allow for greater flexibility in the fibre feed design. However the initial concept (see below) was designed to accommodate only a set of bare fibres and/or micro-slits and was therefore extremely simple (and low cost).

[2]This is RGL grating no. 53.417 which was ruled for the Keck HIRES. The RGL catalogue erroneously gives a size of 204 × 408. The blaze angle also differs slightly from the catalogue value.

Fibre micro-slits

Given the above échelle and collimator properties a 100 μm fibre must be used to obtain a resolving power of 100 000. As shown in Figure 3.5 the throughput of such a fibre would be extremely poor. For this concept design it is proposed that micro-slits be imprinted directly onto the output face of the larger diameter fibres. The concept was discussed above (Section 3.2.2) and optimal configuration of a range of fibres and micro-slits and their throughputs in median seeing was calculated. The results are repeated here in Table 3.7.

Fibre diam. (μm)	Micro-slit width (μm)	Resolving power ($\lambda/\delta\lambda$)	Throughput (%)
400	–	22900	67.8
350	200	37800	41.9
300	100	75500	21.9
400	70	108000	13.9

Table 3.7: The optimal configuration of fibres and micro-slits and their throughputs in median seeing. The throughput is purely geometric.

Cross dispersion

Like the HERCULES instrument, CELESTIA uses prisms in double-pass for cross-dispersion. Prisms have a clear advantage over gratings in that they make better use of the CCD detecting area and they are also significantly more efficient over a large wavelength range (see Figure 3.17).

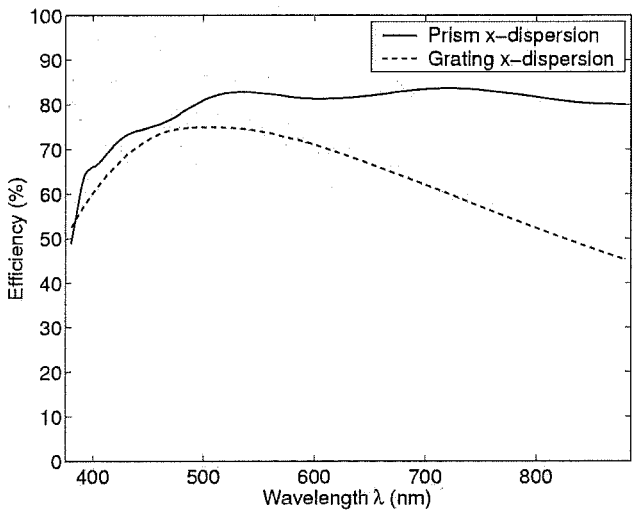

Figure 3.17: The efficiency of two prisms used in double pass compared to the efficiency of a surface relief grating (blazed at $\lambda = 550$ nm). The prisms, made of BK7 (or equivalently, Ohara BSL7), are assumed to have broad-band anti-reflective coatings on each face.

The prism parameters (Table 3.8) have been chosen so that the cross-dispersion will allow the entire visible spectrum to be captured on a 61 mm square frame which would be a mosaic of two adjacent 2k×4k CCDs. This provides for a minimum order separation of 7″. At all but the far red wavelengths it is possible to have one sky fibre at $R = 37800$ when using 350 μm fibres. At $R = 22900$ the 400 μm fibre will only allow a sky fibre to be used up to $\lambda \approx 650$ nm. However, a 300 – 350 μm micro-slit aligned horizontally may be used to minimize the order height to allow a sky fibre to cover the entire visible

spectrum[3]. The prism apex angles have been chosen so that the prism masses are nearly equal. To make the manufacture of these prisms feasible each prism could be formed from two right angle prisms which would have masses similar to the HERCULES prism.

	Prism 1	Prism 2
Apex angle	$\delta_1 = 41.50°$	$\delta_2 = 44.50°$
Angle of incidence	$\theta_1 = 33.05°$	$\theta_2 = 34.06°$
Base	$b_1 = 300\,\mathrm{mm}$	$b_2 = 312\,\mathrm{mm}$
Height	$h_1 = 393\,\mathrm{mm}$	$h_2 = 379\,\mathrm{mm}$
Length	$l_1 = 440\,\mathrm{mm}$	$l_2 = 400\,\mathrm{mm}$
Mass	$M_1 = 61.9\,\mathrm{kg}$	$M_2 = 57.4\,\mathrm{kg}$

Table 3.8: The CELESTIA prism parameters.

Camera

In order to deliver a resolving power of $R = 100\,000$ the focal length of the camera must be $f_{\mathrm{cam}} = 650\,\mathrm{mm}$[4]. With this camera focal length the spectral format is well suited to a 61.4 × 61.4 mm detector; i.e., a mosaic of two 2k × 4k CCDs with 15 μm pixels (see Figure 3.18). The constraints of the échelle grating/collimator geometry, coupled with the desire to minimize the angle of illumination of the échelle (θ), place the camera 3.50 m from the entrance pupil (the échelle grating). In order to capture all the dispersed light the first element of the camera, which is of course a catadioptric design, must be at least 850 mm in diameter. The size of the camera primary mirror has been limited to 1 m for this design. The extremely fast nature of this camera ($\sim f/0.65$ in white light) prohibits an off-axis or folded design. Schmidt camera designs were tried, but none was found to produce the required image quality. It was then realized that Epps and Vogt (1993) came to the same conclusion when designing the camera for the Keck HIRES instrument. After exploring several options involving a variety of aspheric elements, these authors found that an all-spherical design produced satisfactory images. Their design, which involves two large lenses (a biconvex and a meniscus) has been adapted to the much larger pupil distance and faster focal ratio required by CELESTIA and optimized for the use of BK7 glass. The design is essentially a derivative of earlier designs by Houghton (op. cit. and references therein).

The optical design of the CELESTIA camera is shown in Figure 3.19 and the parameters of the camera are given in Table 3.9. Assuming the final element of the camera (the field-flattening lens) is only slightly smaller than the overall cryostat dimensions, the cryostat will vignette at most 30% of the rays for wavelengths near the centre of the CCD frame. Those wavelengths nearer the edge of the field should experience little or no vignetting. The optical performance is superb across the entire visible spectrum (see Figures 3.20 and 3.21).

[3]These calculations were presented to SSWG in October 2001. It was subsequently realized that the effective height of the extracted fibre profile was over-estimated. In fact it is possible to observe two 400 μm fibres at all wavelengths. However, the calculations are still approximately valid when micro-slits are used.

[4]The maximum resolving power obtainable with this focal length is actually $R = 108\,000$

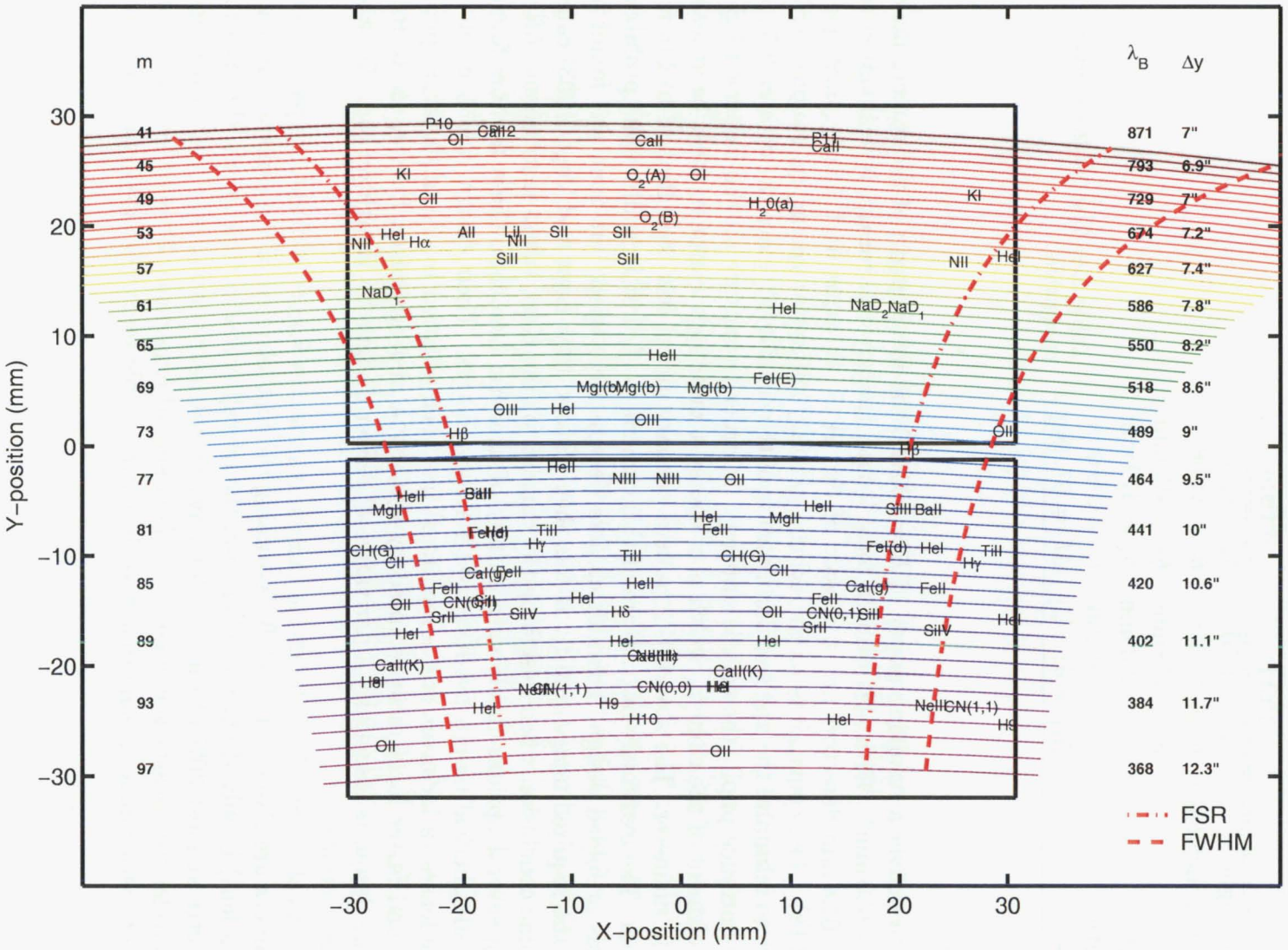

Figure 3.18: CELESTIA spectral format.

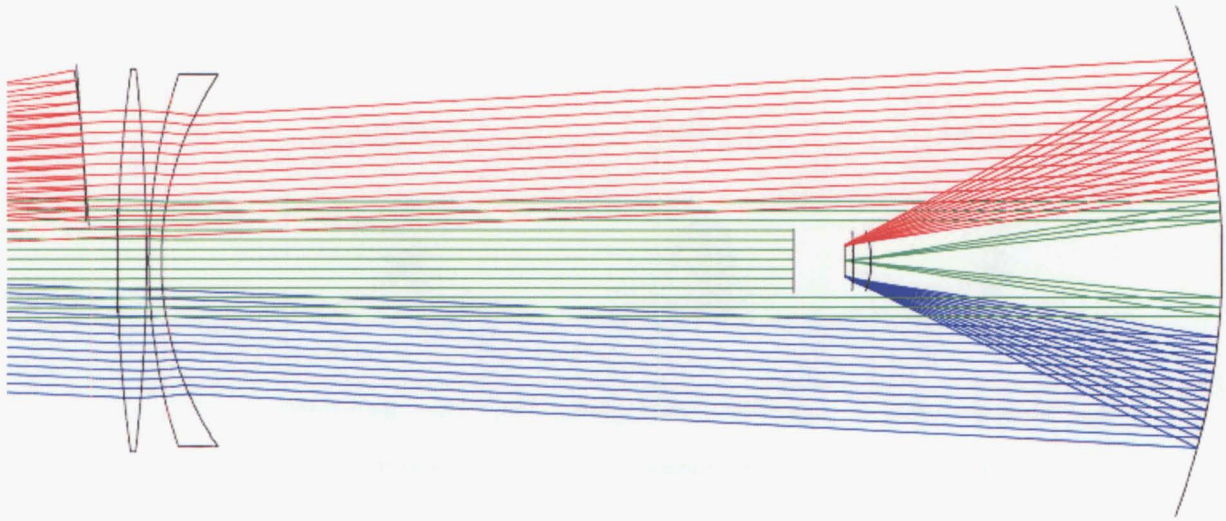

Figure 3.19: CELESTIA camera.

Lens 1:	Radius of curvature	$R_1 = 2794\,\text{mm}$
		$R_2 = -3446\,\text{mm}$
	Thickness	$l = 56\,\text{mm}$
Lens 2:	Radius of curvature	$R_1 = 1194\,\text{mm}$
		$R_2 = 666\,\text{mm}$
	Thickness	$l = 25\,\text{mm}$
Primary mirror:	Focal length	$f = 650\,\text{mm}$
	Diameter	$D = 1.0\,\text{m}$

Table 3.9: Parameters of the CELESTIA camera. All surfaces are spherical and both lenses are BK7.

Mechanical design

The mechanical design of CELESTIA is shown in Figure 3.22. The spectrograph is a completely static structure apart from the ability to focus the CCD. A framework of trusses is used to support the various optical elements and the entire instrument is to be enclosed inside a sealed tank. The tank is completely non-structural and the two end sections are able to be removed by means of an over-head gantry. It was proposed to fill the section containing the dispersive elements with helium in order to avoid temperature and pressure-dependent wavelength shifts. The camera would remain at atmospheric pressure in order to make access to the detector easier.

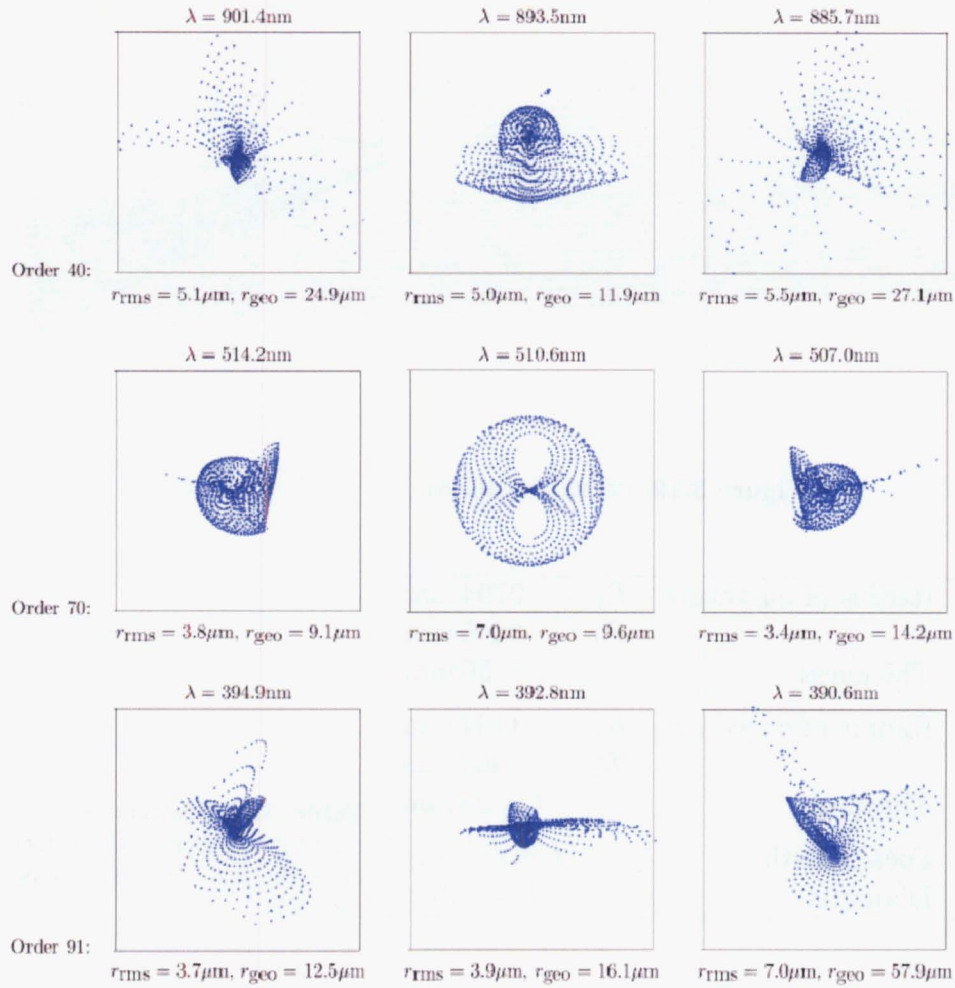

Figure 3.20: Spot diagrams for CELESTIA. Wavelengths are given in the centre and extreme edge of representative orders. All boxes are 2 pixels (i.e., 30 μm.

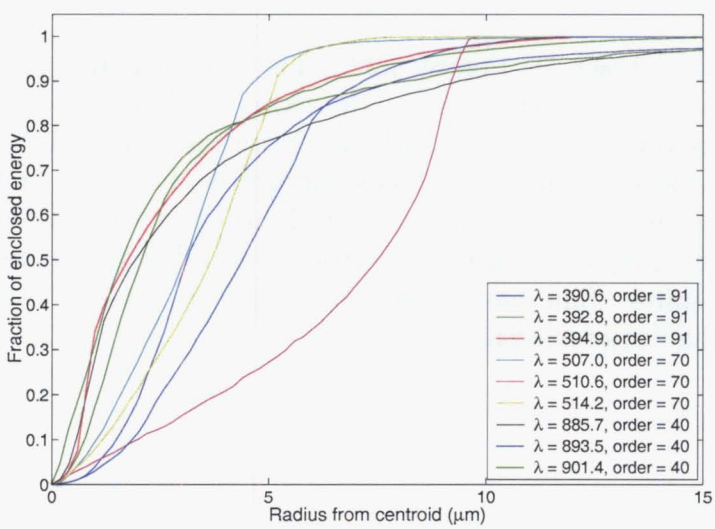

Figure 3.21: CELESTIA geometric encircled energies. The same wavelengths used in Figure 3.20 are shown.

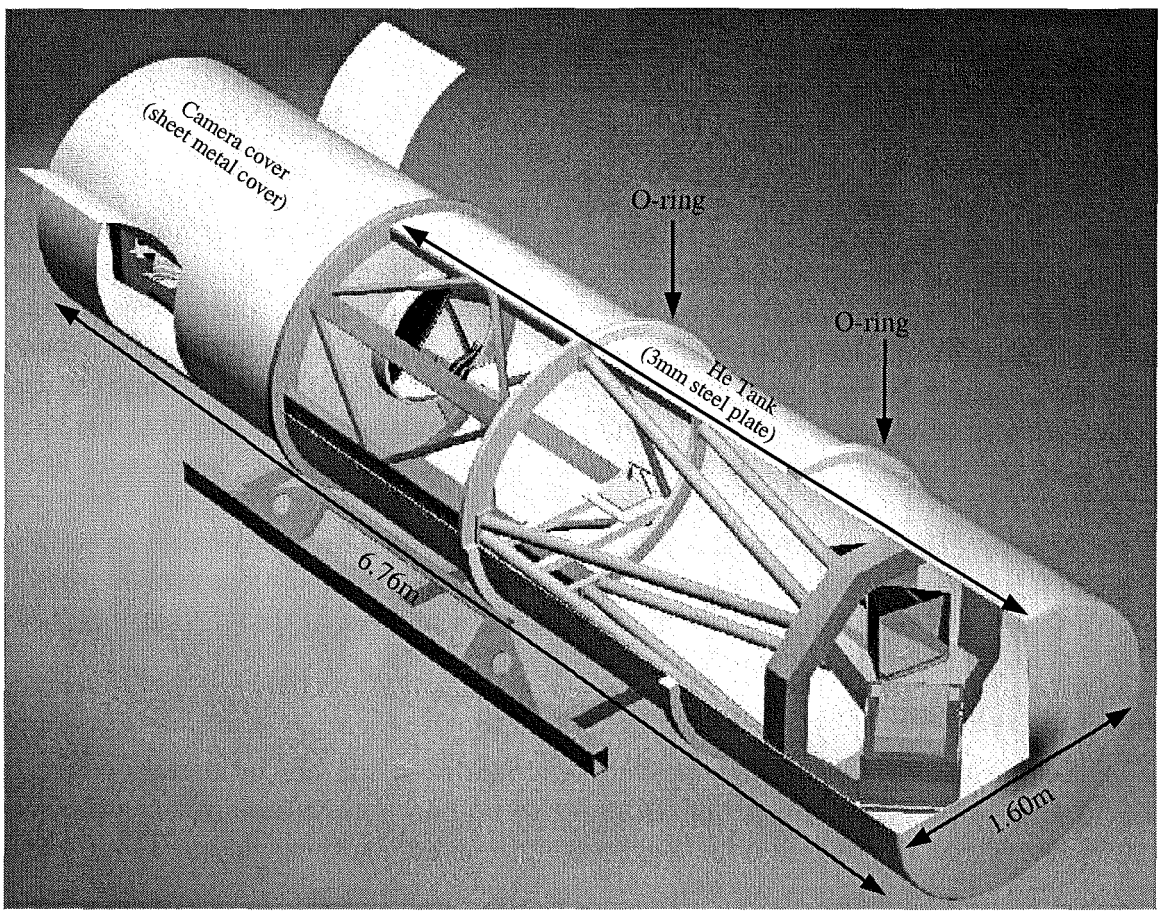

Figure 3.22: Mechanical design of CELESTIA.

3.3.2 Alternative designs

Following SALT meetings in April 2002 a subcommittee of the SALT Science Working Group (SSWG) reviewed the CELESTIA concept and resolved that:

1. As accurate a measurement of the sky background as possible is essential for SALT HRS science. This requirement can be satisfied with one star and one sky fibre.

2. There is sufficient motivation for increasing the inter-order spacing to warrant requesting that the instrument designers investigate this possibility, either with prism or grating cross dispersion.

3. It is imperative for the instrument designers to investigate the effects of a changing pupil on stability of HRS radial-velocity measurements, and weigh the relative merits of an encapsulating tank against other alternatives, e.g., iodine cell, interferometric comb, etc.

Items 1. and 2. reflect the fact that the CELESTIA optical design did not allow sufficient inter-order spacing for an additional sky fibre to be used at all resolving powers and wavelengths. However, as noted above, although the inter-order separation was misrepresented to SSWG this conclusion does not change. The absence of a sky fibre in the red-most wavelengths was felt to be a particular problem as this is where night-sky contaminations becomes particularly severe. The third item is simply a misunderstanding of the principle of enclosing the spectrograph inside a helium or vacuum chamber. This measure is only one aspect of an attempt to make the HRS as stable as it can possibly be, and it does not preclude the use of other measures (e.g., iodine cell and/or fibre double-scrambling) which can further enhance the instrument's stability. Both these options remain possible.

With these resolutions in mind we have explored a number of design concepts below.

Echelle grating and cross-dispersion options

The choices of échelle grating and method of cross-dispersion are intimately connected to the amount of inter-order spacing. In order to find an optical design which increased the inter-order spacing, several échelle grating options among those detailed in Table 3.6 were explored. These gratings were:

Catalogue no.	Ruling density (lines/mm)	Blaze angle θ_B	R# ($\tan\theta_B$)	Ruled size (mm) W	L
53.417	52.67	70.45°	2.8	308	408
53.121	110	64°	2.1	310	413
53.127	87	63°	2.0	308	413

Assuming a beam size $B = 308$ mm, grating 53.417 gives a resolving power of $R \approx 20\,000$ if 500 μm (1.8″) fibres are used. Because gratings 53.127 and 53.121 are ruled at a shallower blaze angle, the same fibre will give $R \approx 20\,000$ only if a beam size of $B = 350$ to 400 mm is used. This beam will overfill both the length and width of the grating mosaic. However a 365 mm beam overfills the R2 gratings by approximately the same amount (~15%) as a 300 mm beam overfills an R2.8 grating with the same dimensions.

The use of BK7 prisms continues to be assumed for cross-dispersion and for each échelle grating an optimum prism apex angle was found which allowed between two and three objects per order to be observed. Three objects are required in order to allow a "nod and shuffle" mode (see Section 3.2). The criteria for sufficient inter-order spacing is that the distance between adjacent objects (or orders) should be at least $3 \times h$ where h is the height of the fibre image on the detector. This allows an optimal extraction slit of $2.5 \times h$ to be used while still allowing the background to be sampled. It is important to note that the extracted height of a fibre is somewhat less than the height of the dispersed fibre. This is for the same reason that a fibre will give a greater resolving power than a slit (see Section 1.2.10)[5]. The minimum apex angles of two identical prisms in double-pass for each of the grating options are given in Table 3.10. Figures 3.23 to 3.33 show the spectral format for some of these grating/prism configurations. A discussion of the various options follows.

Catalogue no.	Ruling density T lines/mm	Blaze angle θ_B	Prism apex angle (α_P) Number fib. = 2	Number fib. = 3
53.417	52.67	70.45°	47.7°	57.4°
53.121	110	64°	23.3°	32.8°
53.127	87	63°	28.3°	38.8°

Table 3.10: Minimum prism apex angles for various échelle gratings. The use of two prisms in double-pass is assumed. For échelle grating no. 53.417 up to three prisms may be required.

Figures 3.23 and 3.24 show the spectral format for the R2.8 échelle grating with 52.67 lines/mm with a pair of 47.7° and 57.4° prisms respectively. The first configuration is essentially the CELESTIA spectral format (Figure 3.18), but with slightly more cross-dispersion so that two fibres can be observed at all wavelengths. The camera focal length is also slightly reduced to allow the entire spectrum to fit on a mosaic of two 2k × 4k CCDs with 15 μm pixels. This would reduce the maximum possible resolving power from around $R_{\max} = 100,000$ to $R_{\max} = 85,000$. The increased cross-dispersion which allows three objects to be observed places a large portion of the spectrum off the detector. These wavelengths could be recovered by either moving the detector or by rocking the prism(s). Alternatively, the camera focal length could be reduced (to $f_{\text{cam}} = 500\,\text{mm}$) which would limit the maximum resolving power to $R_{\max} \approx 80,000$. Such a camera would be even faster than the one proposed for CELESTIA and is possibly not feasible.

The spectral formats shown in Figures 3.25 and 3.26 are for an R2 échelle grating with 110 lines/mm with pairs of 32.8° and 40° prisms respectively. The pair of 32.8° prisms could be replaced by a single 53.8° prism, while still allowing three objects to be observed per order. A more natural format is obtained with the 40° pair of prisms (Figure 3.26). This allows nearly 4 objects to be observed per order. However, because of the high line density of this échelle grating the angular extent of the orders is much greater than can be captured by a 60-mm wide CCD. The missing wavelengths could be recovered by tilting the échelle grating; however this is not an attractive solution for reasons of stability. A larger format CCD (i.e., a 3 CCD mosaic) would reduce the lost wavelengths. However a tiltable grating would still be required to obtain complete coverage. The large inter-order

[5]This aspect was neglected when the spectral formats were presented in October 2002 (Barnes and Albrow, 2002) but this has been corrected here.

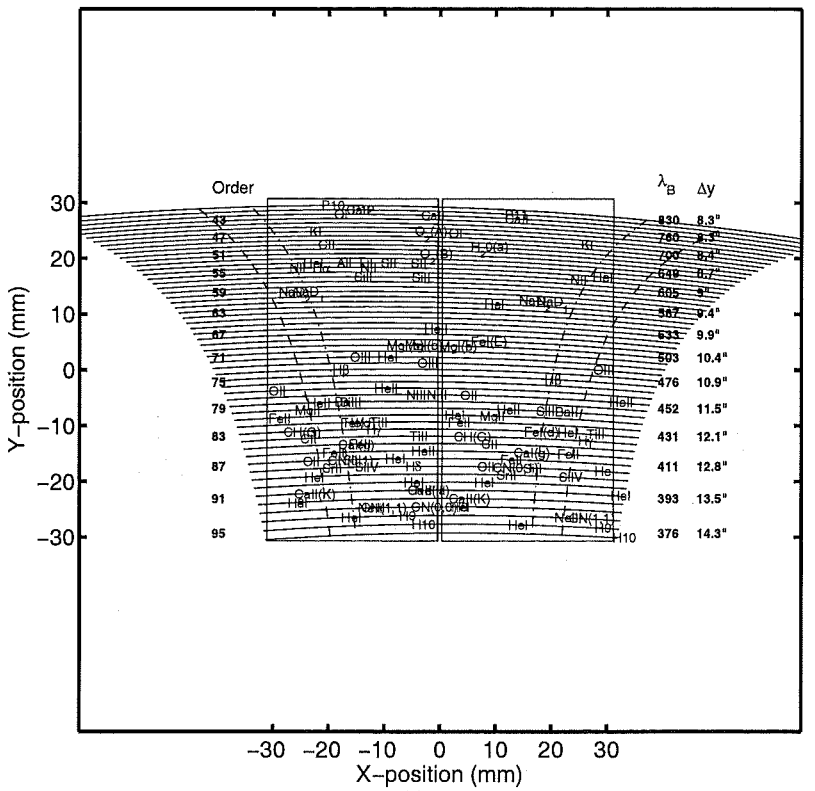

Figure 3.23: The spectral format for an R2.8 échelle grating with 57 lines/mm. Cross-dispersion is with two 47.7° prisms.

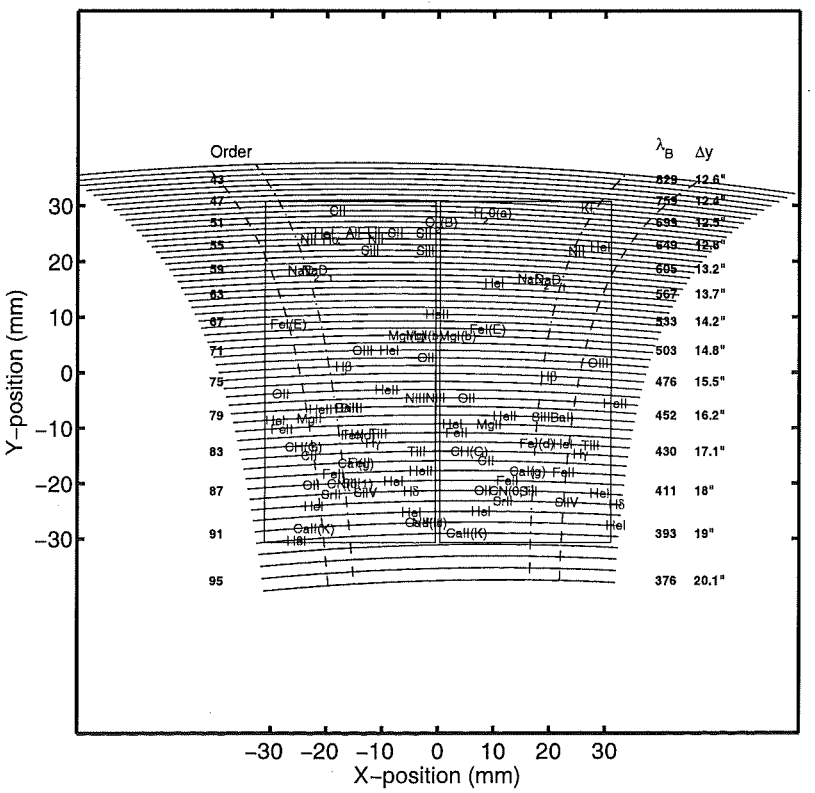

Figure 3.24: The spectral format for an R2.8 échelle grating with 57 lines/mm. Cross-dispersion is with two 57.4° prisms.

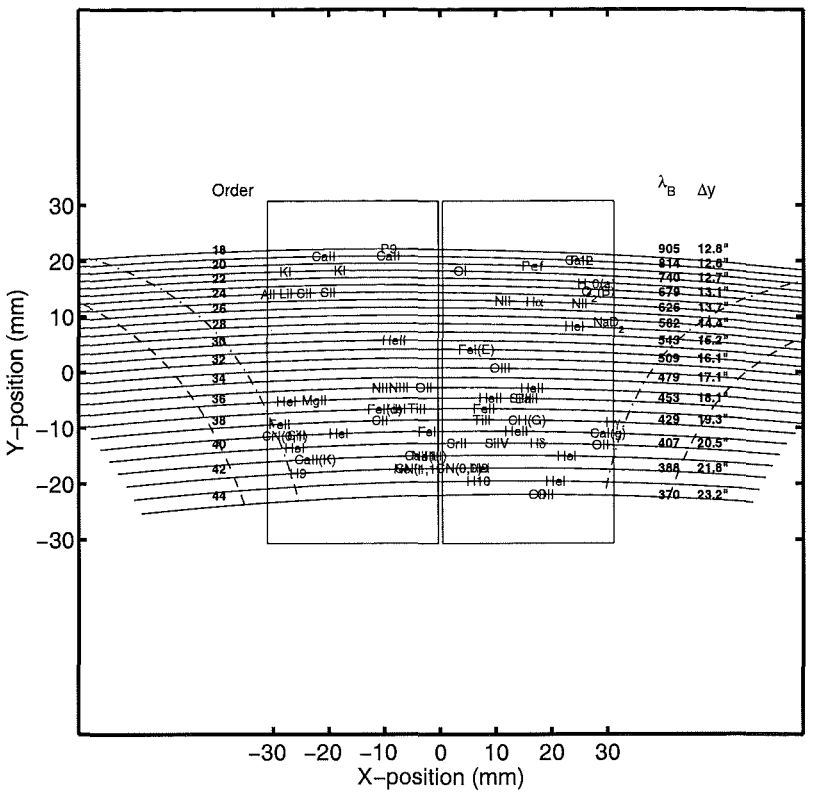

Figure 3.25: The spectral format for an R2 échelle grating with 110 lines/mm. Cross-dispersion is with two 32.8° prisms.

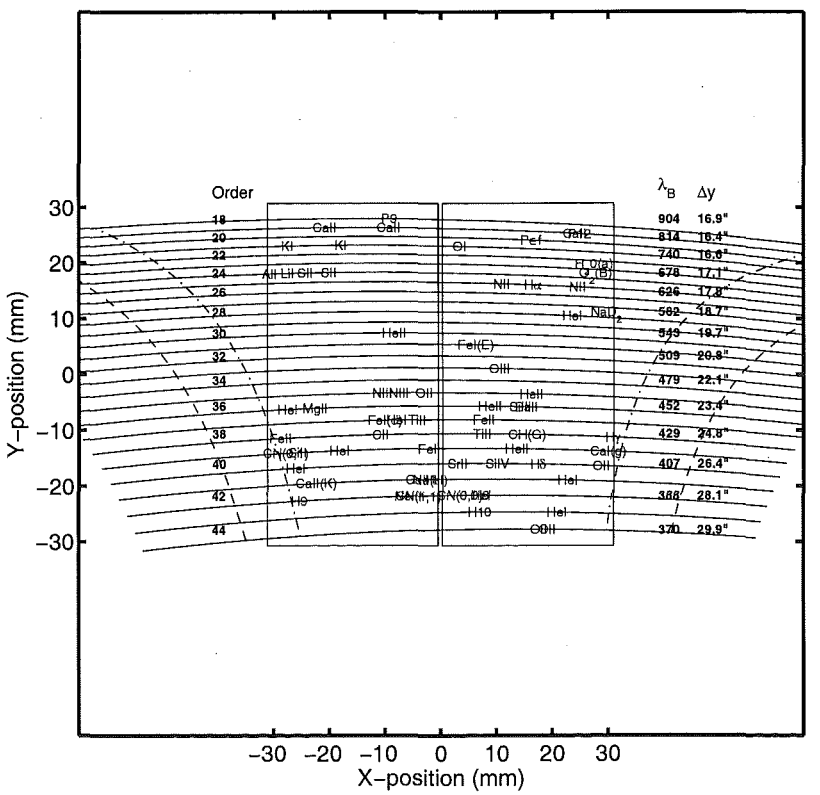

Figure 3.26: The spectral format for an R2 échelle grating with 110 lines/mm. Cross-dispersion is with two 40.0° prisms.

separation makes this option extremely efficient at high resolutions as the space between orders could be used to place either fibre bundles or sliced fibre images.

The final échelle grating investigated was an R2 with 87 lines/mm. The spectral formats with this gratings are shown in Figures 3.27 and 3.28. These spectral formats are obtained using a pair of 38.8° prisms in double-pass. The requirement that up to three objects be observable at all wavelengths is met. However, the wavelength coverage is not complete above 550 nm if a mosaic of two 2k × 4k CCDs with 15μm pixels is used. Complete wavelength coverage may be obtained if the échelle grating can be tilted (Figure 3.28). A camera capable of capturing these spectral formats was developed and is shown in Figure 3.29. The camera design is an all-spherical catadioptric system, with three large lenses and has been derived from the CELESTIA camera. The optical performance is superior to the earlier two-lens design and is a precursor to later designs which require multiple elements in order to obtain good image quality over much larger field angles. The spot diagrams for a range of wavelengths are shown in Figure 3.30. At nearly all wavelengths the encircled energy is better than 80% within one pixel.

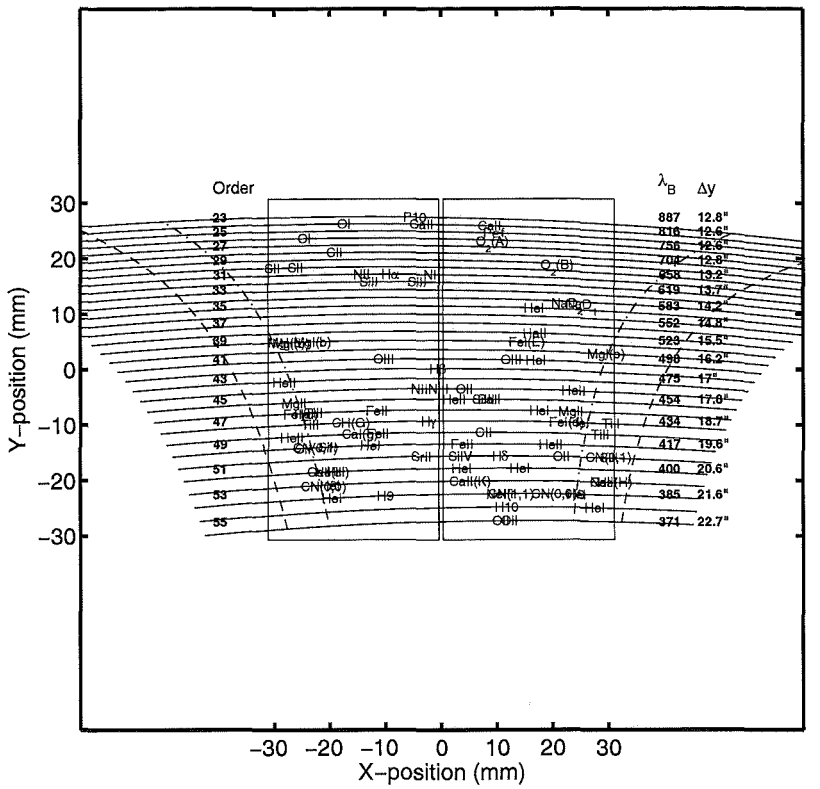

Figure 3.27: The spectral format for an R2 échelle grating with 87 lines/mm. Cross-dispersion is with two 38.8° prisms.

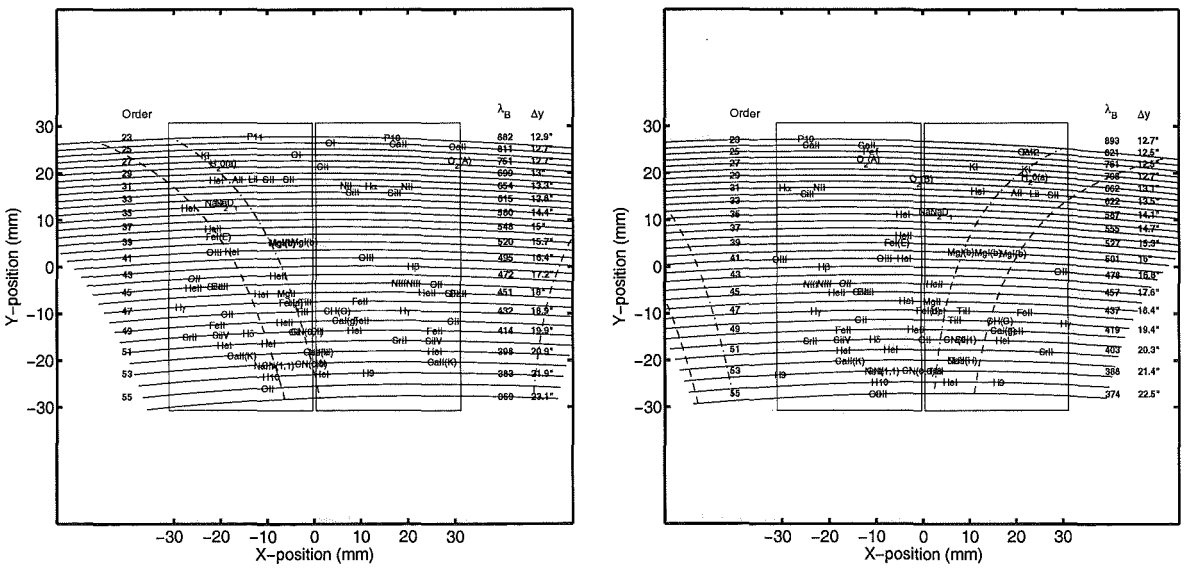

Figure 3.28: The spectral format for an R2 échelle grating with 87 lines/mm. Cross-dispersion is with two 38.8° prisms. Complete wavelength coverage can be obtained by tilting the échelle grating by $\Delta\theta = \pm 0.7°$.

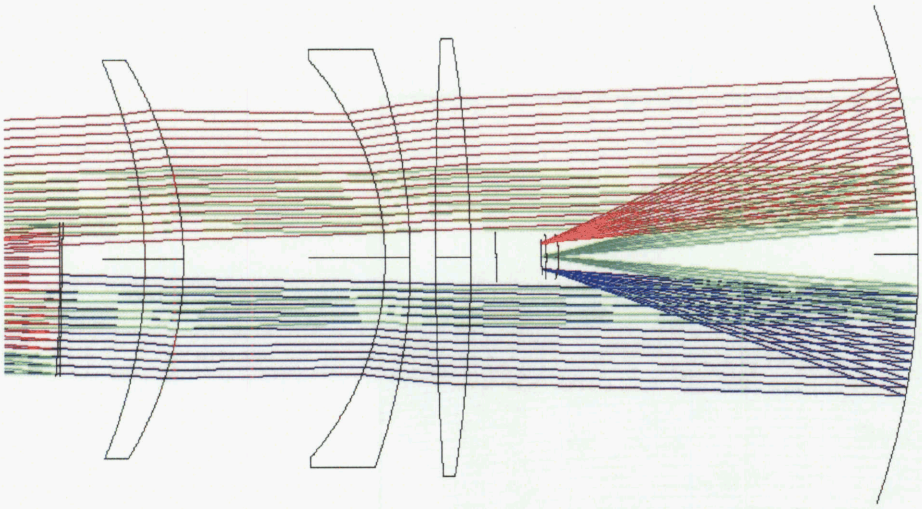

Figure 3.29: SALT HRS camera design concept. The design is derived from the CELESTIA camera but produces superior image quality over a larger field. The camera has been designed for an R2 échelle grating with 87 lines/mm and a pair of 40° prisms.

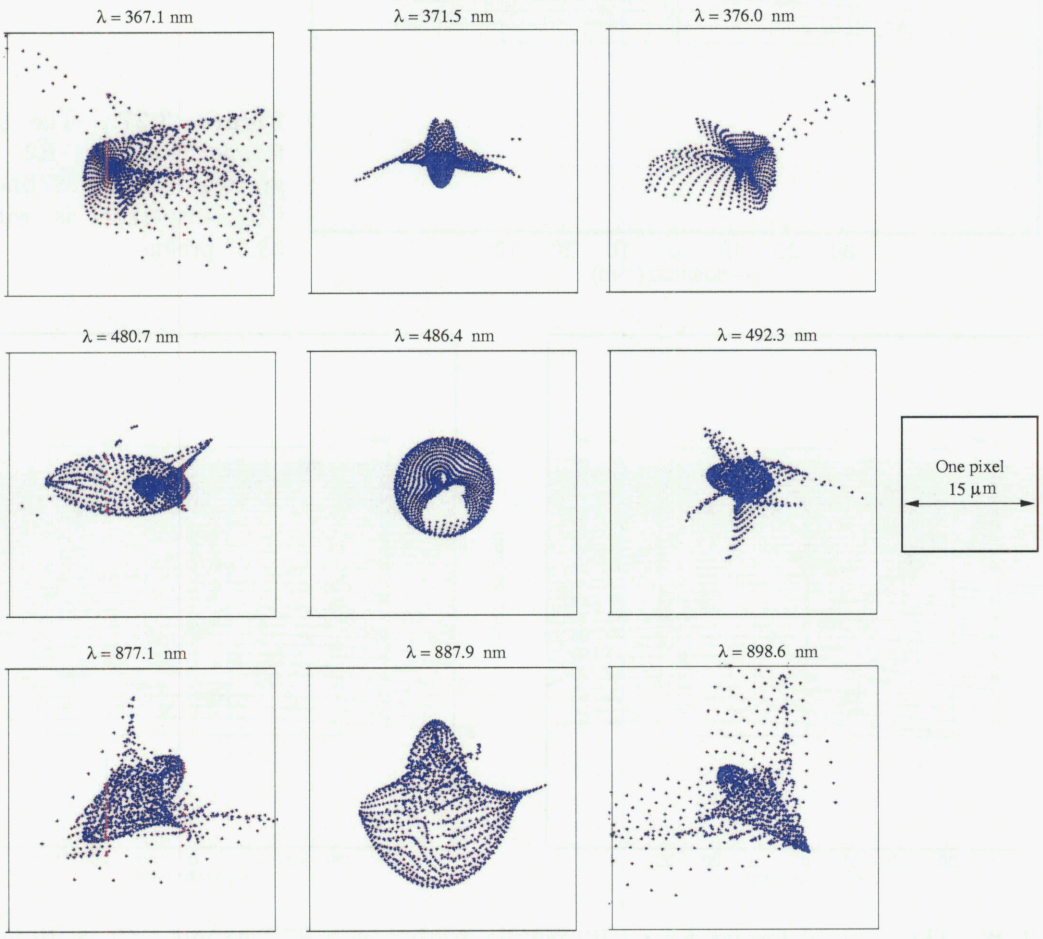

Figure 3.30: SALT HRS concept camera image quality. The top, middle, and bottom rows show wavelengths from orders 55, 42 and 23 respectively. The wavelengths shown are those that strike the left edge, centre and right edge of the detector.

3.3.3 SALT HRS R2

At SALT meetings in April 2003 the final design discussed above was presented. The option of allowing a tiltable échelle grating was rejected in favour of increasing the field of the camera and using a mosaic of three 2k × 4k CCDs. This spectrograph option, hereinafter referred to as SALT HRS R2, was developed in detail and was presented for a Preliminary Design Review (PDR) in 2003 September. The PDR Optical Design Definition Document can be found in Appendix D. The design of SALT HRS R2 necessitated the use of large prism cross-dispersers and the development of a very large catadioptric camera (see Figures 3.31 and 3.32). The spectral coverage is however complete (see Figure 3.33).

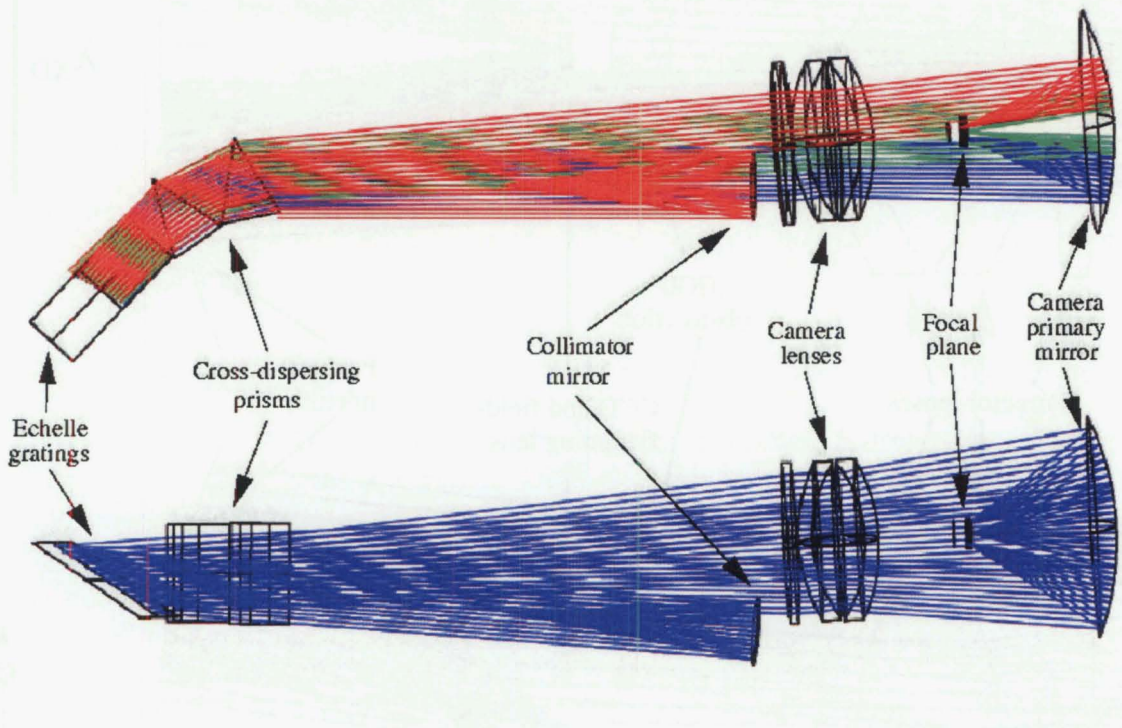

Figure 3.31: Plan and elevation views of SALT HRS R2. The collimator is shown on axis with a focal ratio of $f/3.8$.

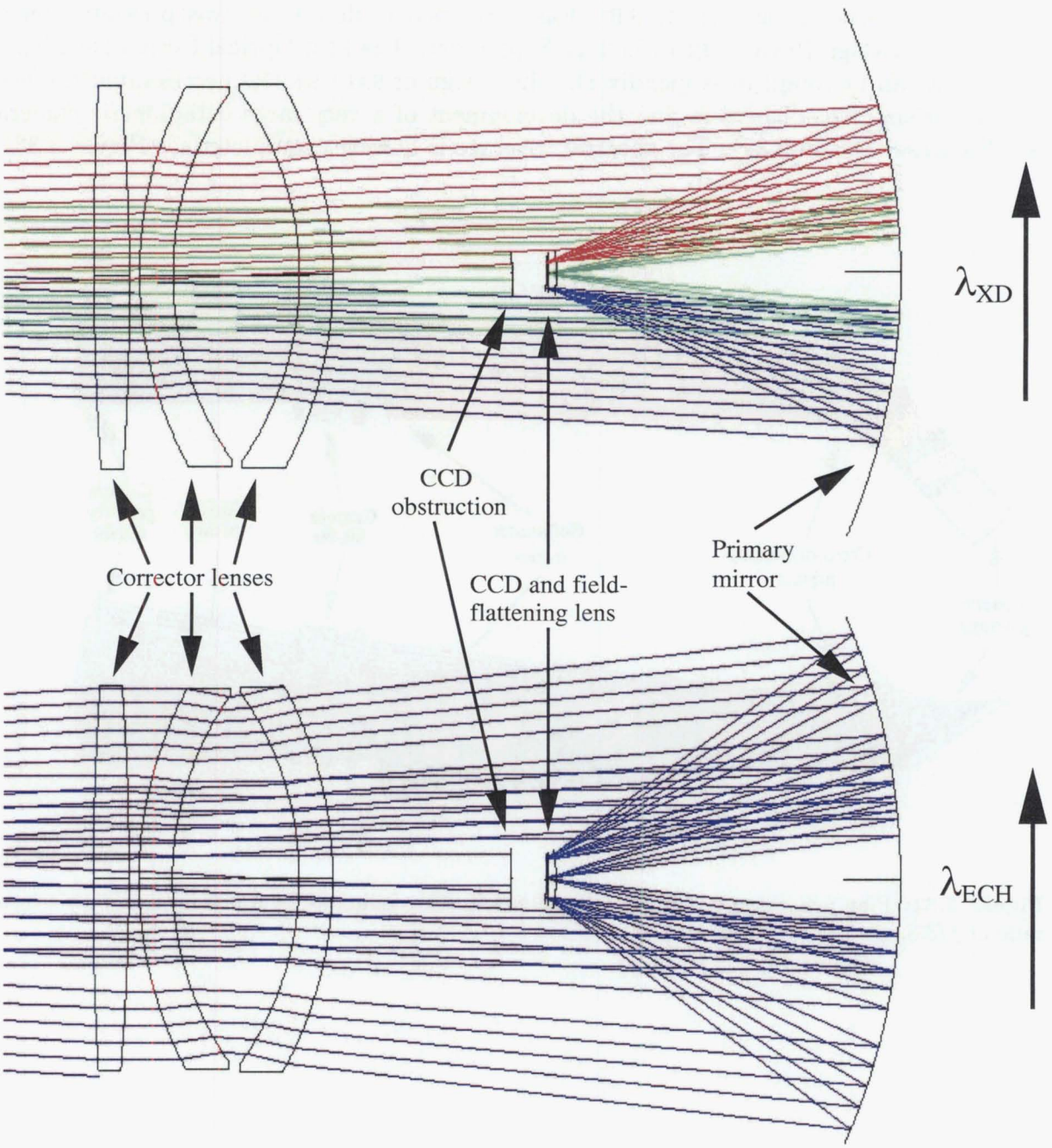

Figure 3.32: The SALT HRS R2 camera. The CCD obstruction approximates the position of the cryostat.

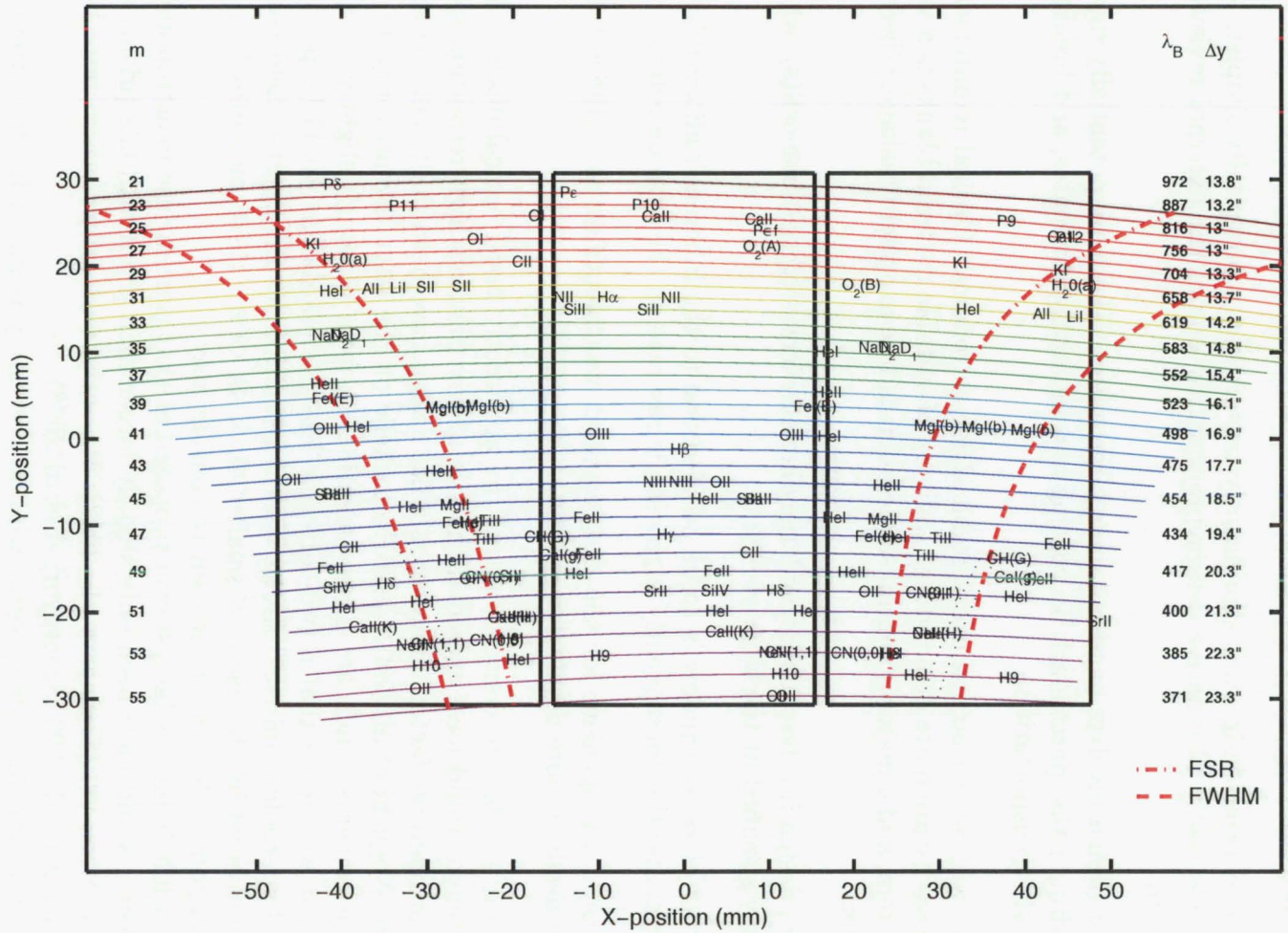

Figure 3.33: SALT HRS R2 spectral format. The échelle grating has 87 lines/mm and cross-dispersion is with two 40°prisms used in double-pass. The wavelength coverage obtainable with a mosaic of three 2k × 4k CCDs is almost complete (apart from the gap between CCDs). The inter-order separation is sufficient for more than three fibre at the lowest resolving power.

Preliminary Design Review result

Formally the SALT HRS R2 did not pass the Preliminary Design Review (PDR) held in September 2003. This was because of concerns about the management (the schedule was perceived somewhat short) and potential costs (some of which may have been underestimated). The optical design itself did formally pass, but there were concerns. These have been summarized by the SALT project scientist (Buckley, 2003); namely:

1. whether the current design was significantly better than a potentially simpler, less risky and less costly alternative design proposed by one of the external reviewers (B. Delabre);

2. the current design involves handling some large optics. There are potentially significant handling risks, particularly in coating and mounting the lenses, and breakage risks in their transportation;

3. the prisms will be the largest ever produced for astronomy. Optical requirements for homogeneity are quite demanding. Delivery of suitable material blanks is a very long lead item, and a major potential single-point failure in either breakage, schedule or cost risk;

4. the camera design involves mounting large diameter lenses (three) in a cell(s), which were poorly specified at the time of PDR;

5. use of a BK7 cryostat window is to be avoided due to the inherent radioactivity of the material and the consequently high cosmic ray rate on the CCD detectors;

6. the heat pipe arrangement for the CCD cryostat was identified as a difficult and risky area needing more detailed attention.

Items 2, 3 and 4, relate to concerns about the apparently novel optical design. The proposed instrument would have exceeded the size of any previous high resolution spectrograph by a considerable factor. However, similar design have been built. For instance, the Subaru HDS (Noguchi et al., 2002) and Hectochelle on the MMT (Szentgyorgyi et al., 1998) both have cameras which are nearly identical in form although slightly smaller. During the PDR it was noted that a two-corrector lens camera design would be possible with a slightly hyperboloid mirror. Along with a reduction in unvignetted field coverage (perhaps motivated by the use of a smaller 4k $\times$ 4k CCD), these measures had the potential to bring down the size of the camera considerably.

The prisms, while being the largest ever proposed at that time for use in astronomy, if made as four pairs, would have been only slightly larger than the HERCULES prisms and those used in the Keck ESI (Sheinis et al., 2002). Recently, even larger prisms have been proposed (Fabricant et al. 2003, Szentgyorgyi et al. 2003).

The issue of the CCD (and its cyrostat window) certainly required further attention. Again numerous working examples exist which suggest that the CCD concept was technically feasible, although this would only have been demonstrable after a not inconsiderable effort.

However, in light of these comments, in particular item 1., an R4 dual beam design has been developed and is presented in the following section.

3.4 R4 designs

In order to make a direct comparison with SALT HRS R2 (see Section 3.3.3) the same baseline functional requirements are demanded of any alternative R4 design. That is, the wavelength coverage, resolving powers and stability requirements are assumed to be unchanged. It is possible that along with a change in the form of the spectrograph some additional functionality could be provided; or that with a change in requirements of either design, the performance could be substantially improved. Such possibilities are beyond the scope of this investigation and will not be discussed in any detail here. In Section 3.4.1 the initial R4 concept is detailed. Section 3.4.2 provides a comparison of the SALT HRS R2 with the R4 design described below.

3.4.1 Conceptual design

The form of the SALT HRS R4 was suggested by one the PDR external reviewers, B. Delabre and is based in part on a design for an HRS for the 4-metre SOAR telescope (Castilho et al., 2003). The design is also quite similar to the UVES instrument on the VLT (Dekker et al., 2000) which uses the white pupil concept of Barrane as adapted by Delabre (op. cit. and references therein). Unlike UVES however, we are assuming that both the blue and red arms use a single échelle grating. A dichroic filter will be used to split the instrument into two beams after échelle dispersion, and each beam will use dedicated cross-dispersers and dioptric cameras.

An initial design, shown in Figure 3.34, uses a single échelle grating blazed at $\theta_B = 76.0°$ with a groove density of 41.5 grooves/mm. A single parabolic mirror is used off-axis, first as the collimator and then again, after échelle dispersion, to form an intermediate focus. At this point the red and blue arms are split by a dichroic at a nominal wavelength of 550 nm. The blue arm then uses the collimator mirror to form an image of the échelle grating ("the white pupil") at the point of cross-dispersion, while the red arm uses a smaller spherical mirror. A novel feature of the design is the assumption that volume phase holographic (VPH) grisms can be used for cross-dispersion. This is only possible because of the recent development of such gratings with high efficiencies over broad bands (see Barden et al., 2000). A pair of flat fold mirrors allows convenient placement of the cameras.

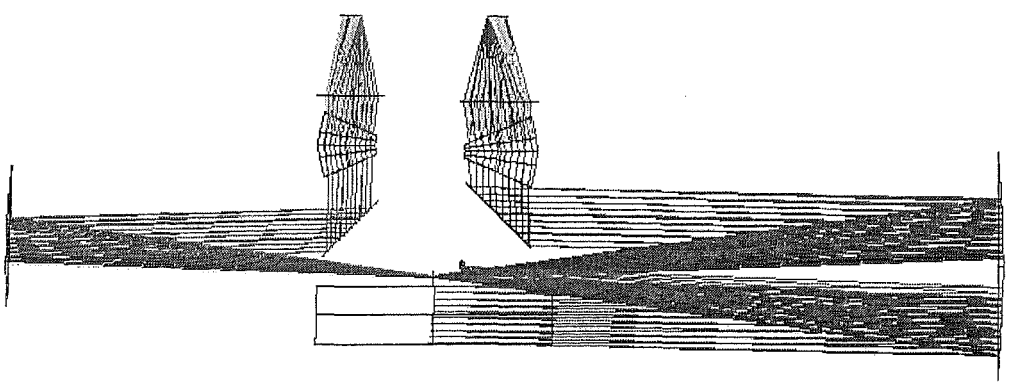

Figure 3.34: The SALT HRS R4 conceptual design. The red camera is on the left and the blue camera is on the right. Both cameras are depicted as paraxial elements.

Fibre input

The use of image slicers is proposed for SALT HRS R4. The form of the fibre input and image slicer (including transfer optics) is assumed to be similar to the R2 design (see Section 3.2) except that the minimum inter-order spacing is different. The parameters of the image slicers and their geometrical throughputs are given in Table 3.12 (see also Appendix E.2.2).

Collimator

The collimator uses a portion of an 800 mm diameter parabola that also serves (twice) as the blue arm white pupil mirror. It would be possible to use a smaller off-axis element, which would also double as the first white pupil mirror. However this mirror would be quite large (i.e., > 400 mm) and would probably necessitate the manufacture of the large mirror in any case. It would then also be necessary to manufacture an additional blue white pupil mirror (which may be spherical). The choice of focal ratio ($f/2.5$) is somewhat arbitrary, although a slower design would require a larger mirror and a faster design would be increasingly difficult to manufacture.

Echelle grating

The splitting of the spectrograph into the red and blue arms occurs near the intermediate focus following the first white pupil mirror. This enables the use of a single échelle grating mosaic, where each grating has the parameters given in Table 3.11. This is not necessarily ideal and more efficient use of the cross-dispersers and camera/detector could possibly have been made if the choice of échelle grating were optimized for each of the red and blue arms. It was proposed to assemble the grating from two individual gratings which will be aligned mechanically into a single mosaic with dimensions 855×204 mm. This would leave a gap of 35 mm between the gratings. With a collimated beam size of $B = 200$ mm there is no overfilling.

Parameter	Specification
Blaze angle, θ_B	76.0°
Groove density, T	41.5 grooves/mm
Grating ruled width	204 mm
Grating ruled length	410 mm

Table 3.11: Echelle grating parameters for SALT HRS R4.

Dichroic

The dichroic has a nominal wavelength division of 555 nm. It is placed at the $f/2.5$ focus of the intermediate échelle spectrum. To capture all the light it must be at least 50×350 mm in size.

Pupil mirrors

The pupil imaging in the blue arm is performed by the large parabolic mirror that also serves as the collimator. The red arm white pupil mirror is a 500 mm diameter spherical

mirror with a 3 m radius of curvature. This allows the white pupil to be demagnified by 1.33 (from 200 mm to 150 mm), which is better suited to the use of VPH gratings.

The fold mirrors

A pair of fold mirrors is placed just in front of the white pupil to make room for the pair of cross-dispersers and cameras. The blue arm fold mirror must be 320 mm in diameter while that for the red arm is 280 mm in diameter. Although the footprint on the mirror will be elliptical, it is assumed that they would be manufactured circular. These mirrors can be repositioned in order to make the camera focal planes approximately coplanar.

VPH cross-dispersers

The development of VPH gratings and their potential for use in astronomical instrumentation has been described by Barden et al. (2000). A report by Clemens and Seagroves (1999) gives an overview of the theory of VPH gratings and an extensive list of technical information can be found on the NOAO VPH website[6].

It is possible to tune the wavelength of peak efficiency by altering the angle of incidence onto the grating. However, if the grating is rotated, the camera must either be articulated, so that it can move into the dispersed beam, or a system of two counter-rotating mirrors employed (i.e., the "butterfly mount", see Bernstein et al., 2000). Another possibility is to immerse the grating inside a prism with apex angles chosen so that the mean deviation is zero. In the case of a minimum deviation grism the efficiency can be tuned simply by rotating the grism about its central axis. This would not significantly alter the spectral format, and the camera may remain fixed (except, perhaps, for a small focus correction). The second mirror of the butterfly mount is therefore not required. It is also possible to increase the overall efficiency of a VPH grating by ensuring that every wavelength reaches the grating at close to the ideal angle of incidence. This may be achieved by using a prism to disperse each wavelength before the grating, although this dispersion must be in the opposite direction to the grating dispersion (Delabre, personal communication). This technique has not been investigated further.

The choice of cross-dispersers depends entirely on the desired wavelength range and order separation. In order to be able to make a direct comparison with the R2 design the R4 design should be capable of at least the same wavelength coverage. Because the amount of CCD real estate is fixed, it is this constraint that limits the order separation. With unity pupil magnification, the blue grating requires $T = 950$ lines/mm with $\theta_i = 12.3°$ ($\lambda_{mid} = 450$ nm). This provides for a nominal wavelength range from 370 to 565 nm in 44 orders ($m = 125$ to 82) and a minimum order separation is $11.5''$. A red cross-disperser used with unity pupil magnification would require a 450-line/mm grating in order to achieve the same minimum order separation. This is considered a low density for the efficient use of VPH gratings. Hence a demagnification of 1.33 in the pupil is required in order to allow a slightly higher groove density (i.e., $T = 600$ line/mm) to be used. The short focal length transfer mirror, used only in the red arm, produces this demagnification.

[6] http://www.noao.edu/ets/vpgratings/

Camera and detectors

The blue camera will be limited to a maximum resolving power of $R = 80\,000$ with two (15 μm) pixel sampling. The focal length required is $f_{\rm cam} = 301$ mm which gives a monochromatic focal ratio of $f/1.5$. With a 30.5 × 61 mm focal plane (i.e., a single 2k by 4k CCD with 15μm pixels) a single FSR can be observed at all wavelengths from 380 to 560 nm (see Figure 3.35). After a 1.33 pupil demagnification the focal length required for two pixel sampling of $R = 100\,000$ is $f_{\rm cam} = 283$ mm. This is also a potentially very challenging focal ratio ($f/1.4$) with a 12.2° field of view – assuming that at least two 2k by 4k CCDs (with 15 μm pixels) are used. The spectral format of the blue camera is shown in Figure 3.36. It may also be possible to use a single 4k by 4k detector with 15 μm pixels. Cameras for each of the blue and red arms were designed by D. Jones[7] (with some assistance by the author) and are described further in Appendix E.

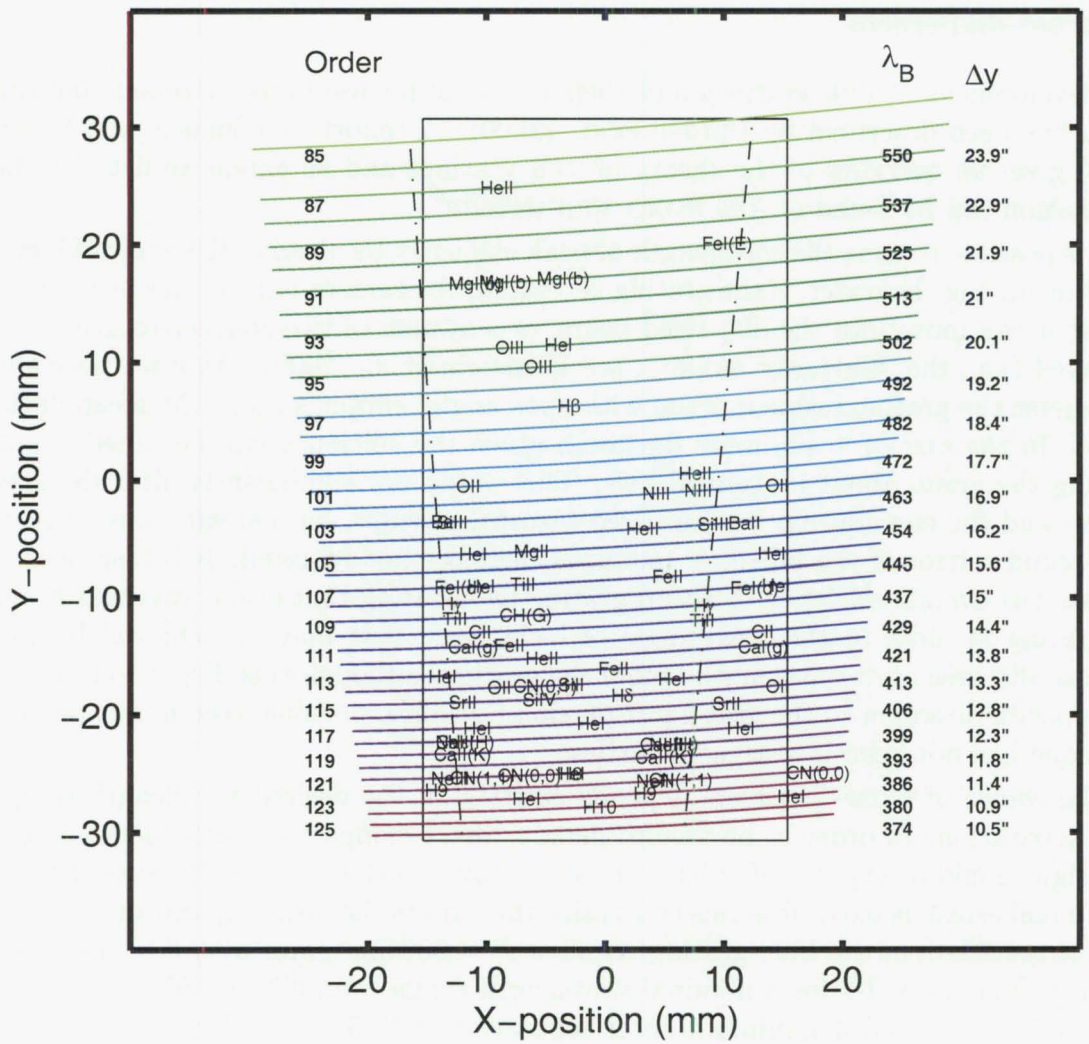

Figure 3.35: The SALT HRS R4 blue camera spectral format. The orders are plotted over two free spectral ranges and the dot-dashed line shows the extent of one free spectral range. The outline of a single 2k by 4k CCD with 15 μm pixels is shown in bold.

[7]Prime Optics, Queensland, Australia.

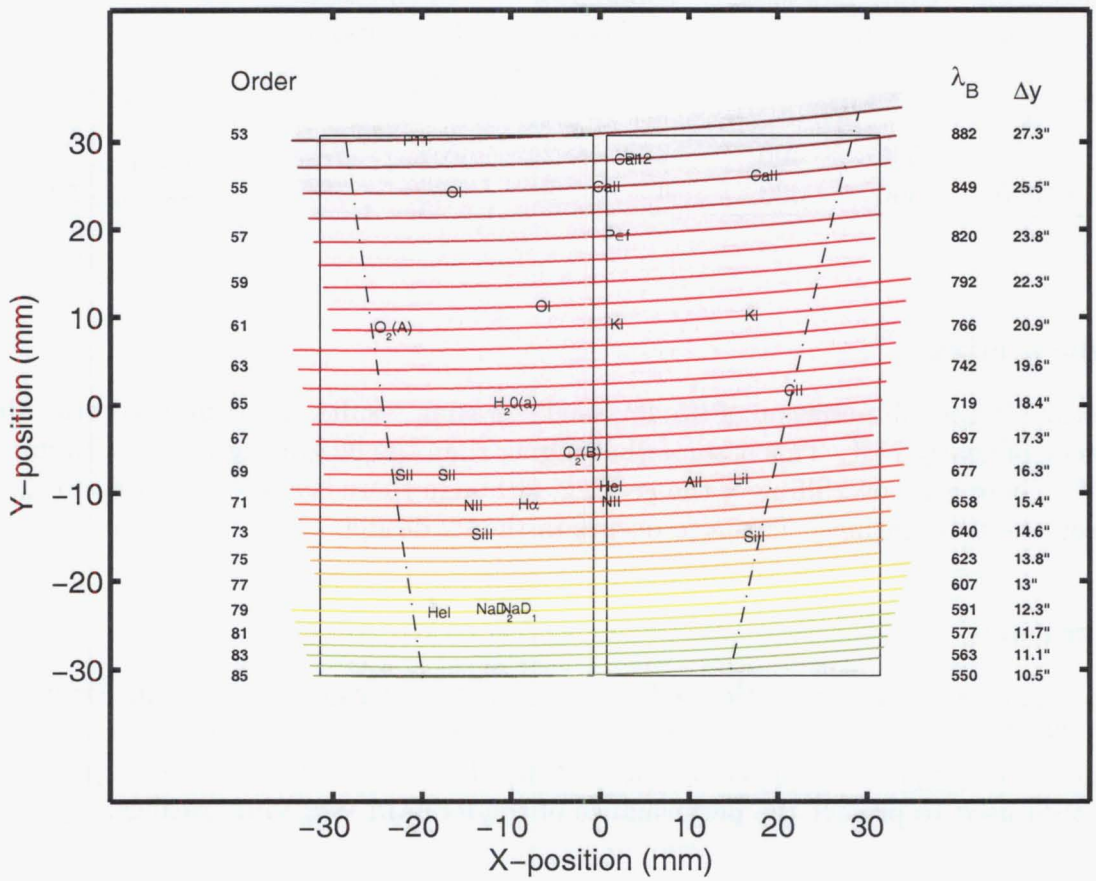

Figure 3.36: The SALT HRS R4 red camera spectral format. The orders are plotted over two free spectral ranges and the dot-dashed line shows the extent of one free spectral range. The outline of a mosaic of two 2k by 4k CCDs with 15 μm pixels is shown.

3.4.2 Comparison of efficiencies: R2 vs. R4

Fibre and collimator

The transmission of the fibres, transfer and fold optics, image slicers and collimator are assumed to be identical to the R2 design, except that the geometrical transmission of the image slicer depends on the inter-order spacing. The parameters of the image slicers, which have been optimized for an 11.5″ order separation (which allows complete wavelength coverage), are given in Table 3.12.

Resolving power	Fibre diameter (microns)		Number of slices		Geometrical transmission	
R	Fixed	N & S	Fixed	N & S	Fixed	N & S
17 000	500		0		82%	
40 000	500	400	3	2	70%	57%
80 000	300	300	4	3	48%	38%

Table 3.12: Fibre and image slicer properties for the SALT HRS R4.

Echelle grating

The near Littrow illumination of the R4 échelle grating results in a peak theoretical blaze efficiency of nearly 75%. This is somewhat higher than the R2 grating which is illuminated at 4.5°. There is no overfilling of the grating, although there is a 5.5% loss due to the gap between the two gratings. This also occurs in the R2 design.

VPH gratings

Some examples of the theoretical efficiency of VPH gratings are shown in Figures 3.37 and 3.38. Also shown in Figure 3.38 is the change in efficiency that results from a small change in the angle of incidence on the grating. These, and other efficiency predictions, have been used to predict the performance of the R4 SALT HRS VPH gratings.

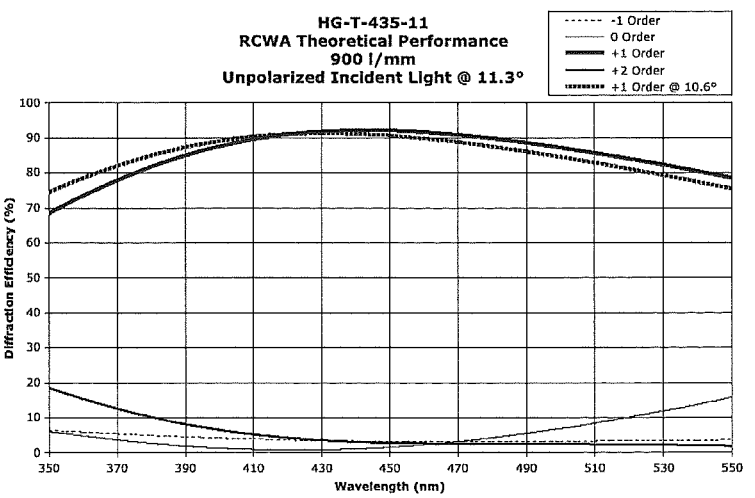

Figure 3.37: The theoretical efficiency of a 900-line/mm VPH grating from 350 nm to 550 nm (from Kaiser Optical Systems Inc.). The efficiency at two angles of incidence is shown.

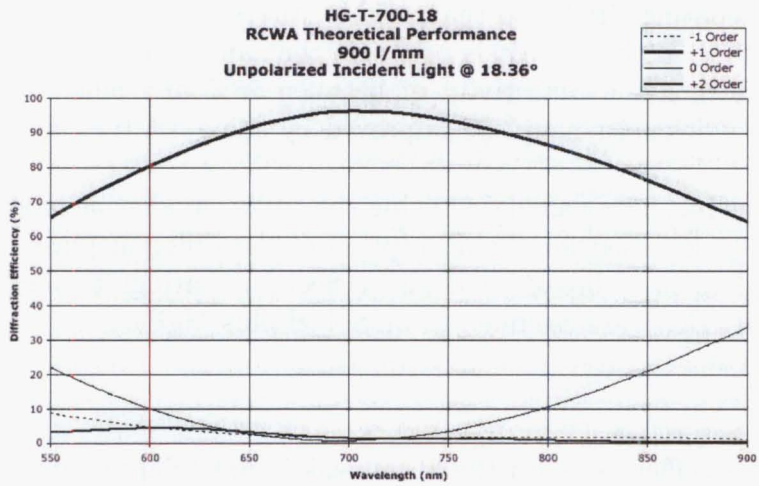

Figure 3.38: The theoretical efficiency of a 900-line/mm VPH gratings from 550 nm to 900 nm (from Kaiser Optical Systems Inc.).

Dichroic

For optimum efficiency the dichroic will transmit the longer wavelengths and reflect the shorter wavelengths. An example of the efficiency of a dichroic is shown in Figure 3.39. The crossover wavelength can be tuned. Numerically this is done simply by shifting the efficiency curves. The mean efficiency is 99.3% (below 510 nm) in reflection and 94% in transmission (above 560 nm). Up to five orders on the red and blue arms will have rapidly reducing efficiencies due to the dichroic's response.

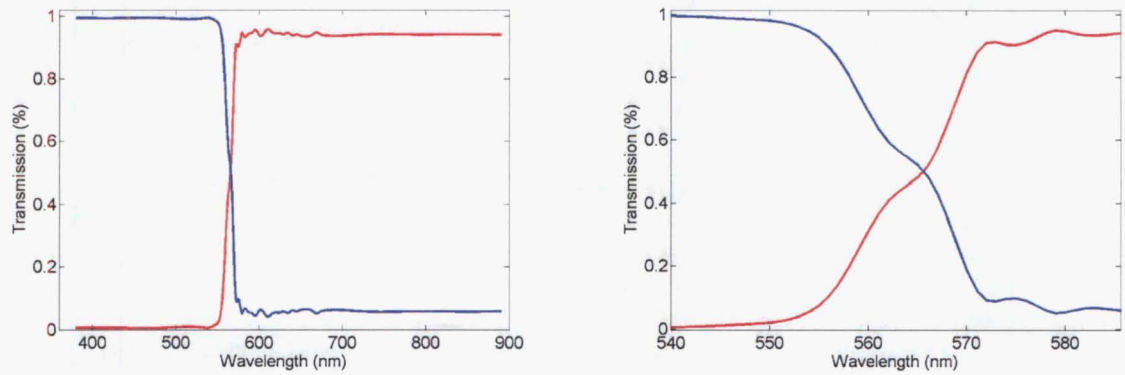

Figure 3.39: The dichroic efficiency. The blue wavelengths are reflected while the red wavelengths are transmitted. A close-up of the crossover region is shown on the right.

White pupil mirrors and camera

The red and blue arms share the same first white pupil mirror (which also doubles as the collimator). In total, this mirror is used three times in the blue and twice in the red. Hence it will need to be coated with a high-efficiency broadband coating – although emphasis should be placed on its blue performance. Alternatively the upper half of the mirror, which is used only by the blue arm, could be coated separately with a blue-optimized coating.

The red arm pupil mirror may be optimized for a more limited wavelength range, as can the two fold mirrors. These coatings have not been specified and the current

calculations assume a broad-band coating similar to that used on the SALT SAC mirrors. This coating has a reflectivity of 97% in the red. It is probable that an enhanced silver coating could be used instead, which has a reflectivity of between 98% and 99% over these wavelengths. Hence the red efficiencies could be improved by some 3% (i.e., after two reflections).

The transmission of the cameras has been calculated using the UVES cameras as models.[8] Standard catalogue data has been used for the absorption of the different glasses. All air/glass surfaces are assumed to have broad-band anti-reflection coatings applied. For the purposes of calculation only these are assumed to be Solgel plus MgF_2.

Summary

A comparison between the R2 and R4 efficiencies (at the blaze peak in fixed fibre mode) is given in Figure 3.40 and their relative efficiencies are given in Figure 3.41. The quantum efficiencies of the CCDs are not included as the efficiencies in the red and blue are assumed to be identical; that is, the R4 design will have blue and red optimized coatings on their respective CCDs, while the R2 design could employ graduated coatings with red and blue optimized regions.

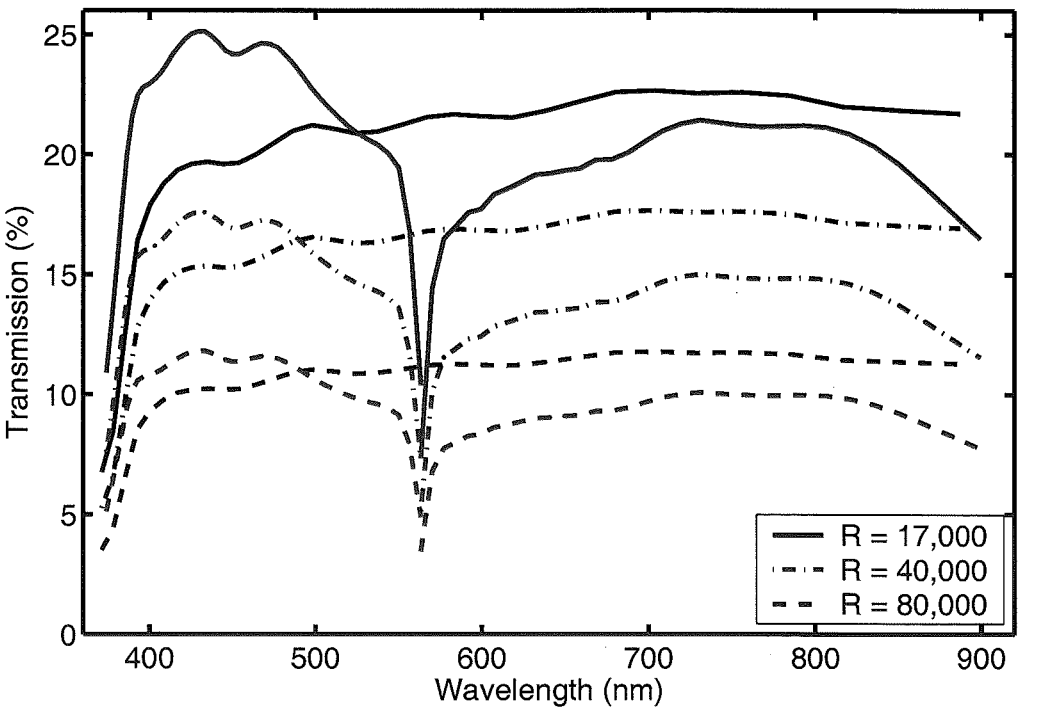

Figure 3.40: Efficiencies of the R2 and the R4 SALT HRS designs. The black line is the R2 design, while the blue and red lines are for the blue and red arms of the R4 design. The efficiencies at higher resolving powers for fixed fibre mode are also shown.

It appears that the blue arm of the R4 design is superior over much of the wavelength range by as much as 40 to 60%. However, the R4 red efficiency is everywhere poorer (by between 10 and 20%) mainly because of the additional reflections required and the poorer

[8]These calculations were made before the cameras were fully designed.

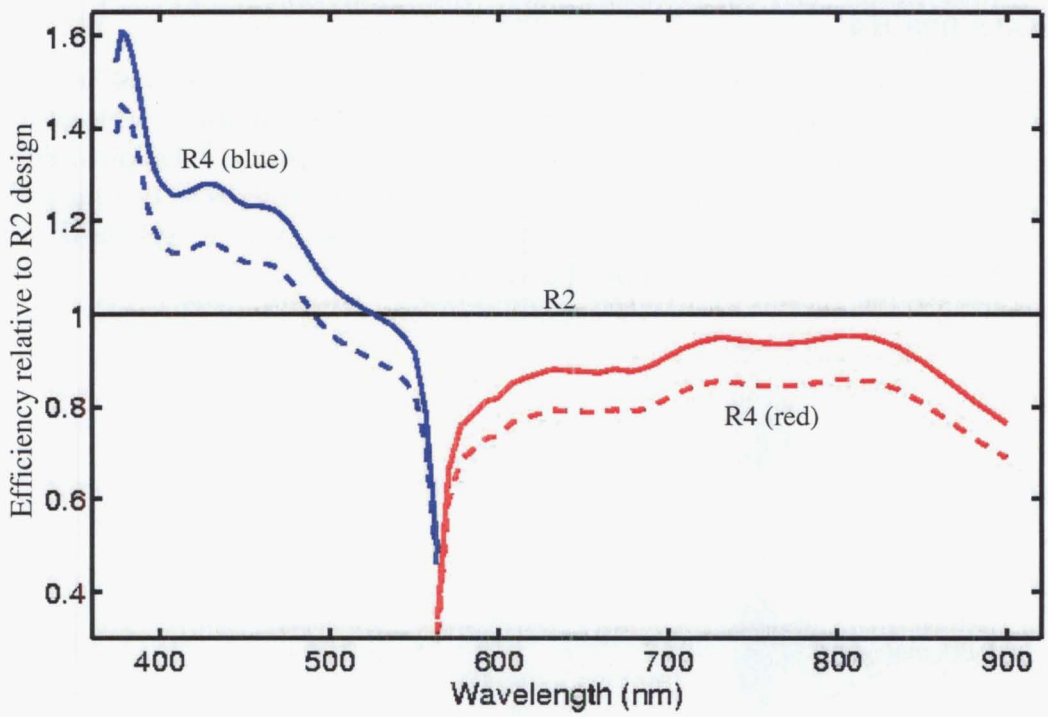

Figure 3.41: Relative efficiencies of the R2 and R4 SALT HRS designs. The dashed lines show the mean relative efficiencies at higher resolving powers in both fixed and nod and shuffle mode.

cross-dispersion efficiency. The efficiencies at higher resolving powers can be found by multiplying by the ratios of the sliced and unsliced efficiencies. With an order separation of 11.5″ the relative efficiency of the R4 design at a resolving power of $R = 40\,000$ is a factor 0.80 and 0.66 lower than at $R = 17\,000$ in fixed and nod and shuffle mode respectively. At $R = 80\,000$ the factor is 0.59 and 0.44 in fixed and nod and shuffle mode respectively. Because the R2 design has a minimum order separation of 13″, the sliced efficiencies are on average 10% better than the R4 design. This mitigates to some extent the decreased blue performance so that it is now only significantly superior (i.e., by more than 10%) at wavelengths less than 420 nm.

It should be noted that the objective of obtaining complete wavelength coverage from 370 to 890 nm, coupled with the fixed amount of CCD real estate and realistic camera fields of view, limits the inter-order spacing. If the wavelength coverage were to be reduced, either by reducing the red or blue coverage (or both), the order separation may be increased, thereby increasing the efficiency at high resolving powers. This applies equally to both the R2 and R4 designs, although only the R4 design will permit interchangeable cross-dispersers. However, it should also be noted that if superior blue performance is required by the R2 design at high resolving powers it would be possible to use dedicated image slicers that can make use of the much larger inter-order spacing provided by prism cross-dispersion in the blue orders. This would be possible without permanently losing wavelength coverage, and could make this design extremely attractive for use in the near UV.

3.4.3 SALT HRS R4

The design of SALT HRS R4 was developed in detail and a second PDR was held in 2004 July. The design is essentially as described above, except that the use of VPH grisms was abandoned, and the spectrograph layout was altered to incorporate a 45° dichroic mirror (see Figure 3.42). This permitted the fold mirrors before the cameras to be removed. The optical design document presented at the 2004 July PDR is given in Appendix E and a summary of the design is given in Appendix A.2.4.

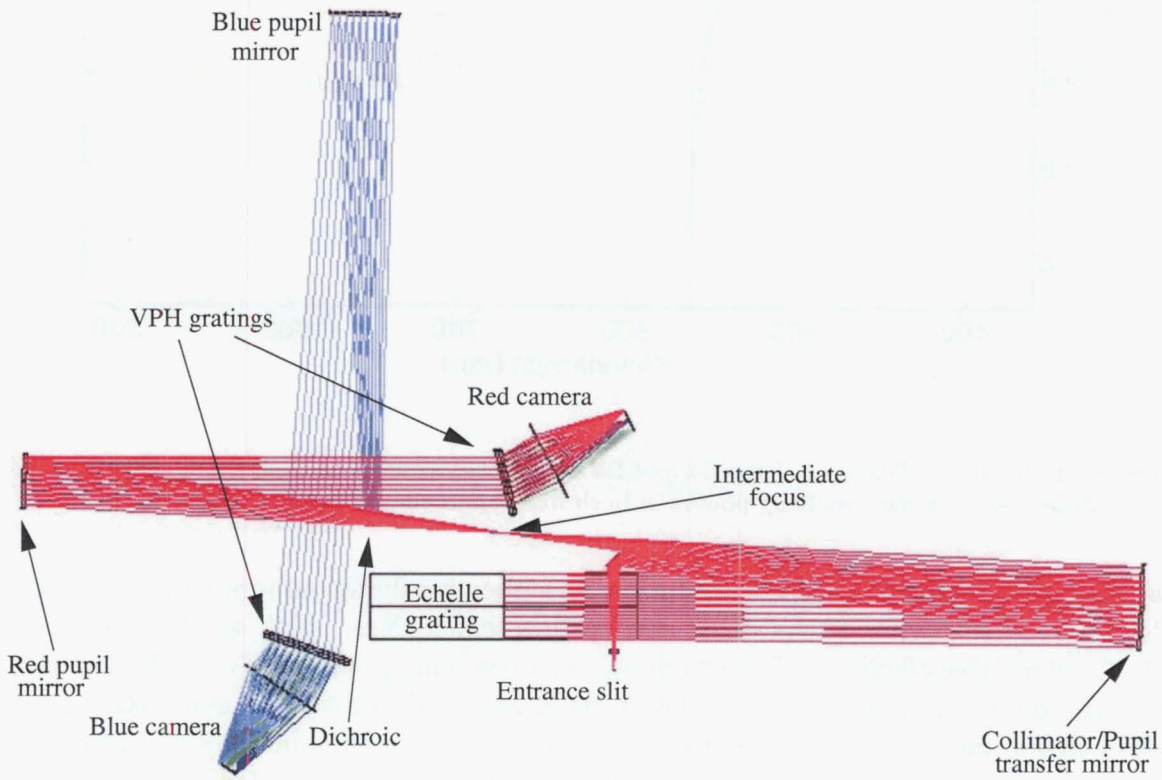

Figure 3.42: The SALT HRS R4 2004 July design. The cameras are shown as paraxial elements.

Post PDR changes

While the 2004 July review was successful, as a result of feedback received at this time some aspects of the design have been subsequently altered. In particular, the large dioptric camera required (especially for the blue arm) was found to be extremely expensive and one of the external reviewers (B. Delabre) pointed out that smaller cameras were possible if the entire optical train was optimized as a whole and if the VPH gratings were immersed inside weak meniscus lenses. The use of smaller cameras is made possible by further demagnifying the pupil in both arms (from an initial 200 mm and 150 mm in the blue and red arms respectively to 100 mm in both arms). This requires that higher line density VPH gratings be used. A second aspect of the design that was found in need of improvement is the dichroic's high angle of incidence. A lower incidence angle dichroic has proved to reduce the extent of the cross-over region and to eliminate the fringing that would otherwise occur at red wavelengths.

The redesign of SALT HRS R4 has allowed a range of spectrograph layouts to be considered. The design chosen is shown in Figure 3.43. The large off-axis mirror is retained as both a collimator and first pupil mirror. Both the blue and red pupil mirrors are spherical and have focal lengths of 1000 mm. These mirrors are slightly displaced from the intermediate focus so that the white pupil (on the VPH gratings) is not exactly collimated. This is corrected by immersing the gratings inside weak meniscus lenses. Fold mirrors are inevitable with a design that uses a low angle of incidence dichroic. There is considerable flexibility in the location of these mirrors, and the chosen option was to use relatively small (130 mm diameter) mirrors immediately prior to the VPH gratings. Finally, two entrance slit locations are shown. The first, which directs light toward a fold mirror, is actually the location of an intermediate slit mask and a set of fore-optics have been designed which transfer the image of sliced fibres to this point. The other slit location can be used by removing the fold mirror, and will be the location of the bare fibres which deliver the lowest resolving power. This will enhance the efficiency of this mode. The entire instrument will be enclosed inside a pair of intersecting cylinders that form a vacuum chamber. The lid of the chamber that surrounds the cameras will provide support for the detectors and fibre fore-optics. The interior bench on which all optical components are mounted will be rigidly coupled to this lid and will be immune to pressure and temperature changes. The spectrograph will in turn be housed inside a temperature stabilized environment.

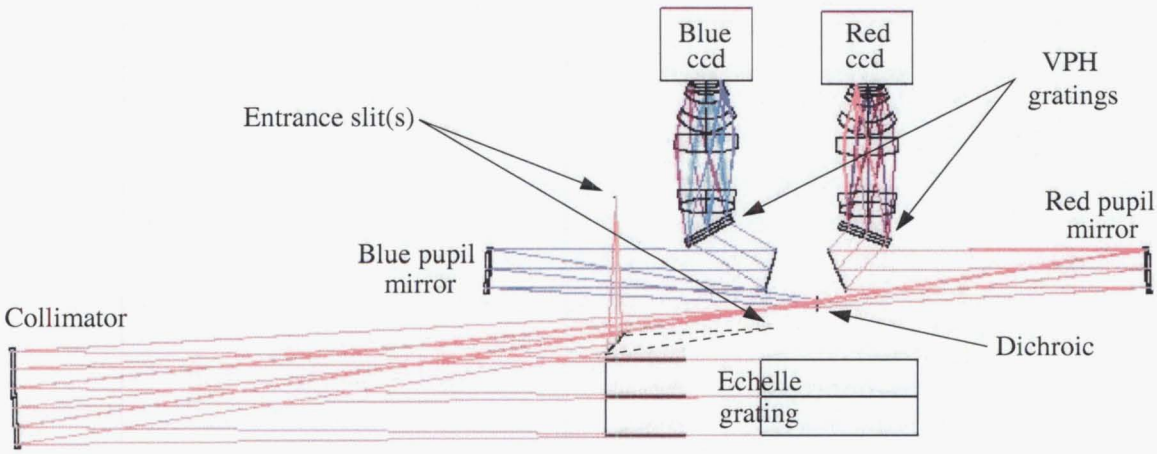

Figure 3.43: The revised SALT HRS R4 design.

The design is currently being finalized and it is expected that a critical design review will be held in 2005 April. Completion of the spectrograph is expected approximately two years following this date.

3.5 Summary

The design of SALT HRS has evolved considerably since its inception. The early design, was in large part very similar to HERCULES, although considerably larger. The R2 double-pass prism design was conceptually rather simple, and while aspects of the design were technically challenging, it was far from apparent (at least to the author) that it was an unrealistic design option for SALT HRS. The alternative R4 design, also described here in detail, while having potentially equal or even slightly better efficiency, has proved to be somewhat more complex. However, the R4 optics are considerably smaller and the CCD options are much more flexible. Both of these facts result in an instrument design about which there can be little doubt in terms of performance and/or manufacturability.

Chapter 4

Conclusion

In Chapter 1 the theoretical background needed for the design of a high resolution fibre-fed spectrograph in astronomy was outlined. The relative merits of various spectrograph forms were explored, and it was made apparent that, for many modes of operation, there is no unique design solution for an HRS.

Chapter 2 describes the design, construction, and performance of the HERCULES instrument in use on the MJUO 1-m telescope. The fibre-fed spectrograph has been in operation for over $3\frac{1}{2}$ years (since 2001 April), and in that time has proved to be capable of excellent performance. The vacuum mounted design allows extremely precise radial velocity measurements, while the double-pass prism and folded Schmidt camera optical layout delivers excellent throughput, image quality and stability. The performance of HERCULES could be improved in a number of ways. A larger format CCD is currently being acquired and extended wavelength coverage will probably be possible by mid-2005. Improved fibres, image slicers, and a more efficient detector are all possibilities for enhancing the efficiency of HERCULES. Greater wavelength coverage, a more stable detector, and improved throughput will all contribute to further improving the radial velocity precision. However, probably the greatest improvement in radial velocity precision can only occur if the effects of telescope guiding errors and incomplete fibre scrambling are removed. Suggestions for improving the guiding include a more sensitive detector, the redesign of the fibre input optics, and possibly the use of adaptive optics (or active fibre positioning). A fibre feed mode incorporating the use of a double-scrambler should also be considered.

Several high resolution spectrograph designs for the SALT 11-m telescope were described in Chapter 3. That quite different instrument designs are capable of comparable performance was demonstrated by the sequential development of first an R2 (and R2.8) design and then an R4 design. These designs were shown to have (on average, over all modes of operation) nearly equivalent performance. It was argued that the R2 optical design, while requiring very large optics, also conveyed considerable simplicity to the mechanical layout, was capable of complete wavelength coverage on a single detector (mosaic), and would have therefore been operationally quite simple. Concerns about the size (and cost) of the optics and/or their handling and coating, could readily have been mitigated against a small loss in throughput (over a small wavelength range). Detector issues were significant. However, several options were possible, and given sufficient resources a solution (most probably based on an existing design on another instrument) would have been possible.

The alternative SALT HRS R4 design has proved to be an attractive solution. The use of the white pupil layout permits a large reduction in the size of the R4 optics. However, the number and complexity of the optical surfaces has increased considerably. The use of volume-phased holographic gratings is vital to making this dual-beam instrument competitive with prism-based spectrographs. The R4 instrument is extremely compact (although space constraints should be of minor concern for a fibre-fed spectrograph) and

will be mounted inside a light vacuum in a temperature-stabilized environment. Apart from the fibre-feed and focus control, the spectrograph will have no moving parts. The design is currently progressing toward a critical design review scheduled to be held in 2005 April. Upon completion, SALT HRS will have the capability to be equivalent to or even to exceed the performance of all other high resolution spectrographs currently on other large telescopes.

Appendix A

ECHMOD – a Matlab tool for échelle spectrograph modelling

A.1 Basic outline

ECHMOD is a tool for modelling échelle spectrographs written in the MATLAB[1] software environment. The program was writen primarily to investigate fibre feed spectrograph solutions for SALT, however it has evolved into a tool that is capable of evaluating and comparing arbritary telescope, slit optics, and spectrograph configurations. Simple ray tracing simulations are possible and these have been used throughout this thesis to compute spectral formats. However, the techniques are not rigourous and an interface to the ray-tracing software Zemax has also been developed for verification and detailed optical performance characterization. Presently this interface is limited to file input/output and exact spectral formats are computed using code written in the Zemax programing language (ZPL). Detailed efficiency models have been constructed. Where possible, optical prescription data (including coatings) are used along with manufacturers data. Appropriate substitutions are made if such data are not available. The efficiency calculations also form the basis of an exposure time calculator.

A.2 Example input/output files

The telescope and spectrograph (including slit optics) properties are defined by instrument specific input files. Example input files for HERCULES, CELESTIA and the SALT HRS R2 and R4 spectrographs are given on the following pages.

[1]The MathWorks, Inc; `www.mathworks.com`

A.2.1 HERCULES

```
[ tel, slt, spc ] = hercules_2001apr

tel.name = 'MJUO 1m' ;
slt.name = { 'HERCULES fibre feed' } ;

spc.lam.minmax = [ 377 , 887 ]*1e-9 ;
spc.R.minmax   = [ 35000 ,  76300 ] ;
spc.samp       = 2.0 ;
spc.B          = 0.210 ;
spc.lam.eff    = { [] } ;
spc.nwav       = 21 ;
spc.dlam       = '2fsr' ;

col.name   = 'HERCULES collimator';
col.F1     = 0;

ech.name   = '53.411-mr152' ;
ech.type   = 'user defined echelle' ;
ech.num    = 1 ;
ech.gap    = 0 ;
ech.theta  = 3.0 ;
ech.dtheta = 0 ;
ech.dgamma = 0 ;

xdp.meth   = 'prism' ;
xdp.type   = 'dbl' ;
xdp.num    = [ 1              ] ;
xdp.glass  = { 'BK7'          } ;
xdp.angle  = [ 49.5           ] ;
xdp.lam    = [ 370            ]*1e-9 ;
xdp.coat   = { 'mgf2 @ 40deg' } ;
xdp.t      = [ 128            ] ;
xdp.T      = [                ] ;

cam.name = { 'HERCULES folded Schmidt' } ;
cam.dmag = [ 1 ] ;

ccd.type   = { 'tk1024_sq'      } ;
ccd.coat   = { 'SITe_SI003ABuv' } ;
ccd.num    = [ 1 , 1 ] ;
ccd.orient = [ 'y'   ] ;
ccd.psi    = [ 0.5   ] ;
ccd.absoff = [ 0 , 8 ] ;
ccd.offset = [ 0 , 0 ; ...
    -15.3 ,  6.7 ; ...
    -2.6 ,   6.7 ; ...
     5.2 ,   6.7 ; ...
    -4.9 , -17.3 ] ;
ccd.offset = ccd.offset - ccd.absoff ;
```

```
==============HERCULES Properties============
Telescope: McLellan telescope
  D = 1.0m, f = 4.55m (f/D = 4.55)
  Plate scale = 22.1 um/arcsec (45.33 arcsec/mm)

Beam size, B = 210.0 mm
R_max        = 76300.0
Wavelength range: 374.8 to 890.1 nm
 (in 89 orders: m = 152 to  64)

Echelle grating:
  Blaze angle    = 64.33 deg (R2.08)
  Littrow angle  = 3.00 deg
  T              = 31.6 grooves/mm
  L x W          = 408.0 x 204.0 mm
  [T_blz,T_ove,T_gap] = [80.6,84.9,0.0]

Cross-dispersion/order separation:
  min = 17.5 arcsec, max = 31.5 arcsec
Method - Prism:
  Glass = BK7
  alphaP = 49.50 deg
  thetai = 40.00 deg

Collimator:
  F  =  3.73, f  =  783.2 mm
  (assumes B = 210.0, f/D_tel = 4.5 and FRD rho = 1.22)
  Plate scale =  22.1 um/arcsec (45.33 arcsec/mm)

Camera:
  F  =  4.65, f  =  976.1 mm
  (assumes 2.0 (24.0um) pixel sampling of R_max
   and pupil demagnification cam_dmag = 1.0)
  Plate scale =  27.5 um/arcsec (36.37 arcsec/mm)
CCD:
  Type        = tk1024_sq
  Coat        = SITe_SI003ABuv
  n_pix [x,y] = [1024,1024] pixels
  s_pix       = 24 microns
  num   [x,y] = [1,1] (y)
  Pixel scale = 1.1 pix/arcsec (0.87 arcsec/pix)
```

Fibre diameter		Slice properties			Resolving Power		Transmission (pc)		
microns	arcsec	width	height	num	R	R_tot	PSF	Geom	Total
100.0	4.53	100.0	100.0	1	43000	---	77.9	100.0	77.9
50.0	2.27	50.0	50.0	1	86100	---	36.2	100.0	36.2
100.0	4.53	50.0	100.0	1	73200	---	77.9	60.9	47.4

```
Assumes...
  Seeing median FWHM = 2.50 arcsecs
```

A.2.2 CELESTIA

```
[tel, slt, spc] = salthrs_celestia

tel.name = 'SALT' ;
slt.name = { 'SALT HRS fibre feed' } ;

spc.lam.minmax = [ 370 , 890 ]*1e-9 ;
spc.R.minmax   = [ 17000 , 108000 ] ;
spc.samp       = 2.0 ;
spc.B          = 0.305 ;
spc.lam.eff    = { [ ] } ;

col.name   = 'SALT HRS R2 collimator' ;
col.F1     = 0 ;

ech.name   = 'R2.8.T57' ;
ech.type   = 'user defined echelle' ;
ech.num    = 2 ;
ech.gap    = 0.035 ;
ech.theta  = 2.75 ;
ech.dtheta = 0 ;
ech.dgamma = 0 ;

xdp.meth   = 'prism' ;
xdp.type   = 'dbl' ;
xdp.num    = 1 ;
xdp.glass  = { 'BK7'           ; 'BK7'           } ;
xdp.angle  = [ 41.5            , 44.5            ] ;
xdp.lam    = [ 370             , 370             ]*1e9 ;
xdp.coat   = { 'Solgel + MgF2' ; 'Solgel + MgF2' } ;
xdp.t      = [ 150             , 156             ] ;
xdp.T      = [                                   ] ;

ccd.type   = { 'ccd44_82'         } ;
ccd.coat   = { 'E2V DDSi astroBB' } ;
ccd.num    = [ 1 , 2    ] ;
ccd.psi    = [ 1.0      ] ;
ccd.orient = [ 'x'      ] ;
ccd.offset = [ 0 , -0.5 ] ;

cam.name = { 'SALT HRS R2 camera' } ;
cam.dmag = [ 1 ] ;
```

```
==============SALT HRS CELESTIA Properties============
Telescope: SALT
  D = 11.0m, f = 46.20m (f/D = 4.20)
  Plate scale = 224.0 um/arcsec (4.46 arcsec/mm)

Beam size, B = 305.0 mm
R_max        = 108000.0
Wavelength range: 368.4 to 893.4 nm
 (in 58 orders: m =  97 to  40)

Echelle grating:
  Blaze angle    = 70.45 deg (R2.82)
  Littrow angle  = 2.75 deg
  T              = 52.7 grooves/mm
  L x W          = 847.8 x 304.8 mm
  (no. gratings = 2; each 406.4 x 304.8 mm, with 35.0mm gap)
  [T_blz,T_ove,T_gap] = [75.7,85.6,4.2]

Cross-dispersion/order separation:
  min = 6.9 arcsec, max = 12.2 arcsec
Method - Prism:
  Glass = BK7 and BK7
  alphaP = [41.50,44.50] deg
  thetai = [32.95,35.55] deg

Collimator:
  F  =  3.82, f  = 1164.5 mm
  (assumes B = 305.0, f/D_tel = 4.2 and FRD rho = 1.10)
  Plate scale = 223.5 um/arcsec (4.47 arcsec/mm)

Camera:
  F  =  2.14, f  =  653.1 mm
  (assumes 2.0 (15.0um) pixel sampling of R_max
   and pupil demagnification cam_dmag = 1.0)
  Plate scale = 125.6 um/arcsec (7.96 arcsec/mm)
CCD:
  Type        = ccd44_82
  Coat        = E2V DDSi astromid
  n_pix [x,y] = [4096,2048] pixels
  s_pix       = 15 microns
  num   [x,y] = [1,2] (x)
  Pixel scale = 8.4 pix/arcsec (0.12 arcsec/pix)
```

Fibre diameter		Slice properties			Resolving Power		Transmission (pc)		
microns	arcsec	width	height	num	R	R_tot	PSF	Geom	Total
400.0	1.79	400.0	400.0	1	25300	---	70.5	100.0	70.5
350.0	1.56	200.0	350.0	1	37900	---	62.2	68.6	42.7
300.0	1.34	100.0	300.0	1	75800	---	52.4	41.6	21.8
400.0	1.79	70.0	400.0	1	108400	---	70.5	22.2	15.6

```
Assumes...
  Seeing median FWHM = 1.12 arcsecs
```

A.2.3 SALT HRS R2

```
[ tel, slt, spc ] = salthrs_r2_2003sep

tel.name = 'SALT' ;
slt.name = { 'SALT HRS R2 fibre feed' } ;

spc.lam.minmax = [ 377 , 950 ]*1e9 ;
spc.R.minmax   = [ 17000 , 80000 ] ;
spc.samp       = 2.0;
spc.B          = 0.365 ;
spc.lam.eff    = { [ ] } ;
spc.nwav       = 11 ;
spc.dlam       = '2fsr' ;

col.name       = 'SALT HRS R2 collimator' ;
col.F1         = 0;

ech.name   = '53.127' ;
ech.type   = 'RGL standard echelle' ;
ech.num    = 2 ;
ech.gap    = 0.035 ;
ech.theta  = 4.5 ;
ech.dtheta = 0 ;
ech.dgamma = 0 ;

xdp.meth   = 'prism' ;
xdp.type   = 'dbl' ;
xdp.num    = 1 ;
xdp.glass  = { 'BK7'           ; 'BK7'           } ;
xdp.angle  = [ 40.0            , 40.0            ] ;
xdp.lam    = [ 370             , 370             ]*1e-9 ;
xdp.coat   = { 'Solgel + MgF2' ; 'Solgel + MgF2' } ;
xdp.t      = [ 150             , 180             ] ;
xdp.T      = [                                   ] ;

cam.name   = { 'SALT HRS R2 camera' } ;
cam.dmag   = 1 ;

ccd.type   = { 'ccd44_82'                  } ;
ccd.coat   = { 'E2V astroBB-mid graduated' } ;
ccd.num    = [ 3 , 1 ] ;
ccd.psi    = [ 2.5   ] ;
ccd.orient = [ 'y'   ] ;
ccd.offset = [ 0 , 0 ] ;
```

```
==============SALT HRS R2 Properties============
Telescope: SALT
  D = 11.0m, f = 46.20m (f/D = 4.20)
  Plate scale = 224.0 um/arcsec (4.46 arcsec/mm)

Beam size, B = 365.0 mm
R_max        = 80000.0
Wavelength range: 371.3 to 972.4 nm
 (in 35 orders: m =  55 to  21)

Echelle grating:
  Blaze angle    = 63.00 deg (R1.96)
  Littrow angle  = 4.50 deg
  T              = 87.0 grooves/mm
  L x W          = 861.0 x 308.0 mm
  (no. gratings = 2; each 413.0 x 308.0 mm, with 35.0mm gap)
  [T_blz,T_ove,T_gap] = [72.8,85.2,3.9]

Cross-dispersion/order separation:
  min = 13.0 arcsec, max = 22.8 arcsec
Method - Prism:
  Glass = BK7 and BK7
  alphaP = [40.00,40.00] deg
  thetai = [31.68,31.68] deg

Collimator:
  F  =  3.82, f  = 1393.6 mm
  (assumes B = 365.0, f/D_tel = 4.2 and FRD rho = 1.10)
  F1 = 10.00, f1 = 3650.0 mm
  Plate scale = 586.6 um/arcsec (1.70 arcsec/mm)

Camera:
  F  =  1.93, f  =  705.9 mm
  (assumes 2.0 (15.0um) pixel sampling of R_max
   and pupil demagnification cam_dmag = 1.0)
  Plate scale = 113.4 um/arcsec (8.81 arcsec/mm)
CCD:
  Type        = ccd44_82
  Coat        = E2V astroBB-mid graduated
  n_pix [x,y] = [2048,4096] pixels
  s_pix       = 15 microns
  num   [x,y] = [3,1] (y)
  Pixel scale = 7.6 pix/arcsec (0.13 arcsec/pix)
```

Fibre diameter		Slice properties			Resolving Power		Transmission (pc)		
microns	arcsec	width	height	num	R	R_tot	PSF	Geom	Total
500.0	2.23	500.0	500.0	1	17300	---	82.2	100.0	82.2
500.0	2.23	160.0	500.0	3	40400	---	82.2	94.6	77.8
400.0	1.79	160.0	400.0	2	40400	---	70.5	87.9	61.9
300.0	1.34	80.0	300.0	4	80900	---	52.4	98.5	51.6
300.0	1.34	80.0	300.0	3	80900	---	52.4	81.7	42.8

```
Assumes...
  Seeing median FWHM = 1.12 arcsecs
```

A.2.4 SALT HRS R4

```
[ tel, slt, spc ] = salthrs_r4_2004jul

tel.name = 'SALT' ;
slt.name = { 'SALT HRS R4 fibre feed' } ;

spc.lam.minmax = [ [375, 555]     ; [555, 880]       ]*1e-9 ;
spc.R.minmax   = [ [17000, 80000] ; [17000, 100000 ] ] ;
spc.samp       = [ 2.0            ; 2.0              ] ;
spc.B          = 0.200 ;
spc.lam.eff    = { []             ; []               } ;

col.name   = 'SALT HRS R4 collimator' ;
col.F1     = 10 ;

ech.type   = 'RGL standard echelle' ;
ech.name   = '53.425' ;
ech.num    = 2 ;
ech.gap    = 0.016 ;
ech.theta  = 0.05 ;
ech.dtheta = 0 ;
ech.dgamma = 2.5 ;

xdp.meth  = 'grating' ;
xdp.type  = 'vph' ;
xdp.glass = { 'bk7'          ; 'bk7'          } ;
xdp.angle = [ 0              ; 0              ] ;
xdp.coat  = { 'mgf2 @ 30deg' ; 'mgf2 @ 30deg' } ;
xdp.lam   = [ 462            ; 700            ]*1e-9 ;
xdp.T     = [ 1050           ; 650            ] ;
xdp.t     = [ 5              ; 8              ] ;

cam.name   = { 'HRS-Blue-CM-2-06' ; 'HRS-Red-CM-2-01' } ;
cam.dmag   = [ 1                  , 1.5               ] ;

ccd.type   = { 'ccd44_82'          ; 'ccd44_82'          } ;
ccd.coat   = { 'E2V StdSi astroBB' ; 'E2V DDSi astromid' } ;
ccd.num    = [ [1,1]               ; [2,1]               ] ;
ccd.orient = [ 'y'                 , 'y'                 ] ;
ccd.psi    = [ 0                   , 0                   ] ;
ccd.offset = [ [0,0]               ; [0,0]               ] ;
```

```
==============SALT HRS R4 Blue Properties============
Telescope: SALT
  D = 11.0m, f = 46.20m (f/D = 4.20)
  Plate scale = 224.0 um/arcsec (4.46 arcsec/mm)

Beam size, B = 200.0 mm
R_max        = 80000.0
Wavelength range: 373.3 to 555.5 nm
 (in 42 orders: m = 125 to  84)

Echelle grating:
  Blaze angle    = 76.00 deg (R4.01)
  Littrow angle  = 0.05 deg
  T              = 41.6 grooves/mm
  L x W          = 836.0 x 204.0 mm
  (no. gratings = 2; each 410.0 x 204.0 mm, with 16.0mm gap)
  [T_blz,T_ove,T_gap] = [82.2,97.5,2.5]

Cross-dispersion/order separation:
  min = 11.2 arcsec, max = 24.3 arcsec
Method - Holographic grating:
  Glass  = bk7
  T      = 1050 lines/mm
  thetai = 14.04 deg (lamB = 462.0 nm)
  coat   = mgf2 @ 30deg

Collimator:
  F  =  3.82, f  =  763.6 mm
  (assumes B = 200.0, f/D_tel = 4.2 and FRD rho = 1.10)
  F1 = 10.00, f1 = 2000.0 mm
  Plate scale = 586.6 um/arcsec (1.70 arcsec/mm)

Camera:
  F  =  1.50, f  =  300.2 mm
  (assumes 2.0 (15.0um) pixel sampling of R_max
   and pupil demagnification cam_dmag = 1.0)
  Plate scale =  88.1 um/arcsec (11.36 arcsec/mm)
CCD:
  Type        = ccd44_82
  Coat        = E2V StdSi astroBB
  n_pix [x,y] = [2048,4096] pixels
  s_pix       = 15 microns
  num   [x,y] = [1,1] (y)
  Pixel scale = 5.9 pix/arcsec (0.17 arcsec/pix)
```

Fibre diameter		Slice properties			Resolving Power		Transmission (pc)		
microns	arcsec	width	height	num	R	R_tot	PSF	Geom	Total
500.0	2.23	500.0	500.0	1	16400	---	82.2	100.0	82.2
500.0	2.23	160.0	500.0	3	38400	---	82.2	81.4	66.9
400.0	1.79	160.0	400.0	2	38400	---	70.5	76.1	53.6
300.0	1.34	80.0	300.0	4	76800	---	52.4	91.4	47.9
300.0	1.34	80.0	300.0	3	76800	---	52.4	68.5	35.9

```
Assumes...Seeing median FWHM = 1.12 arcsecs
```

```
==============SALT HRS R4 Red Properties============
Telescope: SALT
  D = 11.0m, f = 46.20m (f/D = 4.20)
  Plate scale = 224.0 um/arcsec (4.46 arcsec/mm)

Beam size, B = 200.0 mm
R_max        = 100000.0
Wavelength range: 548.9 to 880.4 nm
 (in 33 orders: m =  85 to  53)

Echelle grating:
  Blaze angle    = 76.00 deg (R4.01)
  Littrow angle  = 0.05 deg
  T              = 41.6 grooves/mm
  L x W          = 836.0 x 204.0 mm
  (no. gratings = 2; each 410.0 x 204.0 mm, with 16.0mm gap)
  [T_blz,T_ove,T_gap] = [75.1,97.5,2.5]

Cross-dispersion/order separation:
  min = 10.0 arcsec, max = 25.0 arcsec
Method - Holographic grating:
  Glass  = bk7
  T      =  650 lines/mm
  thetai = 13.15 deg (lamB = 700.0 nm)
  coat   = mgf2 @ 30deg

Collimator:
  F  =  3.82, f  =  763.6 mm
  (assumes B = 200.0, f/D_tel = 4.2 and FRD rho = 1.10)
  F1 = 10.00, f1 = 2000.0 mm
  Plate scale = 586.6 um/arcsec (1.70 arcsec/mm)

Camera:
  F  =  1.88, f  =  250.2 mm
  (assumes 2.0 (15.0um) pixel sampling of R_max
   and pupil demagnification cam_dmag = 1.5)
  Plate scale = 110.1 um/arcsec (9.08 arcsec/mm)
CCD:
  Type        = ccd44_82
  Coat        = E2V DDSi astromid
  n_pix [x,y] = [2048,4096] pixels
  s_pix       = 15 microns
  num   [x,y] = [2,1] (y)
  Pixel scale = 7.3 pix/arcsec (0.14 arcsec/pix)
```

Fibre diameter		Slice properties			Resolving Power		Transmission (pc)		
microns	arcsec	width	height	num	R	R_tot	PSF	Geom	Total
500.0	2.23	500.0	500.0	1	16400	---	82.2	100.0	82.2
500.0	2.23	160.0	500.0	3	38400	---	82.2	81.4	66.9
400.0	1.79	160.0	400.0	2	38400	---	70.5	76.1	53.6
300.0	1.34	80.0	300.0	4	76800	---	52.4	91.4	47.9
300.0	1.34	80.0	300.0	3	76800	---	52.4	68.5	35.9

```
Assumes...Seeing median FWHM = 1.12 arcsecs
```

Appendix B

Optical prescriptions

The optical prescriptions of the spectrographs described in the previous appendix are given below. Only summary surface data are given. Coordinate breaks and apertures are not detailed here. Full Zemax prescriptions can be obtained from the author.

B.1 HERCULES

Surf	Type	Comment	Radius	Thickness	Glass	Diameter	Conic
OBJ	STANDARD	FIBRE	Infinity	0		0.1	0
1	STANDARD		Infinity	783.3		0.1	0
STO	STANDARD	COLLIMATOR	-1566.6	-783	MIRROR	210	-1
3	STANDARD	FIBRE OBSTRUCTN	Infinity	-1667		0	0
4	COORDBRK		-	0		-	-
5	COORDBRK	ANGLE OF INCIDENC	-	0		-	-
6	STANDARD	PRISM FACE 1	Infinity	0	BK7	273.4955	0
7	COORDBRK		-	-129.575		-	-
8	COORDBRK		-	0		-	-
9	STANDARD	PRISM FACE 2	Infinity	0		273.5579	0
10	COORDBRK	ECHELLE/PRISM ANG	-	-300		-	-
11	COORDBRK		-	0		-	-
12	DGRATING	ECHELLE GRATING	Infinity	0	MIRROR	565.5365	0
13	COORDBRK		-	300		-	-
14	COORDBRK		-	0		-	-
15	STANDARD	PRISM FACE 3	Infinity	0	BK7	305.7749	0
16	COORDBRK		-	129.575		-	-
17	COORDBRK		-	0		-	-
18	STANDARD	PRISM FACE 4	Infinity	0		312.6507	0
19	COORDBRK		-	0		-	-
20	COORDBRK		-	2461.5		-	-
21	COORDBRK		-	0		-	-
22	STANDARD	COLL OBSTRUCTION	Infinity	0		0	0
23	STANDARD	COLL OBSTRUCTION	Infinity	0		397.2517	0
24	COORDBRK		-	113.5		-	-
25	COORDBRK		-	0		-	-
**26	EVENASPH	SCHMIDT CORR.	Infinity	15	BK7	406.291	0
27	STANDARD		Infinity	777.679		406.8081	0
28	COORDBRK	PRE FF HOLE	-	0		-	-
29	STANDARD	FOLD-FLAT HOLE	Infinity	0		459.1752	0
30	STANDARD	FOLD-FLAT MIRROR	Infinity	0	MIRROR	459.1752	0
31	COORDBRK		-	-859.79		-	-
32	STANDARD	SCHMIDT PRIM.	1946.26	859.79	MIRROR	495.5923	0
33	COORDBRK		-	0		-	-

34	STANDARD	FOLD-FLAT HOLE	Infinity	0		103.6216	0
35	COORDBRK		-	75.0488		-	-
36	STANDARD	FEILD-FLATTENING	327.6568	10.5	BK7	85	0
37	STANDARD		10310.53	25.0008		85	0
38	COORDBRK		-	0		-	-
IMA	STANDARD	CCD	Infinity			50	0

**Surface 26 : EVEN ASPHERE
Coeff on r 2 : 4.76e-006
Coeff on r 4 : -6.4787989e-011
Coeff on r 6 : -2.2380929e-017

B.2 CELESTIA

Surf	Type	Comment	Radius	Thickness	Glass	Diameter	Conic
OBJ	STANDARD		Infinity	0		0.35	0
1	STANDARD		Infinity	1170		10	0
STO	STANDARD	COLLIMATOR	-2340	0	MIRROR	300	-1
3	COORDBRK		-	-3000		-	-
4	COORDBRK	ANGLE OF INCIDENC	-	0		-	-
5	STANDARD	PRISM 1 FACE 1	Infinity	0	BK7	407.6306	0
6	COORDBRK		-	-124		-	-
7	COORDBRK		-	0		-	-
8	STANDARD	PRISM 1 FACE 2	Infinity	0		407.1239	0
9	COORDBRK		-	-255		-	-
10	COORDBRK		-	0		-	-
11	STANDARD	PRISM 2 FACE 1	Infinity	0	BK7	395.178	0
12	COORDBRK		-	-141		-	-
13	COORDBRK		-	0		-	-
14	STANDARD	PRISM 2 FACE 2	Infinity	0		395.2307	0
15	COORDBRK		-	-520		-	-
16	COORDBRK	DGAMMA	-	0		-	-
17	DGRATING	ECHELLE	Infinity	0	MIRROR	1054.307	0
18	COORDBRK		-	520		-	-
19	COORDBRK		-	0		-	-
20	STANDARD	PRISM 2 FACE 2	Infinity	0	BK7	0	0
21	COORDBRK		-	141		-	-
22	COORDBRK		-	0		-	-
23	STANDARD	PRISM 2 FACE 1	Infinity	0		0	0
24	COORDBRK		-	255		-	-
25	COORDBRK		-	0		-	-
26	STANDARD	PRISM 1 FACE 2	Infinity	0	BK7	595.8322	0
27	COORDBRK		-	124		-	-
28	COORDBRK		-	0		-	-
29	STANDARD	PRISM 1 FACE 1	Infinity	0		638.7895	0
30	COORDBRK		-	3000		-	-
31	STANDARD	COLLIMATOR OBSTR	Infinity	0		0	0
32	COORDBRK		-	50		-	-
33	COORDBRK	CAMERA CENTRE	-	0		-	-

34	STANDARD		Infinity	0		200	0
35	STANDARD	CORRECTOR ONE	2794.205	55.59809	BK7	750	0
36	STANDARD		-3444.976	0		750	0
37	COORDBRK		-	4.205722		-	-
38	COORDBRK		-	0		-	-
39	STANDARD	CORRECTOR TWO	1194.175	24.30712	BK7	730	0
40	STANDARD		665.7248	0		730	0
41	COORDBRK		-	1215.911		-	-
42	COORDBRK		-	0		-	-
43	STANDARD	CCD OBSTRUCTION	Infinity	0		0	0
44	COORDBRK		-	825.5883		-	-
45	COORDBRK		-	0		-	-
46	STANDARD	PRIMARY MIRROR	-1443.243	0	MIRROR	1000	0
47	COORDBRK		-	-675.5883		-	-
48	COORDBRK		-	0		-	-
49	STANDARD	FIELD-FLATTENER	-165.21	-33.94388	BK7	170	0
50	STANDARD		-680.328	-11.84338		170	0
51	COORDBRK		-	-5		-	-
IMA	STANDARD		Infinity			0	0

B.3 SALT HRS R2

Surf	Type	Comment	Radius	Thickness	Glass	Diameter	Conic
OBJ	STANDARD		Infinity	0		0	0
1	STANDARD		Infinity	1340.2		0	0
STO	STANDARD	COLLIMATOR	-2680.4	-2420	MIRROR	351.001	-1
3	COORDBRK	THETA (& ECH CEN)	-	0		-	-
4	COORDBRK	ANGLE OF INCIDENC	-	0		-	-
5	STANDARD	PRISM 1 FACE 1	Infinity	0	BK7	656.5564	0
6	COORDBRK	PRISM APEX ANGLE	-	-188		-	-
7	COORDBRK		-	0		-	-
8	STANDARD	PRISM 1 FACE 2	Infinity	0		637.3285	0
9	COORDBRK		-	-115		-	-
10	STANDARD	REF	Infinity	-115		0	0
11	COORDBRK		-	0		-	-
12	STANDARD	PRISM 2 FACE 1	Infinity	0	BK7	601.0753	0
13	COORDBRK		-	-165		-	-
14	COORDBRK		-	0		-	-
15	STANDARD	PRISM 2 FACE 2	Infinity	0		584.2432	0
16	COORDBRK		-	-500		-	-
17	COORDBRK	BLAZE AND DECENT	-	0		-	-
18	DGRATING	ECHELLE	Infinity	0	MIRROR	920.8308	0
19	STANDARD	ECHELLE GAP	Infinity	0		0	0
20	COORDBRK		-	500		-	-
21	COORDBRK		-	0		-	-
22	STANDARD	PRISM 2 FACE 3	Infinity	0	BK7	0	0
23	COORDBRK		-	165		-	-
24	COORDBRK		-	0		-	-
25	STANDARD	PRISM 2 FACE 4	Infinity	0		0	0
26	COORDBRK		-	115		-	-
27	STANDARD	REF	Infinity	115		0	0
28	COORDBRK		-	0		-	-
29	STANDARD	PRISM 1 FACE 3	Infinity	0	BK7	567.1906	0
30	COORDBRK		-	188		-	-
31	COORDBRK		-	0		-	-
32	STANDARD	PRISM 1 FACE 4	Infinity	0		595.8706	0
33	COORDBRK		-	0		-	-

34	COORDBRK		-	0		-	-
35	COORDBRK		-	2420		-	-
36	STANDARD	COLLIMATOR OBSTR	Infinity	0		0	0
37	COORDBRK	CAMERA XY OFFSET	-	50		-	-
38	COORDBRK	CAMERA ROTATION	-	0		-	-
39	COORDBRK	CAMERA ANG OFFSET	-	0		-	-
40	STANDARD	CORRECTOR ONE	5296.991	75	BK7	870	0
41	STANDARD		-7872.096	5		870	0
42	STANDARD	CORRECTOR TWO	938.3651	75	BK7	860	0
43	STANDARD		744.8469	281.0331		830	0
44	STANDARD	CORRECTOR THREE	-744.8469	75	BK7	840	0
45	STANDARD		-938.3651	400		870	0
46	STANDARD	CCD OBSTRUCTION	Infinity	876.0455		0	0
47	STANDARD	PRIMARY MIRROR	-1505.958	0	MIRROR	1200	0
48	COORDBRK		-	-776.0455		-	-
49	COORDBRK	FF TILT	-	0		-	-
50	STANDARD	FIELD FLATTENING	-365.2816	-22.09066	BK7	162	0
51	STANDARD	LENS	1101.869	0		162	0
52	COORDBRK		-	-3.184869		-	-
53	COORDBRK	CCD TILT	-	0		-	-
IMA	STANDARD		Infinity			106.1381	0

B.4 SALT HRS R4

Note that the prescription for SALT HRS R4 is actually the 2005 April design.

B.4.1 SALT HRS R4 – Blue arm

Surf	Type	Comment	Radius	Thickness	Glass	Diameter	Conic
OBJ	STANDARD	INTERMEDIATE INJECT	Infinity	534.3569		21.2132	0
1	STANDARD	FC1.1	96.81967	15	N-FK51	60	0
2	STANDARD	FC1.2	-85.49425	15	S-LAL7	60	0
3	STANDARD		-563.0025	10		60	0
4	STANDARD	VACUUM WINDOW	Infinity	10	SILICA	60	0
5	STANDARD		Infinity	10		60	0
6	STANDARD	FC2.1	180.6662	15	S-LAL7	50	0
7	STANDARD	FC2.2	49.29438	15	N-FK51	50	0
8	STANDARD		-212.0699	174.6397		50	0
9	STANDARD	"SLIT PLATE"	Infinity	0.5		8.596469	0
10	STANDARD	TC 1.1	18.0863	3	BK7	12.5	0
11	STANDARD		39.198	-2.53		12.5	0
12	COORDBRK	OFF-AXIS ANGLE	-	0		-	-
13	COORDBRK	Y DECENTRE	-	267.47		-	-
14	COORDBRK		-	0		-	-
15	COORDBRK		-	0		-	-
16	COORDBRK	INJECTION ANGLE	-	0		-	-
17	STANDARD	FOLD MIRROR	Infinity	0	MIRROR	187.7476	0
18	COORDBRK		-	0		-	-
19	COORDBRK		-	0		-	-
20	COORDBRK		-	267.47		-	-
21	STANDARD	"DIRECT INJECTION"	Infinity	-267.47		20	0
22	COORDBRK		-	-1735		-	-
23	STANDARD	M1 PASS 1	4000	2000	MIRROR	800	-1
24	COORDBRK	GRATING DECENTRE	-	0		-	-
25	COORDBRK	BLAZE ANGLE	-	0		-	-
26	COORDBRK	THETA	-	0		-	-
27	COORDBRK	ROTATE GROOVES	-	0		-	-
STO	DGRATING	ECHELLE	Infinity	0	MIRROR	887.1472	0
29	COORDBRK	UNROTATE	-	0		-	-

30	COORDBRK		UNDO THETA	-	0		-	-
31	COORDBRK		BLAZE ANGLE UNDO	-	0		-	-
32	COORDBRK		BACK TO GLOBAL-Z	-	-2000		-	-
33	STANDARD		M1 PASS 2	4000	0	MIRROR	800	-1
34	STANDARD		M1 PARENT	Infinity	2000		690	0
35	COORDBRK			-	0		-	-
36	STANDARD		INT. IMAGE	Infinity	150		187.7652	0
37	STANDARD		DICHROIC	Infinity	0	MIRROR	201.3004	0
38	STANDARD			Infinity	-984.8725		152.0777	0
39	COORDBRK		FOCUS	-	0		-	-
40	STANDARD		2ND PUPIL MIRROR	2222.222	0	MIRROR	440	0
41	COORDBRK			-	1075.613		-	-
42	COORDBRK		DEC. TO WH. PUPIL	-	0		-	-
43	STANDARD		WHITE PUPIL	Infinity	-200		144.5143	0
44	COORDBRK			-	0		-	-
45	STANDARD		FOLD MIRROR	Infinity	0	MIRROR	176.0127	0
46	COORDBRK			-	-175		-	-
47	COORDBRK		AOI	-	0		-	-
48	STANDARD		VPH LENS 1	-5117.579	-15	BK7	160	0
49	STANDARD		VPH LENS 1	Infinity	0	BK7	160	0
50	STANDARD		VPH	Infinity	-10	BK7	160	0
51	DGRATING		VPH	Infinity	-10	BK7	160	0
52	STANDARD		VPH	Infinity	0	BK7	160	0
53	STANDARD		VPH LENS 2	Infinity	-15	BK7	160	0
54	STANDARD		VPH LENS 2	-5117.579	0		160	0
55	COORDBRK			-	-40		-	-
56	COORDBRK		CAMERA OFFSET	-	0		-	-
57	STANDARD		"APERTURE STOP"	Infinity	0		168.0042	0
58	STANDARD		BCM1.1	-1500	-35	S-FPL51Y	150	-181.6
59	STANDARD			295.4211	-17.24081		150	0
60	STANDARD		BCM2.1	190.1559	-10	PBM2Y	150	0
61	STANDARD		BCM2.2	-143.4802	-40	S-FSL5	180	0
62	STANDARD			-1385.66	-1		180	0
63	STANDARD		BCM3.1	-275.7727	-50	S-FPL51Y	200	0
64	STANDARD			282.9042	-114.8481		200	0
65	STANDARD		BCM4.1	-323.1683	-42.5	PBM2Y	220	0
66	STANDARD			777.002	-1		220	0

67	STANDARD		BCM5.1	-105.2192	-55	PBM2Y	185	0
68	STANDARD			-79.51249	-18.16142		135	0
69	STANDARD		BCM6.1	-104.7826	-55	PBM2Y	130	0
70	STANDARD			-196.8763	-17.5		90	0
71	COORDBRK			-	0		-	-
72	STANDARD		BCM7.1	154.3904	0	SILICA	85	0
73	TOROIDAL			Infinity	-13	SILICA	95	0
74	TOROIDAL			-567.5836	-6.41121		80	0
IMA	STANDARD		DETECTOR	Infinity			70.03411	0

B.4.2 SALT HRS R4 – Red arm

Surf	Type	Comment	Radius	Thickness	Glass	Diameter	Conic
OBJ	STANDARD	INTERMEDIATE INJECT	Infinity	534.3569		21.2132	0
1	STANDARD	FC1.1	96.81967	15	N-FK51	60	0
2	STANDARD	FC1.2	-85.49425	15	S-LAL7	60	0
3	STANDARD		-563.0025	10		60	0
4	STANDARD	VACUUM WINDOW	Infinity	10	SILICA	60	0
5	STANDARD		Infinity	10		60	0
6	STANDARD	FC2.1	180.6662	15	S-LAL7	50	0
7	STANDARD	FC2.2	49.29438	15	N-FK51	50	0
8	STANDARD		-212.0699	174.6397		50	0
9	STANDARD	"SLIT PLATE"	Infinity	0.5		8.596829	0
10	STANDARD	TC 1.1	18.0863	3	BK7	12.5	0
11	STANDARD		39.198	-2.53		12.5	0
12	COORDBRK	OFF-AXIS ANGLE	-	0		-	-
13	COORDBRK	Y DECENTRE	-	267.47		-	-
14	COORDBRK		-	0		-	-
15	COORDBRK		-	0		-	-
16	COORDBRK	INJECTION ANGLE	-	0		-	-
17	STANDARD	FOLD MIRROR	Infinity	0	MIRROR	188.858	0
18	COORDBRK		-	0		-	-
19	COORDBRK		-	0		-	-
20	COORDBRK		-	267.47		-	-
21	STANDARD	"DIRECT INJECTION"	Infinity	-267.47		20	0
22	COORDBRK		-	-1735		-	-
23	STANDARD	M1 PASS 1	4000	2000	MIRROR	800	-1

24	COORDBRK	GRATING DECENTRE	-	0		-	-
25	COORDBRK	BLAZE ANGLE	-	0		-	-
26	COORDBRK	THETA	-	0		-	-
27	COORDBRK	ROTATE GROOVES	-	0		-	-
STO	DGRATING	ECHELLE	Infinity	0	MIRROR	861.1699	0
29	COORDBRK	UNROTATE	-	0		-	-
30	COORDBRK	UNDO THETA	-	0		-	-
31	COORDBRK	BLAZE ANGLE UNDO	-	0		-	-
32	COORDBRK	BACK TO GLOBAL-Z	-	-2000		-	-
33	STANDARD	M1 PASS 2	4000	0	MIRROR	800	-1
34	STANDARD	M1 PARENT	Infinity	2000		690	0
35	COORDBRK		-	0		-	-
36	STANDARD	INT. IMAGE	Infinity	150		304.1606	0
37	STANDARD	DICHROIC	Infinity	15	F_SILICA	319.3556	0
38	STANDARD		Infinity	988.0404		212.0425	0
39	COORDBRK	FOCUS	-	0		-	-
40	STANDARD	2ND PUPIL MIRROR	-2222.222	0	MIRROR	440	0
41	COORDBRK		-	-1050		-	-
42	COORDBRK	DEC. TO WH. PUPIL	-	0		-	-
43	STANDARD	WHITE PUPIL	Infinity	150		147.716	0
44	COORDBRK		-	0		-	-
45	STANDARD	FOLD MIRROR	Infinity	0	MIRROR	204.4704	0
46	COORDBRK		-	125		-	-
47	COORDBRK	AOI	-	0		-	-
48	STANDARD	VPH LENS 1	4300.759	15	BK7	160	0
49	STANDARD	VPH LENS 1	Infinity	0	BK7	160	0
50	STANDARD	VPH	Infinity	10	BK7	160	0
51	DGRATING	VPH	Infinity	10	BK7	160	0
52	STANDARD	VPH	Infinity	0	BK7	160	0
53	STANDARD	VPH LENS 2	Infinity	15	BK7	160	0
54	STANDARD	VPH LENS 2	4300.759	0		160	0
55	COORDBRK		-	40		-	-
56	COORDBRK	CAMERA OFFSET	-	0		-	-
57	STANDARD	"APERTURE STOP"	Infinity	0		161.9181	0
58	STANDARD	BCM1.1	Infinity	0		200	0
59	STANDARD		Infinity	0		200	0
60	STANDARD	RCM1.1	309.3243	60	S-FSL5	170	-2.763853

61	STANDARD		RCM1.2	-151.3385	20.5	S-TIH1	170	0
62	STANDARD			415.2096	57.31691		170	0
63	STANDARD		RCM2.1	1284.695	55	S-BAH11	220	0
64	STANDARD			-242.0536	47.51831		220	0
65	STANDARD		RCM3.1	148.8329	55	BK7	210	0
66	STANDARD			652.7292	84.59567		210	0
67	STANDARD		RCM4.1	199.7302	40	S-BAH11	140	0
68	STANDARD			261.3614	25		120	0
69	STANDARD		BCM6.1	Infinity	0		150	0
70	STANDARD			Infinity	0		150	0
71	COORDBRK			-	0		-	-
72	STANDARD		RCM5.1	-126.7565	0	SILICA	105	0
73	TOROIDAL			Infinity	13	SILICA	115	0
74	TOROIDAL			693.3784	8.341316		100	0
IMA	STANDARD		DETECTOR	Infinity			84.55915	0

Appendix C

HERCULES observing manual

C.1 Initializing HERCULES

C.1.1 Before observing begins

- Check the CCD supply dewar (located in the main corridor outside the HERCULES room) is at least 30% full. This will allow for at least 2 automatic fills of the CCD dewar. These are usually scheduled to occur at 6 am and 6 pm each day. To refill the dewar:

  - Unscrew the black plug on the dewar lid.
  - Insert the filling funnel.
  - Fill the dewar from a 10 or 20 litre dewar.

  Carry out a manual fill immediately afterward to check that there are no leaks and the filling system is working correctly. The CCD control box temperature reading should be approximately -85°C. The display may be viewed by removing the small cover directly above the supply dewar between the CCD controller vents.

- Make certain all HERCULES room lights are off and that there are no light leaks into the HERCULES room.

- Turn on the exposure meter PMT power supply. This is located on a shelf in the data room beside the computer Octans. *NEVER* switch the HERCULES room lights on while the PMT is switched on. Check that the voltage is set to 1125 V.

- Turn on the exposure meter electronics (the red switch marked `MAINS` on the box with the exposure meter analogue display).

C.1.2 Initializing the HERCULES fibre-feed control

The HERCULES fibre-feed control software operates on the PC running Windows situated beside Hydrus (the Linux computer on which the CCD controller runs). This software controls all aspects of the fibre-feed module including the shutter, the exposure meter, and auto-guiding. It also monitors the temperature and pressure inside the HERCULES spectrograph. To start the HERCULES fibre-feed control:

- In the dome:

  - Ensure that the fibre-feed module is plugged into the telescope pier and turned on.

- Ensure that the telescope drive speed on the main telescope controls (in a small drawer under the displays) is set to the lowest speed (1). This determines the auto-guide slewing rate and is also the manual telescope control on the fibre-feed control.
- Turn on the thorium-argon lamp power supply. The Photron power supply is located next to the fibre-feed module on the telescope.
  1. Before turning on ensure that the current is zero. The current controller should be fully turned anti-clockwise.
  2. Turn mains switch on.
  3. Adjust current control to 7 mA.

  (*Note:* The Photron power supply replaces the original power supply. The small switch by the green LED is now redundant.) The power supply should be turned on an hour or so before observations begin in order to ensure that the lamp has stabilized.
- Turn on the image intensifier. There is a small switch on the fibre-feed module by a red LED.
- The only variable control on the fibre-feed module is the fibre number. Choose between:
  * fibre #1 – a 100 μm fibre,
  * fibre #2 – a 50 μm fibre, and
  * fibre #3 – a 100 μm fibre with a 50 μm micro-slit.

  See Section C.2.3 for details on the fibres.

- In the control room:
  - To start the HERCULES fibre-feed control double-click on the icon named `Hercules fibre-feed control`. The initialization process takes a few seconds. The graphical user interface shown in Figure C.1 should now appear.

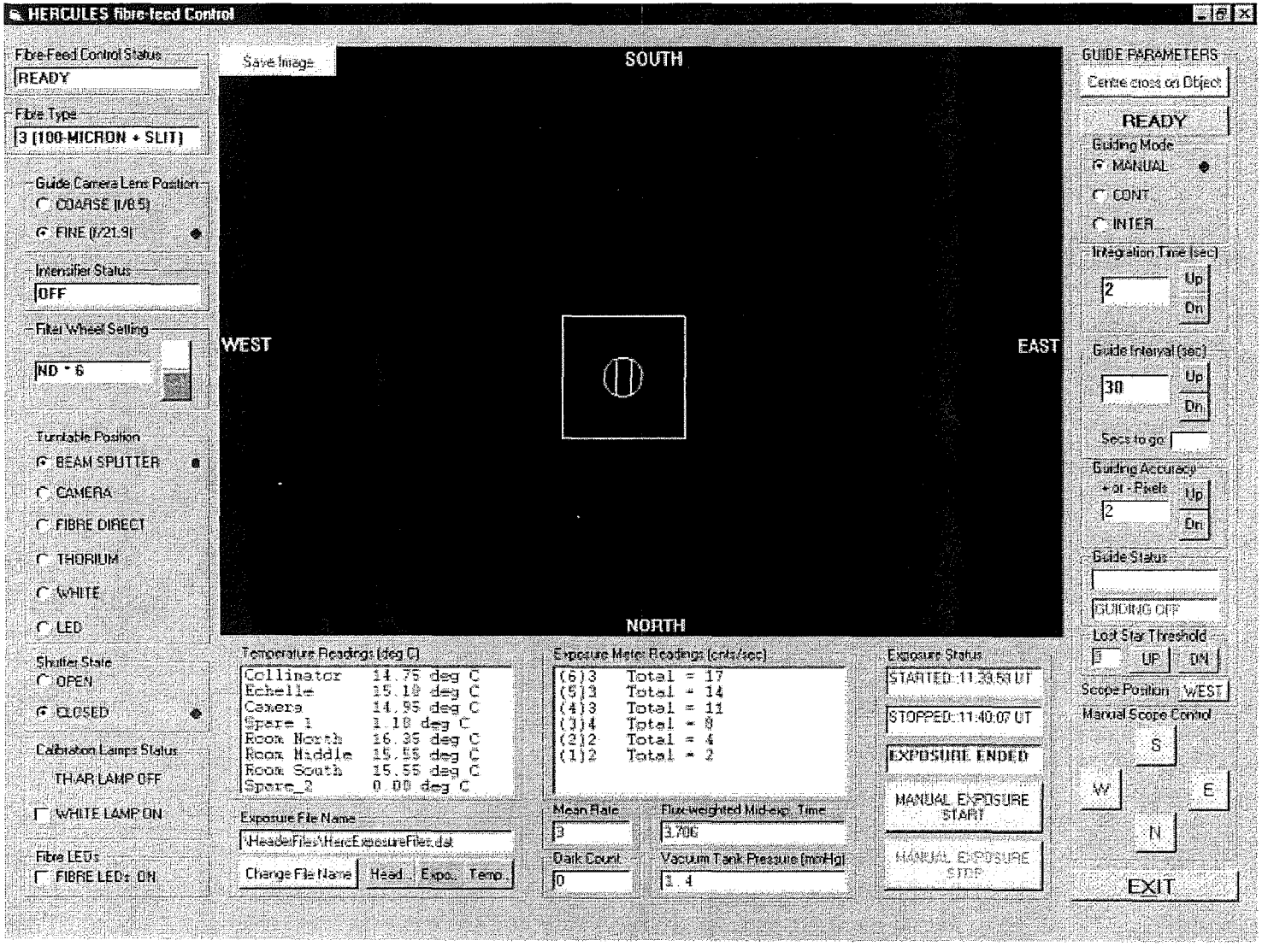

Figure C.1: *The HERCULES fibre-feed control graphical user interface.*

C.1.3 Using MoJo

The Mount John CCD image acquisition software runs only on the Linux machine Hydrus. First start an Xwindows session (i.e., logon) then type `mojo` at a command prompt. Three windows (see Figure C.2) will open:

1. the main control panel,
2. the instrument control panel, and
3. a message window.

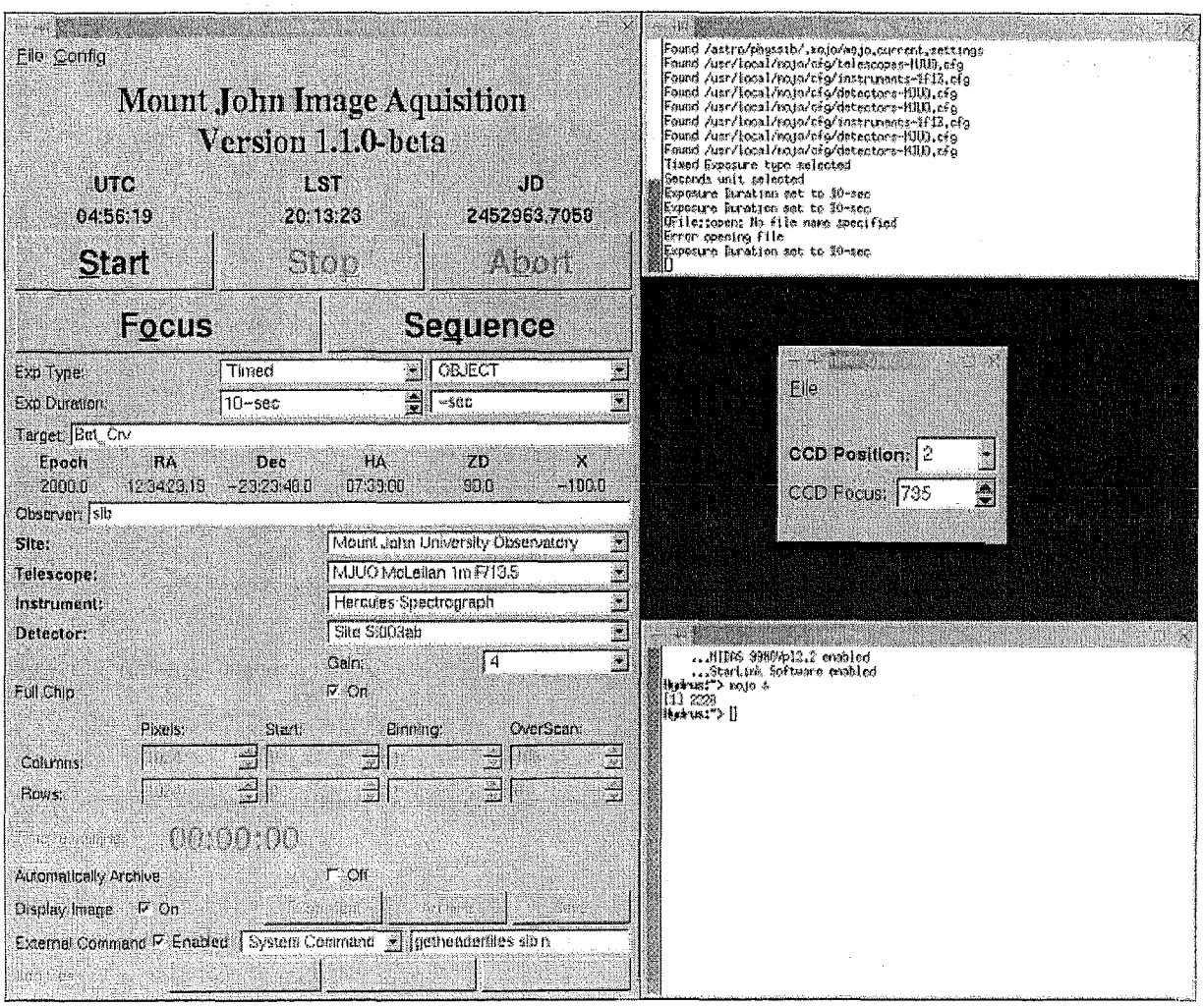

Figure C.2: *The MoJo control panel.*

In the main control panel the observer first needs to set the instrument parameters. The observer should do the following:

- Enter the observers initials or name in the **Observer** box.
- The **Site** should be Mount John University Observatory.
- Set the **Telescope** to `MJUO McLellan 1m f/13.5`.

- Set the **Instrument** to the HERCULES spectrograph. In the HERCULES instrument control panel the following information must be manually entered:

  1. **CCD position** (see Section C.2.1)
  2. **CCD focus**. See Appendix C.5 for instructions on obtaining the best focus.

- The only **Detector** available is the `Site Si003ab`. Set the **Gain** to `4`. This is the appropriate setting for spectroscopy. The inverse gain at this setting is $1.22\,e^-$/ADU, and the base level noise is $2.59\,e^-$.

- The **External Command** should be enabled and set to the system command `getheaderfiles [obs]`, where `[obs]` should be the same as entered in the **Observer** box.

Next, the **Exposure type** should be set. The possibilities are:

- The exposure can be either `Timed` or `Bulb`. The latter allows the user to stop the exposure and read-out the CCD at any time. This is particularly useful when using the HERCULES spectrograph as the observer may stop the exposure when the exposure-meter records sufficient flux.

- The possible exposure types are `bias`, `dark`, `th_arc`, `smooth_field`, and `object`. To ensure that the fits image headers are meaningful the object type should be changed on MoJo when the HERCULES object is changed.

The **Target** can be set while the **Exposure Type** is set to `object`. The system MoJo target list may be found at

`/usr/local/mojo-[latest_version_number]/targets.dat`.

The `targets.dat` file contains the following objects with declinations less than +25°:

1. 1208 stars with Bayer designations (e.g. β Corvi)
2. 1612 stars with Flamsteed numbers (e.g. 9 Corvi)
3. 6431 HR stars
4. 28763 HD stars

When entering these stars into MoJo remember always to use the underscore (_) in the star names. E.g., `9_crv`, `hr_4786`, or `hd_109379`. The Bayer names (Greek letters) in the star list are up to three characters long, so that, for example, `alp` should be used for "alpha", `bet` for "beta", etc. The constellations are given as standard three-letter abbreviations. The search is case insensitive. Additional stars can be included in the observers personal `targets.dat` file. The `mojo.rc` file should then be edited to show the location of this file. For example,

`Targets::~/.mojo/targets.dat`

Be sure that the format of your personal targets file is identical to the system `targets.dat` file.

To start an exposure press **Start**. This sends a command to the fibre-feed control to open the shutter and to start the exposure meter. If the exposure type is `Timed` then the exposure will continue for the **Exposure Duration** or until **Stop** or **Abort** is pressed. Otherwise a `Bulb` image will continue until **Stop** or **Abort** is pressed. If the **Display Image** option is on then after the readout the MoJo image window will display the current image (see Figure C.3). An aborted exposure will not be read out. To save an image click **ARCHIVE**. Archiving is complete when the **ARCHIVE** letters turn grey. It is also possible to **Automatically Archive**.

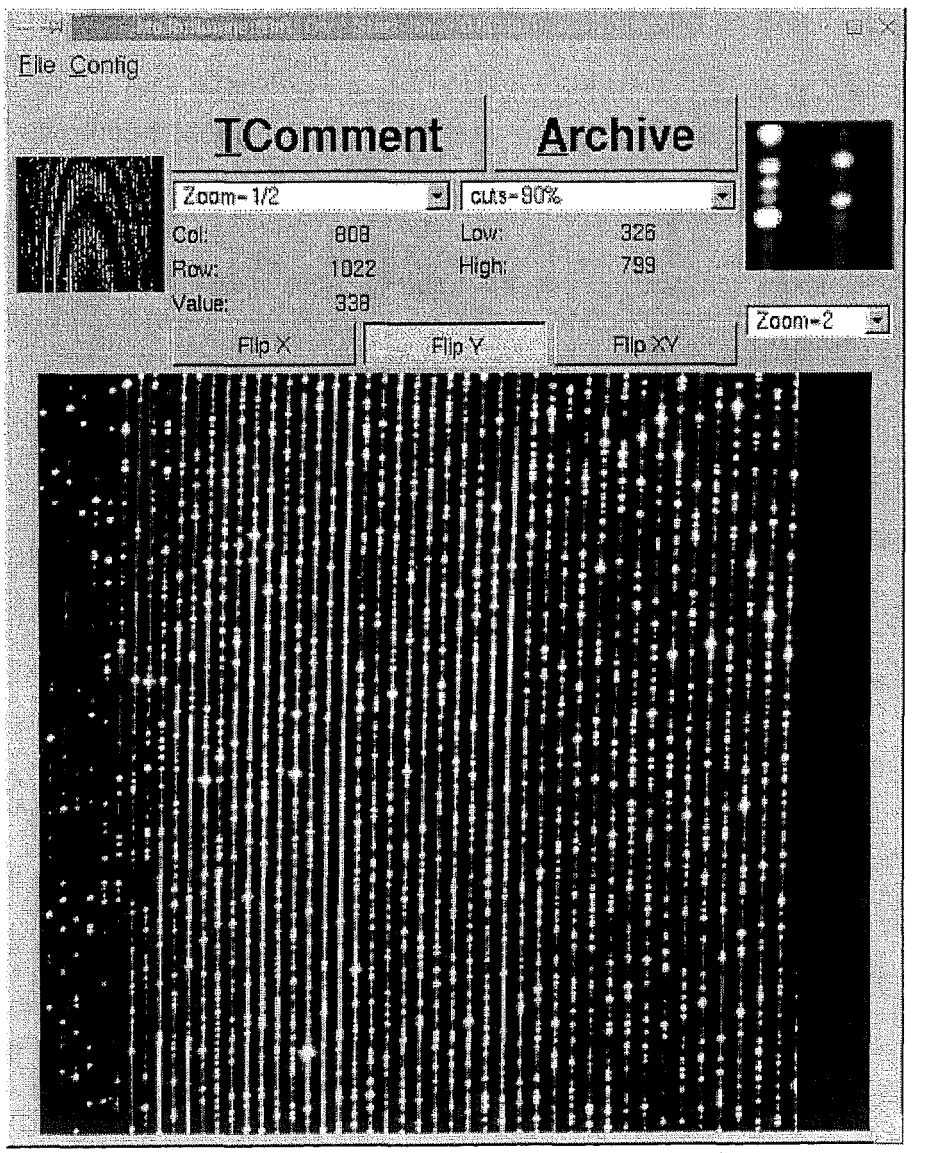

Figure C.3: *The MoJo image display.*

C.2 Observing

C.2.1 CCD position

The CCD position is the only user adjustment inside the HERCULES spectrograph room. There are presently four discrete positions for the CCD which are defined by the brackets for the CCD cradle (see Figure C.4). To reposition the CCD remove the locking nut on the front of the cradle and lift the cradle into the appropriate slot. Be sure that all three locating pins have entered the same slot. This will be easier if the CCD cradle is held steady and level whilst being inserted. The CCD should not be shut down or have the electronics plug removed. Note that it should not be necessary to refocus if the CCD has been repositioned, but the observer would be prudent to check this. Spectra taken with the CCD in each of the four regions may be viewed at:

`http://www.phys.canterbury.ac.nz/research/astronomy/hercules/CCD_regions.shtml`

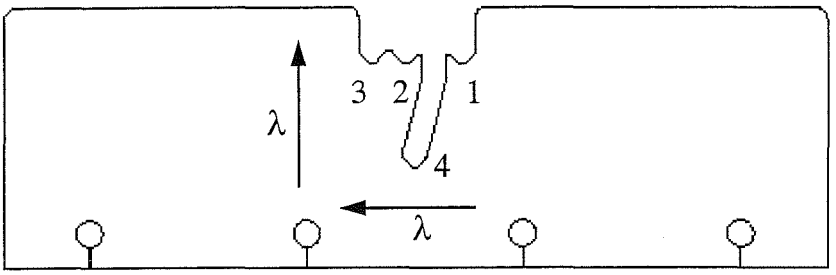

Figure C.4: *The CCD positioning template. The three locating pins on the CCD cradle can be positioned in one of the four numbered slots. The directions of main dispersion and cross-dispersion are shown*

C.2.2 CCD focus

The CCD focus control is in the data room near the computer Hydrus. See Appendix C.5 for instructions on how to focus HERCULES.

C.2.3 Fibre choice

There are three different fibres are available on HERCULES. Changing the fibre type will give the resolving powers given in Table C.1. The relative throughput of the three fibres

Fibre no.	Fibre type	Image scale arcsecs	Resolving power $\lambda/\delta\lambda$
1	100 μm	4.50	41 000
2	50 μm	2.25	82 000
3	100 μm with 50μm microslit	4.50	70 000

Table C.1: *Fibre type and resolving power*

is shown in Figure C.6. When the highest resolving powers is desired the choice between fibres "2" and "3" will depend upon the seeing (see section C.3.1 for instructions on how to compute the seeing). It can be seen that if the seeing is better than about 2″ then it would be better to use the 50 μm fibre. If the seeing is worse than this then the 100 μm with 50μm microslit will give superior throughput for about the same effective resolving

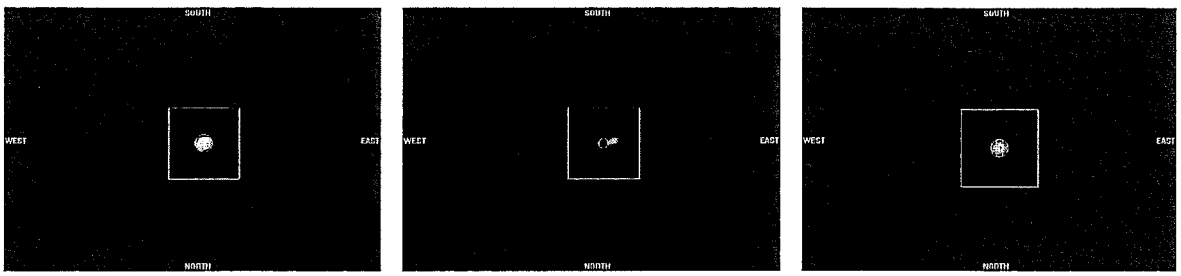

(a) *Fibre 1* (b) *Fibre 2* (c) *Fibre 3*

Figure C.5: *The observer can choose between three fibres; a 100 μm fibre (fibre 1), a 50 μm fibre (fibre 2), and a 100 μm fibre with a 50 μm micro-slit (fibre 3)*

power. Because the exits of all three fibres are in the same plane it is not necessary to refocus the spectrograph every time the fibre is changed however the telescope may need to be repositioned and/or refocused.

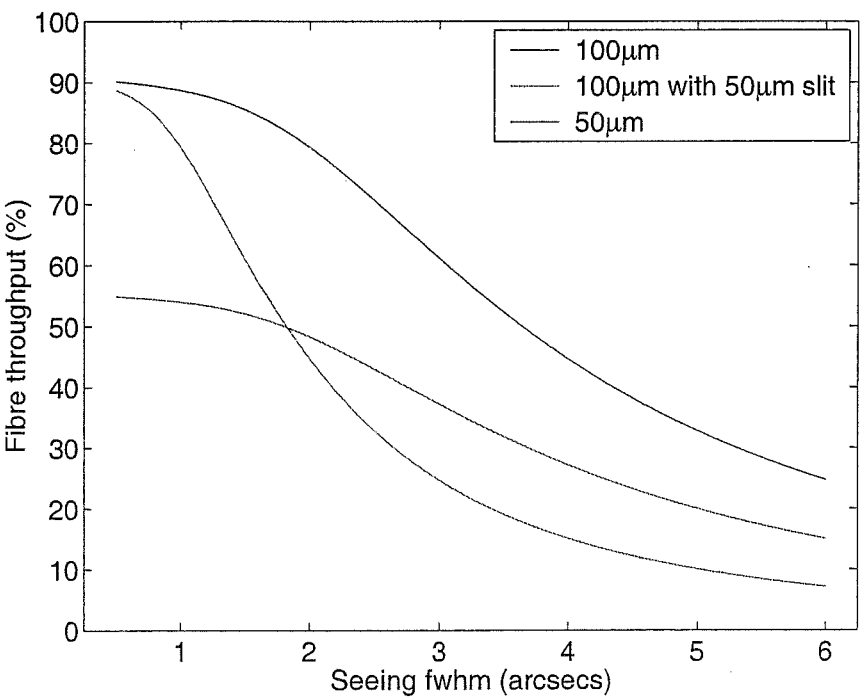

Figure C.6: [*The throughput of the* HERCULES *fibres.*] *The throughput of the three* HERCULES *fibres. Entrance, exit and absorption losses are all accounted for.*

C.2.4 Calibration spectra

White-light spectra

Set the turntable position on the HERCULES fibre-feed to "WHITE". This will automatically turn on the white lamp. Individual observers will require a different set of white light images depending on what their requirements are. For instance, with the CCD in positions "1", "2", and "3" at least different exposure lengths will be required to record a reasonable signal in each third of the CCD. The ratio of these exposures will be of the order 1:3.3:13.3. The red orders will become increasingly saturated as the exposure time increases, but these orders will not be used when flat-fielding. For the purposes of flat-fielding the observer should take at least 9 exposures at each exposure time. However, it should be noted that a single white light spectra suffices for order definition and for approximately normalizing the extracted spectra.

Now on MoJo, select `smooth` as the "Object", set the "Exposure Type" to `timed` and enter the required exposure duration. Click "Start" to begin the exposure. Archive the resulting image. It may be more convenient to use MoJo's "SEQUENCE" function and archive the images automatically.

Thorium-argon spectra

The thorium-argon lamp should already have been turned on at the fibre-feed module. (Note that because the power supply is now external the calibration lamp state will not be displayed on the fibre-feed control.) Set the turntable position to "THORIUM". Again users will have to determine the optimum length of exposure. When the CCD is in position "2", the MIDAS command

```
@c check_thorium [thorium file name]
```

can be used to compute the ideal exposure length. The purpose of this program is to ensure that every thorium image is exposed for a similar duration. It also monitors changes in the output of the thorium lamp which has been observed to change because of some unknown cause.

Now on MoJo set the "Exposure Type" to `timed th_arc` and enter the required exposure duration. Click "Start" to begin your exposure. Archive the resulting image.

C.2.5 Stellar spectra

The guide and acquisition camera

The guide and acquisition camera works by inserting a diagonal mirror or beam-splitter into the telescope beam which directs some or all of the light to an image intensified camera. The acquisition and guide camera has two modes of operation:

1. "COARSE" ($f/8.5$) – FOV $= 5.3' \times 3.7'$ and
2. "FINE" ($f/21.9$) – FOV $= 2.1' \times 1.4'$.

The auto-guiding routines will work in either mode.

The exposure meter

The exposure meter uses a small fraction of light that would otherwise be lost to the hole in the flat fold-mirror of the camera. A diagonal mirror and lens array directs the light to a PMT situated on the outside of the HERCULES tank. It is very useful to have some idea of the total flux the exposure meter needs to record in order to reach a S/N ratio which satisfies the observer's requirements. This can be easily determined by observing a bright star. With the CCD in position "2" an accumulated count of approximately 1.4×10^6 is sufficient to give a S/N of 100 in the middle of the spectrum for K and G type stars. Note that the PMT is very sensitive to small changes in voltage and this value may change.

Locating the fibre

It is not possible simultaneously to view both the star and the fibre input. Therefore the fibre-feed module contains a set of transfer lenses which reimage the fibre input onto the camera. A set of LEDs inside the spectrograph provide the back-light for this operation. To find the approximate location of the fibre set the turntable position to "LED". This will automatically turn on the LEDs and set the camera position to "FINE". The fibre should now be visible. Mark the fibre location by clicking "Centre cross on object" then dragging a box over the fibre image and clicking "OK". The box will be centred over the fibre.

Acquiring a star

First, in MoJo, enter the "Target" name. This is useful to do first because MoJo will display the R.A. and Dec. of the star, as well as its airmass. To acquire a new star set the HERCULES camera mode to "COARSE" and drive the telescope to the appropriate coordinates. The pointing of the McLellan telescope is not perfect and a small offset must be used to locate an object. This offset can easily be determined by observing a bright nearby star. Generally, R.A. is the most reliable adjustment – point the telescope approximately 20^s west of true R.A. Declination is more uncertain but observers note that it is usually 3 to $7'$ north of the true declination.

IMPORTANT: If the movement of the telescope is relatively large the observer should do this while in the dome in order to avoid damaging the fibre. Under NO circumstances should the observer drive the telescope more than once around the polar axis! Not only does this have the potential to damage the fibre, but all the electronic connections in the pier will be destroyed. A small box in the data room under the dome window indicates the telescope's relative position. It has 5 LEDs of which the central one is green and the others are red. If any of the red LEDs are on then the telescope needs to be driven in the opposite direction to unwind the fibre and electronics. The observer should do this while in the dome!

Once a star has been roughly acquired and focused (using the image on the screen), the camera mode may be set to "FINE" so as to precisely place the star. However, it is common practice to use the "COARSE" setting for both acquisition and guiding. The "Filter wheel setting" may need to be changed to brighten or darken the image.

Although the relative alignment of the fibre image and the star image should be sufficiently accurate that starlight will now enter the spectrograph it is possible to improve the pointing of the telescope. This is done using the exposure meter. The following steps are necessary:

- Set fibre-feed position to "BEAM SPLITTER".
- Using the fibre-feed controls only, start a manual exposure. Be sure to set the guide mode to "MANUAL".
- While watching either the analogue meter or the display on the fibre feed control make small adjustments in RA and DEC in order to maximize the light entering the spectrograph. The observer should make adjustments in one axis at a time in order to maximize the count rate.
- It may also be necessary to refocus the telescope. Be warned that this will also move the stellar image. The previous step will then have to be repeated.
- When the flux has been maximized click "Centre Cross On Object". Drag a drag the box over the star and click "OKAY". The guiding box will centre itself on the image.
- Be sure to stop the manual exposure before acquiring a spectrum.

C.2.6 Guiding

Initially the beam-splitter was not installed and acquisition and guiding were performed using the diagonal mirror (i.e., the turntable position "CAMERA"). The installation of a beam-splitter now means that acquisition of an object and guiding during exposures both use the same turntable position. In practice the observer will find this the most useful mode for guiding on all but the faintest stars ($m_V > 10$). However, for the sake of completeness, the following will describe both the original "INTERMITTENT" guiding (which uses only the "CAMERA" turntable position) and "CONTINUOUS" (which will be used with the "BEAMSPLITTER").

Manual guiding

With some patience it is possible to guide a star manually. First the star should be located using the method described above. After making the necessary calibration images the star should be recentred using the procedure described above. Set turntable position to "BEAMSPLITTER" or "FIBRE DIRECT" and the guide mode to "MANUAL". Note that if the latter option is used, it will not be possible to see the star.

Decide whether you want the MoJo exposure type to be "Timed" or "Bulb". If the exposure type is "Bulb" the exposure should end only when the desired exposure meter count has been reached. Click "Start" to begin the exposure. Watch the exposure meter and from time to time make small adjustments in order to maximize the count rate. It should only be necessary to make adjustments every minute or two. It will probably be the case that corrections will always be in the same direction indicating that the tracking rate of the telescope is not perfect and/or that uncorrected telescope flexure is present.

Continuous guiding

Again, centre the star as described in section C.2.5. The box should be set to a minimum size as it is not possible for the star to drift outside its bounds. Set the turntable position to "BEAMSPLITTER" and the guiding mode to "CONTINUOUS". Guiding will begin immediately and will continue until the guide mode is set to manual or the guide star is lost.

Next, the guide parameters should be adjusted. The *integration time* changes the number of images that are co-added before an auto-guiding correction is computed. The integration time should be more in times of bad seeing in order to average out large shifts in the centroid however 1 or 2 seconds is generally sufficient. Note that the filter wheel should be set at the lowest possible setting that still allows the star to be seen. This is to avoid saturating the camera, which could affect the centroid accuracy. The *guiding accuracy* indicates the tolerance on the centroiding. A correction of the telescope position will be made if the current centroid is greater than the stated number of pixels from the centre of the guide box. This number should be less in good seeing and more in poor seeing. Typically 2 to 4 pixels (each $0.2''$) is sufficient. A green light appears in the integration time window to indicate that the camera is exposing. An adjacent red light indicates that the telescope is moving.

Click "Start" on MoJo to begin the exposure.

Intermittent guiding

The star should be centred as described in Section C.2.5 except that the fine-tuning of the star's location should be done with the turntable on "FIBRE DIRECT" and the marking of the guide box with the turntable on "CAMERA". The guide mode should be set to "INTERMITTENT" and before an exposure begins the turntable should be returned to "CAMERA".

Again, adjust the integration time and guiding accuracy. During intermittent guiding the turntable will periodically move from "FIBRE DIRECT" to "CAMERA" and if necessary an auto-guiding correction will be made. This correction will take a few seconds and the *guide interval* is the interval between successive corrections. If the telescope is tracking well then this interval could be anywhere from one to several minutes. A lower limit of 30 seconds is possible.

Click "Start" on MoJo to begin the exposure.

C.3 Miscellaneous additional information

C.3.1 Computing atmospheric seeing

It is possible to use the fibre-feed module's guide camera to compute the seeing. To do this:

- Select "BEAMSPLITTER" or "CAMERA" and set the lens position to "FINE". Find a star. Choose a filter which prevents the star from saturating the camera.

- Click "Centre cross on object" and drag a box over the star. Click "OK".

- Set the integration time to several seconds to compute the average or integrated seeing.
- Click "Save Image". The button is in the top left hand corner of the guide camera display. The image will be saved as `/mnt/herc/IMAGEFILE.DAT`. The pixel scale of this image is 0.205″.
- Finally, at a command prompt on Hydrus type:

  `compute_hercules_seeing`

  The terminal will display the FWHM of a fitted 2-dimensional gaussian. The central position and x and y FWMH values will also be displayed. The average seeing for that night should be recorded in the observer's log book which is found in the data room. If the profile (which is displayed briefly and saved to the file `hercules_seeing.ps`) appears flattened about the centre then the camera has been saturated. Either change the filter and/or switch from/to "BEAMSPLITTER" or "CAMERA" and try again. Otherwise, try a dimmer star.

Alternatively the observer may wish to save the image file `/mnt/herc/IMAGEFILE.DAT` to a permanent location; e.g.,

`cp /mnt/herc/IMAGEFILE.DAT [filename.dat].`

This image may also be used to compute the "seeing". Simply type:

`compute_hercules_seeing [filename]`

where the filename is entered without the `.dat` extension.

C.3.2 HERCULES log files

The Hercules computer will supply at the end of an exposure the following three files:

1. `/mnt/herc/HercHeaderFile.dat`

   This file contains all the information about the status of the fibre-feed controller at the end of each exposure. An example of such a file follows:

```
STARTED::15:23:41 UT
STOPPED::16:11:42 UT
ExposureType::Stellar
Fibre type::1 (100-MICRON NO SLIT)
Temp in deg C::Collimator 10.95 ::Echelle 11.95 ::Camera 13.85 ...
Tank pressure::2.6 mm
Exposure meter flux::1023707
Mean count::356
Flux-weighted mid-exposure::1416.681
```

2. `/mnt/herc/HercExposureFiles.dat`

   This file contains a continuous log of the exposure meter readings every second.

3. `/mnt/herc/HercTemperatureFile.dat`

   This file contains a continuous log of the temperatures.

The following two subsections describe how the information contained in these files is saved for later use.

The HERCULES FITS header

The images produced by MoJo are in the standard FITS (Flexible Image Transport System) format. See NASA's HEASARC webpage

`http://heasarc.gsfc.nasa.gov/docs/heasarc/fits_overview.html`

for detailed information on the FITS image format. Of relevance here is the fact that every FITS image contains an ASCII header unit which has the general form:

```
KEYNAME = value / comment string
```

This is known as the "FITS header". MoJo currently fills the FITS header of each image with a variety of information about the current image, including some details about the instrument on which they were captured. The majority of the information contained in the file `/mnt/herc/HercHeaderFile.dat` is automatically read by MoJo into the current image's FITS header. An example of the how the above file would be included in the FITS header of the current image follows:

```
INSTRUME= 'HERCULES'           / Hercules
HERCUTC1= '15:23:41'           / Hercules START UTC
HERCUTC2= '16:11:42'           / Hercules STOP UTC
HERCEXPT= 'STELLAR'            / Hercules Exposure Type
HERCFIB = '1 (100-MICRON NO SLIT)' / Hercules Fibre 1/2/3
HERCT1  =  1.0950000000000E+01 / Hercules Temperature Collimator
HERCT2  =  1.1950000000000E+01 / Hercules Temperature Echelle
HERCT3  =  1.3850000000000E+01 / Hercules Temperature Camera
HERCT4  =  0.0000000000000E+00 / Hercules Temperature Spare_1
HERCT5  =  1.3550000000000E+01 / Hercules Temperature Room_Nth
HERCT6  =  1.2350000000000E+01 / Hercules Temperature Room_Mid
HERCT7  =  1.2150000000000E+01 / Hercules Temperature Room_Sth
HERCT8  =  0.0000000000000E+00 / Hercules Temperature Spare_2
HERCP   =  2.5000000000000E+00 / Hercules Pressure (mm)
HERCFTC =              1023707 / Hercules flux meter total counts
HERCFMC =                  356 / Hercules mean count
HERCFWMT=  1.4166810000000E+03 / Hercules flux-weighted mean exp time (mins)
```

The data manually entered in the "Hercules instrument controller" window (see Section C.1.3) are also included. That is the following two fields are also found in the FITS header:

```
HERCCCDP=                    2 / Hercules CCD Position [1,2,3 or 4]
HERCCCDF=                  830 / Hercules CCD Focus (mm)
```

The FITS header of an image can be viewed in a number of ways. A simple way to view the FITS header is to use the unix command

```
more [filename].fit
```

Another way is to use Gaia and choose "View" then "fits header".

Archiving header files

It is useful to retain copies of the exposure meter and temperature log files as they are **NOT** automatically saved. All users should be encouraged to follow the following few instructions in order to ensure that all these files will be available for quick and easy examination by anyone who wishes to examine the performance of HERCULES.

It is possible to archive these header files by running a short shell script at the end of each exposure. This can be done automatically as follows:

- Turn ON MoJo's external command
- Enter the following command in the space provided:

  `getheaderfiles [observers initials] [y/n]`

  where the observers initials must match those entered in MoJo's "Observer" field. Enter n if "Automatic Archiving" is turned OFF and y if it is turned ON.

All three files will now be saved to the directories:
`/dos/d/mjuo/si003ab/[ccyymmdd]/Headerfiles_[yymmccdd]`
and
`/dos/e/[obs]/si003ab/[ccyymmdd]/Headerfiles_[ccyymmdd]`
where `[obs]` are the observers initials and `[ccyymmdd]` specifies that night's archive directory. The files will also be named according to their parent archive image. That is, they will have the names:

- `HercHeaderFile.dat` → `[prefix][file#]_header.dat`
- `HercExposureFiles.dat` → `[prefix][file#]_exp.dat`
- `HercTemperatureFile.dat` → `[prefix][file#]_temp.dat`

where `[prefix]` is the night's image prefix (e.g., f2078) and `[file#]` are the successive archived file numbers (e.g., 001, 002, etc).

Monitoring header files

The information contained in the header files for a particular night can be examined by using the command:
`monitorhercules [ccyy] [mm] [dd]`
This information will be displayed on the observer's terminal. Use the Unix pipe command `>!` to direct the output to a file; i.e.,
`monitorhercules [ccyy] [mm] [dd] > ! [filename.dat].`

C.4 Trouble shooting

Note: These trouble shooting notes relate only to problems encountered (so far!) with HERCULES. Check Alan Gilmore's trouble shooting orange pages in the 1-metre Information Folders in the data room and dome for more general telescope/dome problems. Please report any additional problems you encounter and potential solutions to them.

C.4.1 The CCD dark readout is not what was expected

The following problems may have occurred (see C.4.2 and C.4.3 for other CCD problems):

- The CCD is completely saturated.

  If the chip has been saturated by bright light a few darks may be needed to clear it.

  Check the SITe control box temperature is about -94.5°C and that the dewar is not empty.

  Check that the fibre back-light LEDs have not remained on, even though the HERCULES status shows they are off. This known problem is solved by turning the LEDs on and off.

  If all else fails, try reinitializing the fibre-feed control or turning off the SITe control box for a few minutes.

  NEVER unplug the CCD electronics from the dewar in the hope that it may solve a readout problem. The plug is already damaged and a careless observer may break it entirely.

- A bias or short exposure has diagonal waves of light and dark across it.

  This is apparently due to some sort of mains power interference. The observation is that it is not a significant source of noise (try plotting a cross-section of an image).

- The chip has irregular darker vertical bands through it.

  Sometimes this is cleared by turning off the SITe control box for a minute or so. It doesn't seem to affect the chip pixel dark values nor have any effect on subsequent spectra.

C.4.2 CCD is contaminated with thorium or white light

After taking a stellar exposure, make certain that MoJo has successfully closed the HERCULES shutter before changing the turntable to another position. This is because the shutter is actually located in the fibre-feed module and not at the CCD.

Check that the shutter state starts at "CLOSED" and that it then opens and closes when a MoJo exposure begins and ends.

Ensure that a "Manual Exposure" has not been previously started on the Hercules control.

C.4.3 Stellar CCD signal is not what expected from exposure meter counts

If the CCD signal is more than you expected then why are you complaining? Are you sure you have the right star? Check the telescope's pointing offset against a nearby bright isolated star. Otherwise, check for cloud (especially light cloud) and check fibre centring.

C.4.4 Exposure times much longer than expected

Check you have chosen the correct fibre. The fibres look noticeably different when using "LED". Check that the guide-box has been centred for maximum counts. Check the dome rotation, cloud, fog, poor seeing.

C.4.5 Hercules screen locks

This has been observed to occur when either

- an intermittent auto-guide sequence being interfered with an attempt by the observer to do something, such as the observer asking for an exposure to stop or
- occasionally when a manual exposure start/stop sequence on HERCULES is not properly completed.

The fibre feed status (top left corner) will probably show "BUSY".

Check all the status markers (black dots and red lights) are correctly paired off. Set the guide mode to "MANUAL" then fix any un-matched black dots and red lights by clicking on the black dot command line (this is what the fibre-feed control is trying to do).

When fixed, the status should be "READY". If not, reinitialize the fibre-feed control.

C.4.6 Filter wheel or turn-table out of alignment.

The filter wheel may occasionally get out of alignment so that an incorrect filter is been used. The only solution to this is to reinitialize the fibre-feed control.

It has also been observed that the mirror turret gets slightly out of alignment. This causes significant problems when using intermittent guiding. It would be better to use manual or continuous guiding only until the problem is fixed. File a fault report to have this done.

C.4.7 The fibre-feed control is acting "strangely"...

If anything genuinely puzzling is happening it will probably be solved by exiting the fibre-feed control software and restarting it. If this fails, try exiting the software then switching the fibre-feed module off at the mains (by unplugging the black power cable from the white power box). Then restart the fibre-feed control.

If you hear a noise continuously from the fibre-feed module (meaning the mirror turntable or camera lenses are rotating continuously) switch off the module at the telescope (or pull out the plug) and restart the fibre-feed control.

C.4.8 Auto-guide fails

If a previous good exposure meter count rate suddenly drops following an auto-guide then one of the following has probably occurred:

- The telescope slew speed on the control under the dome desk is not on speed "1".
- The star has moved from within the guide box.

- The "scope relative to pier" is on the wrong setting; i.e., east or west.
- The mirror turret may be misaligned. See C.4.6 above.

It may also be the case that the star was too faint because of cloud etc. Change the camera filter to a lighter filter if this is possible. Generally, if you can't see the star (with the beam-splitter) then it will probably be too faint to get a reasonable signal. Otherwise, if you wish, try manual or intermittent guiding using the direct "CAMERA" position.

C.4.9 Exposure meter dark count high

Check for any sources of light either in the dome or in the HERCULES room. Any lights along the fibre's path should be off (or minimized). This includes the data room, passageway, and dome. Note that the fluorescent lights continue to glow for some minutes after they are switched on. Unless you really have to – don't switch them on while observing. You should switch the PMT off first.

C.5 Focusing HERCULES

C.5.1 Introduction

A procedure has been written by J. Skuljan to enable observers to determine the best CCD focus. The following description was initially written by J. Skuljan.

C.5.2 The focuser

HERCULES is focused by adjusting the location of the CCD cradle. The focus control is in the data room near the Hercules control computer and the focus display is on the wall above this same computer. The control has three speed settings:

1. slow,
2. medium, and
3. fast.

The display is in millimeters, however, for historical reasons, the following discussion will assume that 1 unit equal 0.01 mm.

C.5.3 Collecting the images

In order to collect a series of thorium images suitable for focusing, do the following:

1. On Hercules computer:
   - Make sure that the thorium lamp is on (the switch is located on the fibre-feed module on the telescope, next to the image intensifier switch).
   - Choose a fibre. Check that the correct fibre number is displayed. (Note that the actual choice of fibre is unimportant as they are all located at the same focal plane.)
   - Select "THORIUM"
2. On Hydrus computer:
   - Start MoJo.
   - Check your usual settings (observer name, instrument, focal ratio, gain).
   - Select OBJECT, and then set the target name to `focus` (this is only to keep the FITS headers tidy – target name is optional).
   - Select TH-ARC.
   - Set exposure to "Timed", "5-sec".
   - Set "Full Chip" to OFF.
   - Select a 200 × 200 sub-frame around the centre of the CCD chip:

	Pixels:	Start:	Binning:	OverScan:
Columns:	200	400	1	0
Rows:	200	400	1	0

A larger frame may be also be useful. However, read-out times will be longer.

- Finally, collect a series of images at different focus positions. This may be done as follows. The focus should be set to about 50 units (0.5 mm) below the expected value. For example, if you expect the best focus to be at 570, start from 520. Step through the focus position by 10 units while exposing and archiving the images. Take e.g. 11 images, so that you end up at 50 units above the expected value (e.g. if you start from 520, stop at 620). The focus position **MUST** increase linearly for each successive image.

C.5.4 Running `focus_hercules`

Once you have collected the thorium images (as described above), open an X-terminal on Hydrus and change the directory to your usual working directory. Then copy the FITS files from your observing archive. If your observer name is *obsname*, and if the current date is 31 May 2001, then you can do something like this:

```
cp /dos/e/obsname/SI003AB/20010531/*.fit .
```

Alternatively, switch to this directory and run the command there; i.e:

```
cd /dos/e/obsname/SI003AB/20010531/ .
```

The procedure to compute the best focus may be run from a command line as follows

```
focus_hercules [P1] [P2] [P3] [P4] [P5] [P6]
```

where the six input parameters are:

- P1 – Image prefix, i.e. first five characters of the FITS file name (e.g. f2061).
- P2 – First image number.
- P3 – Last image number.
- P4 – First focus position (in units of 0.01 mm).
- P5 – Focus step (in units of 0.01 mm).
- P6 – 'Reference' image number. This will normally be an image in the middle of the sequence, where you expect the focus to be good. Whatever number you specify, the corresponding image will be displayed first, and you will have to choose an isolated spectral line from *that* image.

If your thorium images are numbered from 1 to 11 (e.g., `f2061001.fit` ... `2061011.fit` on 31 May 2001), and if they correspond to focus positions starting from 720 in steps of 10, then your command line will look like this:

```
focus_hercules f2061 1 11 720 10 6
```

Although it is essential that the focus position increases linearly as the image number increases (the program will calculate the focus position for every image from its sequence number) the image sequence does not have to start from 1. The procedure will accept images in any given range. For example, if the first thorium image is 27, then the command line becomes:

```
focus_hercules f2061 27 37 720 10 32
```

Note how the last parameter (the reference image) is now changed from 6 to 32, to stay in the middle of the sequence.

When the procedure is started, a display window will appear on your monitor (see Figure C.7) and you will use the box cursor to select a single unsaturated line. The box can be moved using the mouse and its size altered using the arrow keys (use `help extract/cursor` in MIDAS if you are not sure how to use the box cursor). The program will then go through all your thorium images and examine the same spectral line every time (the display will flash as each image is loaded). Finally, a graphics window will appear with a plot showing how the half-width of your line changes with the focus position (see Figure C.8). A parabola is fitted to the points and the best focus is displayed, as calculated from the fit. It is a good idea to repeat the procedure on several different spectral lines (by restarting `focus_hercules`) before adopting the best focus value. Note that only one line can be selected during one session.

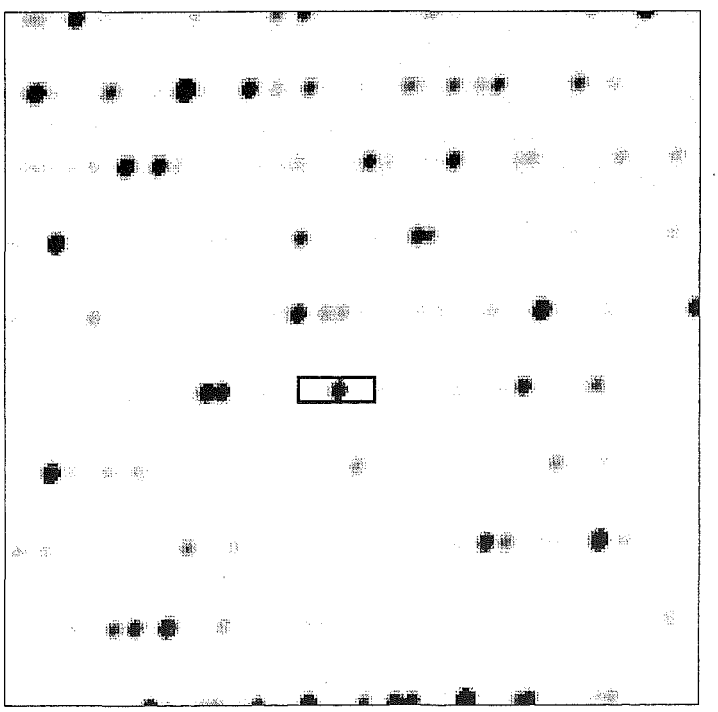

Figure C.7: *Choosing an isolated spectral line for focus determination.*

C.5.5 Some useful tips

- Make sure that your box cursor is not too high (across the orders). The program will construct an average line profile from all pixel rows extracted from the box and a gaussian will be fitted to that profile. If the box is higher than the spectral orders, the average line profile may become degraded.

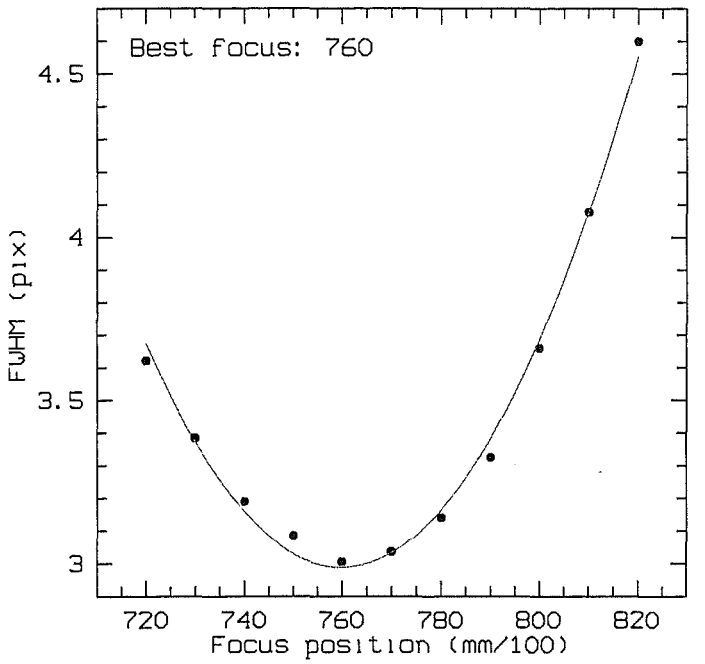

Figure C.8: *Determining the best focus position of the CCD camera using a series of thorium exposures. The best focus is calculated from a parabolic fit to the data points.*

- The box width (along the orders) should be large enough to include a few pixels of the continuum on either side. However, make sure that no other strong lines are found in the same box.
- Always examine the plot (Figure C.8) before you adopt the best focus position returned by the procedure. If the data points are scattered significantly more than in the example shown in Figure C.8, try another line. A parabolic fit to the measured FWHM values around the best focus should have a clear minimum which will not vary from one line to another.
- Do not forget actually to set the CCD focus!
- The MoJo focus CCD focus setting should also be changed.
- Remember to set 'Full Chip' to ON before you start observing.

Appendix D

SALT HRS R2 optical design

This appendix was prepared for the Preliminary Design Review held in 2003, September in Southampton (Barnes et al., 2003). All aspects of the optical design are the authors' while the remaining aspects were developed in conjunction with the coauthors. The document is complete except for the details of SALT which have been discussed at length in Section 3.1.1.

D.1 Scope

This document provides details of the SALT HRS optical design. It provides details of the spectrograph design, beginning at the spectrograph entrance slit. The fibre feed input details are given in *3400AE00XX* and the fibre output, and slit optics, are described in *3230AE0001*.

The performance requirements of the SALT HRS are described in the Functional Performance Requirements Document (*3200AE0001*), and the science requirements are discussed in the Operational Concepts Definition Documents (*3200AE0005*).

D.2 SALT HRS optical design

D.2.1 Overview

The SALT HRS is a fibre-fed spectrograph designed for maximum stability and high throughput. It will be capable of resolving powers up to $R = 80\,000$ with a wavelength range of $\lambda = 370\,\text{nm}$ to $\lambda = 890\,\text{nm}$. In "fixed position" mode a single object can be observed with simultaneous sky monitoring. A "nod and shuffle" mode is also provided to allow accurate sky subtraction. The spectrograph uses a mosaic of two $R2$ échelle gratings with 87 grooves/mm for the main dispersion and two large BK7 prisms with 40°apex angles, which are used in double-pass, for cross-dispersion. The collimated beam size is 365 mm. The camera, which has a focal length of 706 mm, is an all-spherical catadioptric design with a primary mirror 1.2 m in diameter and a detector which uses a mosaic of three 2k by 4k CCD s. The spectrograph will be housed inside an evacuated vessel, and the entire instrument will be kept inside a temperature-stabilised environment.

D.2.2 Fibre input

The fibre instrument feed (FIF) will allow a single object to be observed concurrently with a nearby patch of sky. The relative location of the sky can be selected in azimuth and radial separation. The FIF will allow for the five different observing modes, which are described in the following section. See document series *34XX* for further details of the fibre instrument feed.

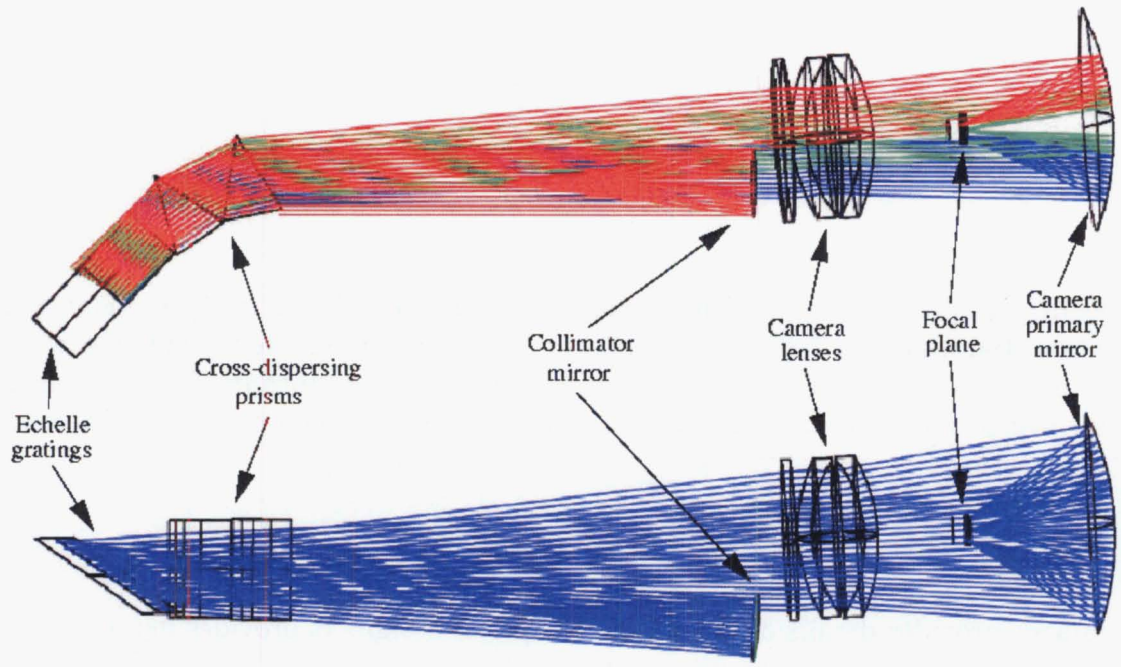

Figure D.1: Plan and elevation views of SALT HRS. The collimator is shown on-axis with a focal ratio of $f/3.8$.

D.2.3 Fibre output, collimator and vacuum window

A more detailed description of the fibre injection into the spectrograph is given in the Fibre Injection Design Document (*3230AE0001*). A range of fibre diameters from 300 μm to 500 μm will be used with and without fibre slicers for resolving powers ranging from $R = 17\,000$ to $80\,000$. A 500 μm fibre with no fibre slicer will be used for the lowest resolving powers in both the fixed position and nod and shuffle modes. A pair of 500 μm and 300 μm fibres will be used in conjunction with fibre slicers for resolving powers of $R = 38\,000$ and $80\,000$ respectively in fixed position mode, while the node and shuffle mode requires pairs of 400 μm and 300 μm fibres for resolving powers of $R = 33\,000$ and $80\,000$ respectively.

Those fibres that will be sliced will have their exit faces reimaged onto the image-slicer. The fibre-slicer is required to operate at a relatively slow focal ratio ($\sim f/17$). This will require the use of transfer optics to convert the $f/3.8$ beam emerging from the fibres to an $f/17$ beam. Because the unsliced 500μm fibres will be placed in the same plane as the fibre-slicers, their focal ratio must be made to match. This will be done with a single micro-lens on each fibre. This micro-lens could be used to transfer the fibre near-field onto the spectrograph pupil. The form of the transfer optics is to be determined (TBD).

It is not possible to accommodate an $f/17$ collimator within the mechanical envelope of the spectrograph. Hence, the focal ratio must be sped up after the fibre slicer. The optics to perform this will be incorporated into the fold mirror, which will now be a prism with a 45° surface of internal reflection, with lenses cemented onto the input and/or output face. This is a modification of the HROS fold-mirror and focal modifier (D'Arrigo

et al., 2000a). The lens on the front surface will also serve as the vacuum window. Given that a vacuum window is necessary, the fold prism and focal modifier should not be seen as introducing any additional optics. The collimator will be an off-axis paraboloid that operates at around $f/6$ to $f/8$. A schematic of this concept is shown in Figure D.2. The form of the collimator optics is TBD.

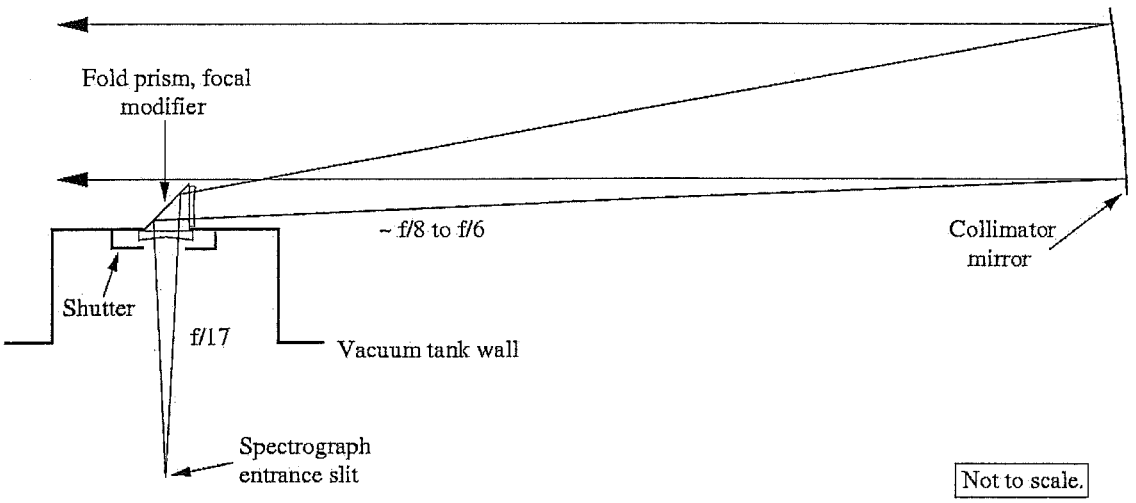

Figure D.2: Schematic of the collimator fold prism and focal modification optics. The scale of the fold prism is greatly exaggerated, as is the distance from the collimator optical axis to the entrance slit.

D.2.4 Dispersive system

The dispersive system comprises a mosaic of two large échelle gratings and two BK7 prisms for cross-dispersion. The prisms are used in double-pass before and after the échelle dispersion.

Echelle gratings

A mosaic of two of the largest gratings available from the Richardson Grating Laboratory (RGL) is required. The parameters of the échelle gratings are given in Table D.1. Note that only standard catalogue gratings are being considered owing to the prohibitive cost of have a grating custom ruled.

Table D.1: SALT HRS grating parameters.

Parameter	Specification
RGL catalogue number	53045ZD01-127E
Blaze angle, θ_B	63.0°
Groove density, T	87.0 grooves/mm
Grating ruled width	308 mm
Grating ruled length	413 mm

The relatively fine ruling of the grating produces orders that have a large angular spread. However, the total number of orders is small and therefore the amount of inter-order spacing is large. This is the reason for rejecting an earlier design that called for a $R2.8$ grating ($\theta_B = 70.45°$) with 52.7 grooves/mm. The dispersed wavelengths fall in 33 orders from $m = 55$ for $\lambda = 370\,\text{nm}$ to $m = 23$ for $\lambda = 900\,\text{nm}$ (see Figure D.9 and Table D.5).

The gratings will be mechanically aligned with a 35 mm gap between the ruled regions of each grating, which allows for a gap of 25 mm between the grating substrates. This gives a total grating length of $L = 861\,\text{mm}$. The facets of the échelle grating are illuminated at a Littrow angle of $\theta = 4.5°$ with respect to the facet normal. The camera is located at a distance of 3.5 metres from the centre of the dispersive system (i.e., the échelle grating). This distance is a compromise between making efficient use of the échelle grating (i.e., a small Littrow angle) and having an excessively large spectrograph, while also ensuring that the collimator obstructs none of the dispersed beam at all wavelengths within one half of a free spectral range from the blaze wavelength.

Resolving power and beam size

If the angular size of a fibre projected onto the sky is θ_s, and the fibre degrades the telescope focal ratio by ρ, then a grating which receives a collimated beam of diameter B is capable of a resolving power $R = \lambda/\delta\lambda$ given by

$$R = \frac{2B \tan\theta_B}{\rho\theta_s D(1 - \tan\theta \tan\theta_B)} \quad , \tag{D.1}$$

where D is the telescope primary mirror diameter. It should be noted that the effective resolving power R of a fibre is somewhat greater than that of a (uniformly illuminated) slit that has the same angular width on the sky. A fibre with a uniformly illuminated output will, after convolution with the point spread function of the spectrograph and extracted to a one-dimensional profile, have a FWHM of between 0.70 to 0.80 times the projected fibre diameter, depending on the image quality. Only the worst image quality (relative to the projected fibre diameter) will result in profiles that can be approximated by a gaussian. It is assumed that $R' = R/0.75$ which concurs with previous results from fibre-fed spectrographs, where the FWHM is universally used as a measure of resolving power.

Assuming that the focal ratio degradation is 10% (i.e., $\rho = 1.1$), and a collimated beam size $B = 365\,\text{mm}$, the resolving powers obtained with a variety of fibre diameters are shown in Table D.2. The transmission through the entrance aperture of an individual fibre under median seeing conditions is also given.

The resolving power/fibre diameter product is $R\theta_s = 28\,800$ arcsec, or in terms of effective resolving power $R'\theta_s = 38\,600$ arcsec. This rather large product is required in order to ensure that the spectrograph is well matched to image quality delivered by SALT. Thus it can be seen that up to 82% of the light is accepted by the fibre entrance aperture for a resolving power of $R = 17\,000$. Clearly for resolving powers greater than $R = 20\,000$ to 25 000 some form of image slicing is required (see *3230AE0001*).

Table D.2: Fibre diameters, resolving powers, and entrance aperture transmissions.

Fibre diameter		Resolving powers		Transmission
d (μm)	θ_s (arcsec)	R'	R	T_{see} (%)
100	0.45	64 700	86 300	8.6
200	0.89	32 300	43 100	29.3
300	1.34	21 600	28 700	52.1
400	1.79	16 200	21 600	70.2
500	2.23	12 900	17 300	82.0

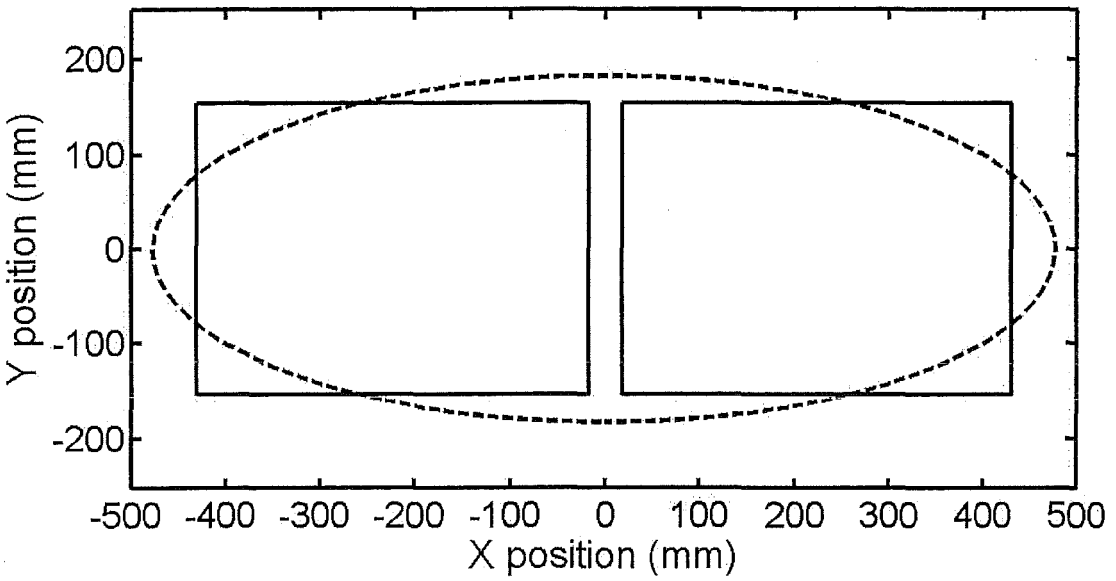

Figure D.3: A schematic of the footprint of the collimated beam on the échelle gratings. Note that this does not depict the effect of cross-dispersion before the gratings.

Overfilling of the échelle grating

The collimated beam overfills the échelle grating in both directions. The fraction of the collimated beam accepted by the échelle grating mosaic is about 85%, which includes a 4% loss due to the gap between échelle gratings. Note that this calculation assumes a uniformly illuminated footprint on the échelle (see Figure D.3), and in reality there will be less light near the edges due to fibre FRD effects. This will mitigate the effect of geometrical overfilling. Note that an overfilling of 85% is comparable to the amount that would be expected with a mosaic of two $R3$ gratings (i.e., $\theta_B = 71.5°$) with the same dimensions that is illuminated with a 300 mm beam.

Cross-dispersion prisms

Two large BK7 prisms with an apex angle of $\alpha_P = 40.0°$are used in double-pass for cross-dispersion. This amount of dispersion allows for complete wavelength coverage from

$\lambda = 370\,\text{nm}$ to $\lambda = 900\,\text{nm}$ with a 705 mm focal length camera and a 61.4 mm high detector. The orders in which these wavelengths appear are near the bottom and top of the CCD (see Figure D.9).

The angle of incidence of the collimated beam on the first prism is $\theta_i = 31.6°$. This is the angle for minimum deviation for $\lambda = 370\,\text{nm}$, which keeps the plane of échelle dispersion of the order in which this wavelength appears in the same plane as the optical axis of the collimator. Because the angular spread of this order is the smallest this allows the angular separation of the collimated and dispersed beams to be minimized without obstructing wavelengths that fall within central free spectral range.

Prism homogeneity

The effect of refractive index inhomogeneity within the cross-dispersing prisms has been estimated. A Monte-Carlo simulation of the cross-dispersion was performed where the refractive index of the prisms at each air-glass interface was varied with a normal distribution about the nominal refractive index. A total of 105 rays was used in each simulation. The deviation of the angle of dispersion from the mean was computed and the results were transformed to the image plane for a camera focal length of 705 mm. This allows the effect of prism inhomogeneity on the line profile in the direction of the cross-dispersion to be estimated. It is assumed that the effect in the direction of échelle dispersion will be of a similar order of magnitude. Examples of these profiles are shown in Figure D.4. The FWHM of the cross-dispersion profile for a point source was calculated. The results are given in Table D.3. Given that the mean RMS image quality is 7 to 8 μm the refractive index homogeniety of less than 1e-6 will degrade the order profile by less than 10%. Hence the prism glass must be H4 or better. This is well within the capability of major glass manufactures (e.g. Schott or Ohara) who routinely supply blanks of BK7 greater than 1 m in diameter with this homogeneity.

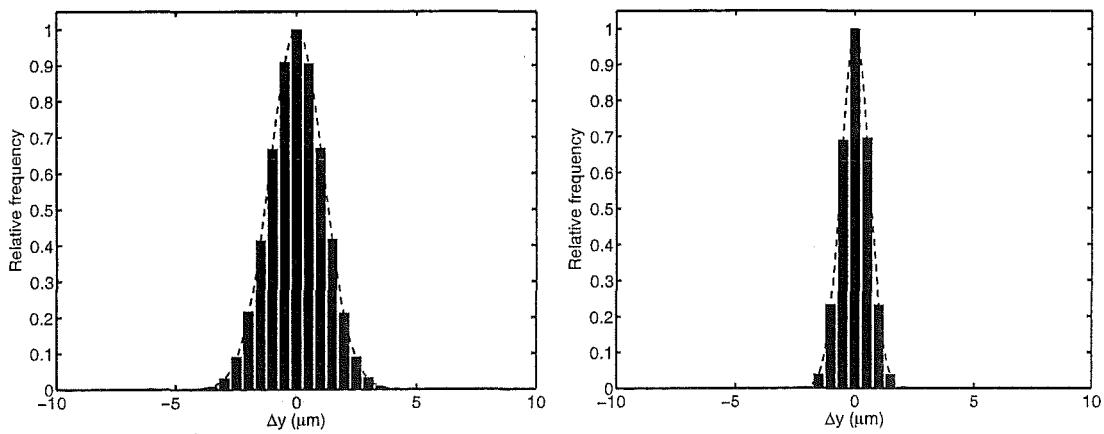

(a) Homogeneity class H4 ($\Delta n = \pm 10^{-6}$)

(b) Homogeneity class H5 ($\Delta n = \pm 5 \times 10^{-7}$)

Figure D.4: The effect of prism inhomogeneity on image quality.

Table D.3: Effect of prism homogeneity on image quality.

Homogeneity class	Refractive index variation $\pm n$	FWHM (μm) $\lambda = 370\,\mathrm{nm}$	$\lambda = 900\,\mathrm{nm}$
H3	2e-6	5.3	4.9
H4	1e-6	2.7	2.5
H5	5e-7	1.4	1.3

The effect of cross-dispersion on line tilt and spectral format

There are some significant effects of using prisms for cross-dispersion on the tilt of spectral lines that must be considered. The first is that due to the dispersion before the échelle. This causes a variable angle of illumination of the échelle facets (in the x-z plane), which has a total range that is equal to one half the total dispersion angle of both passes through the prism. The angle ranges from $\gamma = 0°$ at $\lambda = 370\,\mathrm{nm}$ to $\gamma = 2.5°$ at $\lambda = 890\,\mathrm{nm}$. The fact that $\gamma = 0$ at $\lambda = 370\,\mathrm{nm}$ is a consequence of choosing this wavelength to be minimally dispersed. It can be shown from the grating equation,

$$m\lambda = \sigma(\sin\alpha + \sin\beta)\cos\gamma \quad , \tag{D.2}$$

that due to a small change in γ from the bottom of the slit to the top, the échelle angular dispersion changes slightly. The effect of this is to tilt the lines by an amount given by

$$\tan\phi = 2\tan\theta_{\mathrm{B}}\tan\gamma \quad , \tag{D.3}$$

in the order centre. Hence the line tilt, due to this effect, ranges from $\phi = 0°$ at $\lambda = 370\,\mathrm{nm}$ to $\phi = 10°$ at $\lambda = 890\,\mathrm{nm}$. The tilt also varies across each order. This variation is around $\pm 0.3°$ in order 55 and $\pm 2.3°$ in order 23.

The other effect is due to the fact that the angle of incidence on the prisms in the $y - z$ plane (i.e, the plane of échelle dispersion) is not zero. On the first pass through the prisms the angle of incidence is the Littrow angle ($\theta = 4.5°$). On the second pass through the prism the angle of incidence varies according to the échelle dispersion. The result is that the prism contributes to the échelle dispersion in such a way that the ratio of échelle dispersion to cross-dispersion varies considerably across an order. This gives rise to the considerable order curvature, which would be absent if all the prism cross-dispersion were done at normal incidence. Finally, this last effect also causes the line tilt to increase by around 6 degrees across the entire field. This is due to the ratio of prism dispersion in the x-z and y-z planes. Hence the line tilt will range from $\phi = 6°$ at $\lambda = 370\,\mathrm{nm}$ to $\phi = 16°$ at $\lambda = 890\,\mathrm{nm}$.

It will be possible to orientate the fibre-slicers in order to set the line tilt to zero in the middle of the central order. The range of line tilt will then be between -5° and 5°. Because the line tilt pattern is always the same, it will be possible to remove its effect during the reduction process. This may involve, for instance, a modification of techniques commonly used for the reduction of long slit spectra.

Line tilt and nod and shuffle

The line tilt also has potential consequences for the proposed nod and shuffle mode of operation (see the Operational Concepts Definition Document, *3200AE0005*). In this mode, the science target is moved between object and sky fibres during an exposure while simultaneously charges on the detector are shuffled along its columns. The resulting imaged spectrum for a given order is the sum of two spectra, one of which has been shifted in the dispersion direction by an amount equal to the shuffle distance (normally half the order separation) multiplied by the line tilt angle in radians. We have modeled this effect by shifting and adding synthetic line profiles of various widths. By construction, the equivalent width is always preserved by this operation, but very narrow lines can become noticeably shallower and broader. Since the two added spectra are of almost equal intensity and dispersion solutions will be available for each component spectrum, the dispersion solution for the combined spectrum will be close to the mean of that of the two components. Radial velocity precision may in practice be degraded slightly for spectra acquired in nod and shuffle mode. Extremely sharp emission lines (widths of the order of the resolution limit) will appear doubled near the edges of the spectral format where the line tilt is most severe. Sharp night-sky emission lines will still subtract-out with very high accuracy (even if the profiles are doubled) because the sky for each component of the co-added spectrum is recorded separately.

D.2.5 Camera

The camera is required to be capable of critically sampling the smallest resolution element. This occurs when $R_{\rm max} = 80\,000$ and the required focal length of the camera is given by

$$f_{\rm cam} = \frac{n_{\rm samp}}{2} R_{\rm max} s_{\rm pix} \cot\theta_{\rm B} (1 + \tan\theta_{\rm B} \tan\theta) \quad , \tag{D.4}$$

where $s_{\rm pix}$ is the pixel size. The number of elements required in order to sample critically a resolution element is $n_{\rm samp} = 2$. Assuming $15\,\mu$m pixels, the focal length required is $f_{\rm cam} = 705\,$mm, which gives a monochromatic focal ratio of $f/D = 1.9$. The diameter of the camera primary mirror has been limited to 1.2 m (for practical and budgetary reasons) and hence the white light focal ratio is $f/D = 0.6$.

The camera is a catadioptric design with three large corrective elements (a bi-convex and two meniscus lenses), a deep mirror and a small field-flattening lens that also serves as the cryostat window. All surfaces are spherical. The design evolved from the camera for the Keck HIRES instrument (Epps and Vogt, 1993). However the HIRES design, which uses two large corrective lenses, is incapable of delivering satisfactory image quality, given the large dispersive angles and pupil distance of SALT HRS. This type of camera, which was reoptimized to use BK7 glass, was considered during earlier conceptual designs, when a reduced field of view of the camera allowed for a less demanding camera design.

The final design, which is shown in Figure D.5, is quite similar to the original HROS camera for the Gemini telescope (D'Arrigo et al., 2000b) and the HDS[1] camera for Subaru (Noguchi et al., 2002), although considerably larger than either. Some details of the optical elements will be discussed below.

[1]The PDR document incorrectly stated this was the HIDES camera.

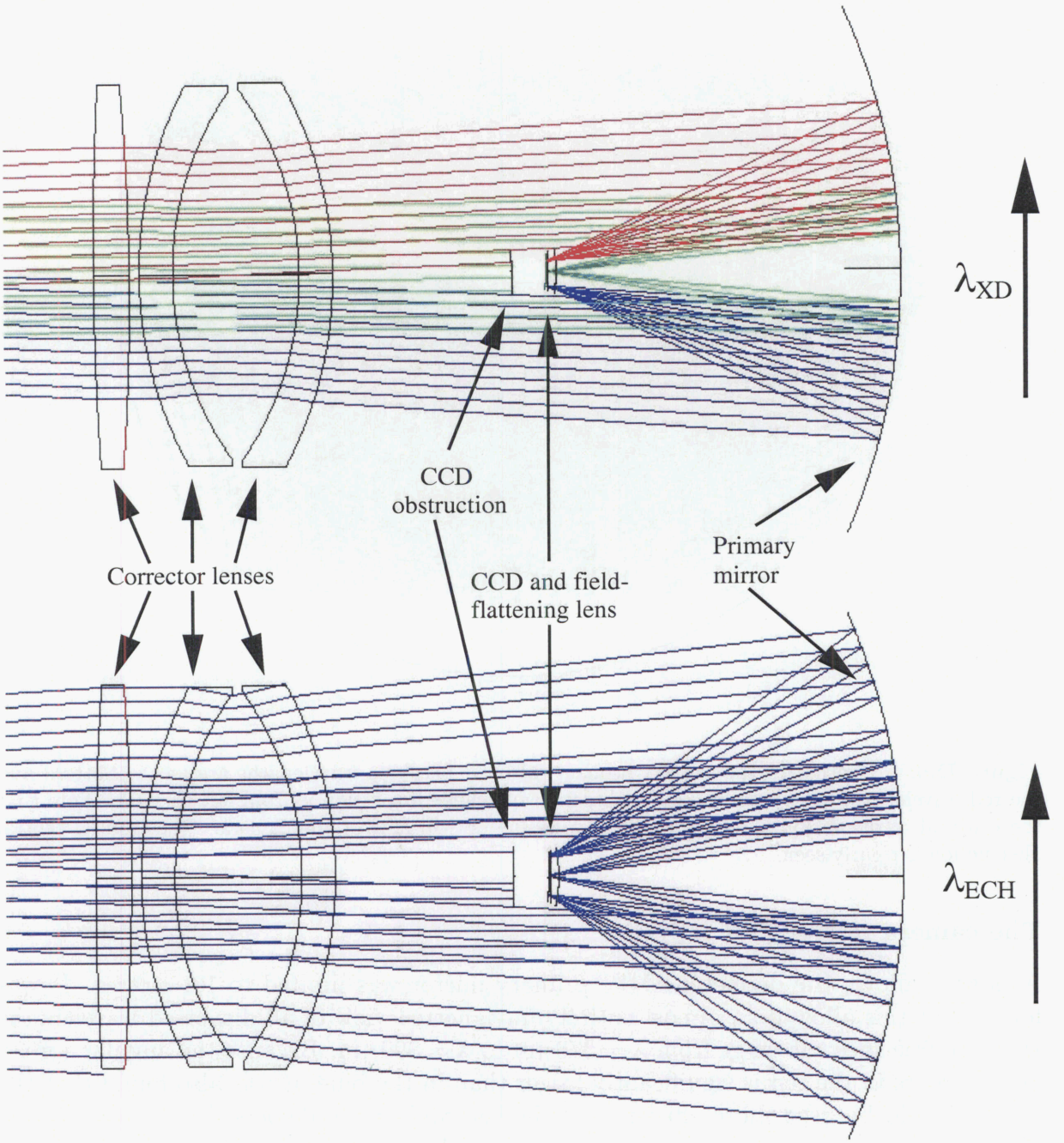

Figure D.5: The SALT HRS camera. The CCD obstruction approximates the position of the cryostat.

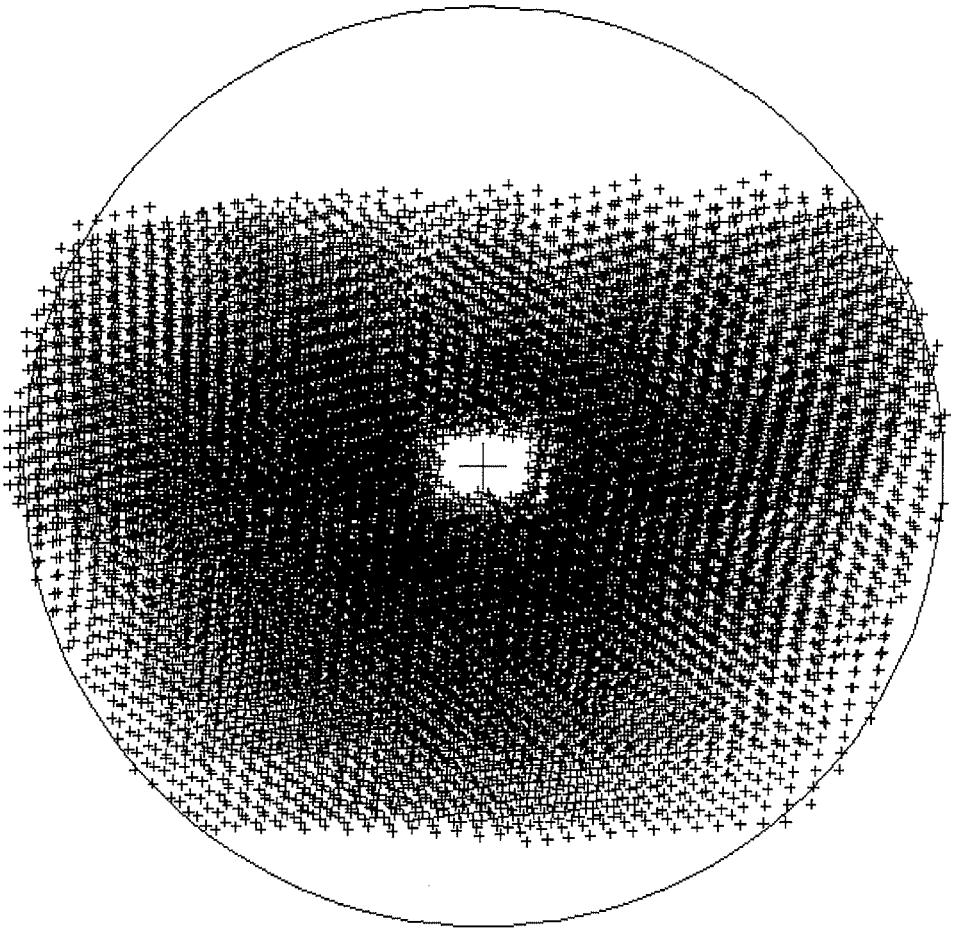

Figure D.6: Footprint on the camera primary mirror. The blue wavelengths are at the bottom and the red wavelengths are at the top. The direction of échelle dispersion is from left to right. Note that the centroid of dispersion does not coincide with the optical axis of the camera. The camera central obstruction is clearly seen.

The camera mirror

As stated above, the diameter of the primary mirror was limited to 1.2 metres. It was found that this allowed an almost entirely unvignetted view of all dispersed wavelengths with the free spectral range from $\lambda = 370\,\text{nm}$ to $\lambda = 890\,\text{nm}$. Because the angular spread of the orders in the red is significantly larger than in the blue, it was also found that the camera could be used more efficiently if the centroid of the dispersed rays was slightly displaced from the optical axis. This is shown in Figure D.6. The dimensions of all the other optical elements, including the prisms, have been determined so as not to cause any additional vignetting.

The large camera lenses

During optimization of the design it was noted that the radii of the two meniscus lenses were quite similar. After coupling the radii of these lenses, and reoptimizing the design,

the performance was only marginally degraded. However, there will be significant savings in the manufacture and testing of these lenses if they have identical figures.

The field-flattening lens

The field-flattening lens will be used as the CCD cryostat window. Initially it was undecided whether to use BK7 or fused silica for the field-flattening lens. Silica is commonly used for CCD windows. However, this is generally because of the good transmittance of this glass at short wavelengths. The decision to use BK7 came after discussions with the manufactures of the CCD cryostat. Although BK7 has a larger coefficient of thermal expansion, materials are readily available with matching CTEs. Materials with lower CTE are more costly in larger dimensions. A possible reason for favouring silica may have been its ease of manufacturability. However, the manufacture of a BK7 lens is not overly difficult, so this was not considered to be relevant. The strength of BK7 and silica is comparable. Table D.4 lists the physical properties of the two materials.[2]

Table D.4: The physical properties of BK7 and fused silica.

Property	BK7	Silica
Density	2.51 g/cm^3	2.20 g/cm^3
Young's modulus	82.0×10^9 N/m^2	72.1×10^9 N/m^2
Poisson's ratio	0.206	0.179
CTE (-30°C to 70°C)	7.1×10^{-6}/K	0.55×10^{-6}/K
Heat capacity	0.858 J/(g.K)	0.741 J/(g.K)
Thermal conductivity	1.11 W/(m.K)	1.38 W/(m.K)

The location of the field-flattening lens relative to the CCD will be fixed. This allows the entire cryostat to be used for focusing. Appropriate tip/tilt and focus adjustments have been allowed for. The size of the field-flattening lens is quite critical as this dictates the size of the CCD cryostat and hence the size of the central obstruction. It was found that a lens that is 130 × 100 mm rectangular would not obstruct any light that falls on the three CCDs (see Figure D.7). A complicating factor in the design of this lens is the necessity for it to be tilted (about the x-axis) with respect to the camera optical axis (i.e., the axis of the camera mirror and three large lenses). The image surface, which is now planar, is also tilted with respect to the optical axis of the field-flattening lens. In order to minimize the size of this lens it must also be decentred by 13 mm in y. This corresponds to the centroid of the échelle spectrum on the CCD mosaic.

D.2.6 Detector

The detector is a mosaic of three E2V 42-82 CCDs. Each detector has 2048 × 4096 pixels that are 15 μm square. In order to allow charge shuffling in the direction of cross-dispersion, the detectors must be aligned with the columns being vertical. As shown in

[2]During the PDR it was pointed out by S. Shectman that because BK7 contains significant quantities of potassium the decay of K-40 will produce an unacceptable level of background radiation. For this reason BK7 should not be used as a CCD window.

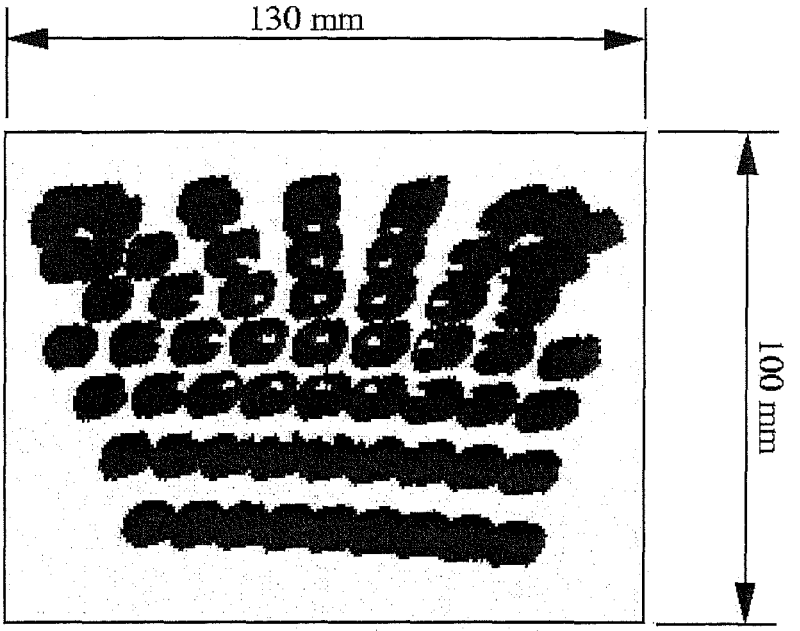

Figure D.7: The footprint diagram on the field-flattening lens. Note that the entire width of the lens is used by wavelengths that lie near the edge of the detector

Figure D.8, this provides a total imaging area of 95.4 × 61.4 mm, where the gap between CCDs is 1.6 mm. This allows for an inactive are on each side of the chip of 0.45 mm and a 0.7 mm gap between the detector packages.

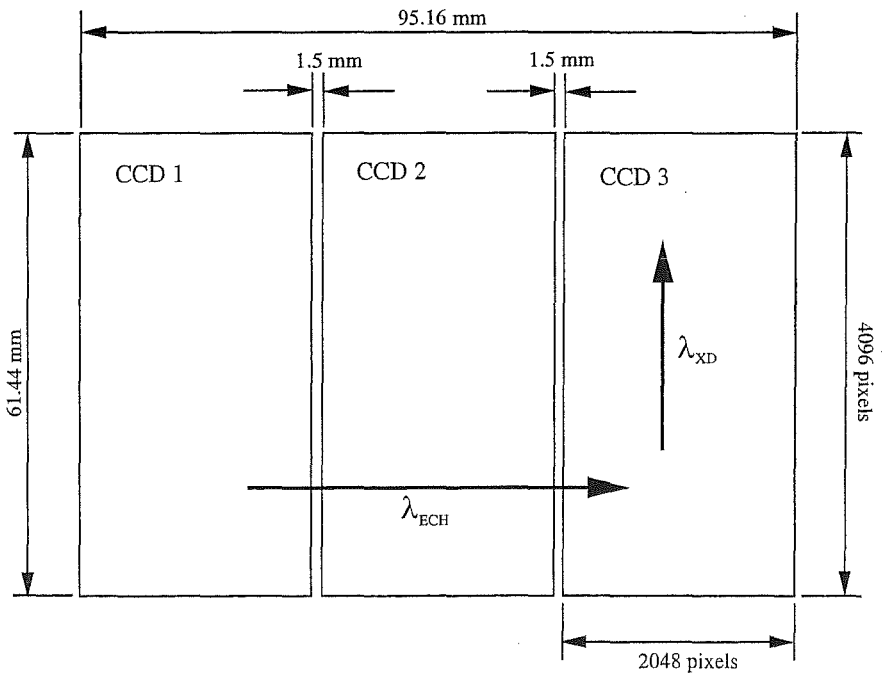

Figure D.8: The format of the SALT HRS CCDs. The direction of échelle dispersion (ECH) and cross-dispersion (XD) are shown. The CCDs are aligned vertically to enable charge shuffle in the direction of cross-dispersion.

D.3 Instrument performance

D.3.1 Spectral format

Table D.5 gives the blaze wavelengths and order numbers for the SALT HRS spectral format that is shown in Figure D.9. The wavelength coverage is from $\lambda = 370\,\mathrm{nm}$ to $\lambda = 890\,\mathrm{nm}$ which corresponds to order numbers $m = 55$ to $m = 23$ respectively. With a mosaic of three CCDs the wavelength coverage is almost complete across this entire range. Above $\lambda = 750\,\mathrm{nm}$ some wavelengths within the free spectral range cannot be captured on the CCDs. The gaps between the CCDs also means there will be gaps in every order. However, for orders above $m = 41$ (i.e., $\lambda < 500\,\mathrm{nm}$) the wavelengths which are lost because of the gaps may be retrieved from either the preceding or following orders.

Table D.5: Order numbers and wavelengths for SALT HRS. The wavelengths at the extent of the free spectral range are also shown. That is, $+/-\lambda_{\mathrm{FSR}} = \lambda_{\mathrm{B}} \pm \lambda_{\mathrm{FSR}}/2$, where λ_{FSR} is the wavelength extent of one free spectral range. λ_{min} and λ_{max} are the wavelengths at the edge of the CCD mosaic.

Order	Wavelength (nm)					Order	Wavelength (nm)				
m	λ_{B}	$-\lambda_{\mathrm{FSR}}$	$+\lambda_{\mathrm{FSR}}$	λ_{min}	λ_{max}	m	λ_{B}	$-\lambda_{\mathrm{FSR}}$	$+\lambda_{\mathrm{FSR}}$	λ_{min}	λ_{max}
55	371.3	367.8	374.6	364.4	378.2	38	537.2	529.9	544.0	526.1	546.5
54	378.1	374.6	381.6	370.8	385.1	37	551.7	544.0	558.9	540.3	561.3
53	385.3	381.5	388.8	377.8	392.3	36	567.0	558.8	574.6	555.2	576.8
52	392.7	388.8	396.4	385.0	399.8	35	583.2	574.5	591.2	571.1	593.3
51	400.4	396.3	404.2	392.5	407.6	34	600.3	591.1	608.8	587.8	610.7
50	408.4	404.2	412.3	400.3	415.8	33	618.5	608.7	627.4	605.6	629.1
49	416.7	412.3	420.8	408.4	424.2	32	637.8	627.4	647.3	624.4	648.7
48	425.4	420.8	429.7	416.9	433.0	31	658.3	647.2	668.5	644.5	669.6
47	434.4	429.7	438.9	425.7	442.2	30	680.3	668.4	691.1	666.0	691.9
46	443.9	438.9	448.5	434.9	451.8	29	703.7	691.0	715.2	688.9	715.7
45	453.7	448.5	458.6	444.6	461.8	28	728.8	715.1	741.1	713.4	741.2
44	464.0	458.6	469.1	454.6	472.2	27	755.8	741.1	769.0	739.8	768.6
43	474.8	469.1	480.1	465.2	483.2	26	784.8	768.9	799.1	768.2	798.1
42	486.1	480.1	491.7	476.2	494.6	25	816.2	798.9	831.5	798.8	830.0
41	497.9	491.6	503.8	487.8	506.7	24	850.1	831.4	866.8	832.0	864.5
40	510.4	503.8	516.5	499.9	519.3	23	887.0	866.6	905.1	868.1	902.0
39	523.4	516.5	529.9	512.7	532.6						

Figure D.10 shows the position of thorium-argon lines that are considered useful for the purposes of wavelength calibration (Ramm, 2003). It can be seen that even when the image plane is divided into three, there are at least 10 or 15 lines per order. Hence there will be some 400 or 500 lines available on each CCD for two-dimensional wavelength calibration.

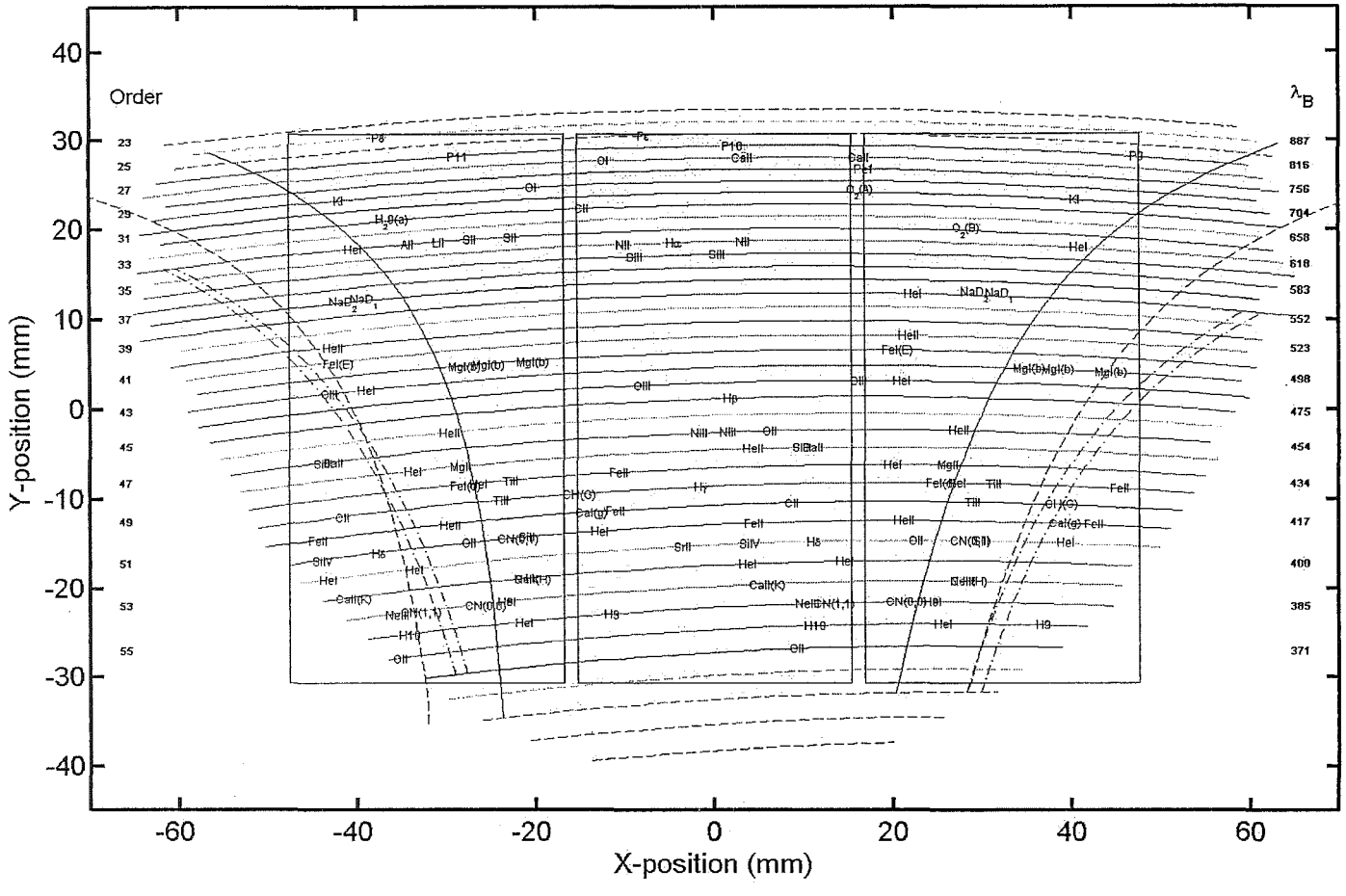

Figure D.9: The SALT HRS spectral format. The orders from $m = 23$ to $m = 55$ are plotted as solid lines. Orders above and below these are shown as dashed lines. The two curved solid lines show the extent of the free spectral range, and the full width at half maximum is shown by the curved dashed lines. The outline of the three CCDs is also shown. Note that some wavelengths that fall in the gaps between CCDs will appear in the preceding or following order. The dot-dashed lines show the position of these wavelengths.

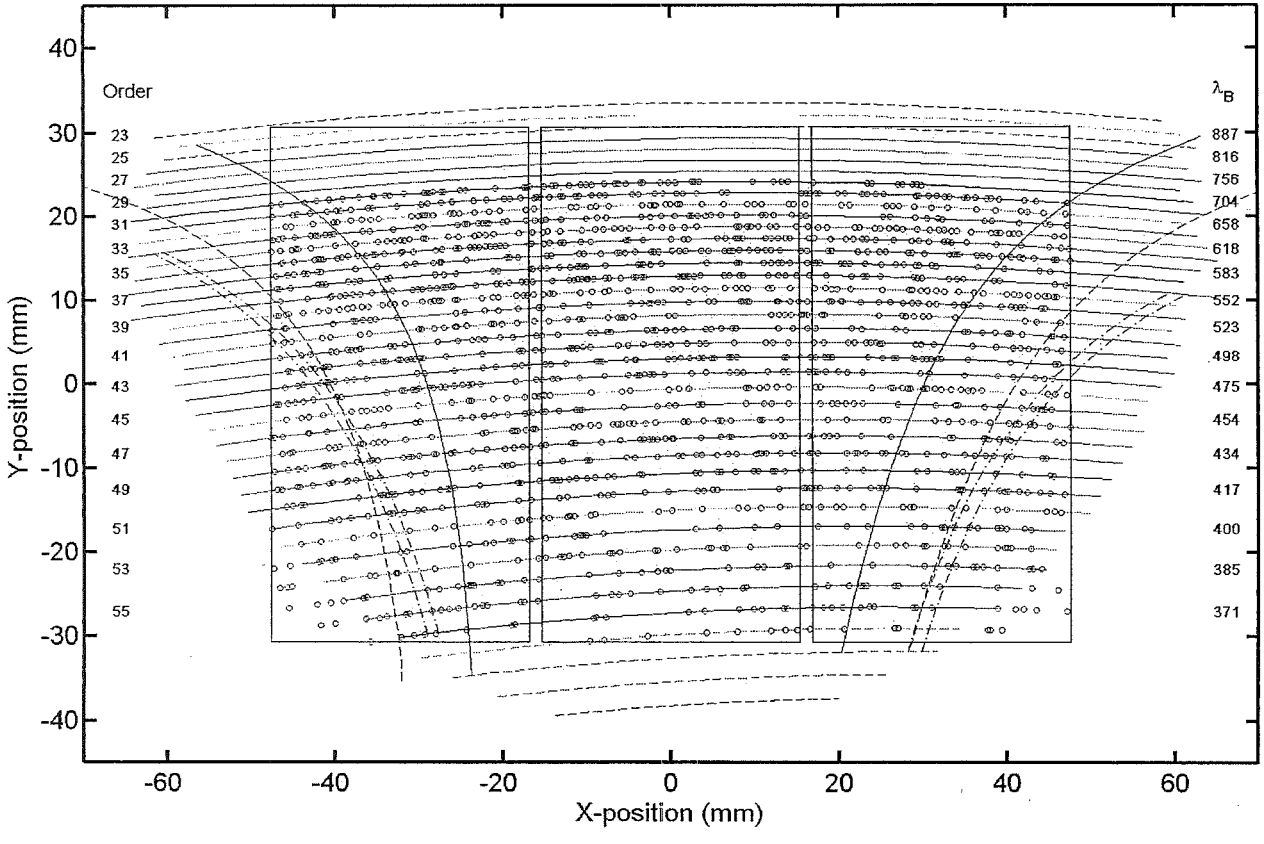

Figure D.10: The position of thorium-argon calibration lines. The input catalogue (Ramm, 2003) is incomplete beyond $\lambda = 750\,\mathrm{nm}$. The plotted lines are those that are considered "good" for the purposes of calibrating the HERCULES spectrograph. Depending on the operating current of the calibration lamp, some of the lines may be either too faint or too bright to be used. This will eliminate around 10% to 20% of lines.

D.3.2 Image quality and vignetting

Spot diagrams for wavelengths at the centre and edges of orders for three orders (at the bottom, middle, and top of the camera field of view) are shown in Figure D.11 and ensquared energies at these wavelengths are shown in Figure D.12. The requirement is that the ensquared energy within one pixel is greater than 80%. However in recognition of the fact that some wavelengths towards the edge of the field have large dispersion angles, and hence have poorer image quality, this requirement was relaxed to the following:

- $\lambda < 700\,\mathrm{nm}$ – greater than 80% ensquared energy within $15\,\mu\mathrm{m} \times 15\,\mu\mathrm{m}$.
- $\lambda > 700\,\mathrm{nm}$ – greater than 80% ensquared energy within $15\,\mu\mathrm{m} \times 15\,\mu\mathrm{m}$ at most wavelengths with greater than 70% at all wavelengths.

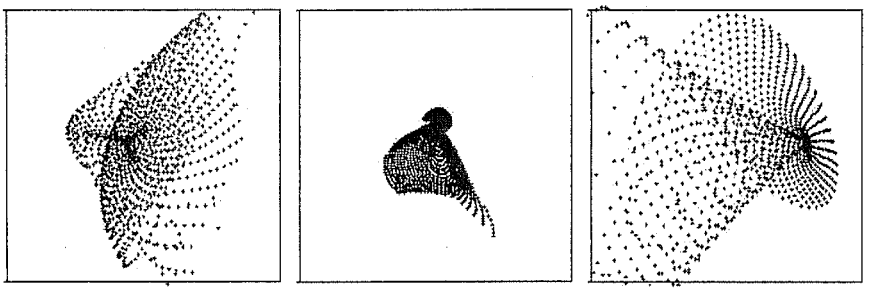

(a) $\lambda = 866.7\,\mathrm{nm}$ (b) $\lambda = 886.8\,\mathrm{nm}$ (c) $\lambda = 905.2\,\mathrm{nm}$

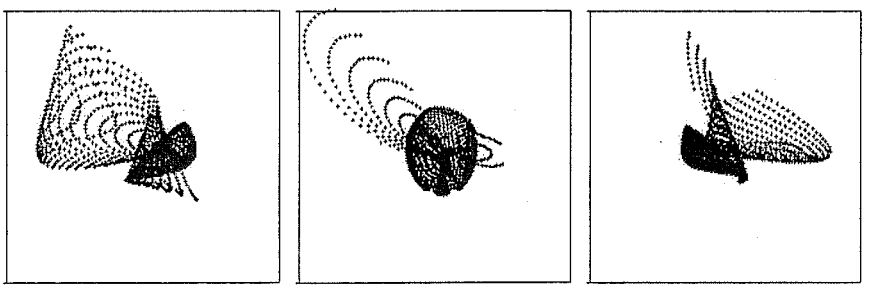

(d) $\lambda = 503.7\,\mathrm{nm}$ (e) $\lambda = 510.3\,\mathrm{nm}$ (f) $\lambda = 516.4\,\mathrm{nm}$

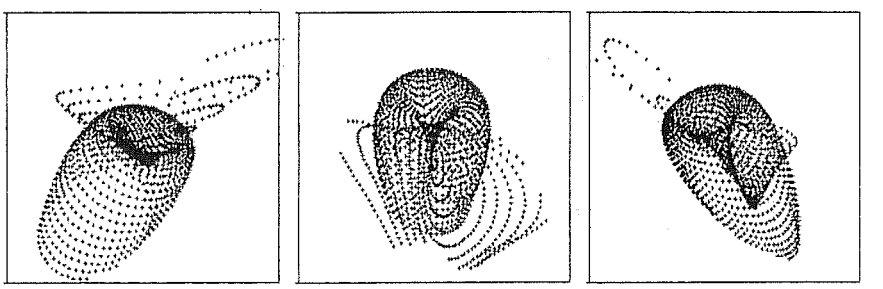

(g) $\lambda = 367.8\,\mathrm{nm}$ (h) $\lambda = 371.2\,\mathrm{nm}$ (i) $\lambda = 374.6\,\mathrm{nm}$

Figure D.11: Spot sizes of representative wavelengths. The wavelengths are from positions near the edges and centre of orders $m = 23$, 40 and 55. The box size is $30\,\mu\mathrm{m}$.

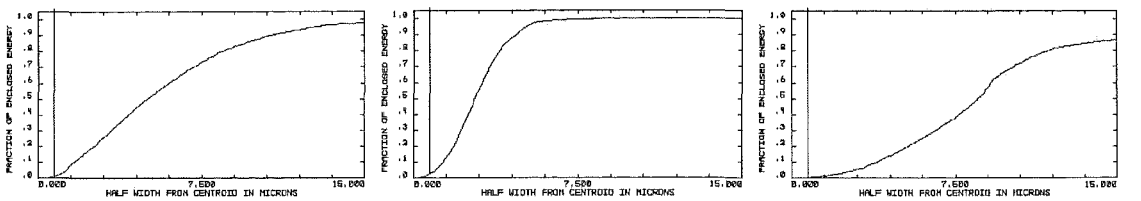

(a) $\lambda = 866.7\,\mathrm{nm}$ (b) $\lambda = 886.8\,\mathrm{nm}$ (c) $\lambda = 905.2\,\mathrm{nm}$

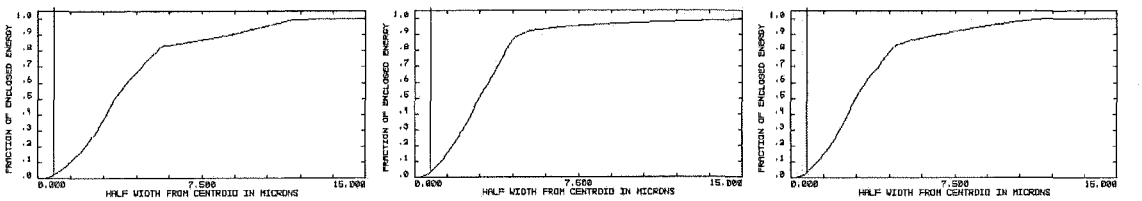

(d) $\lambda = 503.7\,\mathrm{nm}$ (e) $\lambda = 510.3\,\mathrm{nm}$ (f) $\lambda = 516.4\,\mathrm{nm}$

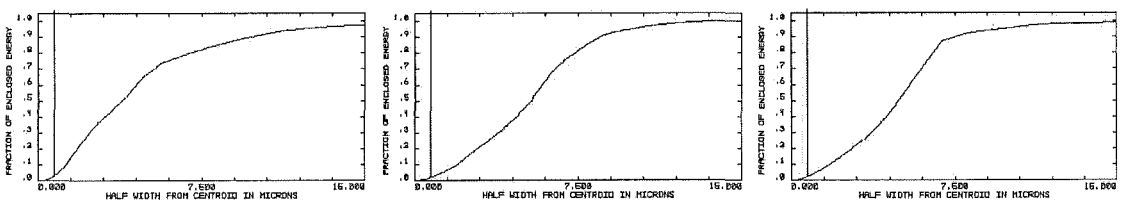

(g) $\lambda = 367.8\,\mathrm{nm}$ (h) $\lambda = 371.2\,\mathrm{nm}$ (i) $\lambda = 374.6\,\mathrm{nm}$

Figure D.12: Ensquared energies of representative wavelengths. The wavelengths and order numbers are the same as in Figure D.11.

Figure D.13 shows the ensquared energy within one pixel at all wavelengths. It can be seen that the image quality is excellent at all wavelengths within the central CCD. At larger dispersion angles there is a gradual degradation of image quality. The image quality rapidly deteriorates at wavelengths where the dispersed beam is not completely captured by the primary mirror. The extreme wings of the blue orders have the worst image quality. However the image quality within the central free spectral range is satisfactory.

The vignetting function of the spectrograph is shown in Figure D.14. It can be seen that a significant proportion of wavelengths are vignetted to some extent by the CCD cryostat. This obstruction contributes between 10% and 12% to the overall vignetting.

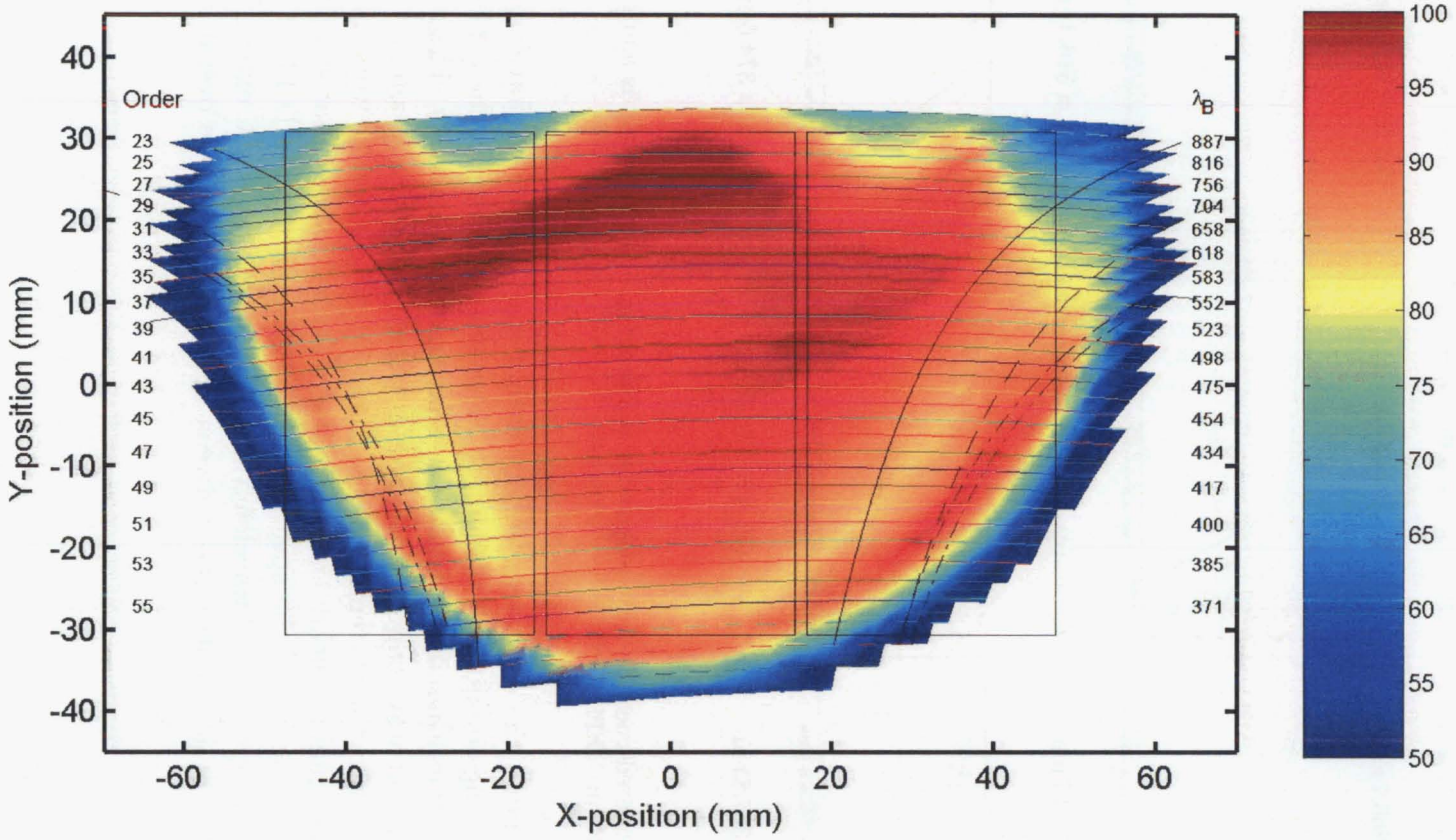

Figure D.13: The ensquared energy (%) within one pixel at all wavelengths.

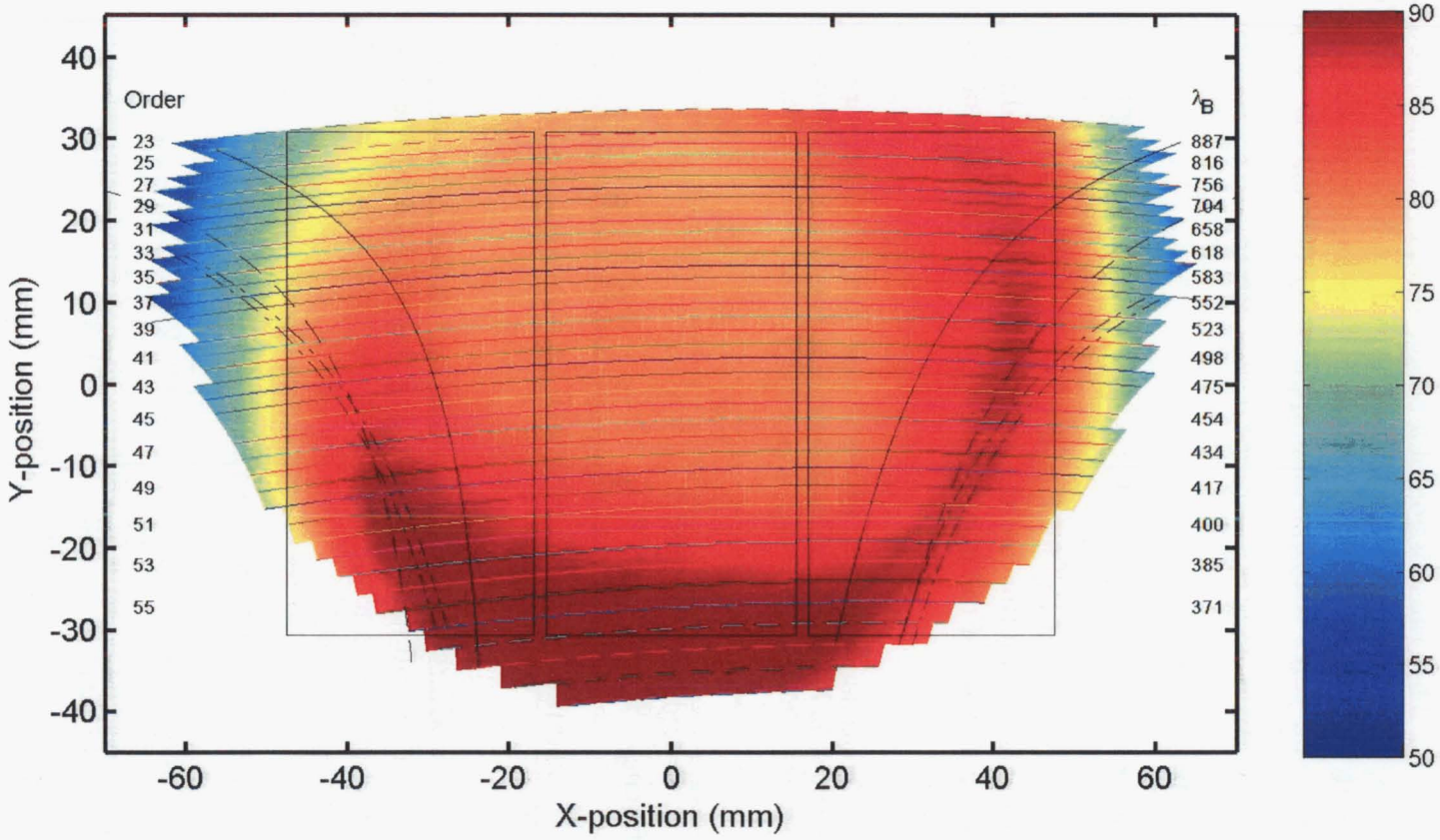

Figure D.14: The vignetting function of the spectrograph. Shown is the unvignetted percentage of rays. The vignetting due to the central obstruction with the camera is clearly visible. The increase in vignetting towards the edges of the field is due to the limited size of the primary mirror. Note that the calculation of the vignetted fraction of rays assumes a uniformly illuminated pupil.

D.3.3 Throughput

The throughput calculations have been done assuming mean seeing conditions. All optics are assumed to have single layer MgF_2 anti-reflection coatings, except the fibre slicer transfer optics, and the focal modifier. The mirrors are assumed to have UV-enhanced silver reflection coatings. There is a possibility that some, or all, of the large optics will also be coated with Solgel. The transmission of a Solgel + MgF_2 coating is around 0.995 (at 600 nm). Therefore, the throughput may be improved by a factor $(0.990/0.98)^{14}$ to $(0.995/0.98)^{14} = 1.15$ to 1.23, where 14 is the number of vacuum/glass surfaces (i.e., two prisms in double-pass, and three lenses). The application of Solgel is therefore to be highly recommended.

Fibre feed and image slicers

The length of fibre needed is about 35 m (TBC). The transmission through a low OH silica fibre at $\lambda = 400$, 600 and 850 nm, is 80.6%, 93.9% and 90.9% respectively.

The geometrical throughput of the fibre feed input and fibre image slicer is given in Table D.6. Included in the calculation are the entrance aperture losses due to the stellar PSF, and the geometrical losses of the fibre image slicer. The efficiency of the fibre slicer is estimated to be 85%.

Table D.6: Geometrical throughput of the fibre feed and image slicer. The modes are F = fixed object plus sky, N = nod and shuffle. L, M, and H, represent low, medium and high resolution respectively (see Section 3.3). The throughput relative to FL (which is equivalent to NL) is also shown.

Mode:	FL	FM	FH	NL	NM	NH
Geometric throughput (%)	87.2	78.6	54.0	87.2	69.2	42.8
Slicer efficiency (%)	100.0	85.0	85.0	100.0	85.0	85.0
Total (%)	87.2	66.8	45.9	87.2	58.8	36.3
Relative throughput	1.00	0.76	0.52	1.00	0.67	0.41

The fibre image slicer will require some transfer optics, the form of which is TBD. It is assumed that these lenses will have high efficiency broad-band anti-reflection coatings applied. A throughput of 97% is assumed. The total throughput of the fibre feed and image slicers are given in Table D.7.

Table D.7: Fibre feed and image slicer throughput.

Mode	Resolving Power	Throughput (%) $\lambda = 400$ nm	$\lambda = 600$ nm	$\lambda = 800$ nm
FL	17,000	65.3	76.3	74.0
FM	38,000	48.3	56.9	55.4
FH	80,000	33.3	39.1	38.0
NM	33,000	42.5	50.1	48.7
NH	80,000	26.3	31.0	30.2

Fold mirror/focal modifier and collimator

The reflectivity of the fold mirror is assumed, for the moment, to be that of a standard mirror (with enhanced silver coatings). The focal modifier (whose design is TBD), is assumed to have only two air/glass surfaces (of which one will be inside the vacuum tank), and to be made from BK7 glass with a total glass length of around 100 mm. Of course, the final optical elements will be formed from several glass types, but the overall transmittance will not change substantially. Broad-band anti-reflection coatings are assumed. The throughput at $\lambda = 400$, 600, and 850 nm is 92.4%, 95.9%, and 95.0% respectively.

The overfilling of the collimator mirror due to focal ratio degradation in the fibre is assumed to be 5%. Combined with the reflectivity of the mirror, the transmittance is 92.0%, 93.5%, and 91.9% at $\lambda = 400$, 600, and 850 nm respectively. The total throughput of the fold mirror/focal modifier and collimator is given in Table D.8.

Table D.8: Fold mirror/focal modifier and collimator throughput.

	Throughput (%)		
	400 nm	600 nm	800 nm
Fold mirror/focal modifier	92.4	95.9	95.0
Collimator	92.0	93.5	91.9
Total	85.0	89.6	87.3

Prism and échelle

The throughput of two prisms, used in double-pass is 63.5%, 76.9%, and 80.0% at $\lambda = 400$, 600, and 850 nm respectively. The blaze efficiency of the échelle grating is approximately 73.8% at these wavelengths (assuming a Littrow angle of 4.5°). It will be assumed that the grating is coated with standard aluminium. This gives an absolute efficiency of the échelle grating of 62.7%, 65.7%, and 62.5%. The overfilling of the grating gives a transmission of 85.2% (including light lost to the gaps).

Table D.9: Prisms and échelle throughput.

	Throughput (%)		
	400 nm	600 nm	800 nm
Prisms	63.5	76.9	80.0
Echelle grating	62.7	65.7	62.5
Overfilling	85.2	85.2	85.2
Total échelle and prisms	33.9	43.0	42.6

Camera

The efficiency calculations of the camera includes the following:

- three large lenses (average thickness 75 mm),
- the primary mirror,
- a field-flattening lens, and
- the central obstruction due to the CCD cryostat.

A summary of the calculated efficiencies is given in Table D.10.

Table D.10: Camera throughput.

	Throughput (%)		
	400 nm	600 nm	800 nm
Lenses (×3)	79.5	88.9	86.4
Primary mirror	96.8	98.4	96.7
Field-flattening lens	94.5	97.0	95.7
CCD cryostat obstruction	84.8	78.8	78.5
Total camera	61.7	66.8	62.7

CCD

The CCDs will be E2V 42-82 chips. The most likely coating will be E2V's "astro-mid" coating. At $\lambda = 400$, 600, and 850 nm, these CCDs have quantum efficiencies of 60.1%, 89.0% and 71.8% respectively. The possibility has been raised, with the support of Dr Paul Jorden from E2V, that the lower half of the three CCDs could have "astro-BB" (broad-band) coatings. At a wavelength of $\lambda = 400$ nm the quantum efficiency increases to 80.1% (a 33% increase in efficiency). The gain at $\lambda = 370$ nm is even greater. Here the quantum efficiency would increase from 35.1% to 61.7% (a gain of 75%!). Clearly this would greatly enhance the blue-wavelength performance of SALT HRS.

Summary

The total spectrograph throughput, from the fibre feed entrance to the CCD detector is given in Table D.11.

The efficiency of the SALT telescope has been estimated to be 56.8%, 66.2%, and 66.4% at the three representative wavelengths. This gives a total detective quantum efficiency of the SALT HRS and telescope as given in Table D.12.

Finally, as noted in the introduction to this section, a dramatic improvement in throughput is to be expected if all large refracting optics have Solgel coatings applied in addition to MgF_2. The efficiency of the SALT HRS and telescope with such coatings is given in Table D.13.

D.3.4 Stray light and ghosts

A complete analysis of the stray light properties of the spectrograph has not yet been completed. It should be pointed out that the use of prisms for cross-dispersion ensures

Table D.11: Total SALT HRS throughput. The efficiencies at $\lambda = 400\,\mathrm{nm}$ for "astro-BB" are in brackets in this and all subsequent tables.

Mode	Resolving Power	Throughput (%) 400 nm	600 nm	800 nm
FL	17,000	7.0 (9.3)	18.0	12.4
FM	38,000	5.2 (6.9)	13.4	9.3
FH	80,000	3.6 (4.7)	9.2	6.4
NM	33,000	4.6 (6.1)	11.8	8.2
NH	80,000	2.8 (3.8)	7.3	5.1

Table D.12: SALT HRS and telescope detective quantum efficiency.

Mode	Resolving Power	Throughput (%) 400 nm	600 nm	800 nm
FL	17,000	4.0 (5.3)	11.9	8.2
FM	38,000	2.9 (3.9)	8.9	6.2
FH	80,000	2.0 (2.7)	6.1	4.2
NM	33,000	2.6 (3.4)	7.8	5.4
NH	80,000	1.6 (2.1)	4.8	3.4

that the amount of stray light is significantly less than if a grating had been used. It is expected that the most significant source of stray light will be from the échelle grating. Based on previous experience (e.g., the HERCULES spectrograph), and the work of others (c.f. D'Arrigo et al., 2000a) it is expected that stray light will contribute approximately 1% to 2% of the local continuum. The variation in the intensity of this stray light across the CCD is also expected to be smooth. Again, this is based on prior experience with similar instruments.

The impact of ghosts is also expected to be minimal. This is due in part to the very fast nature of the camera, which will ensure that any ghosts will be significantly out of focus. For a preliminary analysis of the effects of ghosts we refer the reader to a study of ghosting in the original HROS spectrograph (D'Arrigo et al., 2000a). The format of

Table D.13: SALT HRS and telescope detective quantum efficiency assuming Solgel coatings.

Mode	Resolving Power	Throughput (%) 400 nm	600 nm	800 nm
FL	17,000	4.9 (6.5)	14.6	10.1
FM	38,000	3.6 (4.8)	10.9	7.6
FH	80,000	2.5 (3.3)	7.5	5.2
NM	33,000	3.2 (4.2)	9.6	6.7
NH	80,000	2.0 (2.6)	6.0	4.1

the camera is very similar, and hence their conclusions are expected to be valid for the present spectrograph. Here it was shown that even the strongest ghosts will contribute no more than 0.02% with respect to the local continuum. However, it was noted that "picket-fence" ghosts are produced with intensities 10 to 20 times larger. These ghosts are due to light being reflected off the CCD, recollimated by the camera, and then being redispersed by the échelle.

D.4 Exposure meter

The exposure meter has been designed (see Figure D.15) to use light that would otherwise be obstructed by the CCD cryostat. A fold mirror will be placed between the last large camera lens and the rear of the cryostat. A doublet placed before the fold mirror will bring the light to a focal plane near the vacuum tank wall. A singlet, which will also act as a window, is used to reduce the scale of the field to a reasonable size. At most wavelengths around 3% of the light is captured by the exposure meter.

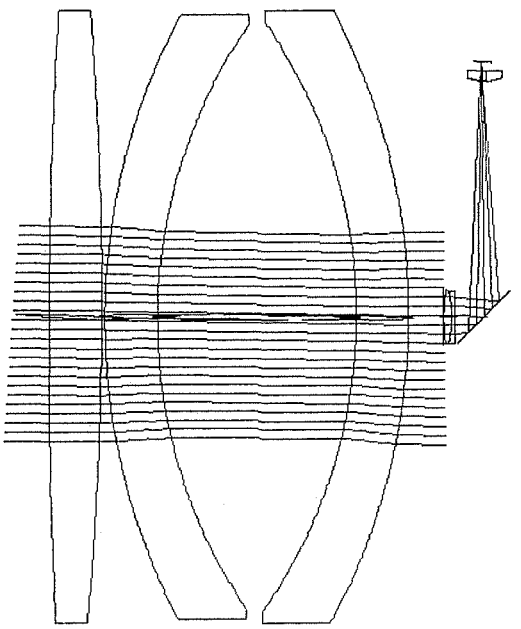

Figure D.15: The exposure meter. A fold mirror and doublet lens are used to bring the light to a convenient location near the tank wall. A singlet lens will then be used as a window into the tank and the detector will be placed externally.

Because the metered light has been dispersed, the exposure meter optics have been designed to produce a spectrum on the image plane. This allows the possibility of using a CCD detector to capture this spectrum, where the image quality is sufficient for low-resolution extraction. The detector under consideration has 1024 × 1024 pixels, each 24 μm square, and possibly frame transfer capability. This will permit two modes of operation. The first will be a traditional metering of spectrograph throughput, where the CCD is read out semi-continuously, and the accumulated signal is calculated. The other mode will use a less frequent readout, and the spectra will then be rapidly reduced and displayed. After appropriate corrections are made, this will allow continuous assessment of the signal to noise of the current exposure. Comparative measurements of the sky and object signal will also be possible.

D.5 Opto-mechanical tolerances

For an analysis of the opto-mechanical tolerances, and an analysis of manufacturability, of the spectrograph we refer the reader to the study by A. Rakich from KiwiStar Optics (*3210AA0003*).

D.6 Procurement

D.6.1 Optical components

We are currently investigating three sources for the procurement of the main optical elements. These are:

- GlassFab, Rochester, NY,
- LZOS Optics Group, Moscow region and
- Ohara GmbH, Hofheim, Germany.

Inquiries have been made with WZW-Optic to supply the fibre slicers. The alternative design of Robert Content (see *3230AA0002*) could be manufactured by the University of Durham.

No vendor has been identified for the supply of miscellaneous optics (e.g., the fold-prism/focal-modifier and the exposure meter optics).

D.6.2 Figuring

Our preferred vendor for the figuring of the optics is KiwiStar Optics, Wellington, New Zealand. We have also sent an RFQ to Sagem-REOSC.

D.6.3 Coatings

Cleveland Crystals (Ohio, USA) has received an RFQ to supply Solgel coatings to all large refractive optical elements. They may also supply MgF_2 through a vendor they have identified. Sagem-REOSC also have the facilities to provide AR coatings to the optics and have been sent an RFQ.

The preferred coating for the reflective optics is enhanced and overcoated silver. No specific vendor has been identified to coat the camera primary mirror. Laserdyne Technologies (Queensland, Australia) are able to coat the collimator mirror.

Appendix E

SALT HRS R4 optical design

This appendix is the optical design document for the SALT HRS R4 instrument which was presented to the SALT Science Working Group on 2004 July 29, in Göttingen, Germany. The document forms part of a larger package of documents that were presented on this date. The document is essentially complete, except that the introductory material on SALT has been removed. Details of the telescope can be found in Section 3.1.1.

E.1 Scope

This document provides details of the SALT HRS R4 optical design, including a small amount of information on the telescope design, the fibre feed and slit optics. More specific details of the fibre feed can be found in 3400AE00XX (FIF) and the fibre exit and image slicers are also described in 3230AE0003 (R4 Fibre Injection Design). The performance requirements of the SALT HRS R4 are described in 3200AE0015 (R4 FPRD), and the science requirements and operation modes are discussed in 3200AE0018 (R4 OCDD). Some possible upgrade paths are also described in this last document.

E.2 SALT HRS R4 optical design

The complete optical design of the SALT HRS R4 will be discussed in detail in this section. Section E.3 will contain details of the spectrograph's performance. A discussion of the merits of the design and justification for some of the design choices will be contained in Section E.4. This section will also contain suggestions for further improving the design in terms of either performance and/or cost.

E.2.1 Overview

The ray diagram of SALT HRS R4 is shown in Figure E.1 and Figure E.2.

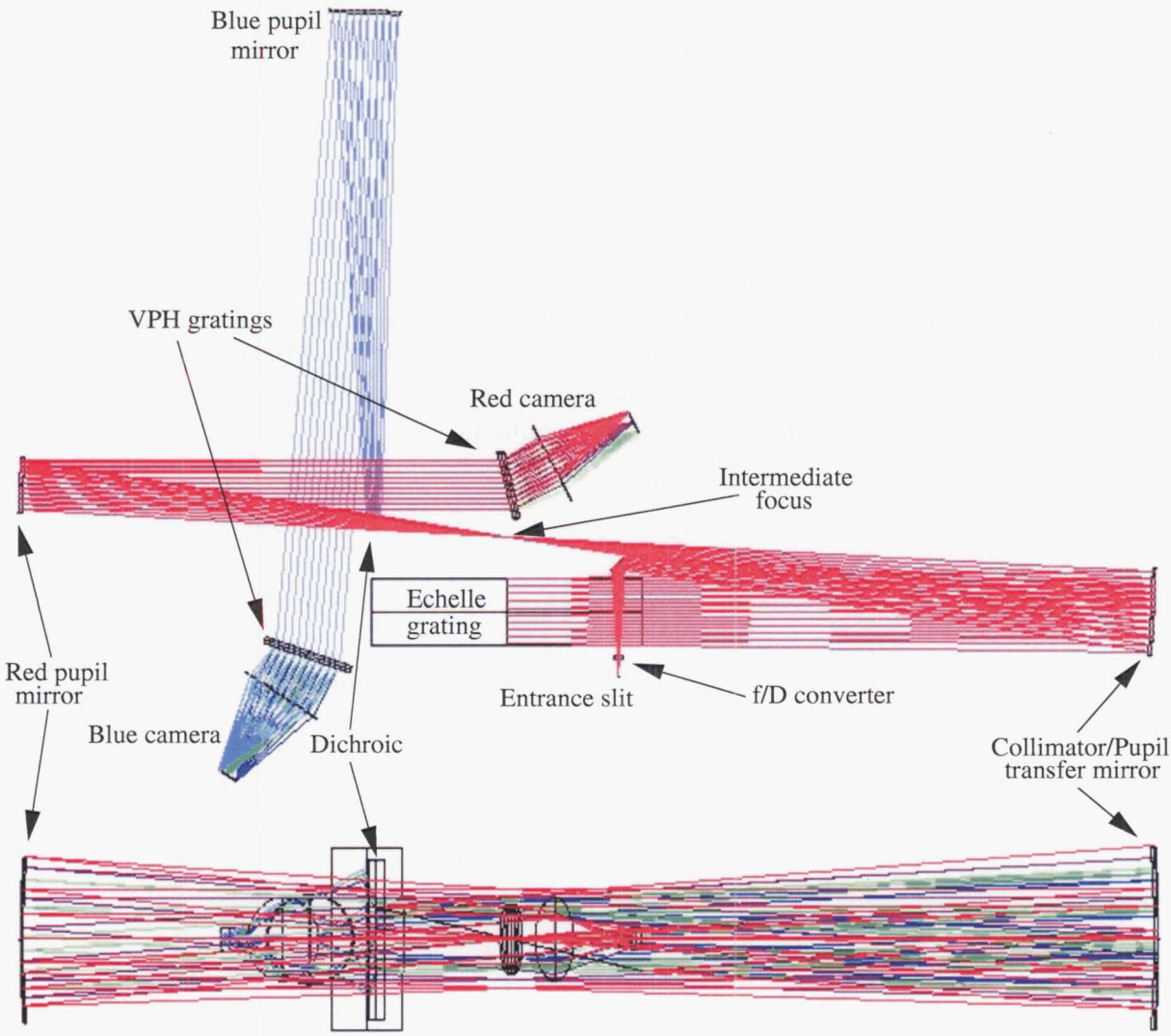

Figure E.1: The ray diagram of SALT HRS R4. The slit area is accessed by a fold mirror across the échelle grating. The collimator serves as the first pupil mirror for both arms. A dichroic located just after the intermediate focus splits the spectrograph into red and blue arms. Each arm will have its own VPH cross-disperser and camera (shown here as paraxial elements). The slit fore-optics are not shown.

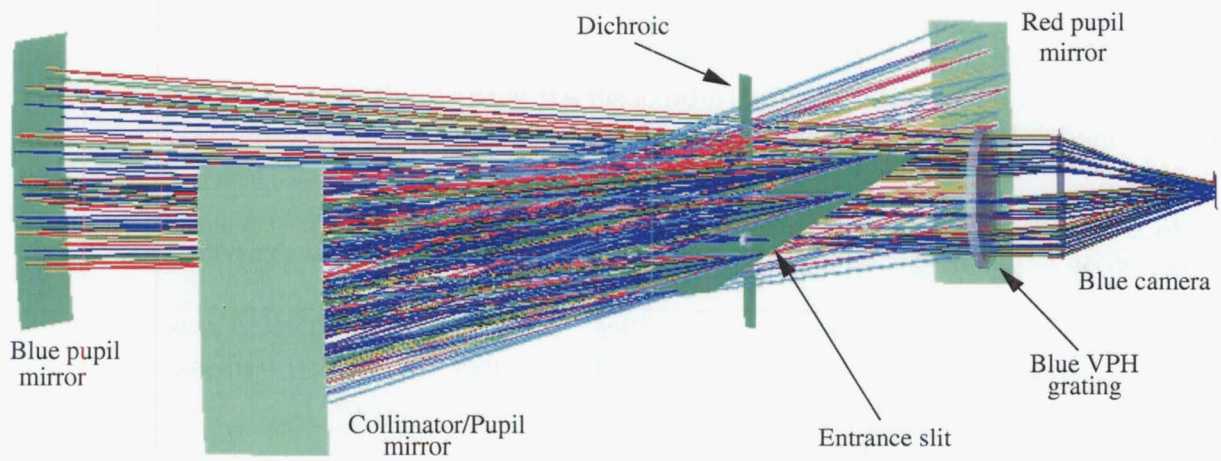

Figure E.2: A solid model view of the SALT HRS R4 optics. The red and blue cameras are shown as paraxial elements.

The spectrograph is a dual beam white pupil design, with a single R4 échelle grating, a dichroic beam-splitter, and VPH cross dispersers. The échelle grating has 41.6 grooves/mm and is illuminated with a 200 mm diameter beam. Two fully dioptric cameras are used to aquire complete wavelength coverage from 370 nm to 890 nm at a maximum resolving power of $R = 80\,000$ and in a fixed spectral format. Up to two objects can be observed simultaneously with a minimum separation between adjacent orders of $11''$. The highest resolving powers are obtained by using dual fibre image slicers.

Apart from shutters, the camera focusing, and the fibre interchange mechanism, SALT HRS R4 will contain no moving parts. In order to provide complete immunity from pressure and temperature changes the dispersive elements will be enclosed with a light (2 hPa) vacuum. The entire instrument will in turn be housed in a temperature-stabilized environment.

E.2.2 Fibre injection design

The details of the fibre injection design are described in a separate document (3230AE0003). This document contains details of the fibres (including the possibility of operating with micro-lenses) the slit fore-optics and the spectrograph's focal conversion optics. A brief summary (of the optical design, which is the work of the current author) is given below.

Fibre modes

A summary of the SALT HRS R4 fibre modes, and their transmission (due to stellar PSF overfilling and geometrical slicing) is given in Table E.1. Each of the fibre modes is as follows:

1. low resolution fixed object and sky (FL); also used in nod and shuffle mode (NL),
2. medium resolution fixed object and sky (FM),
3. medium resolution nod and shuffle (NM),
4. high resolution fixed object and sky (FH), and
5. high resolution nod and shuffle (NH).

The low resolving power mode (L) will deliver $R = 17\,000$, while the medium (M) and high (H) resolving powers give $R = 38\,400$ and $R = 76\,800$ respectively. The "fixed" object modes (F) will allow a single object to be observed with simultaneous sky. The "nod and shuffle" modes (N) will allow more precise subtraction of the background sky.

Table E.1: Summary of the SALT HRS R4 fibre modes. The transmission has been calculated assuming median seeing conditions and include fibre and image slicer vignetting only. (See 3230AE0003 for details.)

	Fibre mode	Fibre diameter (μm)	Fibre diameter (arcsec)	Slice width (μm)	Slice number	Resolving Power ($\lambda/\delta\lambda$)	Transmission (%)
1.	FL/NL	500	2.23	-	-	16 400	82
2.	FM	500	2.23	160	3	38 400	67
3.	NM	350	1.57	160	2	38 400	56
4.	FH	350	1.57	80	3	76 800	48
5.	NH	250	1.12	80	3	76 800	37

Slit fore-optics

The slit fore-optics convert the the fibre output $f/3.8$ into $f/20$ as accepted by the image slicers. A triplet/doublet pair (LAL7 and N-FK517, all 20 mm in diameter) provides the focal conversion, and a meniscus corrects the telecentricity. The design shown in Figure 9 allows for a field of ± 1.22 mm at the fibre exit plane, or $\pm 5.7''$on the sky, which covers the available inter-order space. The spectrograph's entrance slit is at the far right of Figure E.3. This will be the location of the Walraven-type image slicers. The fibre to slit distance is 350 mm. The fibres in Figure 9 are depicted butted up to a flat glass plate which can be easily anti-reflection overcoated.

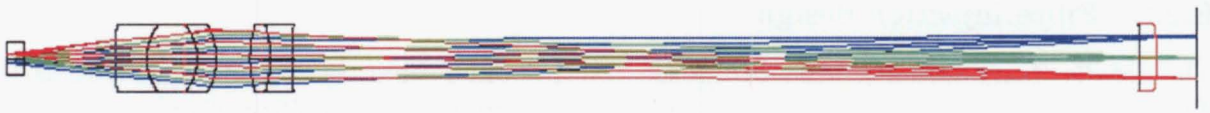

Figure E.3: The slit fore-optics convert from $f/3.8$ to $f/20$. The spectrograph's entrance slit is at the right.

Focal conversion optics

A second set of focal conversion optics converts from $f/20$ back to $f/10$ as accepted by the spectrograph's collimator while also maintaining telecentricity. A triplet consisting of BK7/N-FK51/CaF_2 is shown in Figure E.4. However, it is probable that a doublet of some other combination would be adequate. The first element (BK7) will also serve as the window into the spectrograph's vacuum. There is 150 mm of path length between the entrance slit and the vacuum window. As shown in Figure E.1, a small fold mirror located approximately 350 mm after the vacuum window folds the light towards the collimator.

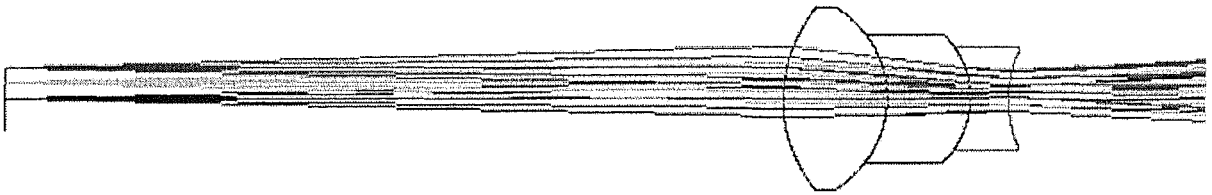

Figure E.4: The focal conversion optics provide the conversion from $f/20$ to $f/10$. The entrance slit (on the left) is the same as depicted at the right of Figure E.3.

E.2.3 Collimator and blue pupil mirror

The collimator (M_1) is an $f/10$ off-axis parabaloid. This choice of focal length is a compromise between an excessively large instrument (i.e., slow focal ratio), and a tolerably fast focal ratio which can be readily manufactured. In order to accommodate the dual use of the collimator as the first pupil transfer mirror, the total aperture must be 270 mm $\times$ 570 mm. Both this mirror and the blue pupil mirror (M_2), which is 220 mm $\times$ 570 mm, can be sourced from a single 720 mm diameter parabolic parent with a 4000 mm radius of curvature (see Figure E.5).

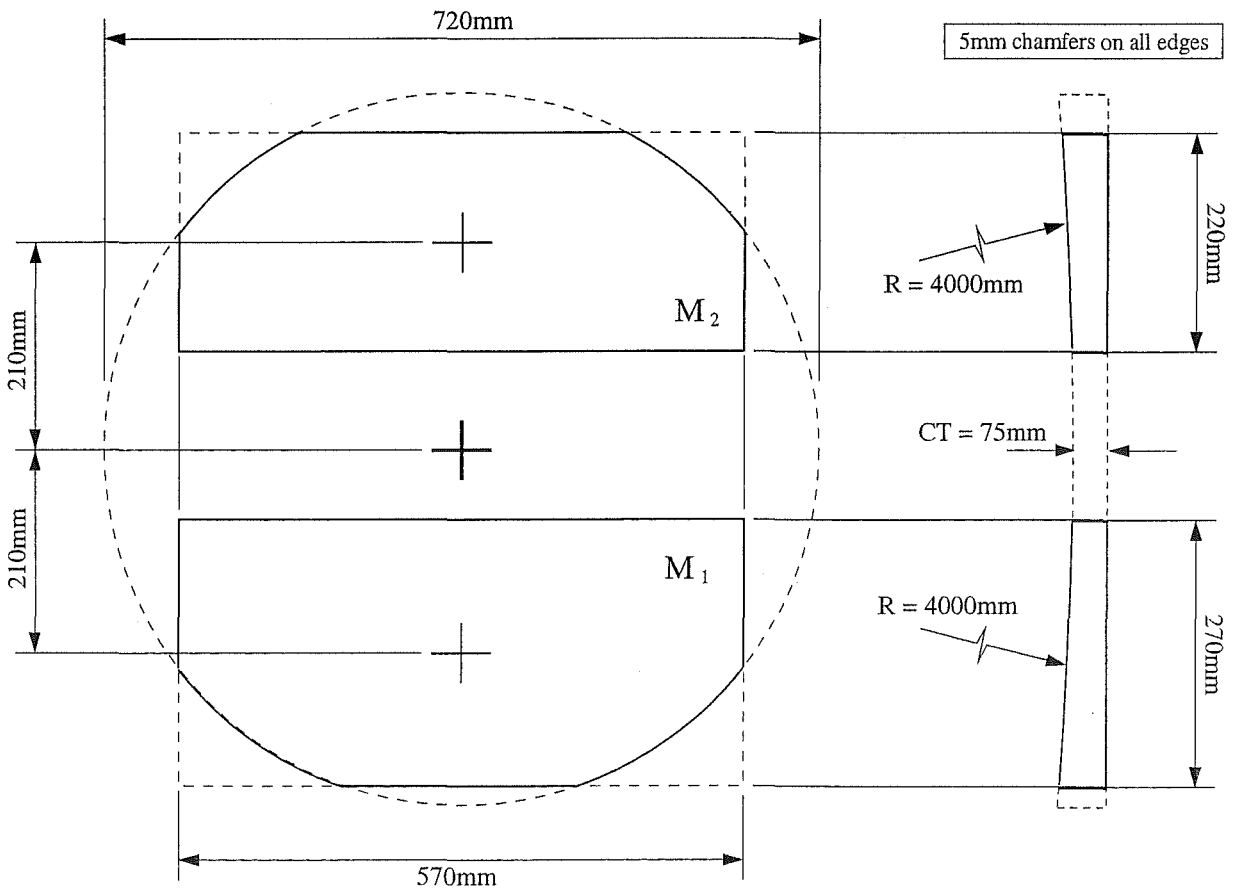

Figure E.5: Collimator (M_1) and blue pupil mirror (M_2) dimensions.

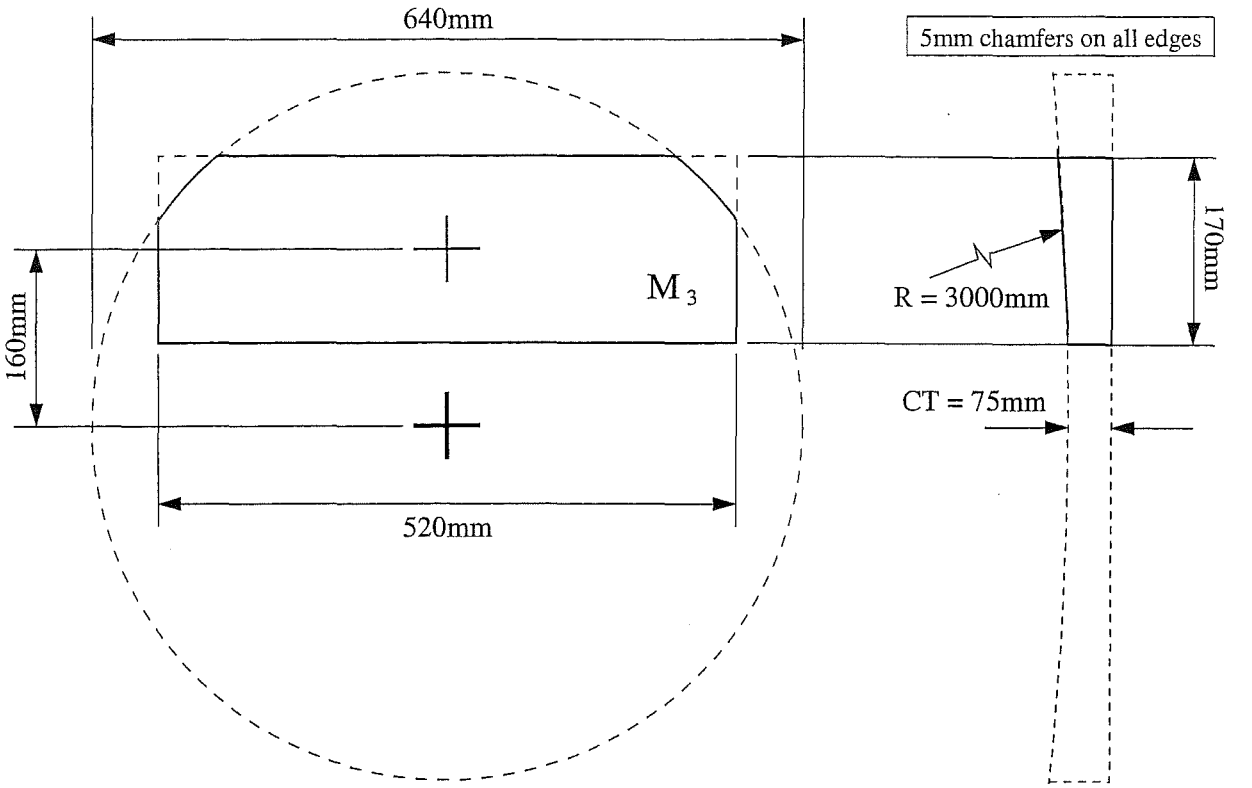

Figure E.6: Red pupil mirror (M_3) dimensions.

E.2.4 Red pupil mirror

The red arm white pupil mirror is a 170 mm × 520 mm off-axis paraboloid with a 3000 mm radius of curvature. This allows the red arm white pupil to be demagnified by a factor of 1.33 (from 200 mm to 150 mm), which is better suited to the use of VPH gratings. The red pupil mirror can be sourced from a 640 mm diameter mirror (see Figure E.6).

E.2.5 Echelle grating

The splitting of the spectrograph into red and blue arms occurs just after the intermediate focus following the first white pupil mirror. This enables the use of a single R4 échelle grating mosaic, where each grating has the parameters given in Table E.2. The mosaic has dimensions 855 mm × 204 mm, and has a gap of 35 mm between the gratings. With a collimated beam size of $B = 200$ mm, and FRD of 10%, there is no overfilling and about 5% of the light is lost to the gap between gratings. Each grating will be replicated on a 220 × 420 × 74 mm block of Zerodur and the coating will be aluminium.

Parameter	Specification
Blaze angle, θ_B	76.0°
Groove density, T	41.5 grooves/mm
Grating ruled width, W	204 mm
Grating ruled length, L	410 mm

Table E.2: The SALT HRS R4 grating parameters.

The gratings are illuminated in quasi-Littrow mode; i.e $\theta \approx 0$ and $\gamma \approx 0$. The angle of illumination with respect to the grating facet normal is $\theta = 0.35°$. This allows a more centred blaze function on each of the CCDs, and is in fact representative of the tolerance in the blaze angle of each replicated grating.

A feature of large blaze angle échelle gratings is the considerable anamorphic magnification they introduce. In the blue arm the anamorphic magnification (r) is in the range $0.82 < r < 1.22$ from one side of the free spectral range to the other. In the red arm, the spread is $0.76 < r < 1.41$. This effect is relatively unimportant, except that it will cause a variation in the sampling of each resolution element, and will lead to a small fraction of the wavelengths being undersampled at the highest resolving powers.

E.2.6 Dichroic

The dichroic has a nominal wavelength division of 550 nm. It will be located a short distance after the intermediate échelle spectrum. To capture all the light it must have a clear aperture of 75 mm × 360 mm.

E.2.7 The cross-dispersers

The parameters of the VPH gratings have been optimized in order to provide the maxium possible order separation while maintaining complete wavelength coverage. Without demagnifying the red arm pupil an ~450-line/mm grating would be required. This is considered a low density for the efficient use of VPH gratings. Hence a demagnification of 1.33 of the red pupil has been specified in order to allow a higher groove density to be used. The short focal length transfer mirror used only in the red arm produces this demagnification. Finally, while each grating is situated at the "white pupil", because of the échelle anamorphic magnification each grating must have a clear aperture somewhat larger than the projected beam size. The properties of the blue and red VPH gratings are summarized in Table E.3. The gratings will be manufactured on a substrate of BK7 which is 15 mm thick for the blue grating and 12 mm thick for the red. Identical cover glasses will be applied to each grating. Each grating air/glass surface will be post-polished to at least $\lambda/4$ and anti-reflection coatings will be applied.

Grating	Line density T (lines/mm)	Wavelength range (nm)	Clear aperture (mm)	Substrate diameter (mm)
Blue:	1050	$370 < \lambda < 560$	260	280
Red:	650	$550 < \lambda < 890$	195	215

Table E.3: Parameters of the VPH gratings for SALT HRS R4.

E.2.8 Cameras

Two cameras have been designed for SALT HRS R4 by D. Jones of Prime Optics. These are described in detail in the document 3210AA0007 (R4 Camera). Ray diagrams of the two cameras are shown in Figures E.7 and E.8.

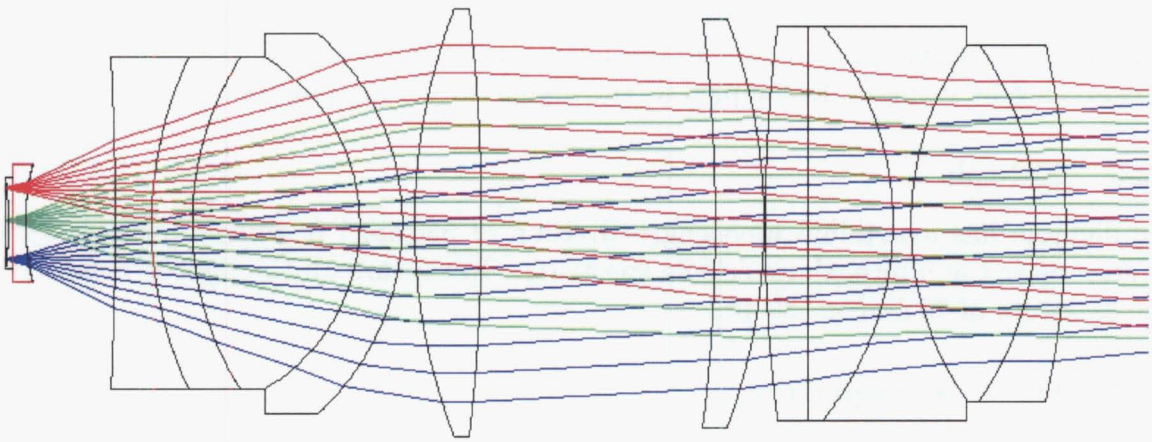

Figure E.7: The SALT HRS R4 blue arm camera.

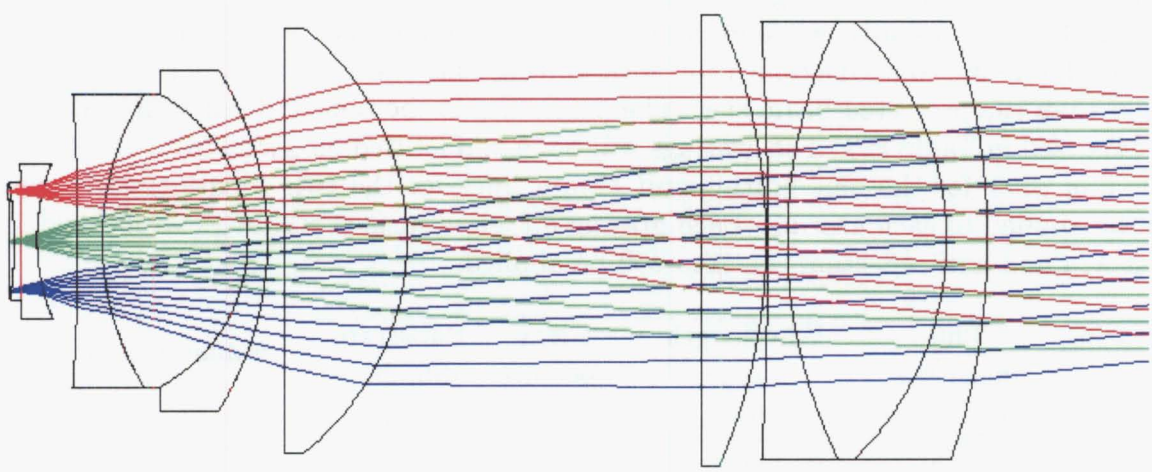

Figure E.8: The SALT HRS R4 red arm camera.

The blue camera (Figure E.7) has a focal length of 300 mm and an effective focal ratio of $f/1.5$. The diameter of the largest element is 356 mm, and the field size is 30.72 mm × 61.44 mm (i.e., a single 2k × 4k CCD) or 5.8° × 11.6°. The camera's optical performace allows the Nyquist sampling to be limited by the 15μm CCD pixels.

The red camera (Figure E.8) has a focal length of 280 mm, which with a 150 mm entrance pupil gives an effective focal ratio of $f/1.88$. The diameter of the largest element is 278 mm. With a 61.44 mm × 61.44 mm field (i.e., either a 4k × 4k CCD, or a mosaic of two 2k by 4k CCDs) the camera's field of view is 12.3° × 12.3°. Again, the camera's optical performance is sufficient (across most of the field) to allow the Nyquist sampling to be detector-limited.

As described in the camera design document (3210AA0007), the combination of white pupil optics and cross-dispersion at the white pupil causes the ideal focal plane to be cylindrical. As shown in Figures E.9 and E.10, this curvature may be corrected by a combination of spherical and cylindrical lenses. As depicted in these figures, each field-flattening lens will be manufactured in two parts, the first element of which will act as the CCD cryostat vacuum window.

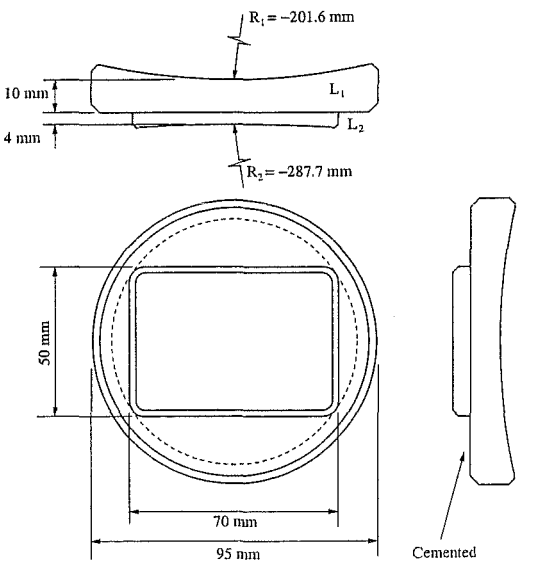

Figure E.9: Blue camera field-flattening lens.

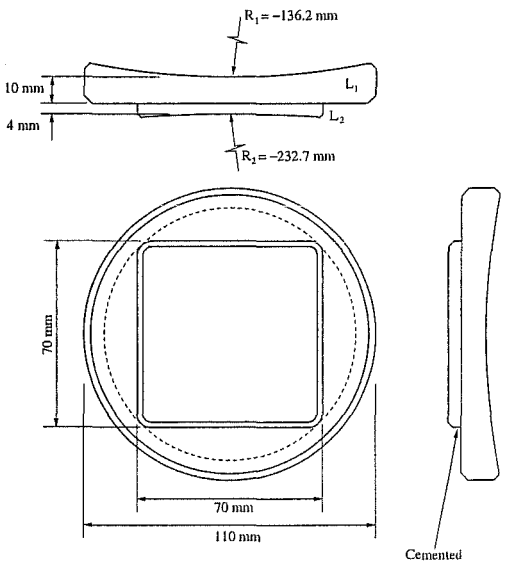

Figure E.10: Red camera field-flattening lens.

E.2.9 CCDs

The specifications of the CCDs are described in detail in the document series 3297AE00XX. It is assumed that a single 2k × 4k chip with 15 μm pixels is used in the blue camera. This is sufficient to just capture a single free spectral range. The red camera will use a mosaic of two 2k × 4k CCDs, again with 15 μm pixels. In order to accommodate a nod and shuffle mode, the red camera mosaic must have the columns aligned in the direction of cross-dispersion. This means a small fraction of each order will be lost to the gap. An alternative would be to use a single 4k × 4k CCD. There would be some advantage in using such a chip in the blue as well. CCDs of this size are available from Fairchild Imaging and Semiconductor Technology Associates. The suitability of these devices is yet to be assessed.

E.2.10 Exposure meter

It is proposed to insert a fold mirror in the gap between the échelle gratings. This mirror will direct light towards a focusing element, which will in turn illuminate either a photoelectric photometer or an avalanche photodiode. It is probable that a pair of detectors will be used, so that optimization for each of the blue and red arms can occur. This would also facilitate the use of different exposure times for each camera.

E.3 Performance

E.3.1 Spectral formats

The spectral formats in each of the two spectrograph arms are shown in Figures E.11 and E.12. The choice of cross-dispersion line density, and dichroic crosss-over wavelength has been optimized to ensure that complete wavelength coverage from 370 nm to 890 nm is obtained while maintaining the same minimum order separation in each arm. The spectral formats are based on detailed ray-tracing using the complete Zemax optical models. The exact CCD orientation (i.e., rotation) is yet to be fully optimized.

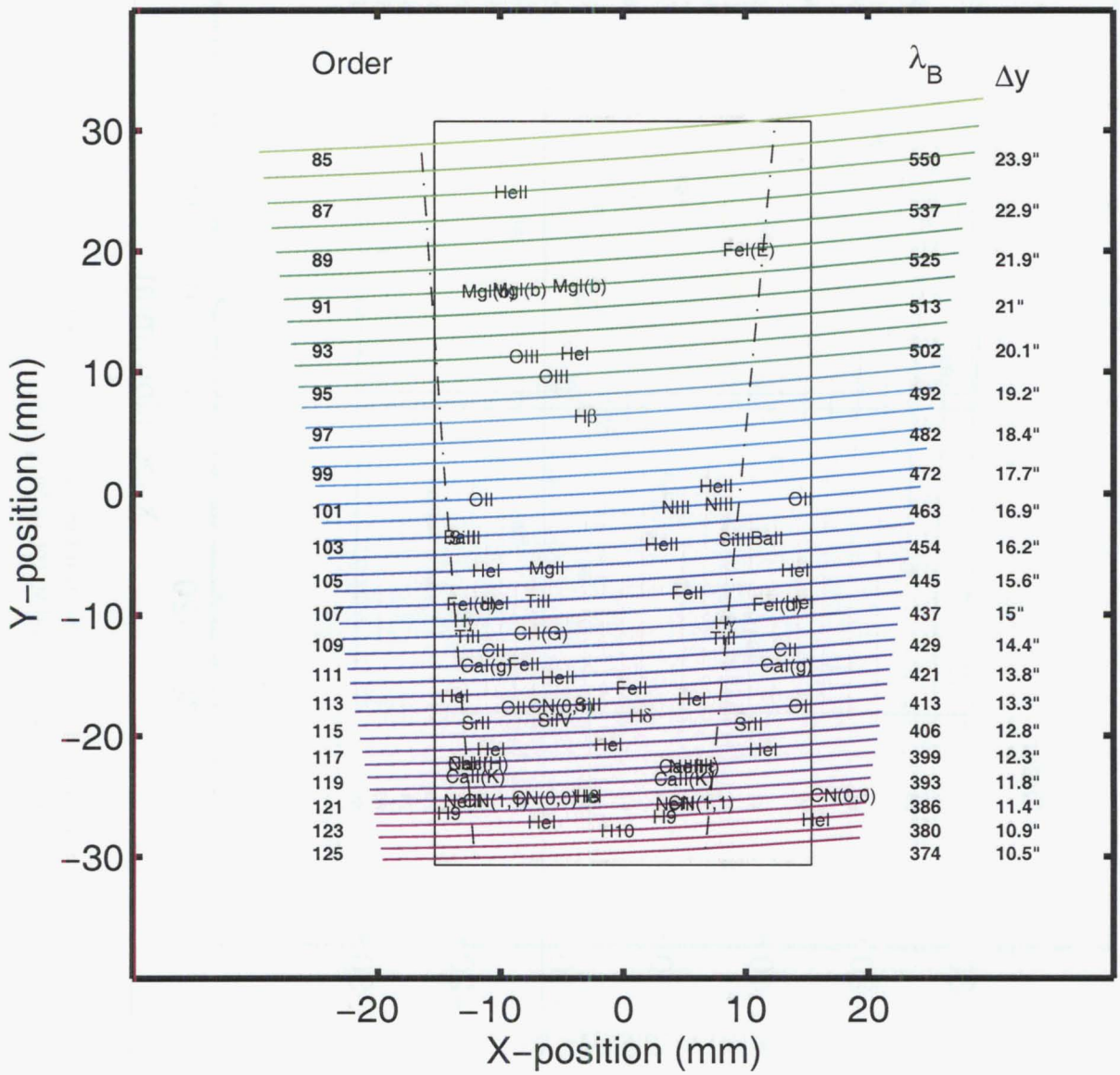

Figure E.11: SALT HRS R4 blue camera spectral format. The extent of one free spectral range is shown by the dashed lines. A single 2k by 4k detector with 15 μm pixels is depicted by the rectangle. Wavelengths correspond to the order centre.

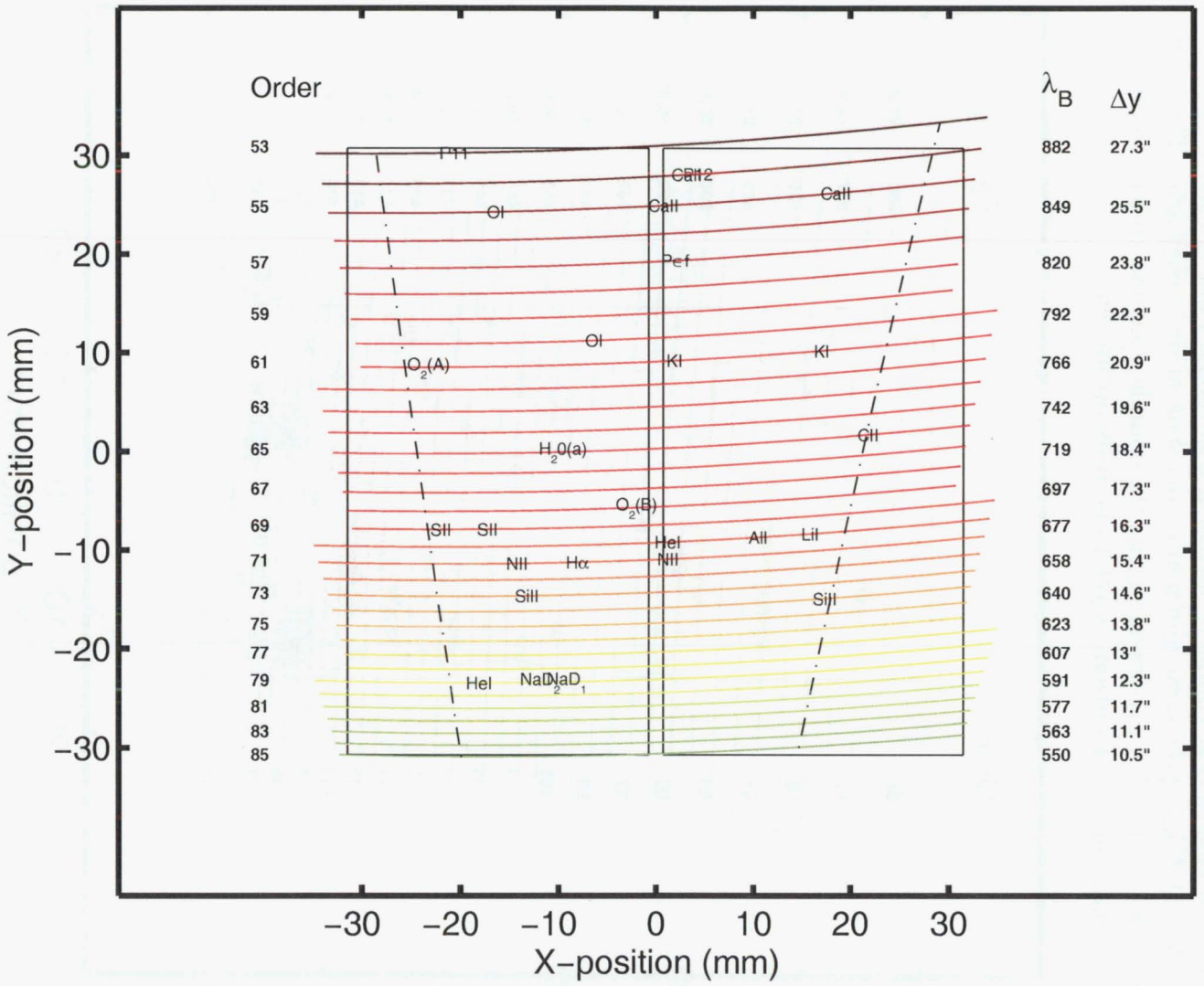

Figure E.12: SALT HRS R4 red camera spectral format. A pair of 2k by 4k detectors with 15 m pixels is depicted by the rectangles. Wavelengths correspond to the order centre.

E.3.2 Image quality

Slit fore-optics

The image quality of the slit fore-optics is shown in Figure E.13. The RMS image quality, as measured at the spectrograph's $f/20$ entrance slit, is less than 20 μm at all wavelengths from 380 nm to 890 nm. This corresponds to a diameter at 80% encircled energy of around 25 μm. This equates to about 5% of the smallest resolution element, and hence the effect on image quality will be negligible.

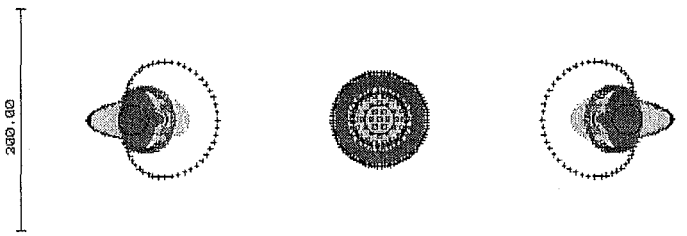

Figure E.13: Spot diagrams of the slit fore-optics. The image is at the spectrograph's entrance $f/20$ slit and spots at ± 1.2 mm are shown. The scale bar is 200 μm and the bold circle represents the diffraction limit.

The focal conversion optics

The image quality of the focal conversion optics is shown in Figure E.14. The optics introduce considerable lateral colouration. However, this is not of concern as the final imaging will occur after dispersion within the spectrograph. The RMS spot size is less than 24 μm across a field ± 6 mm at the $f/20$ entrance slit and the diameter at EE(80) is less than 20 μm at each individual wavelength. This is less than 5% of the projected size of the smallest resolution element.

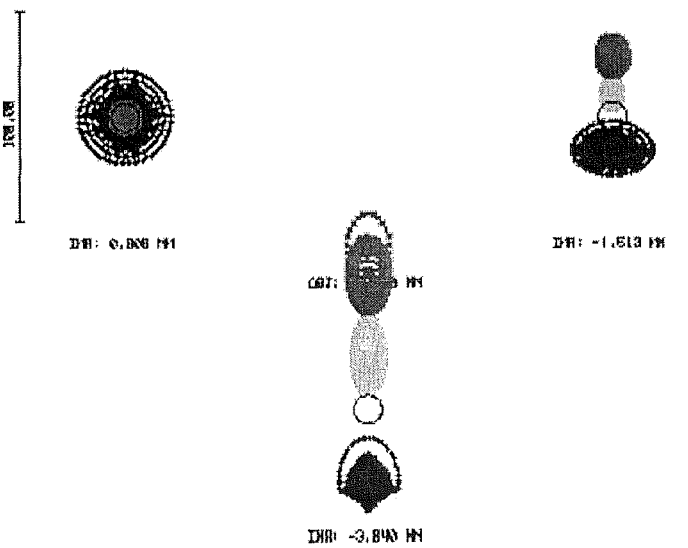

Figure E.14: The image quality of the focal conversion optics. There is considerable lateral colouration. However, this will not be perceived by the spectrograph. The scale bar is 100 μm and the bold circle represents the diffraction limit.

E.3.3 The white pupil optics

The image quality of the white pupil optics can be assessed by replacing the red and blue cameras with paraxial cameras and by using a toroidal detector surface. The results for the blue and red arms are given in Figures E.15 and E.16.

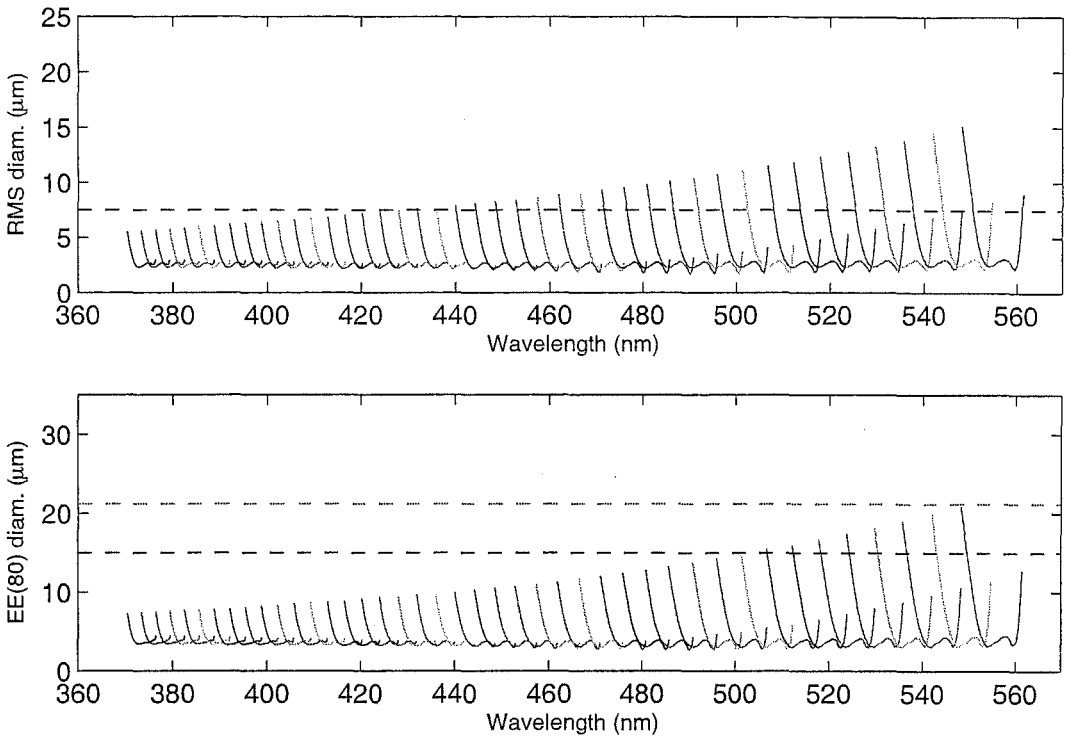

Figure E.15: The RMS spot diameters and the diameter at 80% encircled energy for the SALT HRS R4 blue arm white pupil relay. The slit optics are not included and the camera is paraxial. Two free spectral ranges are covered by each order.

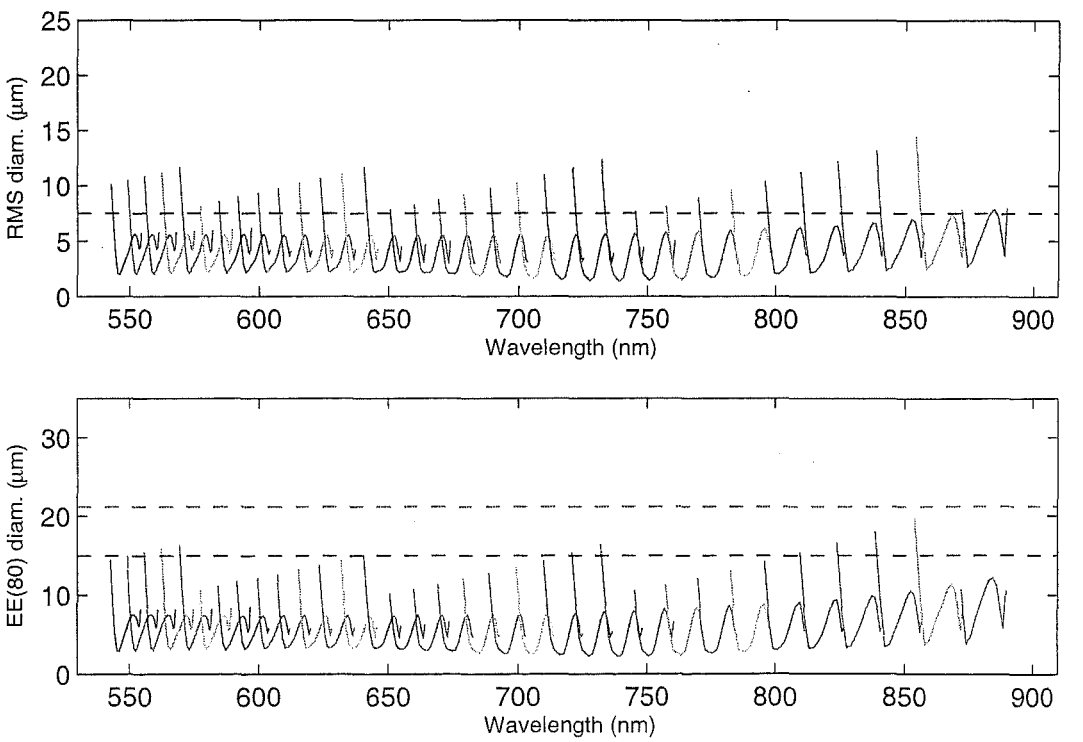

Figure E.16: The RMS spot diameters and the diameter at 80% encircled energy for the SALT HRS R4 red arm white pupil relay. The slit optics are not included and the camera is paraxial. Two free spectral ranges are covered by each order.

It can be seen that the blue arm white pupil optics are essentially diffraction limited (i.e., $d_{\mathrm{RMS}} < 3\,\mu$m) everywhere within one half of a free spectral range of the blaze wavelength in each order. The red arm white pupil optics have slightly worse image quality, but the RMS diameter is still less than $5\,\mu$m everywhere within one half of a free spectral range of the blaze wavelength.

The spectrograph with cameras

The image quality of the cameras was assessed by the camera optical designer at selected wavelengths (see 3210AA0007) and spot diagrams are shown in Figures E.17 and E.18.

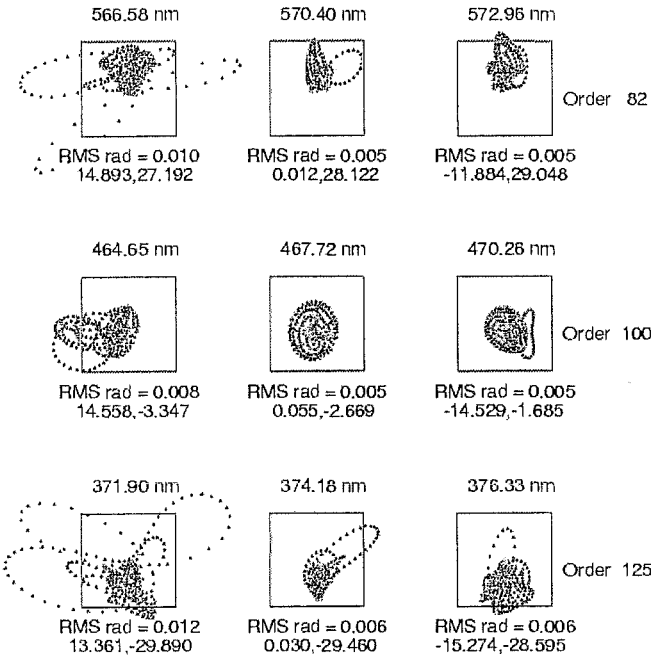

Figure E.17: Spot diagrams for the SALT HRS R4 blue camera (v2.08). The boxes are two pixels square. Figure courtesy of D. Jones.

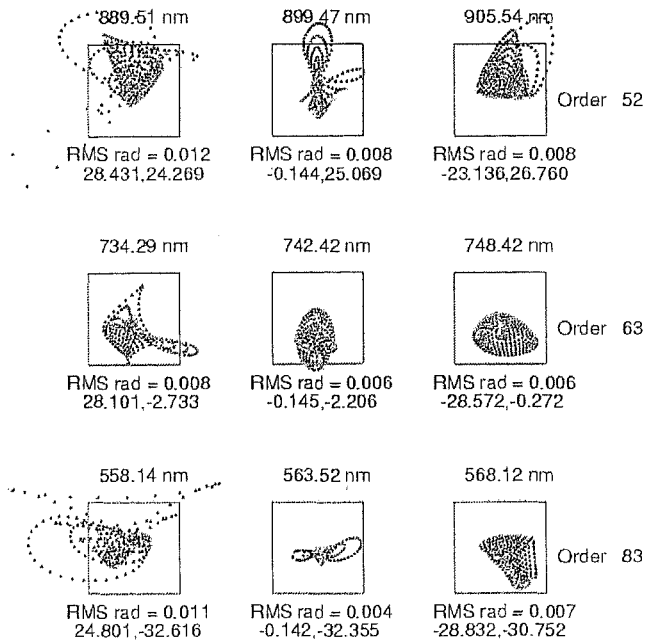

Figure E.18: Spot diagrams for the SALT HRS R4 red camera (v2.01). The boxes are two pixels square. Figure courtesy of D. Jones.

The image quality at all wavelengths from 370 nm to 890 nm is shown in Figures E.19 and E.20.

The image quality of the blue camera is excellent; at all wavelengths that fall on a single 2k by 4k CCD the encircled energy within one pixel is greater than 80%. This is sufficient to ensure that the Nyquist sampling limited resolving power ($R = 80\,000$) is possible with minimal degradation due to the optics.

The image quality of the red camera is not quite as good. From $\lambda = 625$ nm to $\lambda = 725$ nm the encircled energy within one pixel is around 70%, which is below the specified 80%. However, because the sampling limited resolving power of the red arm is in fact $R = 100\,000$, the slight degradation due to image quality ($\sim$15 to 20%) will lower the effective resolving power to match that of the blue arm.

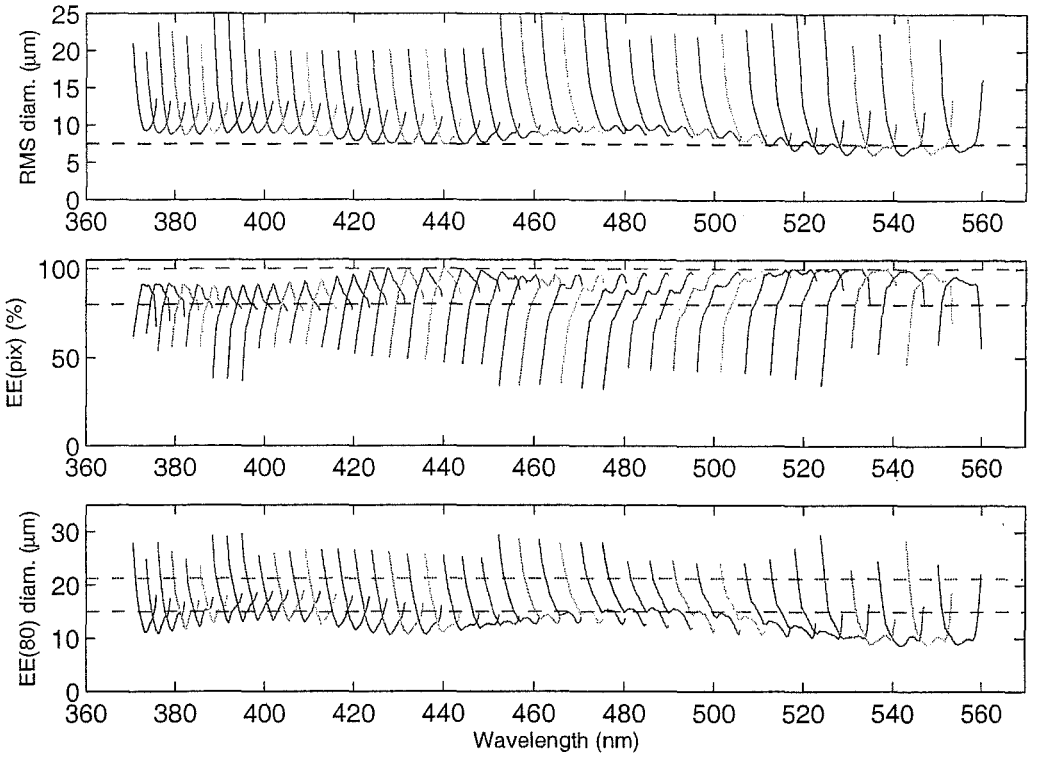

Figure E.19: The RMS spot diameter, the encirled energy within one pixel, and the diameter at 80% encircled energy for the SALT HRS R4 blue arm. The slit fore-optics and focal conversion optics are not included.

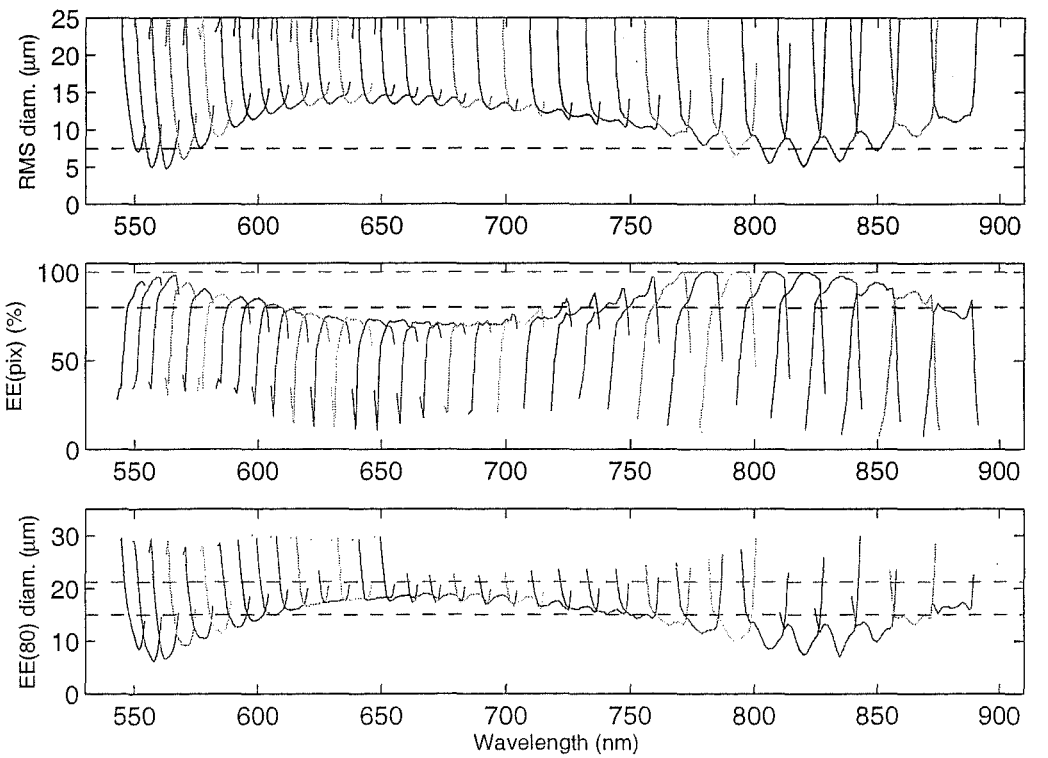

Figure E.20: The RMS spot diameter, the encirled energy within one pixel, and the diameter at 80% encircled energy for SALT HRS R4 red arm. The slit fore-optics and focal conversion optics are not included.

E.3.4 Efficiency

Wherever possible the measured efficiencies of equivalent components have been used. Other efficiences are based on theoretical measurements supplied by the coating vendor, or other coatings have been scaled according to the vendor's minimum specification.

SALT

The reflectance of each SALT mirror has been measured. The SAC reflectivities are from witness samples made at the time of coating, while the primary mirror (aluminium) reflectivity is that of a standard coating. The image quality is assumed to be EE(80) = 2.15″.

FIF and fibres

For these efficiency calculations Optran UV fibres from Ceramoptec are assumed. It is likely that either Polymicro FBP or an equivalent which uses Hearaus STU preforms will be used in the final design. This will improve performance of the fibres at wavelengths shorter than 400 nm and will also remove the presence of the OH feature at ~600 nm. The fibres are assumed to have overcoated micro-lenses at both the input and output. A multi-layer broad-band coating supplied from measurements made by Fisba Optik for a HERCULES micro-lens has been assumed.

Slit fore-optics, image slicers and focal conversion optics

The material of all of the slit fore-optics, image-slicers and focal conversion optics is in most cases that of the prescriptions described above. However, in some cases the glass has been substituted for another with better UV transmission (e.g., silica or CaF_2) and therefore the material absorption is insignificant. Each face of all the elements (including the image slicers) is assumed to have a broadband coating from Denton (UBBAR).

Mirrors

The reflectivity of a selection of mirror coatings from Laserdyne Technologies (Queensland, Australia) is shown in Figure E.21. Each of the coatings, apart from the new UV enhanced silver coat are from historical measurements. Data for the new UV enhanced silver coat is from theoretical predictions supplied by Laserdyne. Each of Laserdyne's historical coatings also match the minimum specification supplied by Spectrum Thin Films, while the new UV coating is equivalent to the SAC mirror coatings. Currently the coatings specified for each of the mirrors are:

M_1 (collimator and first pupil mirror):	UV enhanced silver,
M_2 (blue pupil mirror):	enhanced aluminium, and
M_3 (red pupil mirror):	enhanced silver.

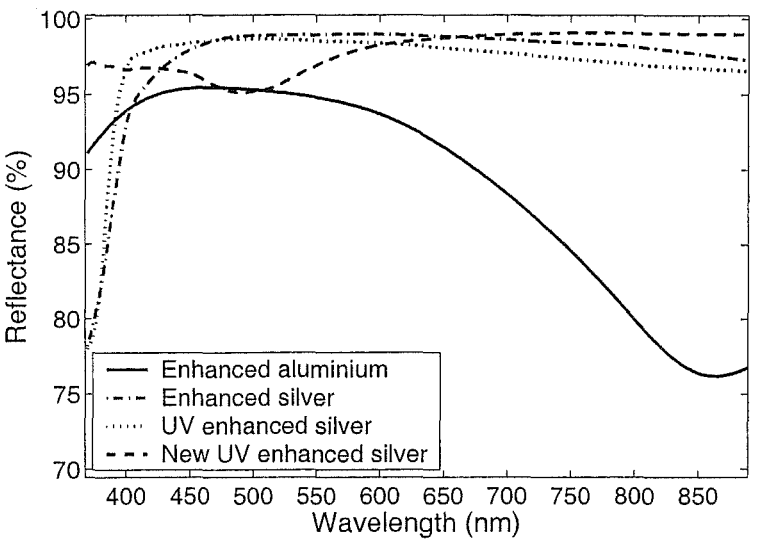

Figure E.21: The reflectivities of various coatings by Laserdyne. The new UV enahnced coating is theoretical only.

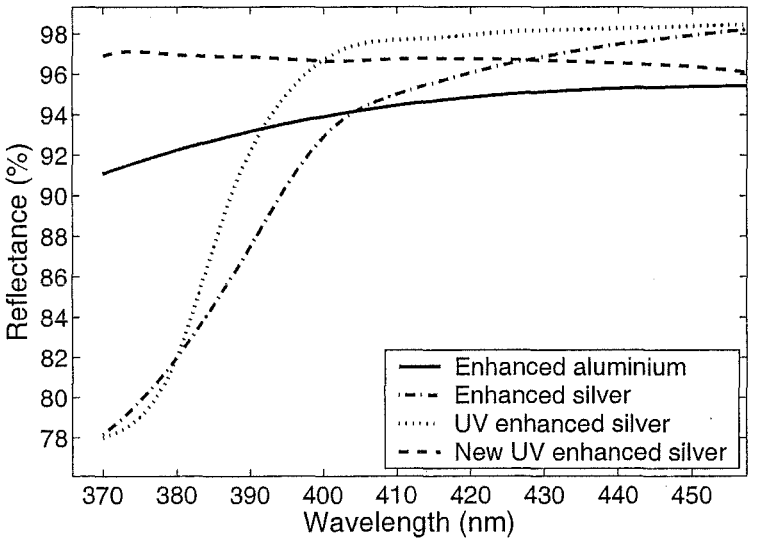

Figure E.22: The UV close-up of the Laserdyne mirror reflectivities.

The new UV coating from Laserdyne has the potential to improve the response at 370 nm to 380 nm by over 10% if it were used on both the collimator and blue pupil mirrors (see Figure E.22). However, the response between 450 nm and 600 nm would actually decrease. Discussions are continuing with Laserdyne with regard to improved mirror coatings. It is assumed that the small input fold mirror will have a very efficient multi-layer coating.

Dichroic

The transmission of a high efficiency dichroic supplied by Barr Assoicates is shown in Figure E.23. The transmissions have been scaled to 95% of those shown here to reflect the minimum specifications indicated by Barr Associates for the SALT HRS dichroic.

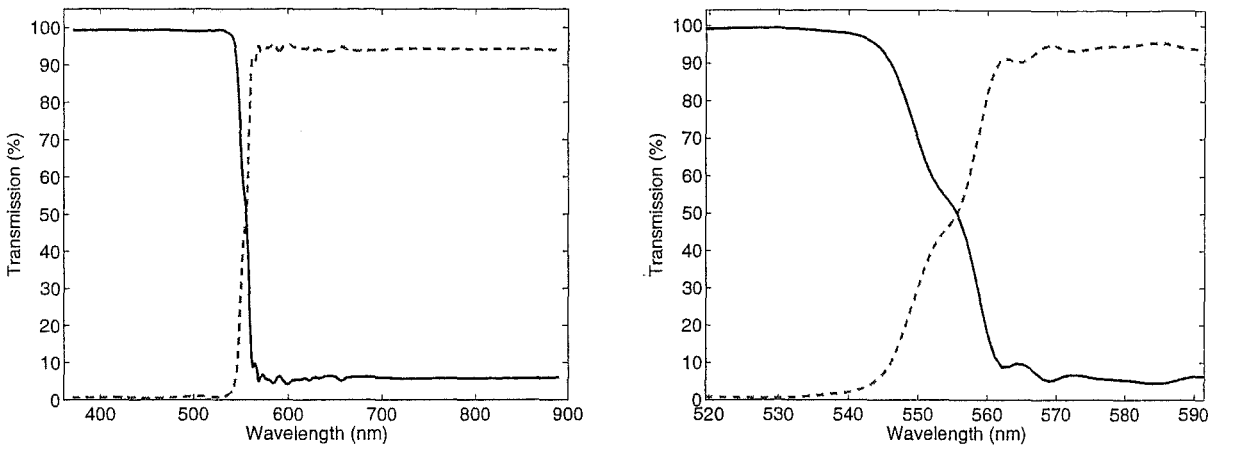

Figure E.23: The dichroic efficiency. The blue wavelengths are reflected while the red wavelengths are transmitted. A close-up of the crossover region is shown on the right.

VPH gratings

The theoretical efficiencies of the two VPH gratings required have been computed by Wasatch Photonics (Figures E.24 and E.25).

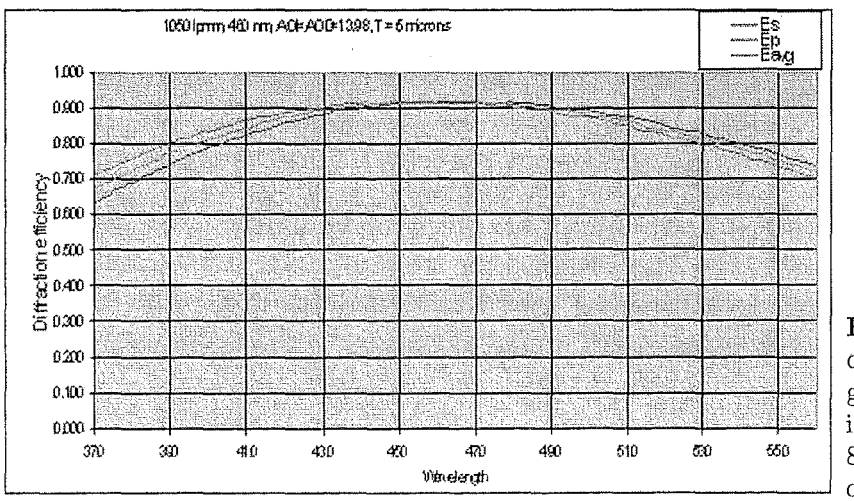

Figure E.24: Theoretical efficiencies of a 1050 line/mm VPH grating from Wasatch Photonics. The calculations assume 8% Fresnel losses from uncoated surfaces.

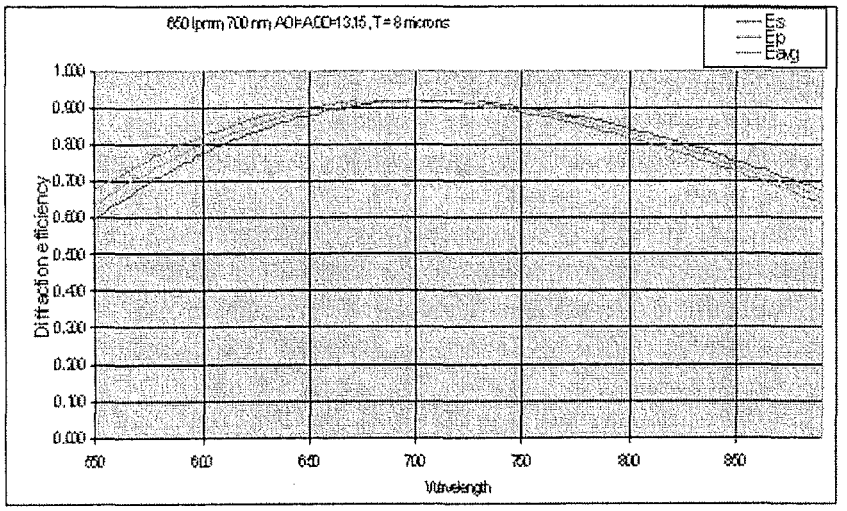

Figure E.25: Theoretical efficiencies of a 650 line/mm VPH grating from Wasatch Photonics. The calculations assume 8% Fresnel losses from uncoated surfaces.

A comparision with a number of measured VPH gratings is given in Figure E.26. The gratings are assumed to be anti-reflection coated with $R_{\text{ave}} < 0.7\%$.

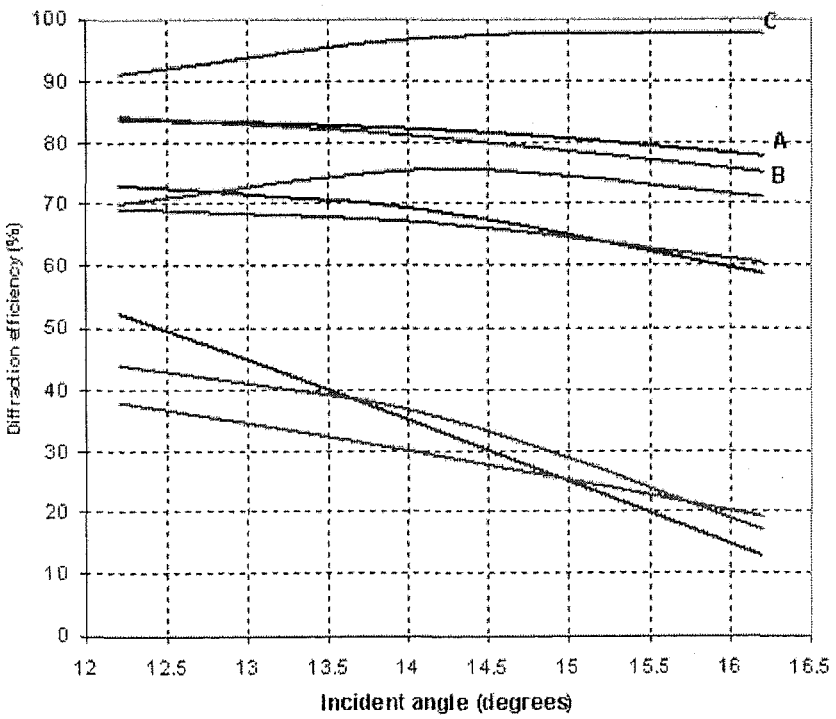

Figure E.26: The measured efficiencies of VPH gratings supplied by three different vendors A, B and C (Dekker 2004). The efficiencies have been corrected for reflection losses due to the grating substrate. Measurements at the blaze wavelength are marked. The results show quite a large variation in absolute grating efficiency between vendors. However, they demonstrate that high throughput is achievable.

Cameras

Standard absorption data are used for each of the camera lens elements. A generic broad-band coating has been specified on each element apart from the field-flattening lens which is single-layer MgF_2. Both Laserdyne and Spectrum Thin Films have supplied theoretical data for the air/glass overcoated surfaces. Laserdyne's data are shown in Figure E.27 and Figure E.28. The transmission of the oil interfaces has been computed using Fresnel losses, where the oil's refractive index is assumed to be an average of that of the two glasses being interfaced. The resultant losses are negligible.

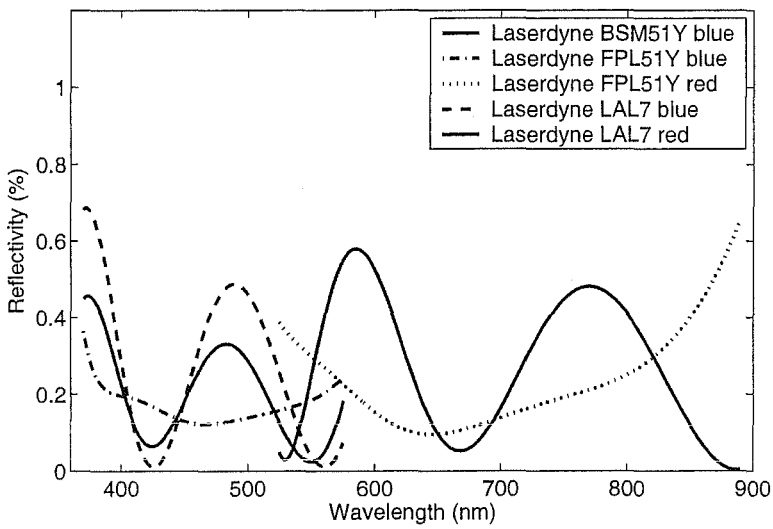

Figure E.27: The reflectivity of the multi-layer coatings from Laserdyne.

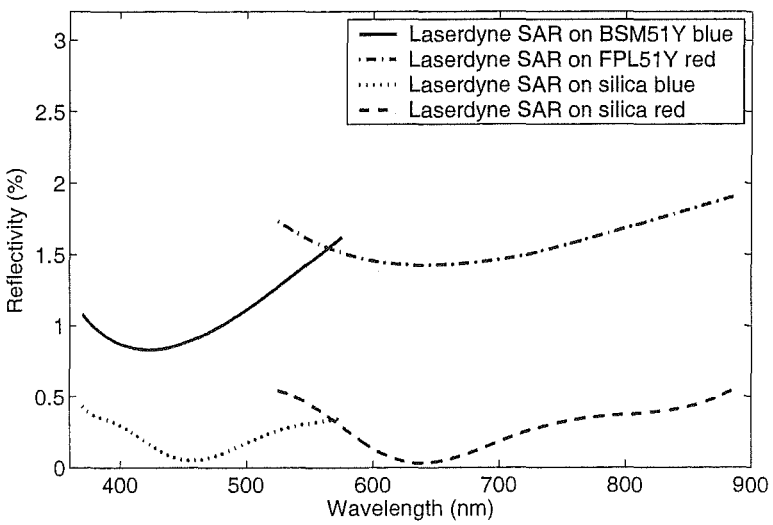

Figure E.28: The reflectivity of the single-large MgF_2 coatings from Laserdyne.

Summary

The computed efficiencies of SALT HRS R4 are given in the following tables. The spectrograph efficiencies (SPC) include everything except the telescope (TEL) and slit optics (SLT). The slit optics include fibres, slit fore- optics, and (where appropiate) image slicers. The other items are the collimator (COL), which includes FRD, the échelle grating (ECH), the cross-dispersers (XDP), the camera (CAM), and the CCD. The camera includes the white pupil mirrors and dichroic.

Table E.4: Detailed efficiciencies of the SALT HRS R4 blue arm in "Fixed Object" mode at the lowest resolving power.

Wavlength and Order		Component by component efficiencies							Totals		
										SPC+	SPC+
									SPC+	SLT+	
λ	m	TEL	SLT	COL	ECH	XDP	CAM	CCD	SPC	SLT	TEL
380	123	0.622	0.570	0.737	0.553	0.804	0.611	0.674	0.135	0.077	0.048
480	97	0.642	0.688	0.900	0.605	0.910	0.800	0.803	0.319	0.219	0.141
540	86	0.630	0.681	0.890	0.589	0.737	0.799	0.795	0.245	0.167	0.105

Table E.5: Detailed efficiciencies of the SALT HRS R4 red arm in "Fixed Object" mode at the lowest resolving power.

Wavlength and Order		Component by component efficiencies							Totals		
										SPC+	SPC+
									SPC+	SLT+	
λ	m	TEL	SLT	COL	ECH	XDP	CAM	CCD	SPC	SLT	TEL
560	83	0.631	0.684	0.890	0.584	0.835	0.788	0.923	0.315	0.216	0.136
650	72	0.617	0.708	0.884	0.571	0.951	0.816	0.898	0.352	0.249	0.154
800	58	0.602	0.724	0.884	0.565	0.596	0.794	0.794	0.188	0.136	0.082

Fibre mode	Resolving power $\lambda/\delta\lambda$	Transmissions SPC	SPC + SLT	SPC + SLT + TEL
FL/NL	16 400	31.9%	21.9%	14.1%
FM	38 400	31.9%	17.0%	10.9%
NM	38 400	31.9%	13.6%	8.7%
FH	76 800	31.9%	12.1%	7.8%
NH	76 800	31.9%	9.1%	5.8%

Table E.6: Summary of efficiencies of the SALT HRS R4 blue arm at all resolving powers and modes at a wavelength of 480 nm.

Fibre mode	Resolving power $\lambda/\delta\lambda$	Transmissions SPC	SPC + SLT	SPC + SLT + TEL
FL/NL	16 000	35.2%	24.9%	15.4%
FM	38 000	35.2%	19.3%	11.9%
NM	38 000	35.2%	15.4%	9.5%
FH	77 000	35.2%	13.8%	8.5%
NH	77 000	35.2%	10.3%	6.4%

Table E.7: Summary of efficiencies of the SALT HRS R4 red arm at all resolving powers and modes at a wavelength of 650 nm.

E.3.5 Signal to noise predictions

Using the efficiency calculations from Section E.3.4 the signal to noise expected for a range of observing conditions has been computed. The calculations assume a G dwarf star and a telescope airmass of $X = 1.3$. The Moon is assumed to be at quarter phase. The calculated signal-to-noise ratios (S/N) are for each extracted half-resolution element (to allow correct Nyquist sampling).

The predicted signal to noise ratio of the red arm (at 650 nm) at the lowest resolving power is shown in Figure E.29. With a signal to noise ratio of $S/N = 10$, the limiting magnitudes in all other observing modes for a 3600-second exposure are as follows:

Blue arm ($\lambda = 480$ nm):
- FL/NL: $V = 20.7$,
- FM: $V = 19.7$,
- NM: $V = 19.5$,
- FH: $V = 18.7$, and
- NH: $V = 18.4$.

Red arm ($\lambda = 650$ nm):
- FL/NL: $V = 21.0$,
- FM: $V = 20.0$,
- NM: $V = 19.8$,
- FH: $V = 19.0$, and
- NH: $V = 18.7$.

At a wavelength of $\lambda = 650\,\mathrm{nm}$, at the lowest resolving power, it will be possible to reach a signal to noise of $S/N = 100$ in 5 minutes for a $V = 14.4$ magnitude object, or $V = 15.6$ in 15 minutes, and $V = 16.3$ in a half-hour exposure.

At the highest resolving powers, at a wavelength of $\lambda = 650\,\mathrm{nm}$, a signal to noise ratio of $S/N = 100$ will be achieved after 5 minutes for $V = 12.1$, after 15 minutes for $V = 13.4$, after 30 minutes for $V = 14.0$ and after one hour for $V = 14.8$.

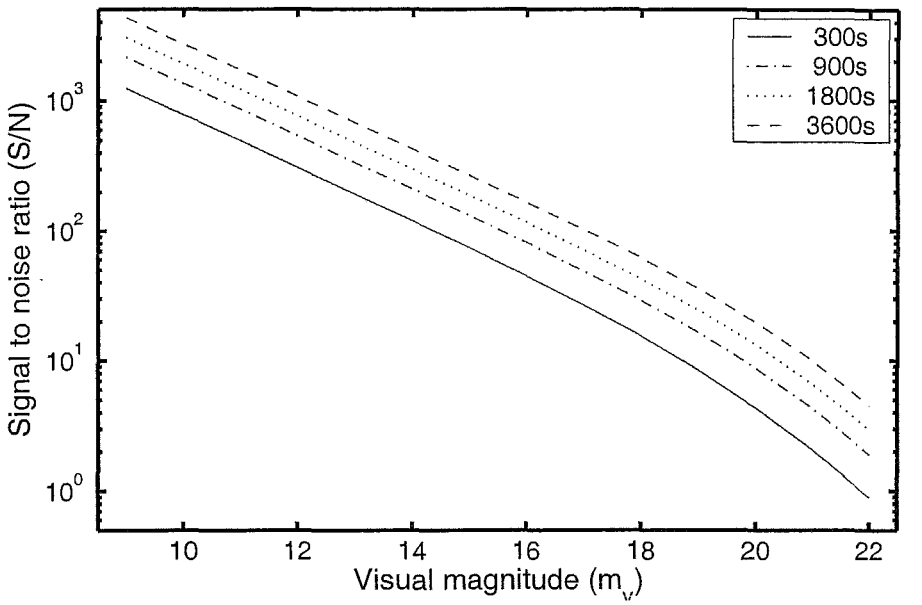

Figure E.29: The predicted signal to noise ratio (S/N) of SALT HRS R4 at $\lambda = 650\,\mathrm{nm}$ in "Fixed object" fibre mode at the lowest resolving powers.

E.4 Discussion

E.4.1 The white pupil optics

A suggestion by B. Delabre made at the time of the 2004 September PDR for the SALT HRS R2 design was that each of the white pupil transfer mirrors be made spherical. This possibility was explored. However the large beam size and short focal length of SALT HRS R4 prevents such a system from achieving the required image quality. The system was found to be adequate only when a refractive correcting element was introduced prior to the VPH gratings. Such a catadioptric white pupil relay is in fact being used on PEPSI for the LBT (see Figure E.30) where each white pupil mirror has a companion correcting lens. The complication to the optical layout, the added expense, and the additional light losses from between 4 and 6 air/glass reflections support the use of the marginally more difficult off-axis parabolic mirror system.

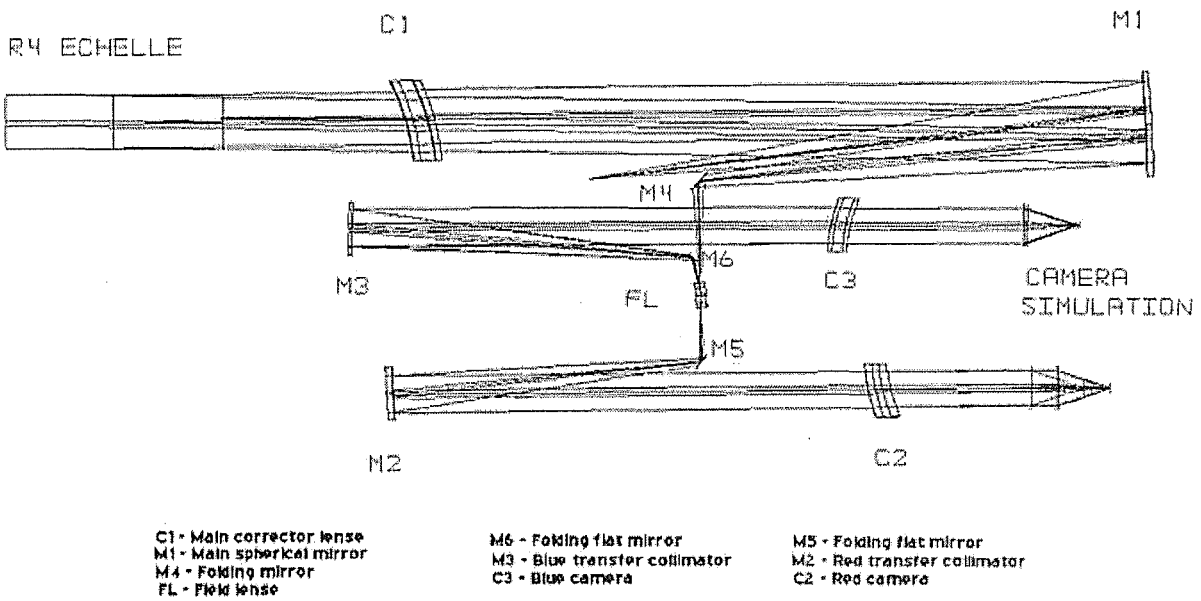

Figure E.30: The PEPSI catadioptric white pupil relay (Pallavicini et al., 2003).

E.4.2 VPH gratings

The 2004 January concept for the SALT HRS R4 used VPH grisms for cross-dispersion. A small increase in the average order separation can be achieved by this means. However, the gain was not considered sufficient to warrant the added complexity to the design and manufacture of the cross-dispersers. Nevertheless, it will be necessary to use grisms if VPH gratings other than those installed at the time of commissioning are to be considered in future. This will avoid the need to articulate the camera.

E.4.3 Cameras

This section explores some of the camera design issues. The effect of using the first element as a vacuum window is discussed first, and the remainder of the issues relate to

the various means by which the cameras could be made simpler, smaller and possibly less expensive. The options presented here will only impact on the total system throughput, and are not expected to degrade the image quality. There is in fact some scope for further improving the camera's imaging performance.

Vacuum windows

The elements of the spectrograph camera will be held at atmospheric pressure in order to simplify the maintanance of the oil coupling between the various multiplets that make up each camera. Therefore, the first lens will be used as a window between the partial vacuum inside the spectrograph and the external atmosphere. This lens will be deformed by this pressure difference and there will be some effect on image quality.

The deformation of the lens can modelled using finite element analysis (FEA). A constant force (pressure) is assumed to be acting across the surface of the lens which is held rigidly against an annulus (the "o-ring"). The deformed surface can then be described by a general asphere, where the aspheric terms come from a polynomial fit to the deviation of the surface from the undeformed sphere. At the time of writing only the red camera vacuum window has been modelled in detail. The deformation of the red camera window is shown in Figure E.31.

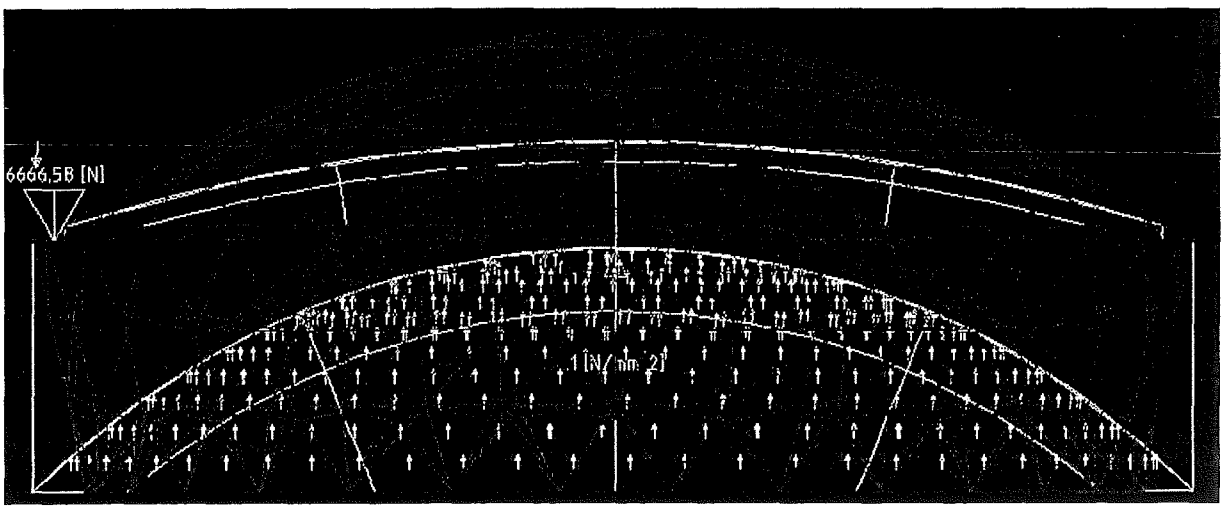

Figure E.31: The FEA of the red camera vacuum window. The mesh is an exaggerated profile of the deformed lens. The total deformation is nearly 3 μm and can be well modelled by a 4th order polynomial (see Figure E.32). This surface was used to assess the effect on image quality and spot diagrams are shown in Figure E.33. The forces within the glass ($< 2\,\mathrm{N/mm^2}$) are far from the theoretical yield point (<10%).

The effect on image quality is small (Figure E.33). This can be explained by noting that while the total deformation of each lens appears quite large (nearly 3 μm, or several wavelengths) the deformed surface is itself still quite well described by a displaced sphere. Figure E.34 shows the residuals of the deformed surface and the best fit sphere. The RMS residual is around $\lambda/8$, which is considerably less than the surface quality required on individual camera elements.

In principle the camera could be slightly reoptimized in order to compensate entirely for the vacuum window deformation. This could be done by ensuring that the best fit

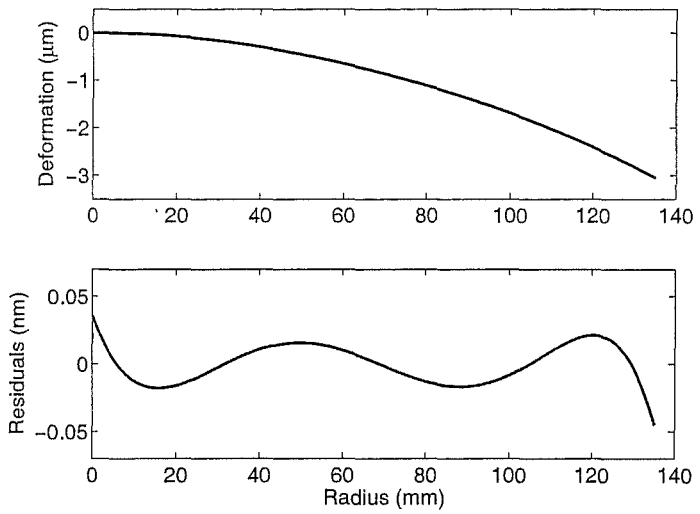

Figure E.32: The deformation of the red camera vacuum window with respect to the original sphere (upper panel) and the residual of a 4th order polynomial fit to this deformation (lower panel).

sphere of the deformed surface is actually the prescribed sphere. However, in the case of the red camera the radius of curvature of the best fit sphere is less than 0.1 mm different from the original sphere. This is well within the ±0.7 mm allowed by manufacturing tolerances alone (see 3210AA0007 R4 Camera) and hence is not worth considering.

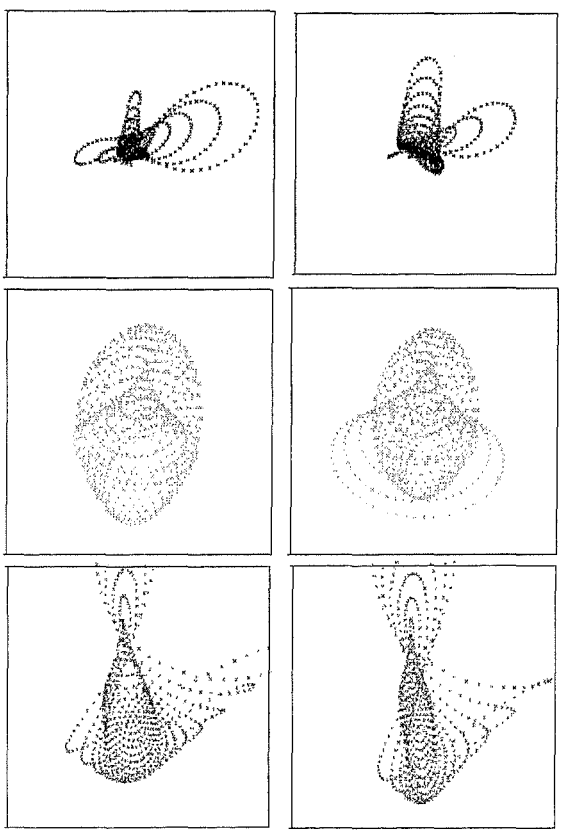

Figure E.33: Spot diagrams showing the effect on image quality of the deformation of the camera vacuum window. Spots are shown for wavelengths in the centre of orders at the bottom (blue), middle (green), and top (red) of the field. Each box is two pixels square.

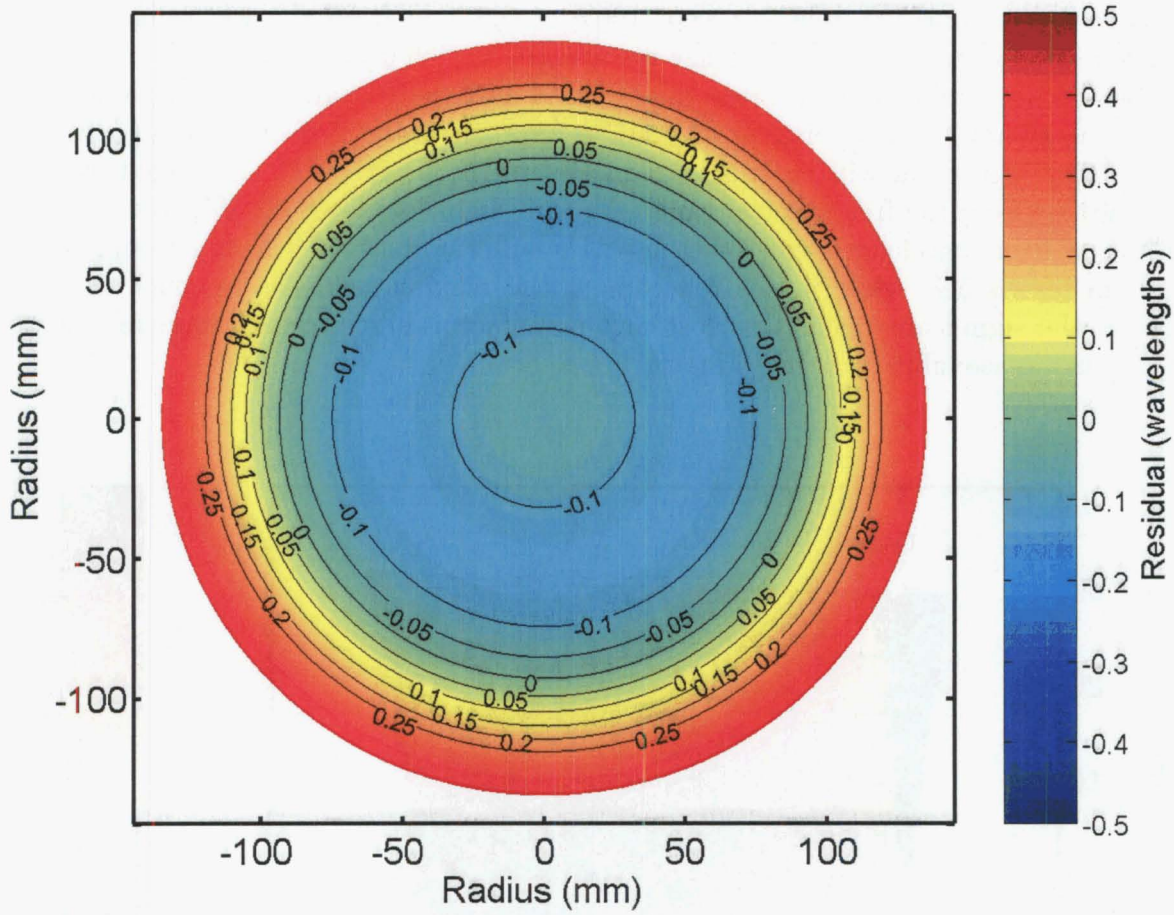

Figure E.34: The residuals of the red camera vacuum window with respect to the best fit sphere.

Camera apertures

Currently the cameras are able to accept 100% of the light from any wavelength within one half a free spectral range of the blaze wavelength in each order. The camera apertures therefore become quite large because of the effect of échelle anamorphic magnification. If the cameras have their apertures reduced to approximately 85% of the design values, the resultant vignetting will be as shown in Figures E.35 and E.36. Averaged over all wavelengths within the free spectral range the total light loss is about 2%. Wavelengths near the shorter wavelength end of each order suffer worst. In the blue camera the maximum loss is 5%, while in the red camera the maximum loss is as much as 15%. However, the significant savings in cost and manufacturability of each camera suggest that this is a reasonable tradeoff to make.

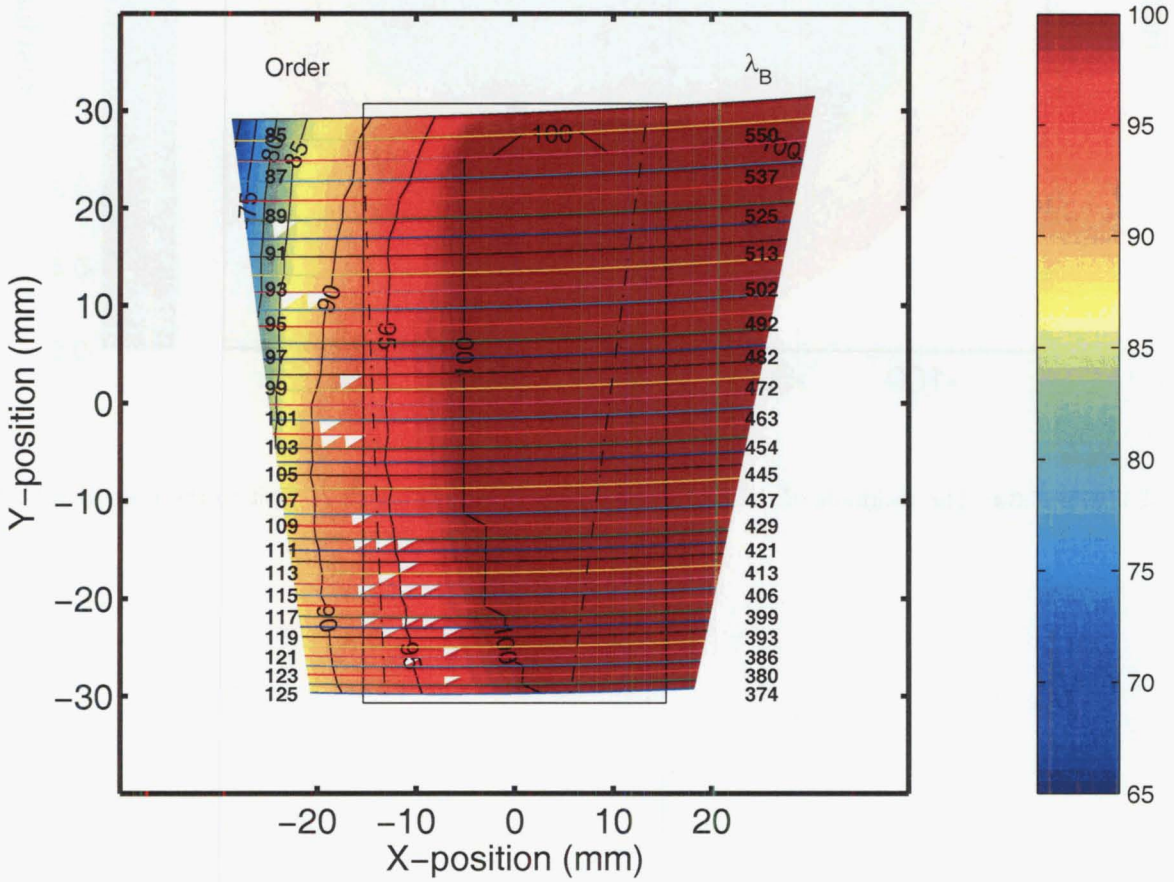

Figure E.35: The vignetting of the blue camera with reduced apertures.

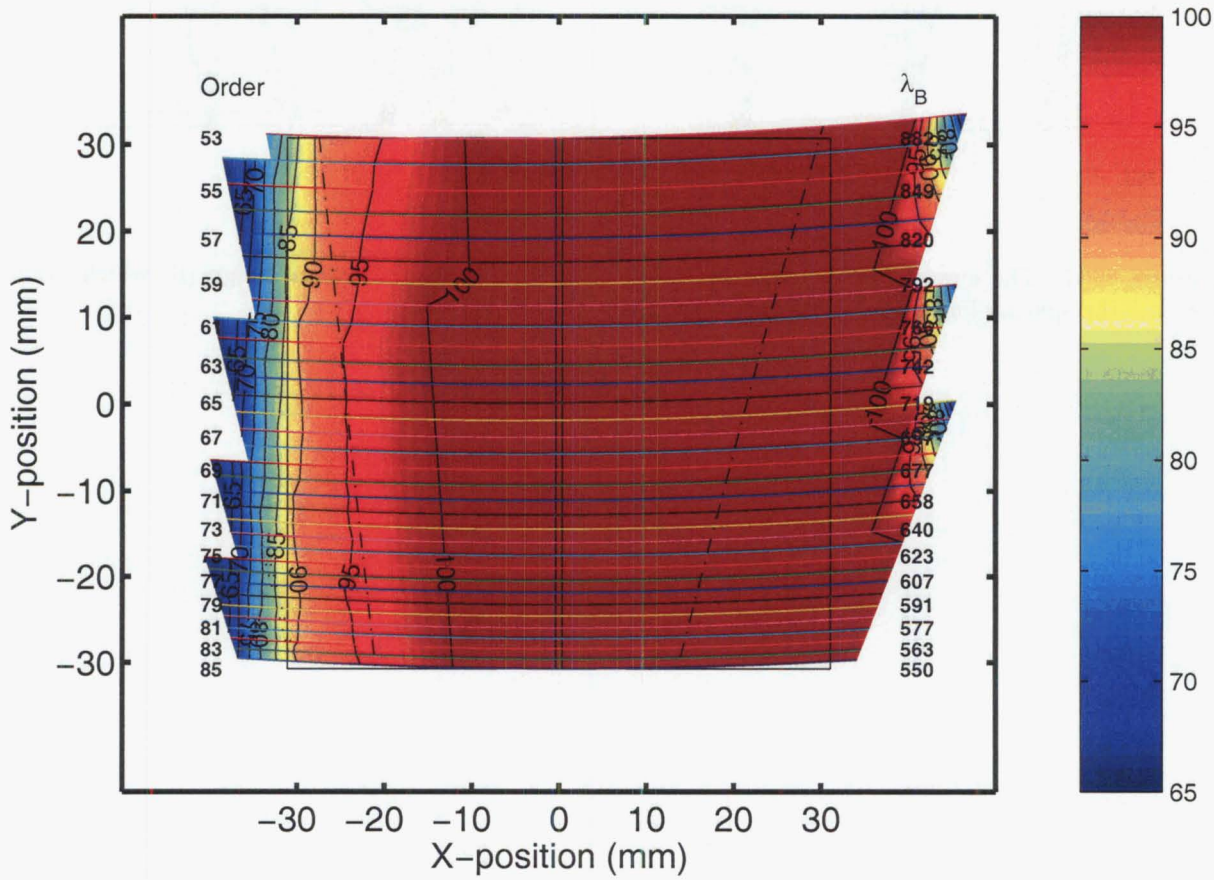

Figure E.36: The vignetting of the red camera with reduced apertures.

Field-flattening lens

The current field-flattening lens is shown in Figure E.37a. This design requires that the distance between the field-flattening lens and the CCD be as little as 1.5 mm. This is smaller than currently perceived possible by the preferred detector subcontractor and an alternative solution is shown in Figure E.37b. This design requires that the field-flattening lens be constructed from at least three pieces of two types of glass (e.g., lal7 and silica). Only the last element (silica) is cylindrical. The distance between the CCD and the lens can be increased to more than 3 mm before the image quality deteriorates significantly.

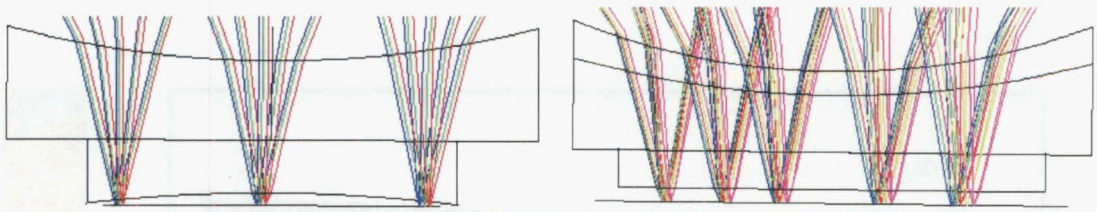

(a) (b)

Figure E.37: The current camera field-flattening lens (a) and an alternative design (b) which would increase the spacing between the CCD and this lens.

Bibliography

Alekseeva, G. A.; Arkharov, A. A.; Galkin, V. D.; Hagen-Thorn, E. I.; Nikanorova, I. N.; Novikov, V. V.; Novopashenny, V. B.; Pakhomov, V. P.; Ruban, E. V. and Shchegolev, D. E.: "Pulkovo Spectrophotometric Catalog (Alekseeva+ 1997)", *VizieR Online Data Catalog*, **3201**, pp. 0–+, 1997 Sep.

Angel, J. R. P.; Adams, M. T.; Boroson, T. A. and Moore, R. L.: "A very large optical telescope array linked with fused silica fibers", *ApJ*, **218**, pp. 776–782, 1977 Dec.

Baranne, A.; Queloz, D.; Mayor, M.; Adrianzyk, G.; Knispel, G.; Kohler, D.; Lacroix, D.; Meunier, J.-P.; Rimbaud, G. and Vin, A.: "ELODIE: A spectrograph for accurate radial velocity measurements.", *A&AS*, **119**, pp. 373–390, 1996 Oct.

Barden, S. C.; Arns, J. A.; Colburn, W. S. and Williams, J. B.: "Volume-Phase Holographic Gratings and the Efficiency of Three Simple Volume-Phase Holographic Gratings", *PASP*, **112**, pp. 809–820, 2000 Jun.

Barden, S. C. and Wade, R. A.: "DensePak and spectral imaging with fiber optics", in "ASP Conf. Ser. 3: Fiber Optics in Astronomy", pp. 113–124, 1988.

Barnes, S. and Albrow, M.: "Revised SALT HRS concept proposal", *A presentation to the* SALT *Science Working Group*, 2002 Oct.

Barnes, S.; Cottrell, P.; Albrow, M. and Kershaw, G.: "3210AE0001: SALT HRS optical design defintion document", *A presentation to the* SALT *Science Working Group*, 2003 Sep.

Barnes, S. I.; Clark, M.; Cottrell, P. L.; Hearnshaw, J. B.; Petterson, O. K. L.; Pollard, K. R.; Pritchard, J. D.; Richards, A. and Tobin, W.: "Characteristics of the Mt John Series 200 CCD system", *Southern Stars*, **39**, pp. 1–8, 2000.

Bernstein, G. M.; Athey, A. E.; Bernstein, R.; Gunnels, S. M.; Richstone, D. O. and Shectman, S. A.: "Volume-phase holographic spectrograph for the Magellan telescopes", in "Proc. SPIE Vol. 4485, p. 453-459, Optical Spectroscopic Techniques, Remote Sensing, and Instrumentation for Atmospheric and Space Research IV, Allen M. Larar; Martin G. Mlynczak; Eds.", pp. 453–459, 2002 Jan.

Bingham, R. G.: "Grating spectrometers and spectrographs re-examined", *QJRAS*, **20**, pp. 395–421, 1979 Dec.

Bottema, M.: "Echelle efficiencies - theory and experiment; comment", *Appl. Opt.*, **20**, pp. 528–530, 1981 Feb.

Bowen, I. S.: "The Image-Slicer a Device for Reducing Loss of Light at Slit of Stellar Spectrograph.", *ApJ*, **88**, pp. 113–+, 1938 Sep.

Breger, M.: "Catalog of spectrophotometric scans of stars.", *Astrophys. J., Suppl. Ser.*, **32**, pp. 7–87, 1976 Sep.

Brown, T. M.: "High precision Doppler measurements via echelle spectroscopy", in "ASP Conf. Ser. 8: CCDs in astronomy", pp. 335–344, 1990.

Brown, T. M.; Noyes, R. W.; Nisenson, P.; Korzennik, S. G. and Horner, S.: "The AFOE: A spectrograph for precise Doppler studies", *PASP*, **106**, pp. 1285–1297, 1994 Dec.

Buckley, D. A. H.: "Annual Report of the SAAO", p. 35, 1995.

Buckley, D. A. H.: "SALT Science Requirements", SALT *Document DB000531*, 2000.

Buckley, D. A. H.: "Summary of SALT HRS Preliminary Design Review", SALT *internal document*, 2003 September.

Buckley, D. A. H.; Cottrell, P. L.; Nordsieck, K. H.; O'Donoghue, D. E. and Williams, T. B.: "The first-generation instruments for the Southern African Large Telescope (SALT)", in "UV and Gamma-Ray Space Telescope Systems. Edited by Hasinger, Günther; Turner, Martin J. L. Proceedings of the SPIE, Volume 5492, pp. 60-74 (2004).", pp. 60–74, 2004 Sep.

Buckley, D. A. H. and Sessions, N.: "FIF pre-CDR", SALT *document SALT-3400-AE-0024*, 2004.

Carrasco, E. and Parry, I. R.: "A method for determining the focal ratio degradation of optical fibres for astronomy", *MNRAS*, **271**, pp. 1–12, 1994 Nov.

Castilho, B. V.; Delabre, B.; Gneiding, C. D. and Tull, R. G.: "New solution in echelle crossdispersing - the soar telescope echelle spectrograph", *Bulletin of the Astronomical Society of Brazil*, **23**, pp.

195–195, 2003 Aug.

Clemens, J. C. and Seagroves, S.: "Volume holographic gratings", Tech. rep., Goodman Laboratory, 1999.

Comte, A.: *Cours de Philosphie Positive*, chap. II, 19th lesson, 1835.

Cuillandre, J.; Fort, B. P.; Picat, J. and Soucail, G.: "Back and forth spectroscopy: optimization of an optical nod-and-shuffle technique to reach fainter objects and increase the multiplex gain on multi-object spectrographs", in "Instrument Design and Performance for Optical/Infrared Ground-based Telescopes. Edited by Iye, Masanori; Moorwood, Alan F. M. Proceedings of the SPIE, Volume 4841, pp. 1531-1538 (2003).", pp. 1531–1538, 2003 Mar.

Cummings, I. N.; Hearnshaw, J. B.; Kilmartin, P. M. and Gilmore, A. C.: "High-Precision Radial-Velocity Measurements of Late-Type Evolved Stars", in "ASP Conf. Ser. 185: IAU Colloq. 170: Precise Stellar Radial Velocities", pp. 204–210, 1999.

D'Arrigo, P.; Bingham, R.; Diego, F.; Crawford, I.; A., C.; Savidge, T. and Percival, J.: "Optical Design Definition Document for High Resolution Optical Spectrograph (HROS) (CDR version)", Tech. rep., University College London, 2000 Apr.a.

D'Arrigo, P.; Bingham, R. G.; Charalambous, A.; Crawford, I. A.; Diego, F.; Percival, J. F. and Savidge, T. E.: "Design of the high-resolution optical spectrograph (HROS) for the Gemini telescope", in "Proc. SPIE Vol. 4008, p. 159-166, Optical and IR Telescope Instrumentation and Detectors, Masanori Iye; Alan F. Moorwood; Eds.", pp. 159–166, 2000 Aug.b.

Dekker, H.; D'Odorico, S.; Kaufer, A.; Delabre, B. and Kotzlowski, H.: "Design, construction, and performance of UVES, the echelle spectrograph for the UT2 Kueyen Telescope at the ESO Paranal Observatory", in "Proc. SPIE Vol. 4008, p. 534-545, Optical and IR Telescope Instrumentation and Detectors, Masanori Iye; Alan F. Moorwood; Eds.", vol. 4008, pp. 534–545, 2000 Aug.

Dekker, H.; Nissen, P. E.; Kaufer, A.; Primas, F.; D'Odorico, S. and Hanuschik, R. W.: "High S/N, high resolution Image Slicer observations with UVES", in "Specialized Optical Developments in Astronomy. Edited by Atad-Ettedgui, Eli; D'Odorico, Sandro. Proceedings of the SPIE, Volume 4842, pp. 139-150 (2003).", pp. 139–150, 2003 Feb.

Diego, F. and Walker, D. D.: "On the possibility of increasing the throughput of astronomical spectrographs by overfilling the dispersing element", *MNRAS*, **217**, pp. 347–354, 1985 Nov.

Epps, H. W. and Vogt, S. S.: "Extremely achromatic f/1.0 all-spherical camera constructed for the high-resolution echelle spectrometer of the Keck telescope", *Appl. Opt.*, **32**, pp. 6270–6279, 1993 Nov.

Erasmus, A.: "SALT Site Survey Results", *SAAO Newsletter*, p. 32, 1999.

Fabricant, D. G.; Szentgyorgyi, A. and Epps, H. W.: "Segmented Zero-Deviation Cross-Dispersion Prisms for the Hectochelle Multiobject Spectrograph", *PASP*, **115**, pp. 235–242, 2003 Feb.

Glazebrook, K. and Bland-Hawthorn, J.: "Microslit Nod-Shuffle Spectroscopy: A Technique for Achieving Very High Densities of Spectra", *PASP*, **113**, pp. 197–214, 2001 Feb.

Harrison, G. R.: "The production of diffraction gratings: I. the design of échelle gratings and spectrographs", *J. Opt. Soc. Am.*, **39**, pp. 522–528, 1949.

Harrison, G. R.; Loewen, E. G. and Wiley, R. S.: "Echelle gratings: their testing and improvement", *Appl. Opt.*, **15**, pp. 971–976, 1976 Apr.

Heacox, W. D.: "Radial image transfer by cylindrical, step-index optical waveguides", *Optical Society of America, Journal, A: Optics and Image Science (ISSN 0740-3232), vol. 4, March 1987, p. 488-493.*, **4**, pp. 488–493, 1987 Mar.

Hearnshaw, J.: *The analysis of starlight: one hundred and fifty years of astronomical spectroscopy*, Cambridge University Press, 1986.

Hearnshaw, J.; Barnes, S.; Cottrell, P. and Kershaw, G.: "Draft Preliminary Design Document for CELESTIA", *A presentation to the* SALT *Science Working Group*, 2001 Oct.

Hearnshaw, J.; Rumsey, N. and Nankivell, G.: "Some comments on the design of échelle spectrographs using R2 or R4 gratings for precise radial velocity measurements", in "ASP Conf. Ser. 185: IAU Colloq. 170: Precise Stellar Radial Velocities", pp. 29–35, 1999.

Hearnshaw, J. B.: "The Cassegrain Echelle Spectrograph at Mt. John Observatory", *Proceedings of the Astronomical Society of Australia*, **3**, pp. 102–103, 1977 Sep.

Hearnshaw, J. B.: "An echelle spectrograph", *S&T*, **56**, pp. 6–8, 1978 Jul.

Hearnshaw, J. B.; Barnes, S. I.; Kershaw, G. M.; Frost, N.; Graham, G.; Ritchie, R. and Nankivell, G. R.: "The Hercules Échelle Spectrograph at Mt. John", *Experimental Astronomy*, **13**, pp. 59–76, 2002.

Hill, J. M.; Angel, J. R. P.; Scott, J. S.; Lindley, D. and Hintzen, P.: "Multiple object spectroscopy - The Medusa spectrograph", *ApJ*, **242**, pp. L69–L72, 1980 Dec.

Hubbard, E. N.; Angel, J. R. P. and Gresham, M. S.: "Operation of a long fused silica fiber as a link between telescope and spectrograph", *ApJ*, **229**, pp. 1074–1078, 1979 May.

Huggins, W.: *The Nineteenth Century Review*, 1897 Jun.

Hunter, T. R. and Ramsey, L. W.: "Scrambling properties of optical fibers and the performance of a double scrambler", *PASP*, **104**, pp. 1244–1251, 1992 Dec.

Jacquinot, P.: "The lminosity of spectrometers with prisms, gratings, or Fabry-Perot etalons", *J. Opt. Soc. Am.*, **44**, pp. 761–765, 1954.

Kaufer, A.: "A Two-Beam Two-Slice Image Slicer for Fiber-Linked Spectrographs", in "ASP Conf. Ser. 152: Fiber Optics in Astronomy III", pp. 337–+, 1998.

Kaufer, A.; Stahl, O.; Tubbesing, S.; Nørregaard, G., P.and Avila; Francois, P.; Pasquini, L. and Pizzella, A.: "Commissioning FEROS, the new high-resolution spectrograph at La Silla", *Messenger*, **95**, pp. 8–18, 1999.

Kershaw, G. M. and Hearnshaw, J. B.: "High precision radial velocities using an optical fibre feed", *Southern Stars*, **33**, pp. 89–97, 1989.

Kirchhoff, G. and Bunsen, R.: *Poggendorff's Ann.*, **110**, 1860.

Kitchin, C. J.: *Optical Astronomical Spectroscopy*, Institute of Physics Publishing, 1995.

Knyazeva, L. N. and Kharitonov, A. V.: "Energy distribution in stars at 320-760 nm (Knyazeva+, 1996)", *VizieR Online Data Catalog*, **3186**, pp. 0–+, 1996 Nov.

Libbrecht, K. G. and Peri, M. L.: "A fiber-fed echelle spectrograph for the hale 5-m telescope", *PASP*, **107**, pp. 62–67, 1995 Jan.

MacQueen, P. J.: *Solid-state image detector development: a Linear Diode Array for astronomical spectroscopy*, Ph.D. thesis, University of Canterbury, 1986.

Mayor, M.; Pepe, F.; Queloz, D.; Bouchy, F.; Rupprecht, G.; Lo Curto, G.; Avila, G.; Benz, W.; Bertaux, J.-L.; Bonfils, X.; dall, T.; Dekker, H.; Delabre, B.; Eckert, W.; Fleury, M.; Gilliotte, A.; Gojak, D.; Guzman, J. C.; Kohler, D.; Lizon, J.-L.; Longinotti, A.; Lovis, C.; Megevand, D.; Pasquini, L.; Reyes, J.; Sivan, J.-P.; Sosnowska, D.; Soto, R.; Udry, S.; van Kesteren, A.; Weber, L. and Weilenmann, U.: "Setting New Standards with HARPS", *The Messenger*, **114**, pp. 20–24, 2003 Dec.

Meiring, J. G. and Buckley, D. A. H.: "Southern African Large Telescope (SALT) project progress and status after four years", in "Proceedings of the SPIE, Volume 5489, pp. 592-602 (2004).", pp. 592–602, 2004 Oct.

Merrill, P. W.: "A Plane-Grating Spectrograph for the Red and Infra-Red Regions of Stellar Spectra", *ApJ*, **74**, pp. 188–+, 1931 Oct.

Michelson, A. A.: "The Echelon Spectroscope", *ApJ*, **8**, pp. 37–+, 1898 Jun.

Moffat, A. F. J.: "A Theoretical Investigation of Focal Stellar Images in the Photographic Emulsion and Application to Photographic Photometry", *A&A*, **3**, pp. 455–+, 1969 Dec.

Mohr, J. L.; Johnston, R. A.; Lane, R. G. and Cottrell, P. L.: "Adaptive optics at Mount John University Observatory", in "Proceedings of Image and Vision Computing New Zealand 2004", pp. 233–236, Akaroa, New Zealand, 2004 21–23 November.

Murdoch, K. A.; Hearnshaw, J. B. and Clark, M.: "A search for substellar companions to southern solar-type stars", *ApJ*, **413**, pp. 349–363, 1993 Aug.

Nankivell, G. R. and Rumsey, N. J.: "The Optical System of the MT.JOHN 1-METRE Telescope", in "IAU Symp. 118: Instrumentation and Research Programmes for Small Telescopes", pp. 101–+, 1986.

Noguchi, K.; Aoki, W.; Kawanomoto, S.; Ando, H.; Honda, S.; Izumiura, H.; Kambe, E.; Okita, K.; Sadakane, K.; Sato, B.; Tajitsu, A.; Takada-Hidai, T.; Tanaka, W.; Watanabe, E. and Yoshida, M.: "High Dispersion Spectrograph (HDS) for the Subaru Telescope", *PASJ*, **54**, pp. 855–864, 2002 Dec.

Nordsieck, K. H.; Burgh, E. B.; Kobulnicky, H. A.; Williams, T. B.; O'Donoghue, D.; Percival, J. W. and Smith, M. P.: "The Prime Focus Imaging Spectrograph for the Southern African Large Telescope", *Bulletin of the American Astronomical Society*, **33**, pp. 1465–+, 2001 Dec.

O'Donoghue, D.; Bauermeister, E.; Carter, D. B.; Evans, G. P.; Koorts, W. P.; O'Connor, J.; Osman, F.; van der Merwe, S. and Bigelow, B. C.: "SALTICAM: $0.5M acquisition camera: every big telescope should have one", in "Instrument Design and Performance for Optical/Infrared Ground-based Telescopes. Edited by Iye, Masanori; Moorwood, Alan F. M. Proceedings of the SPIE, Volume 4841, pp. 465-476 (2003).", pp. 465–476, 2003 Mar.

Pallavicini, R.; Zerbi, F. M.; Spano, P.; Conconi, P.; Mazzoleni, R.; Molinari, E. and Strassmeier, K. G.: "The ICE spectrograph for PEPSI at the LBT: preliminary optical design", in "Instrument Design and Performance for Optical/Infrared Ground-based Telescopes. Edited by Iye, Masanori; Moorwood,

Alan F. M. Proceedings of the SPIE, Volume 4841, pp. 1345-1356 (2003).", pp. 1345–1356, 2003 Mar.

Palmer and Verrill: "Diffraction gratings", *Contemp. Phys.*, **9**, pp. 257–276, 1968.

Palmer, C.: *Diffraction Grating Handbook*, Richardson Grating Laboratory, 2000.

Pfeiffer, M. J.; Frank, C.; Baumueller, D.; Fuhrmann, K. and Gehren, T.: "FOCES - a fibre optics Cassegrain Echelle spectrograph", *A&AS*, **130**, pp. 381–393, 1998 Jun.

Racine, R.: "The Telescope Point Spread Function", *PASP*, **108**, pp. 699–706, 1996 Aug.

Ramm, D.: "Atlas of thorium and argon spectra", , 2003 March.

Ramm, D. J.; Skuljan, J. and Hearnshaw, J. B.: "The orbit of a new double-lined spectroscopic binary: HD 161958", *The Observatory*, **124**, pp. 167–173, 2004 Jun.

Ramsey, L. W.: "Focal ratio degradation in optical fibers of astronomical interest", in S. C. Barden (ed.), "Fiber Optics in Astronomy, Astronomical Society of the Pacific Conference Series", vol. 3, pp. 26–40, 1988 Aug.

Richardson, E. H.; Moore, A.; Tilleman, T. and Crampton, D.: "Focussing Image Slicers: Refractive and Reflective (Poster)", in "ASP Conf. Ser. 195: Imaging the Universe in Three Dimensions", pp. 540–+, 2000.

Schroeder, D. J.: "Echelle efficiencies - theory and experiment; author's reply to comment", *Appl. Opt.*, **20**, pp. 530–531, 1981 Feb.

Schroeder, D. J.: *Astronomical Optics*, Academic Press, 2nd ed., 2000.

Schroeder, D. J. and Hilliard, R. L.: "Echelle efficiencies - theory and experiment", *Appl. Opt.*, **19**, pp. 2833–2841, 1980 Aug.

Sheinis, A. I.; Bolte, M.; Epps, H. W.; Kibrick, R. I.; Miller, J. S.; Radovan, M. V.; Bigelow, B. C. and Sutin, B. M.: "ESI, a New Keck Observatory Echellette Spectrograph and Imager", *PASP*, **114**, pp. 851–865, 2002 Aug.

Skuljan, J.; Hearnshaw, J. B. and Cottrell, P. L.: "Absolute Radial Velocities by Cross-Correlation with Synthetic Spectra", in "ASP Conf. Ser. 185: IAU Colloq. 170: Precise Stellar Radial Velocities", pp. 91–101, 1999.

Skuljan, J.; Ramm, D. J. and Hearnshaw, J. B.: "Accurate orbital parameters for the bright southern spectroscopic binary ζ Trianguli Australis - an interesting case of a near-circular orbit", *MNRAS*, **352**, pp. 975–983, 2004 Aug.

Stobie, R.; Meiring, J. and Buckley, D. A.: "Design of the Southern African Large Telescope (SALT)", in "Proc. SPIE Vol. 4003, p. 355-362, Optical Design, Materials, Fabrication, and Maintenance, Philippe Dierickx; Ed.", pp. 355–362, 2000 Jul.

Swart, G.: "SALT Specification and Error Budget Status", *A presentation to* SSWG, 2001.

Swat, A.; O'Donoghue, D.; Swiegers, J.; Nel, L. and Buckley, D. A. H.: "The optical design of the Southern African Large Telescope", in "Large Ground-based Telescopes. Edited by Oschmann, Jacobus M.; Stepp, Larry M. Proceedings of the SPIE, Volume 4837, pp. 564-575 (2003).", pp. 564–575, 2003 Feb.

Szentgyorgyi, A. H.; Cheimets, P.; Eng, R.; Fabricant, D. G.; Geary, J. C.; Hartmann, L.; Pieri, M. R. and Roll, J. B.: "Hectochelle: a multiobject echelle spectrograph for the converted MMT", in "Proc. SPIE Vol. 3355, p. 242-252, Optical Astronomical Instrumentation, Sandro D'Odorico; Ed.", pp. 242–252, 1998 Jul.

Szentgyorgyi, A. H.; Fabricant, D. G.; Brown, W. R. and Epps, H. W.: "Cross dispersion and an integral field unit for Hectochelle", in "Instrument Design and Performance for Optical/Infrared Ground-based Telescopes. Edited by Iye, Masanori; Moorwood, Alan F. M. Proceedings of the SPIE, Volume 4841, pp. 1026-1035 (2003).", pp. 1026–1035, 2003 Mar.

Tobin, W.: "Gain, noise and related characteristics of the Mt John Photometrics CCD system", *Southern Stars*, **34**, pp. 421–429, 1992.

Tobin, W.; Hearnshaw, J. B.; Kershaw, G. M.; Nankivell, G. R.; Persson, S.; Rumsey, N. J. and Thirkettle, R.: "A focal reducer for the Mt John échelle spectrograph", *Southern Stars*, **37**, pp. 197–205, 1998.

Tull, R. G.: "High-resolution fiber-coupled spectrograph of the Hobby-Eberly Telescope", in "Proc. SPIE Vol. 3355, p. 387-398, Optical Astronomical Instrumentation, Sandro D'Odorico; Ed.", pp. 387–398, 1998 Jul.

Vaughnn, D.: "What's wrong with the throughput-resolution product? A fiber-fed spectrograph forces a reevaluation of instrument design parameters", in "Proc. SPIE Vol. 2198, p. 31-43, Instrumentation in Astronomy VIII, David L. Crawford; Eric R. Craine; Eds.", vol. 2198, pp. 31–43, 1994 Jun.

Vogt, S. S.; Allen, S. L.; Bigelow, B. C.; Bresee, L.; Brown, B.; Cantrall, T.; Conrad, A.; Couture, M.; Delaney, C.; Epps, H. W.; Hilyard, D.; Hilyard, D. F.; Horn, E.; Jern, N.; Kanto, D.; Keane, M. J.;

Kibrick, R. I.; Lewis, J. W.; Osborne, J.; Pardeilhan, G. H.; Pfister, T.; Ricketts, T.; Robinson, L. B.; Stover, R. J.; Tucker, D.; Ward, J. and Wei, M. Z.: "HIRES: the high-resolution echelle spectrometer on the Keck 10-m Telescope", in "Proc. SPIE Vol. 2198, p. 362-375, Instrumentation in Astronomy VIII, David L. Crawford; Eric R. Craine; Eds.", pp. 362–375, 1994 Jun.

Walker, D. D. and Diego, F.: "Design philosophy of the forthcoming echelle spectrographs for the AAT and LPO", *MNRAS*, **217**, pp. 355–365, 1985 Nov.

Walraven, T. and J.H, W.: in S. Lausten and A. Riez (eds.), "Aux. Instrumentation for Large Telescopes", p. 175, 1972.

Wood, R. W.: "The échelette grating for the infra-red", *Phil. Mag.*, **20**, pp. 770–778, 1910.